New perspectives on the evolution of B-lymphocytes in germinal centers

DISSERTATION

zur Erlangung des akademischen Grades
doctor rerum naturalium
(Dr. rer. nat.)
im Fach Biologie

eingereicht an der
Mathematisch-Naturwissenschaftlichen Fakultät I
Humboldt-Universität zu Berlin

von
Frau Dipl.-Ing. Nicole Wittenbrink
geboren am 19.08.1975 in Gütersloh

Präsident der Humboldt-Universität zu Berlin:
Prof. Dr. Christoph Markschies

Dekan der Mathematisch-Naturwissenschaftlichen Fakultät I:
Prof. Dr. Christian Limberg

Gutachter:

1. Dr. Michal Or-Guil
2. PD Dr. Rudolf Manz
3. Prof. Dr. Hans-Dieter Volk

eingereicht am:	21. Mai 2007
Tag der mündlichen Prüfung:	21. November 2007

One cannot divine nor forcast the conditions that will make happiness; one only stumbles upon them by chance, in a lucky hour, at the world's end somewhere, and holds fast to the days, as to fortune or fame.

Willa Cather, Le Levandou, 1902

Abstract

Central to the humoral immune response is the commonly observed improvement of antibody affinity over time, a phenomenon referred to as AFFINITY MATURATION. Affinity maturation takes place in so-called GERMINAL CENTERS (GC) that are transiently formed in secondary lymphoid tissues (e.g. spleen) following immunization with T cell-dependent antigens. Within GC, B LYMPHOCYTES are subjected to a micro-evolutionary process that includes multiple rounds of diversification of their B cell receptors (BCRs) by somatic hypermutation (SHM) and subsequent SELECTION of those B cells showing improved binding characteristics towards the antigen. However, despite recent advances in defining the mechanisms contributing to diversification of B lymphocytes within GC, the dynamics, mechanisms and forces of their selection are poorly understood. The current thesis aims at providing new insights into the evolution of B cells within GC by assessing the overall GC growth behavior (Chapter 4), by documenting changes of the cellular composition of GC over time (Chapter 5) and by, for the first time, specifying the kinetics (Chapter 5) and sequence properties (Chapter 6) of negative selection occurring within GC.

The results obtained during cross-sectional evaluation of spleen sections revealed a robust average growth kinetics of GC, that was, however, based on a notable size distribution of GC within individual sections. This could not be explained by random sectioning of GC. However, simulations of random sectioning of hypothetical ensemble kinetics have shown that the experimentally recorded cross-sectional profile of GC growth is consistent with others than the accepted notion. To solve this problem, GC growth was subsequently addressed by three-dimensional volumetric evaluation of splenic GC, that finally contradicted the accepted notion by revealing non-synchronized formation and growth of GC as characterized by ongoing new formation and marked, broad volume distributions of GC. According to these findings, a revised model of affinity maturation was proposed that involves recirculation of GC emigrant B cells and a multilevel selection strategy (intercalation of local and global selection).

It was further shown that the kinetics of GC T cells and macrophages follow the overall growth kinetics of GC. However, whereas T cells populated B cell zones not until antigenic challenge, macrophages already represented a constituent cell population of primary B cell follicles. Noteworthy, the number of macrophages was found to strictly correlate with the underlying size of B cell zones. In this context, an acquired imbalance due to phagocytosis-induced macrophage death was further shown to be associated with disease progression in the NZB/W autoimmune mouse model of systemic lupus erythematosus (SLE). Furthermore, costaining of macrophages and apoptotic cells revealed that cell death occurs throughout GC, thereby indicating that selection takes place in both, dark and light zones of GC.

The establishment of a reliable method for recovery of primary BCR sequences of phagocytosed GC B cells has proven to be powerful, in that it provides new insights into the selection process of GC B cells by, for the first time, allowing for access to yet unexplored negatively selected GC B cells. In this context, the traditionally proposed molecular signatures - as for instance the distribution of mutations within framework (FR) and complementary determining regions (CDRs), ratios of replacement (R) to silent mutations (S) and the incidence of key mutations - were all shown to fail to demarcate winners and losers of selection. The obtained results indicated that the survival fate of GC B cells is governed by the cumulative effect of replacement mutations within CDRs, though, in which the as yet proposed positive effect of R mutations turned out to be overemphasized. By contrast, R mutations in CDRs turned out to possess marked deleterious effects, thereby lending support to the proposition that survival of GC B cells is particularly driven by the absence of excess mutations within CDRs that have an adverse effect with respect to antigen binding. Moreover, the high interclonal diversity of phagocytosed B cell fractions demonstrated that interclonal competition is sustained throughout the GC response most probably incited by ongoing replenishment of the pool of interacting B cells. Finally, this finding closes the circle to the central asssumption of the revised model of affinity maturation, that is recirculation of GC emigrant B cells.

In conclusion, the current thesis provides new insights into the evolution of B cells within GC by proposing:

- non-synchronized GC formation and growth
- a multilevel selection strategy (intercalation of local and global selection by recirculation of GC emigrant B cells)
- a central role for macrophages in retaining germinal center B cell homeostasis and preventing autoimmunity
- the failure of commonly supposed molecular signatures to demarcate positively and negatively selected B cells
- survival fate of GC B cells is particularly driven by absence of excess mutations within CDRs that have an adverse effect with respect to antigen binding

Keywords:
B lymphocytes, affinity maturation, germinal center, selection

Zusammenfassung

Ein zentrales Merkmal der humoralen Antwort ist die im Laufe der Zeit ansteigende Affinität der Antikörper gegenüber dem Antigen, ein Phänomen, das man generell als Affinitätsreifung bezeichnet. Die Affinitätsreifung von Antikörpern ist an die transiente Ausbildung von Keimzentren gebunden, die man nach Immunisierung mit einem T-Zell-abhängigen Antigen in sekundär lymphatischen Geweben wie der Milz beobachtet. Innerhalb der Keimzentren durchlaufen B-Zellen einen mikro-evolutionären Prozess, in dessen Verlauf es zu einer Diversifizierung der von den B-Zellen kodierten B-Zell-Rezeptoren durch somatische Hypermutation und anschließender Selektion derjenigen B-Zellen mit den besten Bindungseigenschaften gegenüber dem Antigen kommt. In den letzten Jahren waren große Fortschritte hinsichtlich der Aufklärung der molekularen Mechanismen die zur Diversifizierung der B-Zell-Rezeptoren beitragen zu verzeichnen, wohingegen die Dynamik, der Mechanismus und die treibenden Kräfte der Selektion bisher weitgehend unverstanden sind. Das Ziel dieser Arbeit ist es zum Verständnis der Evolution von B-Zellen in Keimzentren beizutragen. Aus diesem Grund wurden das Wachstumsverhalten von Keimzentren (Kapitel 4) und die Veränderung der zellulären Zusammensetzung von Keimzentren (Kapitel 5) untersucht. Des Weiteren wurde in dieser Arbeit zum ersten Mal auch die Kinetik der negativen Selektion (Kapitel 5) aufgenommen sowie die B-Zell-Rezeptor Sequenzen von negativ selektierten Keimzentrums B-Zellen analysiert (Kapitel 6).

Anhand der Auswertung von Milzschnitten konnte eine robuste mittlere Größenkinetik von Keimzentrumsflächen nachgewiesen werden, die jedoch auf einer ausgeprägten Größenverteilung von Keimzentren innerhalb der einzelnen Schnitte beruhte. Diese ließ sich nicht durch zufälliges Anschneiden der Keimzentren erklären. Des Weiteren wurde anhand von Simulationen gezeigt, dass das Profil der experimentell aufgenommenen Größenverteilungen von Keimzentren nicht nur mit dem traditionell angenommenen synchronisierten Wachtumsverhalten von Keimzentren, sondern auch mit anderen hypothetischen Wachstumskinetiken übereinstimmt. Die anschließend durchgeführte dreidimensionale, volumetrische Analyse hat gezeigt, dass das Wachstumverhalten von Keimzentren - anders als bisher angenommen - nicht-synchronisiert ist und sich durch fortgesetzte Neuformation und beträchtliche Volumenverteilungen von Keimzentren auszeichnet. Auf Grundlage dieser Ergebnisse wurde ein neues, überarbeitetes Modell der Affinitätsreifung entwickelt, dessen Hauptmerkmale die Rezirkulation von ausgewanderten Keimzentrums-B-Zellen sowie die zusätzliche Einführung eines globalen Selektionsprozesses sind.
Es wurde weiterhin gezeigt, dass die Kinetiken von Keimzentrums-T-Zellen und Makrophagen der mittleren Gesamtwachstumskinetik der Keimzentren folgen. Die Besiedlung der B-Zell-Zonen durch T-Zellen setzte erst nach der Immunisierung ein, dagegen waren Makrophagen bereits in B-Zell-Zonen naiver Mäuse nachweisbar. Dazu konnte nachgewiesen werden, dass die Anzahl der Makrophagen strikt mit der Größe der B-Zell-Zonen korreliert. Ein durch Zelltod von Makrophagen erworbenes

Ungleichgewicht zwischen Makrophagen und B-Zellen konnte mit dem Fortschreiten der Erkrankung in NZB/W Mäusen, einem Mausmodell für systemischen Lupus erythematodes (SLE), in Verbindung gebracht werden. Die Analyse der Kinetik und der Lokalisation von apoptotischen Zellen hat des Weiteren gezeigt, dass Selektion sowohl in der dunklen als auch in der hellen Zone von Keimzentren stattfindet.
Die Etablierung einer Methode zur Gewinnung von B-Zell-Rezeptor Sequenzen von phagozytierten B-Zellen hat sich als sehr effektiv erwiesen, da sie zum ersten Mal die Betrachtung von bis dahin völlig unerforschten negativ selektierten Keimzentrums-B-Zellen zuließ und auf diesem Weg zu neuen Erkenntnissen bezüglich des Selektionsprozesses geführt hat. In diesem Zusammenhang konnte gezeigt werden, dass die bisher angenommenen molekularen Signaturen wie z.B. die Verteilung der Mutationen in den Gerüst (FR)- und komplementaritätsbestimmenden Regionen (CDR), das Verhältnis von Austauschmutationen zu stillen Mutationen (R/S) sowie das Vorkommen von Schlüsselmutationen, keine Unterscheidung bzw. Identifizierung von Gewinnern und Verlierern der Selektion zulassen. Dahingegen hat sich die kumulative Wirkung von Austauschmutationen in den CDRs als ein für das Überleben von Keimzentrums-B-Zellen sehr wichtiges Kriterium herausgestellt, wobei jedoch nicht wie bisher angenommen der positive Effekt, sondern die schädliche Wirkung von Austauschmutationen entscheidend ist. Das Überleben von Keimzentrums-B-Zellen ist demnach von der Abwesenheit überschüssiger, nachteiliger Mutationen in den CDRs abhängig. Die hohe interklonale Diversität der phagozytierten B-Zellen hat zusätzlich gezeigt, dass es einen andauernden interklonalen Wettbewerb von Keimzentrums-B-Zellen gibt, der wahrscheinlich durch ständiges "Äuffüllen"des Pools interagierender B-Zellen angetrieben wird. Hier schließt sich der Kreis zum Kernpunkt des überarbeiteten Models der Affinitätsreifung, der Rezirkulation von ausgewanderten Keimzentrums-B-Zellen.

In Kürze zusammengefasst trägt diese Arbeit durch folgende Erkenntnisse zum Verständnis der Evolution von B-Zellen in Keimzentren bei:

- nicht-synchronisiertes Wachstumsverhalten von Keimzentren
- mehrstufige Selektionsstrategie (Verknüpfung von lokaler und globaler Selektion durch Rezirkulation von ausgewanderten Keimzentrums-B-Zellen)
- zentrale Rolle von Makrophagen für die Homöostase von Keimzentren und die Verhinderung von Autoimmunität
- bisher angenommene molekulare Signaturen sind unzulänglich, um posititv und negativ selektierte B-Zellen zu unterscheiden
- das Überleben bzw. positive Selektion von Keimzentrums-B-Zellen ist von der Abwesenheit überschüssiger, nachteiliger Mutationen in den CDRs abhängig

Schlagwörter:
B-Zellen, Affinitätsreifung, Keimzentrum, Selektion

MEINEN ELTERN ♡

Contents

List of Figures **xii**

List of Tables **xv**

1 Introduction **1**
- 1.1 The immune response . . . 1
- 1.2 Mission of B cells and their antibodies . . . 2
  - 1.2.1 The molecular structure of antibodies . . . 2
  - 1.2.2 Antibody diversity . . . 3
  - 1.2.3 Development and maturation of B lymphocytes . . . 4
- 1.3 The architecture of the spleen and migratory pathways . . . 5
- 1.4 The formation of germinal centers (GC) . . . 7
  - 1.4.1 Commitment of B cells to GC . . . 8
  - 1.4.2 Cellular players of GC . . . 8
  - 1.4.3 Affinity maturation . . . 9
  - 1.4.4 Assessing the transient nature of germinal centers . . . 11
  - 1.4.5 Contribution of germinal centers to autoimmunity . . . 14

2 Objectives **16**

3 Material and methods **17**
- 3.1 Applied software and databases . . . 17
- 3.2 Solutions and buffers . . . 18
- 3.3 Consumables supplies . . . 18
- 3.4 Mice, antigen and immunization . . . 18
- 3.5 Tissue collection and cell preparation . . . 19
- 3.6 Immunohistology . . . 19
  - 3.6.1 Cryosectioning of spleen tissue . . . 19
  - 3.6.2 Standard protocol for immunofluorescence staining . . . 20
  - 3.6.3 Detection of apoptotic cells applying TUNEL technology . . . 20
  - 3.6.4 Improvement of Ki-67 staining . . . 22
  - 3.6.5 Immunofluorescence staining of thick spleen sections . . . 22
  - 3.6.6 Establishment of four color immunofluorescence staining of macrophages, T cells, proliferating cells and FDC networks . . . 22
- 3.7 Confocal microscopy . . . 23
  - 3.7.1 Image acquisition Leica DM Ire2 . . . 23
  - 3.7.2 Image processing and quantitative analysis . . . 23

3.7.3 Image acquisition, processing and analysis for three dimensional reconstruction of murine spleens 23
3.8 3-D reconstruction 24
3.9 Flow cytometry 24
3.9.1 Extracellular staining of cells for analysis by flow cytometry . 25
3.9.2 Intracellular staining of cells for analysis by flow cytometry . . 25
3.9.3 FACS sorting of germinal center B cells and follicular Mϕ . . . 25
3.10 Molecularbiology 26
3.10.1 Isolation of RNA 26
3.10.2 Amplification of Ig light chain rearrangements 26
3.10.3 Analytical and preparative agarose gel electrophoresis 28
3.10.4 Extraction of DNA from agarose gels 29
3.10.5 Cloning of IgL amplificates 29
3.10.6 Plasmid minpreparation 31
3.10.7 Sequencing of IgL amplificates 31
3.11 Mathematical simulations 31
3.12 Statistical analysis 31

4 Revising the kinetics of germinal center growth 33
4.1 Assessing the kinetics of GC growth by 2-D cross-sectional evaluation 33
4.1.1 2-D cross-sectional evaluation of GC size and geometry 33
4.1.2 Robust overall GC growth kinetics is based upon notable size distribution of GC within individual sections 36
4.1.3 Mathematical simulation of virtual random sectioning fails to explain the high intra-section variance of GC size. 37
4.2 A theoretical approach to GC ensemble kinetics 39
4.2.1 Formulation of hypothetical growth kinetics of individual GC . 39
4.2.2 Simulation of random sectioning of different GC ensemble kinetics 40
4.3 Assessing the kinetics of GC growth by 3-D volumetric evaluation . . 41
4.3.1 3-D volumetric evaluation of GC growth kinetics 43
4.3.2 The 3-D volumetric evaluation of occupation of follicular niches indicates continuous new formation of GC throughout the immune response 43
4.3.3 3-D reconstructions reveal that GC possess an ellipsoid shape and cover a wide range of volumes 46
4.3.4 GC possess an uniform ellipsoid shape that is preserved upon GC growth and progression 50
4.3.5 The 3-D evaluation of GC size reveals a considerable volume distribution that is not consistent with the accepted notion of GC growth kinetics 53
4.4 Discussion 55
4.4.1 2-D cross-sectional evaluation of GC growth kinetics 55
4.4.2 Theoretical approach to GC ensemble kinetics 56
4.4.3 3-D volumetric evaluation of GC growth kinetics 58
4.4.4 Revised model of affinity maturation 61

5 **Kinetics of the cellular players of germinal centers** **66**
5.1 Kinetics of germinal center T cells 66
5.1.1 The number of GC T cells reflects cross-sectional GC size . . . 68
5.1.2 Very different correlation of proliferating and non-proliferating GC T cells with cross-sectional GC size 68
5.1.3 Mean kinetics of GC T cells 71
5.2 Kinetics of germinal center Mϕ 74
5.2.1 The number of GC Mϕ reflects cross-sectional GC size 76
5.2.2 Mean kinetics of GC Mϕ 76
5.2.3 GC Mϕ do not invade B cell zones due to GC formation but are already detectable in B cell zones of naive mice 77
5.2.4 The frequency of Mϕ per cross-sectional GC is regulated in a superordinate fashion by the overall B cell zone size 78
5.3 Kinetics of cell death and uptake of apoptotic cells within germinal centers 80
5.3.1 Less pronounced inner-section correlation of numbers of apoptotic nuclei and cross-sectional GC size 80
5.3.2 The number of apoptotic nuclei does not reflect cross-sectional GC size 81
5.3.3 Mean kinetics of apoptotic nuclei 83
5.3.4 Uptake of apoptotic cells by GC Mϕ 85
5.3.5 The shape of the Mϕ size distribution potentially acts as an regulatory element - Implications of a phenomenological mathematical model 88
5.4 Excursus: Perturbed GC Mϕ compartment in autoimmune NZB/W mice 93
5.4.1 Aberrant morphology of GC Mϕ in NZB/W mice 93
5.4.2 Decreased frequencies of follicular Mϕ in NZB/W mice due to disease progression 95
5.5 Discussion 98
5.5.1 Kinetics of GC T cells 98
5.5.2 GC Mϕ and uptake of apoptotic cells 99
5.5.3 An acquired imbalance of follicular Mϕ and B cells contributes to progression of autoimmunity in NZB/W mice 102

6 **Comparison of B cell receptor light chain sequences derived from living and apoptotic germinal center B cells** **106**
6.1 Strategy for identification and recovery of living and apoptotic GC B cells 106
6.2 Isolation of GC B cells and follicular Mϕ 107
6.3 IgL repertoire analysis of live and phagocytozed B cell fractions . . . 111
6.3.1 Equivalent V gene family and J gene segment use among IgL of live and phagocytozed B cell fractions 111
6.3.2 Variational kappa J gene segment use among phOx specific IgL of live and phagocytozed B cell fractions 113

6.3.3 Differences in interclonal diversity of phOx specific IgL between live and phagocytozed B cell fractions 114
6.3.4 Phagocytozed B cell fractions are generally not enriched in LCDR3s showing characteristics related to autoreactivity . . . 115
6.3.5 Accumulation of positively charged LCDR3s among phOx specific IgL sequences of phagocytozed B cells 116
6.4 Hypermutation among live and phagocytozed B cell fractions 118
6.4.1 Hypermutation of overall IgL sequences from live and phagocytozed B cell fractions 118
6.4.2 Hypermutation of phOx specific IgL sequences from live and phagocytozed B cell fractions 123
6.4.3 Special mutational events: Translational stop codons, deletions and key mutations 126
6.5 Discussion 128
6.5.1 Reliability of recovery of live and apoptotic GC B cell fractions 128
6.5.2 Live and phagocytozed GC B cells carry the generally accepted molecular signatures of antigen-driven selection 129
6.5.3 Positive selection of GC B cells relies on the absence of adverse mutations within CDRs 130
6.5.4 Low interclonal diversity of phOx specific GC B cells is due to continual massive clonal failures 130
6.5.5 Some closing remarks 131

7 Conclusions and perspectives 133

Bibliography 136

A Supplemental material 153
A.1 Absorption and emission maxima of Alexa dyes 153
A.2 Confocal microscope and image acquisition settings 153
A.3 Survey of ImageJ based macros 154
A.4 Supplemental figures 156
A.5 IgL sequence alignments 159
A.6 Manufacturer listing 160

B Abbreviations 161

List of Figures

1.1 Schematic depiction of the Ig molecule 3
1.2 B lymphocyte development and maturation. 5
1.3 Architecture of the murine spleen. 7
1.4 Illustration of a *textbook GC* reaction. 12
1.5 Time evolution of *de novo* arising murine splenic GC. 13

3.1 Primer map. 27

4.1 Quantitative analysis of acquired GC images. 34
4.2 Verification of Ki-67 as consistent marker for detection and measurement of GC. 35
4.3 Correlation of cross-sectional GC size and number of Ki-67^{+} cells. . . 35
4.4 Kinetics of GC growth in spleens of phOx-CSA immunized mice based on cross-sectional GC areas. 36
4.5 Kinetics of GC growth in spleens of phOx-CSA immunized mice by means of numbers of Ki-67^{+} cells. 37
4.6 Schematic illustration of Wicksell's corpuscle problem. 38
4.7 Simulation of virtual random sectioning. 38
4.8 Formulation of hypothetical short and long-lived growth kinetics of individual GC. 40
4.9 Simulation of random sectioning of different GC ensemble kinetics. . . 42
4.10 3-D evaluation of the kinetics of GC growth. 44
4.11 3-D evaluation of occupation of follicular niches. 46
4.12 3-D reconstructions of splenic volumes. 48
4.13 3-D reconstruction of splenic volumes reveals a broad volume distribution of geometrically uniform GC. 49
4.14 Spatial orientation of GC within the spleen. 50
4.15 Low interindividual variation of GC 3-D geometry. 51
4.16 The 3-D shape of GC is preserved upon GC growth and progression of the immune response. 52
4.17 The 3-D evaluation of GC size reveals a considerable volume distribution. 54
4.18 A revised model of affinity maturation. 63

5.1 Data acquisition for assessing the kinetics of GC T cells. 67
5.2 Correlation of numbers of GC T cells and cross-sectional GC size. . . 69
5.3 Interrelation of GC T cell proliferation and cross-sectional GC size. . 70

5.4 Illustration of highly variable numbers of proliferating GC T cells recorded for GC of equivalent cross-sectional size. 71
5.5 Mean kinetics of GC T cells. 72
5.6 Antigen-driven influx of T cells into follicular niches due to GC formation. 73
5.7 Kinetics of frequencies of GC T cells. 73
5.8 Data acquisition for assessing the kinetics of GC Mϕ. 75
5.9 Strict correlation of numbers of GC Mϕ and cross-sectional GC size. . 76
5.10 Mean kinetics of GC Mϕ. 77
5.11 Mϕ do not invade B cell zones due to GC formation but are already detectable in B cell zones of naive mice. 78
5.12 Steady frequencies of Mϕ within B cell zones of naive and immunized mice. 79
5.13 Data acquisition for assessing the kinetics of cell death within GC. . . 80
5.14 Correlation of numbers of apoptotic nuclei and cross-sectional GC size. 82
5.15 The number of apoptotic nuclei does not reflect cross-sectional GC size. 83
5.16 Mean kinetics of apoptotic nuclei within GC. 84
5.17 Apoptotic nuclei become a major cellular constituent of GC and entail the formation of abundant clusters. 85
5.18 Rating of uptake of dying cells within GC by means of Mϕ size. . . . 87
5.19 Mean kinetics of uptake of apoptotic cells and underlying Mϕ size distribution. 87
5.20 Model interactions of GC B cells and Mϕ. 89
5.21 The model reproduces the experimentally recorded kinetics of GC B cells and Mϕ. 91
5.22 The model reproduces the experimentally recorded kinetics of uptake of apoptotic cells and predicts the Mϕ size distribution. 92
5.23 Aberrant morphology of GC Mϕ in NZB/W mice. 94
5.24 Strict correlation of numbers of Mϕ and cross-sectional B cell zone size in NZB and NZB/W mice. 96
5.25 Age-dependent decline in numbers of follicular Mϕ in NZB/W. 97
5.26 Model for the pathogenesis of autoantibodies in GC of NZB/W mice. 104

6.1 Identification of GC B cells by flow cytometry. 107
6.2 Implications of intracellular staining of CD68. 108
6.3 Follicular Mϕ are distinguished from splenic macrophages by absence of the macrophage marker F4/80. 108
6.4 Identification of follicular Mϕ by flow cytometry. 109
6.5 Isolation of GC B cells and follicular macrophages. 110
6.6 IgL repertoire analysis among live and phagocytozed B cell fractions. 113
6.7 J_κ gene segment use of phOx-specific IgL among live and phagocytozed B cell fractions. 114
6.8 Comparison of LCDR3s of phOx specific IgL sequences among live and phagocytozed B cell fractions. 115
6.9 Frequency of overall clones bearing positively charged amino acids. . . 116

6.10 Frequency of phOx-specific clones bearing positively charged amino acids among live and phagocytozed B cell fractions. 117
6.11 Distribution of the frequencies of mutations within IgL sequences of live and phagocytozed B cell fractions. 120
6.12 Pattern of mutations within IgL sequences of live and phagocytozed B cell fractions. 122
6.13 Distribution of the frequencies of mutations in phOx specific IgL sequences of live and phagocytozed B cell fractions. 125
6.14 Pattern of mutations among phOx specific IgL sequences of live and phagocytozed B cell fractions. 126
6.15 Traditional and revised explanation for the domination of GC responses by few clones. 131

A.1 Murine Igκ locus representation. 156
A.2 The 3-D shape of GC as assessed by 3-D alignment of whole spleen sections. 157
A.3 Penetration depths of follicular niches. 158
A.4 V_L gene segment usage among live and phagocytosed B cell fractions. 159

List of Tables

3.1 Survey of antibodies applied for immunofluorescence staining. 20
3.2 Composition of the TUNEL reaction mixture applying the *In situ* cell death detection kit provided by Roche. 21
3.3 Composition of the TUNEL reaction mixture applying the DeadEnd colorimetric TUNEL system provided by Promega. 21
3.4 Survey of antibodies applied in flow cytometry. 25
3.5 Primers used in amplification of Ig light chain rearrangements. 27
3.6 Composition of RT-PCR samples applying the OneStep RT-PCR kit provided by Qiagen. 28
3.7 Composition of second round PCRs samples, AmpliTaq Gold DNA Polymerase, Applied Biosystems. 29
3.8 Composition of the ligation mixture applying the TOPO TA Cloning kit provided by Qiagen. 30
3.9 Composition and preparation of selective agar plates. 30

4.1 Survey of spleen specimens analyzed for 3-D evaluation of GC growth kinetics. 45
4.2 Survey of numbers and volumes of GC resulting from 3-D reconstructions. 49

5.1 Survey of spleen sections analyzed for tracing the kinetics of GC T cells. 66
5.2 Survey of recorderd parameters for assessing the kinetics of GC T cells. 67
5.3 Survey of spleen sections analyzed for tracing the kinetics of GC Mϕ. 74
5.4 Survey of recorded parameters for assessing the kinetics of GC Mϕ. . 74
5.5 Survey of spleen sections analyzed for assessing the frequency of Mϕ within B cell zones of naive and immunized BALB/c. 75
5.6 Survey of spleen sections analyzed for tracing the kinetics of apoptotic nuclei within GC. 81
5.7 Parameter values and initial conditions. 90
5.8 Survey of spleen sections analyzed for assessing the frequency of Mϕ within B cell zones of NZB/W and NZB mice. 93

6.1 Comparison of IgL sequences of live and phagocytozed B cell fractions post immunization. 119
6.2 Comparison of phOx specific IgL sequences of live and phagocytozed B cell fractions post immunization. 125
6.3 Survey of special mutational events. 127

6.4 Survey of changes regarding the distribution of mutations in FRs and CDRs post immunization. 130

A.1 Absorption and emission maxima (A_{max}, E_{max}) of Alexa dyes. 153
A.2 Applied settings for image acquisition using the Leica DM Ire2 confocal laser scanning microscope, DRFZ Berlin. 153
A.3 Applied settings for image acquisition using the Leica TCS SP2 confocal laser scanning microscope, IFN Magdeburg. 154
A.4 Survey of ImageJ based macros. 154
A.5 List of manufacturers. 160

B.1 Abbreviations. 162

Chapter 1

Introduction

1.1 The immune response

The immune system is permanently challenged with myriads of foreign substances, pathogens of different nature and origin. The most prominent pathogens comprise bacteria, viruses, fungi and parasites - in their entirety referred to as antigens. In order to guarantee protection against exogenous pathogens, the immune system is build upon diverse modules that comprise barriers, soluble substances and cellular constituents. The demand on the immune system to act globally is warranted by the distribution of its components across the whole organism. Besides circulation of "loose" immune cells, immune cells also constitute an integral part of various tissues and preferentially accumulate in specialized immune organs. These immune organs are classified as generative (primary) tissues, where immune cells are generated and attain maturity and as peripheral (secondary) tissues where the response of immune cells proceeds. The primary immune organs are bone marrow and thymus, whereas spleen, lymph nodes, the cutaneous and the mucosal immune system are among secondary immune organs and tissues.

The immune system is made up of three pillars that are immune barriers, innate immunity and adaptive immunity. Potential pathogens first have to trespass the immune barriers of an organism, such as physico-mechanical (e.g. epidermis, mucosa), biochemical (e.g. pH, enzymes) and microbiological (e.g. intestinal flora) restraints. After penetrating the immune barriers, invading pathogens are recognized by the innate immune system. As the evolutionary oldest arm, the innate immune system comprises germline coded immune mediators (e.g. cytokines, complement) and immune cells (e.g. macrophages, granulocytes, NK cells). Activation of the innate system typically evokes local immune reactions that prelude the rapid and effective elimination of pathogens by either phagocytosis or cell lysis. In addition, the innate immune system also stimulates the adaptive immune system that represents a highly evolved defense mechanism, taking advantage of exquisite specificity, pronounced diversity and the capacity to establish immunological memory. The components of the adaptive immune system are specialized immune cells named lymphocytes and their products. There are two types of adaptive immunity that are mediated by different components of the immune system. Cell-mediated immunity relies on cytotoxic

T lymphocytes that promote elimination of intracellular pathogens like viruses and some bacteria by either inducing the destruction of the residing pathogens or the lysis of affected cells. Humoral immunity is mediated by blood-borne proteins, termed antibodies, that are derived from B lymphocytes. Because antibodies are secreted and thereby highly mobile they account for the major defense against extracellular pathogens and their toxins. Binding of antibodies marks their targets for elimination and subsequently activates adequate effector mechanisms.

This thesis deals with a feature of humoral immunity that is to adapt to an infection by a process referred to as affinity maturation of antibodies. Affinity maturation takes place in specialized structures called germinal centers (GC), that transiently develop in the B cell areas of secondary lymphatic tissues such as the spleen. Before giving a detailed survey on the cells and mechanisms involved in the rather complex affinity maturation machinery, the following sections will first introduce the properties of B cells and antibodies as well as the architecture and migratory pathways of the murine spleen.

1.2 Mission of B cells and their antibodies

The adaptive immune system uses three classes of molecules for recognition of antigens: major histocompatibility complexes (MHC), T cell antigen receptors (TCR) and antibodies. Within these three classes of molecules, antibodies display the highest specificity and capability to discriminate among antigenic structures. Antibodies institute a family of structurally related glycoproteins that participate in both the recognition and effector phase of the humoral immune response. In their membrane-bound form, antibodies are referred to as B cell antigen receptors (BCR). The interaction of antigen and BCR initiates the B cell response and therefore accounts for the recognition phase. In the effector phase, binding of secreted antibodies masks the antigens and thereby triggers various effector mechanisms that finally result in the elimination of the antigen. Due to their migrational behavior in electrophoresis, antibodies are classified as gamma globulins and are commonly named immunoglobulins (Ig). Therefore, antibody and immunoglobulin are used interchangeably throughout this thesis.

1.2.1 The molecular structure of antibodies

The entirety of antibodies share the same basic structure but exhibit high variability regarding the antigen binding region. The symmetric core structure of an antibody is a heterodimer, composed of two heavy and two light chains that are covalently connected via disulfide bonds (see Figure 1.1). Each heavy and light chain consists of an amino terminal variable (V) and a carboxy terminal constant region (C). Due to differences in the constant part, antibodies are subdivided into Ig classes (IgM, IgD, IgA, IgG and IgE). The constant region of an antibody assigns the molecule its Ig class and thereby permits different effector functions, such as complement activation and mediation of cell cytotoxicity. By contrast, the variable region designates the antigen specificity to the antibody and thereby accounts for the recognition respectively binding of antigens. The antigen binding sites of an antibody are formed by juxtaposing the V region of one heavy (V_H) and one light chain (V_L). The variable regions feature three highly divergent stretches termed hypervariable segments that are positioned by rather conserved framework regions (FR) (see Figure 1.1). In three-dimensional space, the three hypervariable segments of the (V_H) chain and the three hypervariable segments of the (V_L) chain are brought together to form the antigen binding surface. Because the antigen binding surface is complementary to the three-dimensional structure of bound antigen, the hypervariable segments are also referred to as complementarity-determining regions (CDR).

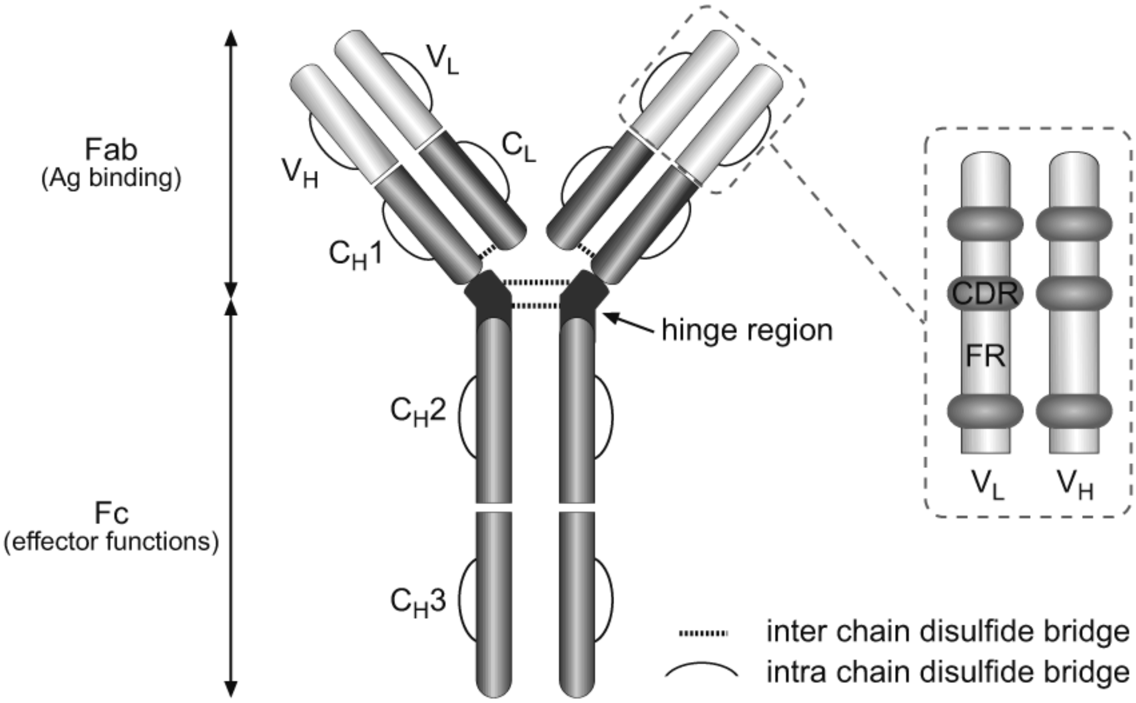

Figure 1.1: Schematic depiction of the Ig molecule exemplified for IgG. The antigen binding sites are formed by juxtaposition of variable light chain (V_L) and variable region heavy chain domains (V_H). C; constant region, CDR; complementarity determining region, Fab; fragment antigen binding, Fab; fragment antigen binding, Fc; fragment crystallizable, FR; framework, H; heavy chain, L; light chain, V; variable region. Modified according to [1].

1.2.2 Antibody diversity

The enormous diversity of the antibody repertoire is generated by somatic recombination - also referred to as rearrangement - of Ig genes during the development of B lymphocytes in the bone marrow (see Section 1.2.3 and Figure 1.2). Three separate loci encode the two Ig light chains (IgL; Igκ, Igλ) and the Ig heavy chain (IgH). Each light chain locus is composed of three different clusters of gene segments, referred to as variable (V), constant (C) and joining (J) gene segments. The IgH locus bears an additional cluster of diversity (D) gene segments. The repertoire analyses performed for the current thesis are exclusively related to the murine light chain loci. Therefore, the germline organization of the Igκ locus on chromosome

6 is exemplarily depicted in the appendix (Figure A.1). The nomenclature of the Igκ locus and a detailed description of its organization is given by Martinez-Jean et al. [2]. Each cluster of gene segments comprises a defined number of functional genes, for example the murine Igκ locus features a V segment cluster of 93 genes, a J segment cluster of 5 genes and a C segment cluster of 1 gene. The genes within a cluster are each separated from one another by regions of non-coding DNA that vary in length. The somatic recombination of gene segments within each Ig locus is a requisite for the production of a functional antibody molecule and follows a precise order (reviewed in Krangel [3]). The first recombination, occurring in the IgH locus results in joining of one of the D to one of the J gene segments. Thereafter, one of the V gene segments is joined to the DJ complex. Due to the lack of D gene segments within the light chain loci, somatic recombination directly joins one of the V to one of the J gene segments. The somatic recombination of gene segments within each locus occurs randomly. Therefore, the diversity that can be generated at each locus depends on the number of genes within its clusters. In case of the murine Igκ locus - by multiplying the number of Vκ (93) and Jκ (5) genes - the combinatorial diversity adds up to $93 \cdot 5 = 465$ possible combinations. The overall combinatorial diversity of antibodies - calculated by multiplication of the combinatorial diversities of the IgH, Igκ and Igλ loci - ranges in an order of magnitude of about 10^6.
The diversity of antibodies is further enhanced by the so-called junctional diversity that is due to "non-precise" joining of gene segments. During somatic recombination, nucleases may remove nucleotides of the recombining gene segments. In addition, the enzyme terminal deoxyribonucleotidyl transferase (TdT) mediates the random addition of up to 20 non-germline encoded nucleotides (n-nucleotides) at the junctions. The junctional diversity raises the overall diversity of antibodies by a factor of approximately 10^7 [4]. Taken together, the theoretical murine antibody repertoire comprises marvelous 10^{13}-10^{14} different specificities. Because formation of the B lymphocyte repertoire in the bone marrow is antigen independent, it is also referred to as *pre-immune repertoire.*

1.2.3 Development and maturation of B lymphocytes

In mammals, the B lymphocyte ontogeny starts in the fetal liver and spleen and proceeds in the bone marrow of adult individuals [5]. The "B" in B lymphocyte refers to bursa-derived. This is because proliferating foci of newly generated B lymphocytes were first defined in the bursa fabricius (latin: *Bursa cloacalis* or *Bursa fabricii*) of birds [6], nicely reviewed in Ribatti et al. [7]. Almost a decade after the description of the bursa, research discovered that the development of B lymphocytes of mammals - that do generally not possess a bursa equivalent organ - takes place in the bone marrow. The B cell lymphopoiesis and maturation can be divided into an antigen-independent and an antigen-dependent phase (outlined in Figure 1.2). The antigen-independent development of B-lymphocytes takes place in the locale of the bone marrow, where hematopoietic stem cells differentiate to immature B lymphocytes. During this developmental phase, the Ig loci are subjected to somatic recombination (reviewed in Section 1.2.2). B cells that do not succeed in generating a functional BCR undergo apoptosis. Immature B lymphocytes that express functional BCRs are subsequently subjected to a selection process that preserves useful but eliminates potentially harmful self-reactive cells. A powerful description of the maturation of B lymphocytes in the bone marrow and in particular the selection events operating at the various developmental stages is given by Melchers et al. [8] and Rolink et al. [9]. Apart from instant elimination, self-reactive B lymphocytes may also undergo active genetic correction of their receptors by secondary recombination of the DNA (referred to as receptor editing, reviewed by Nemazee [10]). Due to the cell death occurring at various stages of the development of B lymphocytes, less than 10% of the originally generated B lymphocytes acquire functional competence and leave the bone marrow. In the late stages of B cell development the immature B lymphocytes emerging from the bone marrow have to migrate to the spleen, where they may finally differentiate to mature B cells [11].

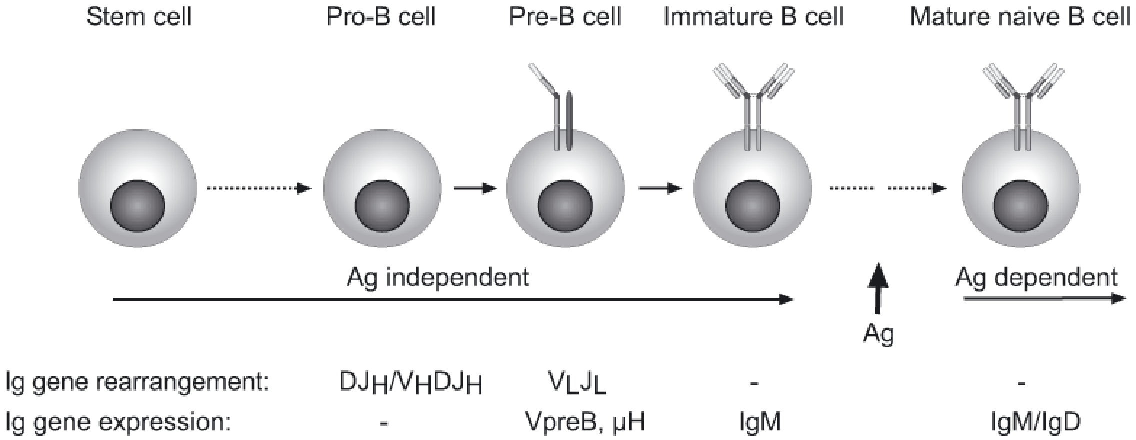

Figure 1.2: B lymphocyte development and maturation. Illustrated are both, the developmental stages of a B lymphocyte and the status of Ig gene rearrangement and expression during maturation in the bone marrow. μH; μ heavy chain protein, VpreB; pre-B cell receptor. Modified according to [1].

1.3 The architecture of the spleen and migratory pathways

The spleen constitutes the largest secondary lymphatic organ of mammals and combines the implementation of two important functions: filtration of blood and defense against pathogens. Its effectiveness is based on the organization of functional compartments, each featuring adapted microarchitecture (Figure 1.3). The splenic red pulp is characterized by a specialized network of open sinuses that facilitates filtration of the blood and removal of old or damaged erythrocytes. Due to the high abundance of erythrocytes, it is macroscopically tinged red - to which the red pulp owes its name. The red pulp is intermingled with white pulp cords that lack erythrocytes but instead mostly consist of white blood cells such as lymphocytes, macrophages and dendritic cells. Within the white pulp, T and B lymphocytes accumulate in well separated compartments. Whereas T lymphocytes are located within the periarteriolar sheaths (PALS) surrounding the incoming central arterioles, B lymphocytes reside in adjacent B cell follicles. The white pulp is further encompassed by the so-called marginal zone that harbors specialized macrophages, dendritic cells and a particular subset of B lymphocytes referred to as marginal zone B cells (for further reading about marginal zone B cells, see Lopes-Carvalho and Kearney [12]). Within the marginal zone, the blood leaks from the terminal arterioles into the open sinuses resulting in a slow-down of the blood flow. This facilitates the marginal zone, in particular its residing macrophages, to act as an important trap for particulate antigens [13].

The initial organization and maintenance of the splenic architecture is supervised by a set of factors that includes cytokines, chemokines and adhesion receptors. Studies in lymphotoxin (LT) as well as tumor necrosis factor (TNF) deficient mice support a pivotal role of signals transmitted by LTα for the correct formation of secondary lymphoid tissue [14]. As shown by Kim et al. [15], local LTα expression is capable to provoke basic lymphoid organogenesis even in the absence of functional B and T lymphocytes. Reconstitution experiments further demonstrate that LTα is required for the segregation of B and T lymphocytes in the splenic white pulp. LTα expression by B cells on the one hand causes the recruitment of follicular dendritic cells (FDC) towards B cell areas [16] and on the other hand provides a signal that is essential for retention of the T cell zones [17].

Even though the splenic compartments are well-established, they are subjected to a permanent flux of lymphocytes - within and between compartments, in and out. Lymphocytes enter the white pulp via the blood that is released in the marginal zone. The transit of lymphocytes from the marginal zone towards white pulp cords depends on both the presence of adhesion molecules such as leukocyte function-associated antigen (LFA-1) and very late antigen (VLA)-4 [18] and chemokine receptor signaling. The importance of chemokine receptor signaling was first pointed out by Cyster and Goodnow [19] who observed accumulation of lymphocytes that fail to enter the white pulp due to uncoupling of chemokine receptor signaling following pertussis toxin treatment. Since then, the gain in knowledge steadily increased and meanwhile, the lymphoid chemokines that control attraction of lymphocytes to their respective compartments are identified. B lymphocytes are directed towards B cell follicles due to CXCL13 (chemokine (C-X-C motif) ligand 13) expression by FDC and adjacent stromal cells. The migration of B cells relies on the expression of the chemokine receptor for CXCL13 by B lymphocytes, that is CXCR5 [20, 21]. On the other hand, T lymphocytes are attracted to the T cell areas due to stromal cell derived delivery of the chemokines CCL19 and CCL21, both interacting with the chemokine receptor CCR7, expressed by T lymphocytes [22, 23].

B lymphocytes first encounter antigen in the marginal zone or outer part of the T cell zone (bridging area). In response to antigen engagement, B lymphocytes downregulate CXCR5 but instead upregulate CCR7 expression that facilitates their migration towards the B-T border. Interaction with T lymphocytes at the B-T border, finally activates B lymphocytes that afterwards may either become antibody secreting plasma or GC precursor cells [24, 25, 26]. The B lymphocytes committed to GC upregulate CXCR5 and migrate back towards a B cell follicle. Alike, a subset of T cells acquires CXCR5 expression that makes it enter the B cell follicles or GC, respectively [27].

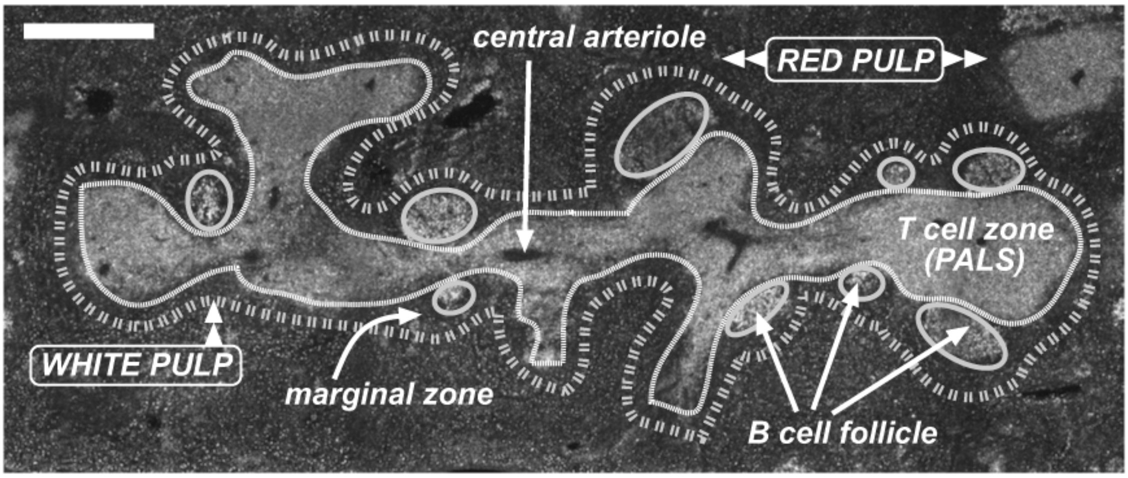

Figure 1.3: Architecture of the murine spleen. The murine spleen is composed of two major compartments that are referred to as red pulp and white pulp. The red pulp is characterized by a network of open sinuses that facilitate filtration of the blood and in particular removal of old erythrocytes. The red pulp is intermingled with white pulp cords that mostly harbor white blood cells. Within white pulp cords, B and T lymphocytes are confined to well-separated subcompartments. T lymphocytes are located within the PALS, B lymphocytes reside in adjacent follicles. Red pulp and white pulp are separated by the marginal zone. PALS; periarteriolar lymphoid sheath. Scale bar 0.5 mm.

1.4 The formation of germinal centers (GC)

The term germinal center (GC) was introduced by Walther Flemming - a pioneer in the field of cytogenetics - more than 120 years ago. While studying cell division in lymph nodes, he observed strong proliferation of lymphocytes within the follicles and suggested that these sites constitute the origin of lymphocyte generation or germination, respectively [28]. Flemming assigned the term germinal center to these structures according to their supposed function (discussed in Berek [29]). The term outlasted until today although we now know that not Flemming's GC but bone marrow and thymus are the primary lymphoid organs and sites of lymphocyte differentiation. Nevertheless, Flemming's interpretation was not quite wrong, because GC are indeed the source of generation of unique B cells (GC B cells) featuring high affinity B cell receptors. The process leading to high affinity B cell receptors is referred to as affinity maturation and was first assigned to the locale of GC about 20 years ago [30, 31, 32, 33]. In addition, the formation of B cell memory as well as immunoglobulin (Ig) isotype class-switching are likewise associated with the GC reaction. The importance to elucidate GC formation, progression and not least mode of operation is stressed by the fact that malfunction or deregulation is linked to the onset of severe diseases, most prominent cancer and autoimmunity (reviewed in Section 1.4.5).

1.4.1 Commitment of B cells to GC

Appropriate immunization with T cell dependent (TD) antigens typically results in the transient formation of GC in secondary lymphoid tissues. The sites and dynamics of responding antigen-specific B cells in a primary immune response were first revealed in a series of seminal *in situ* studies by Kelsoe and colleagues as well as Liu et al. in the early 1990's. Via their migratory pathway, B cells are believed to first interact with antigen in the marginal zone or outer parts of the interfollicular T cell zones, that are - in context of the spleen - referred to as periarteriolar lymphoid sheath (PALS). After initial B cell activation, B lymphocytes either commit to an extrafollicular proliferative focus response or to enter primary B cell follicles and found GC. The basis of direction towards one of these pathways is still under discussion. Initial experiments performed with hapten-carrier conjugates (NP-CGG) suggested that recruitment of B cells to either of the pathways is essentially a stochastic process [34, 35]. In contrast, very recent studies based on the adoptive transfer of B cells, that express defined anti-hen egg lysozyme (HEL) BCRs, and subsequent immunization with HEL coupled to SRBC indicate that the direction towards one of the pathways is not stochastic but rather determined by the strength of the initial interaction between BCR and antigen. In this scenario, B cells featuring a strong initial interaction with antigen contribute to the early T dependent response by rapidly differentiating to extrafollicular plasma cells. B cell clones of weak antigen reactivity are primarily drawn to found GC and thereby to undergo affinity maturation [36]. In either case, becoming a GC precursor B cell and above all propagation of GC requires adequate T cell help. The need for adequate T cell help is underlined by the both, rare and abortive formation of GC observed in response to T cell independent type 2 (TI-2) antigens such as NP-Ficoll. TI-2 antigens evoke an immune response with a strong bias towards an extrafollicular focus response and GC are only generated if antigen dose and precursor frequencies are sufficiently high [37].

1.4.2 Cellular players of GC

Besides GC B cells, at least three other cellular players participate in the GC reaction: follicular dendritic cells (FDC), GC T cells and GC macrophages (GC Mϕ).

Follicular dendritic cells (FDC)

The dendritic processes of FDC form dense networks (FDC networks) that are already detectable in the primary B cell follicle and provide a follicular niche for the formation of GC. Therefore, the maximal number of GC is predetermined by the limited number of follicular niches [38]. FDC present non-processed antigen in form of either antigen-antibody or antigen-complement complexes, collectively referred to as immune complexes.

GC T cells

As aforementioned, T cells are a requisite for formation and progression of GC. The T cell help required for antibody production has long been considered a Th2 property [39, 40] but was recently shown to rely on a third class of effector-type T cells referred to as follicular B helper T cells (T_{FH}) [41, 27, 42]. Homing of T_{FH} cells to B cell follicles occurs after gain of responsiveness to the chemokine CXCL13 that is expressed by follicular stromal cells. CXCL13 binds to the CXC chemokine receptor (CXCR)5 that is expressed by T cells upon T cell activation in the T cell zone. Indeed all T cells that localize in B cell follicles are $CXCR5^{+}$. The relationship of T_{FH} to Th1 and Th2 cells - in particular the question if T_{FH} cells represent a separate subset or if they are derived from either Th1 or Th2 cells - is still unresolved.

GC macrophages (Mϕ)

Noteworthy, GC macrophages represent the earliest identified cellular players of GC. In 1885, Walther Flemming did not only discover GC but yet he additionally reported the emergence of *tingible bodies* within GC for the first time [28]. Already suggested by Flemming and finally proven by Swartzendruber and Congdon [43], the tingible bodies of GC represent phagocytosed nuclear debris of lymphocytes. Accordingly, the macrophages of GC were referred to as tingible body macrophages. Although well-known for more than a century, the macrophages of GC somehow got neglected. The rather marginal knowledge of macrophages within GC solely attributes to a series of publications of Smith et al. [44, 45, 46]. They suggest that the macrophages within GC represent a unique, vigorously phagocytic subset of mature macrophages. Furthermore, they claim that these macrophages are not a requisite for the induction of GC, because they are absent from B cell follicles prior to the GC reaction. On the other hand, Smith et al. [44] propose that GC macrophages may be specialized in downregulating the GC reaction. In the recent past, the discussion of GC macrophage origin and function was revived, actuated by their malfunction being associated with development of autoimmune diseases such as systemic lupus erythematosus(SLE). The contribution of GC and GC macrophages to autoimmunity is reviewed in a discrete section (Section 1.4.5).

1.4.3 Affinity maturation

A striking phenomenon of humoral immune responses is the progressive improvement of binding properties of antibodies. This so-called affinity maturation is due to further diversification of B lymphocytes after antigen engagement of their BCR, realized by introduction of somatic mutations into the sequences encoding the variable regions of the BCR. Subsequently, an efficient selection process ensures the detection and promotion of the B lymphocytes featuring the highest affinity for the antigen.

How does the immune system accomplish affinity maturation on the cellular and mechanistical level? Basically, affinity maturation is confined to the presence of follicular GC, albeit GC-like structures were discovered outside of B cell follicles or even outside lymphatic tissues under certain conditions (ectopic GC) [47, 48, 49]. There is a standard view on the GC reaction even propagated by immunology text books that was entitled as *textbook GC response* in an innovative review by Manser

[50]. The need for such a label is emphasized by the fact that the transitions between experimental certainty and deductive theoretical assumptions are often obliterated with respect to the GC reaction. The following paragraphs will concentrate on affinity maturation in the light of *textbook GC* (schematically illustrated in Figure 1.4), disclosing only some of the discrepancies of recent studies and *textbook* behavior (a full review is given by Manser [50]).

After commitment (Section 1.4.1), GC precursor B cells migrate towards B cell follicles, settle down in the stromal environment created by FDCs and commence an expansion phase characterized by brisk proliferation [51, 52]. The vigorously proliferating GC B cells (also referred to as centroblasts) then give rise to formation of the so-called dark zone of GC. Subsequently, centroblasts are subjected to mutational activity of their Ig genes, implemented by the induction of a mechanism referred to as somatic hypermutation (SHM).

Diversification by mutation of Ig genes was already suggested more than 40 years ago [53, 54]. However, it was first experimentally validated by sequencing of Ig genes of λ light chains of murine myeloma cells [55]. Although the mechanisms underlying SHM - briefly, deamination of cytidines due to an enzyme referred to as activation induced cytidine deaminase (AID) [56, 57, 58, 59] followed by excision mismatch repair - were identified in the last years, both, the induction and regulation of SHM constitute an enduring enigma [60]. The rate of somatic mutation in Ig genes is about 10^3 to 10^4 higher than the spontaneous rate of mutation in other genes, a fact that somatic *hyper*mutation owes its name. Merging the estimated rate of SHM ($10^{-}3$/bp per cell/generation) [61] and the total number of base pairs that encode the variable region of an antibody (n=700) results in an average rate of accumulation of mutations of almost 1 per cell division.

As a consequence of mutations in their Ig genes, many of the GC B cells feature declined or even annihilated antigen binding properties. However, some of the cells are likely to acquire useful mutations generating high affinity antibodies. The next pivotal step of affinity maturation comprises the preferential selection and propagation of the very GC B cells that have acquired mutant BCR of high affinity. Selection is attributed to the so-called light zone of the GC that is rich in FDC and additionally harbors GC T cells. The centroblasts are believed to exiT cell cycle and to migrate towards the light zone of GC. The henceforth non-proliferating GC B cells within the light zone (also referred to as centrocytes) vastly compete for survival signals provided by engagement of their BCR with antigen on FDCs. Unless they do not receive these survival signals, all centrocytes are prone to apoptosis. This disposition ensures that only the centrocytes that feature high affinity towards the antigen are retained. The remainder centrocytes undergo apoptosis by default. Within GC, apoptotic cells are immediately recognized, engulfed and finally degraded by macrophages. Surviving centrocytes are thought to internalize, process and afterwards present the antigen to GC T cells resulting in IgH class-switching and terminal differentiation to either pre-antibody forming cells (AFC) or memory B cells that subsequently exit GC.

Although the basis of the outlined *textbook* selection procedure seems quite comprehensible, it should be interpreted as a hypothesis, because direct experimental validation is still missing. Although FDC are certainly capable of retaining antigen for extended periods of time [62], their impact on the selection process is quite arguable. Recent studies of mice, deficient in mounting secreted antibodies and thus incapable of deposition of immune complexes on FDC, point out that formation of GC as well as the first stages of SHM and subsequent selection may occur even in the absence of detectable levels of antigen on FDC [63]. Additionally, Vora et al. [64] demonstrate that enhanced deposition of immune complexes on FDC does not result in relaxed stringency of selection, as anticipated from the *textbook* model. Besides their questionable involvement in the selection process, FDC seem to be essential for maintaining the response, by providing an indispensable niche for B cell clustering, proliferation, survival and differentiation [65, 66].

The central dogma of *textbook GC* is the spatial separation of processes by installing two compartments: proliferation and hypermutation are confined to the dark zone, whereas selection and differentiation occur in the FDC-rich light zone of GC. This concept was initially inspired by analysis of chronically inflamed human tonsils. However, as demonstrated by Camacho et al. [67], it does not hold true in case of murine *de novo* arising GC. Although acutely induced GC develop two compartments - one rich and one poor in FDC - the cellular composition of these compartments is subjected to a rather complex time evolution (schematically outlined in Figure 1.5). As a result, the installment of a typical *textbook* dark and light zone structure turns out to be constricted to a rather late and short time-frame - at a time when selection is known to already have been deployed. As a hallmark, proliferating GC B cells were detected in the FDC-rich compartment at all times. Furthermore, murine GC B cells display a rather uniform histological phenotype and the vast majority stays in cell cycle throughout the response [68, 69]. Taken together, these data indicate that besides selection and differentiation also proliferation and hypermutation may take place in the FDC-rich compartment of GC. Moreover, hypermutation and selection seem to act on a rather homogeneous GC B cell population, thereby challenging the concept of centroblasts and centrocytes.

1.4.4 Assessing the transient nature of germinal centers

As aforementioned, the formation of GC in response to TD antigens is not stable but transient. Independent studies applying various antigens demonstrate in unison that GC are detectable within an interval of 3 to 4 weeks after antigenic challenge. In each case, the overall growth kinetics - comprising appearance, expansion and decay of GC - was deduced from evaluation of planar tissue sections of either spleen or lymph node (cross-sectional evaluation). Besides counting the actual numbers of GC per tissue section [70], a more precise measure was introduced by either recording the relative volume of all GC [24] or the distribution of volumes of individual GC [45] at different time points after immunization. In either of the latter two cases the volume represents an extrapolated quantity, derived from evaluation of planar

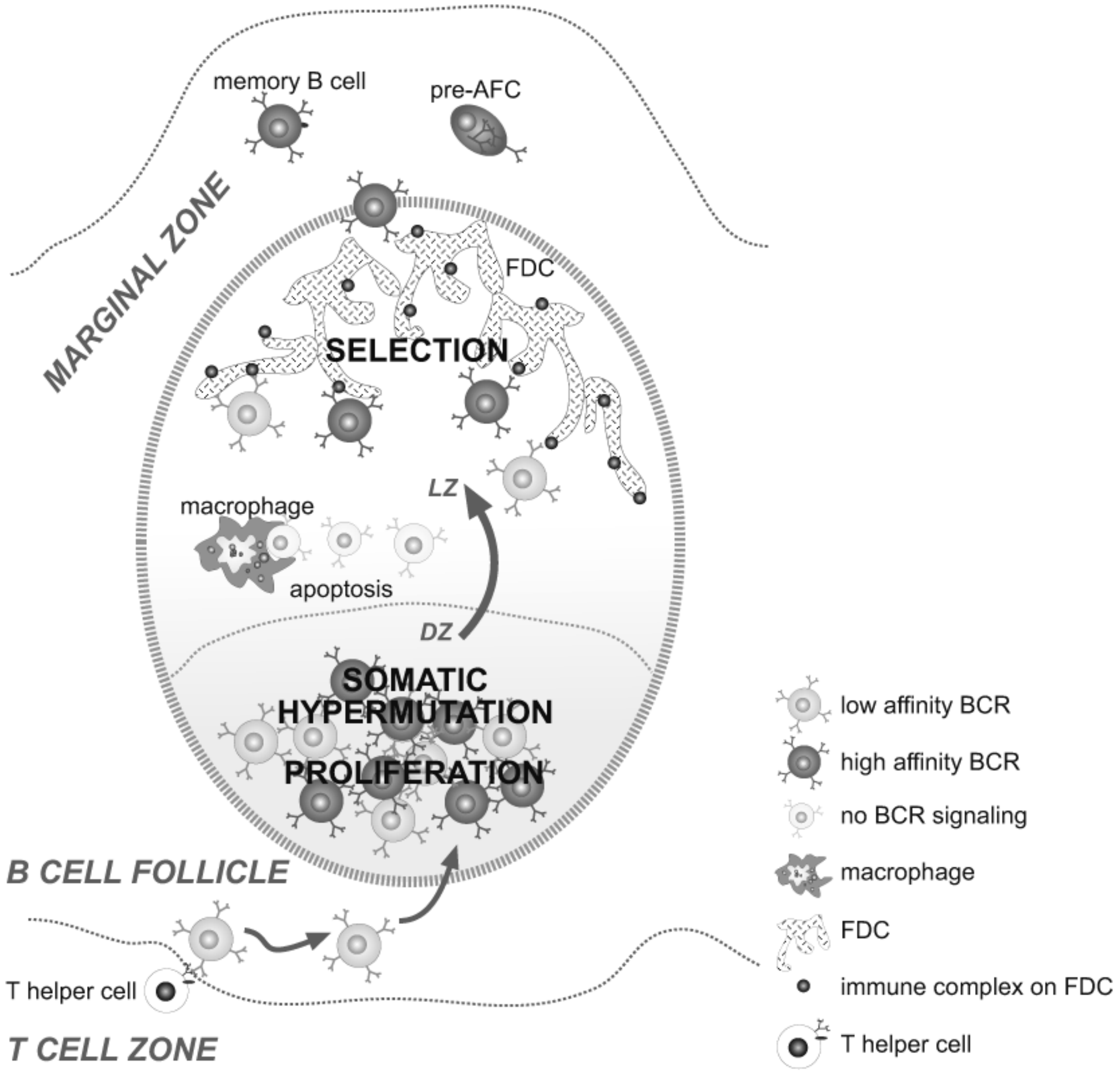

Figure 1.4: Illustration of a *textbook GC* reaction. Committed B lymphocytes enter GC and there undergo affinity maturation. While proliferating in the dark zone (DZ), B lymphocytes are subjected to somatic hypermutation. After migration towards the light zone (LZ) of the GC, high affinity B lymphocytes are selected due to engagement of their BCR and immune complexes deposited on FDC. B lymphocytes featuring low or annihilated affinity become apoptotic and are immediately engulfed and degraded by macrophages. Positively selected B lymphocytes interact with T cells, resulting in IgH class-switching and final differentiation to either pre-AFC or memory cells that exit the GC.

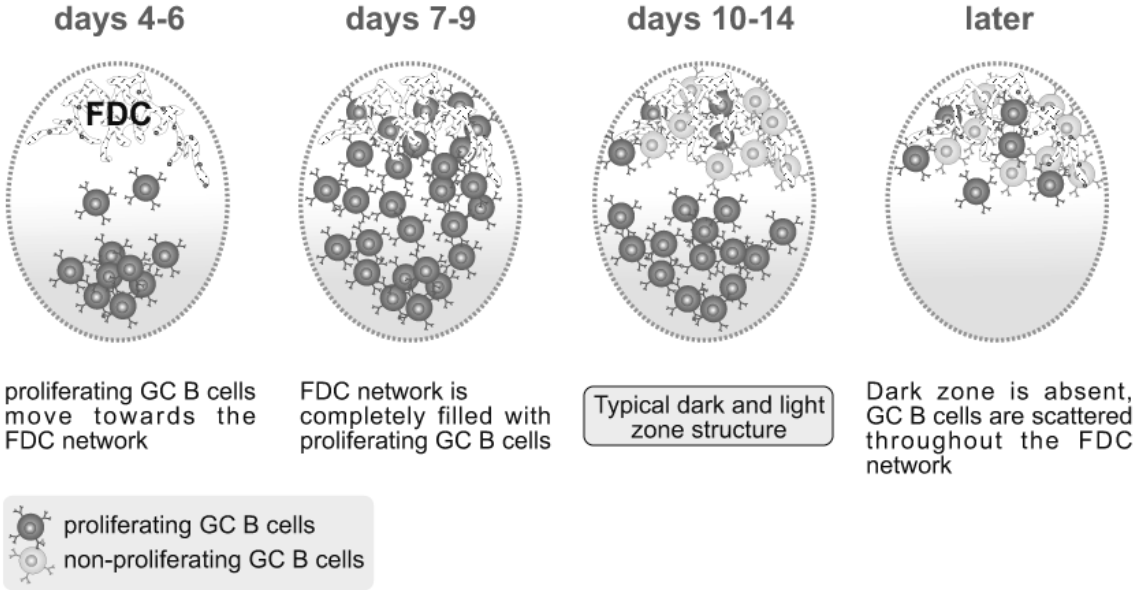

Figure 1.5: Illustration of the time evolution of *de novo* arising murine splenic GC, according to Camacho et al. [67]. Proliferating GC B cells are first detected in the FDC poor compartment and subsequently move to the FDC network. Around days 7-9 after immunization the FDC network is completely filled with proliferating GC B cells. Afterwards a typical dark and light zone structure is installed, characterized by non-proliferating GC B cells within the FDC network. By day 15 the dark zone is absent and proliferating and non-proliferating GC B cells are scattered throughout the FDC network.

tissue sections. Nevertheless, the course of the recorded overall growth kinetics is concordantly characterized by an initial expansion phase of GC - peaking at around day 10 - thereafter followed by gradually decay phase. At the peak of the response, GC harbor a maximal number of a few thousand GC B cells [71]. Taken together, the above cited works provide the basis for assuming a lifetime of GC of about 3 weeks.

Another yet puzzling feature of GC is their termination. Due to the lack of direct experimental proof, the factors that govern the termination of a GC reaction remain unidentified until now. Nevertheless, scientists put forward various hypothesis regarding the termination of the GC reaction that will be outlined in the following.
One explanation for the termination of the GC reaction is the gradual antigen depletion due to extraction and uptake of antigen from FDCs by GC B cells. Although the mathematical model proposed by Kesmir and De Boer [72] demonstrates that such a phenomenon may result in termination of GC, it is rather unlikely that it contributes to the decay of GC *in vivo*, because considerable amounts of antigen are retained on FDC, even after the response has waned [73]. Tarlinton and Smith [74] suggested that a declined antigen accessibility - due to the successive masking of antigen by secreted antibodies - may account for the termination of GC. In contrary, Meyer-Hermann et al. [75] envisioned a scenario, where increased emigration of GC B cells results in the termination of GC. In a very recent publication Moreira and Faro [76] propose yet another model, that is based on the decay of a hypothetical proliferation signal, thereby limiting the number of cell divisions.

1.4.5 Contribution of germinal centers to autoimmunity

The significance to study and to eventually understand GC is emphasized by the strong association of its malfunction with the onset of severe disease. In case of B lymphocytes, the generation of specifities is not restricted to the primary lymphoid organ or bone marrow, respectively, but is reinstalled within the environment of GC after antigen exposure. Figuratively, GC can be understood as insular "generative" microstructures, therefore necessitating tight regulation. Basically, somatic hypermutation of B lymphocytes within GC poses two risks: emergence of self-reactivity and B cell malignancy (lymphoma, leukemia) [77]. The following paragraphs will concentrate on the aspect of autoimmunity, in particular on the generation of anti-DNA antibodies. Nevertheless, an informative review on the contribution of GC to B cell malignancy is given by Kuppers [78].

The emergence of activated autoreactive B lymphocytes always indicates a functional loss of central or peripheral tolerance, respectively. In the healthy state, B lymphocytes featuring self-reactivity are eliminated from the repertoire at various checkpoints during B cell development. Concordantly, failure of either one or even several of these checkpoints during B lymphocyte development results in the accumulation of potentially harmful B lymphocytes.

In systemic autoimmune diseases, the major targets of self-reactive B lymphocytes comprise a limited set of autoantigens, such as ribonuclein, IgG and chromatin [79, 80]. As a hallmark, autoimmune disorders are generally not driven by single but rather by a medley of self-epitopes. In addition, the targeted epitopes often alternate during a response, a phenomenon referred to as epitope-spreading. Nevertheless, there is evidence for predominance of certain epitopes in different autoimmune diseases. Whereas rheumatoid arthritis (RA) and Sjogren's syndrome feature high titers of anti-IgG (rheumatoid factor (RF)) autoantibodies, RF are less frequent in systemic lupus erythematosus (SLE). Lupus-like diseases are rather characterized by the high prevalence of anti-nuclear autoantibodies. In SLE, autoantibodies to double-stranded DNA (anti-dsDNA) typically have a IgG isotype and their serum titer correlates positively with disease activity. In addition, progressive deposition of the very autoantibodies in glomeruli of the kidney causes fatal lupus nephritis.

The generation of anti-dsDNA antibodies in lupus-like diseases is of special interest for the current thesis, because studies performed by Wellmann et al. [81] point out that anti-DNA reactivity is generated during a normal immune response. Figuratively, once harmless non-autoreactive B lymphocytes acquire de novo anti-DNA specificity during somatic hypermutation within GC. Due to the failure of a GC-confined tolerance checkpoint, the autoreactive cells are not eliminated but give rise to antibody secreting plasma cells.

How do anti-DNA reactive GC B cells manage to bypass negative selection, or the other way round why do they become positively selected? As an answer to this question, Gaipl et al. [82] propose an elegant model. They suggest that as a consequence of impaired uptake by macrophages, apoptotic cells accumulate and undergo secondary necrosis within GC, thereby releasing danger signals and modified autoantigens. These "free" autoantigens become accessible due to binding to FDC, most probably through complement receptor (CR) 2/CD21 [83]. Consequently, autoreactive GC B cells are positively selected because their BCR engages the henceforth accessible autoantigen on FDC. In case of SLE, chromatin - that is well-known to activate complement [84] - is believed to represent the triggering antigen for positive selection of anti-DNA reactive GC B cells. After being positively selected, autoreactive B lymphocytes finally exit the GC and may give rise to autoantibody secreting plasma cells.

The outlined model is affirmed by a set of experimental findings. Histological examination of lymph node biopsies reveals that SLE patients indeed feature accumulation of apoptotic cells within GC. Furthermore, the number of GC macrophages is significantly decreased in GC of SLE patients [83]. A crucial function for the removal of apoptotic cells in GC is assigned to milk fat globule epidermal growth factor (EGF) factor 8 (MFG-E8), that is strongly expressed by GC macrophages. Notably, MFG-E8 deficient mice develop a lupus-like disease, featuring high titers of anti-DNA antibodies and glomerulonephritis. The same applies for wildtype mice, if MFG-E8 function is impaired due to administration of anti-MFG-E8 antibodies [85, 86]. Although there is strong evidence that the pathogenesis of SLE-like diseases is related to disturbances in the macrophage compartment, the cause of altered clearance capacities of macrophages is still ill-defined. As reviewed by Gaipl et al. [87], intrinsic defects of macrophages as well as defects of serum factors may contribute to impaired uptake of apoptotic cells. As already stated by Zullig and Hengartner [88], *tickling macrophages* is a serious business.

Just recently, two novel GC-related tolerance checkpoints - both engaged only after initial activation of autoreactive B lymphocytes - were reported by [89]. One checkpoint prevents AFC but allows GC formation of autoreactive RF-expressing B lymphocytes. The other checkpoint impairs selection of RF-expressing B lymphocytes within GC. Both of these checkpoints are shown to fail in autoimmunity.

Chapter 2

Objectives

There has been continuous progress in understanding the micro-evolutionary process resulting in affinity maturation of B cells over the last decades, which lead to a general conception of the GC reaction that is now found in immunology textbooks. However, the gain in knowledge mostly applies to particular subprocesses occurring within GC, as for instance somatic hypermutation and the signaling involved in differentiation of GC B cells along either, the plasmacytoid or memory pathway. By contrast, the actual crux of the matter, that is how GC B cells that gained heightened affinity are selected within GC, remains rather elusive, in that experimentally validated verities often mingle with theoretical hypotheses. The current thesis aims at providing new insights into the evolution of B cells within GCs by particularly addressing the *when*, *where* and *how* they are SELECTED and not least PROPAGATED during the primary immune response. A major approach to this problem is to overcome the unilateral winner-sided view on B cell evolution by placing special emphasis on the "dark side" of the GC reaction, that is negative selection and cell death of GC B cells.

Specific aims

- Documentation of overall GC growth behavior and changes of cellular composition of GC/GC subcompartments following immunization, regarding all major players of GC, namely GC B cells, macrophages and T cells. This should help to answer questions of tempo-spatial organization and regulation of affinity maturation. Moreover, such analysis might reveal new aspects regarding the interplay of the cellular players of GC.

- In-depth analysis of the kinetics of cell death/negative selection occurring within GC (where, when and how much?). This should provide new insights regarding the temporal and spatial extent of the selection process.

- Comparative analysis of positively (*living*) and negatively selected (*dying*) GC B cells by means of their BCR sequences in order to explore why or by which criteria/molecular signatures GC B cells are selected.

Chapter 3

Material and methods

Chemicals were purchased from Merck unless otherwise noted. The sources of supply are documented in the appendix (Table A.5).

3.1 Applied software and databases

Software/Database	Version
Amira	Version 3.0 (Mercury Computer Systems)
Analyze-It	Version 1.7.2
Arivis browser	Version 1.6
CLC Free Workbench	Version 2.5.2 (CLC)
Chromas Lite	Version 2.01
FCS Express	Version 3 (De Novo Software)
ImageJ	Version 1.35q (NIH)
IMGT database/IMGT/V-Quest	[90]
Leica LCS	Version 2.6.1
MatLab	(The MathWorks)
Photoshop CS	Version 8.0.1
R	Version 2.4.1
SigmaPlot	Version 9.0 (Systat)
VBase2	http://www.vbase2.org/

3.2 Solutions and buffers

Buffer/solution	Components
50x TAE buffer	242 g/L Trisbase, 57.1 mL/L 96% acetic acid, 10% EDTA 0.5M pH 8.6
Blocking buffer	PBS, 3% BSA (Fraktion V, Sigma)
Erythrocyte lysis buffer	10 mM $KHCO_3$, 155 mM NH_4Cl, 0.1 mM EDTA
FACS buffer	PBA, 4 mM EDTA, pH 8.0
Fixation buffer (FACS)	2% paraformaldehyde (PFA)
Fixation buffer (TUNEL)	1% PFA
LB medium (Bio101)	10 g/L tryptone, 5 g/L yeast extract, 10 g/L NaCl
LB agar	LB medium + 15 g/L Selekt Agar (Sigma)
Sodium phosphate buffer	1 M Na_2HPO_4, 1 M NaH_2PO_4
PBA	PBS, 0.5% BSA (Fraktion V, Sigma)
PBS	130 mM NaCl, 10 mM sodium phosphate buffer
Permeabilization buffer (FACS)	0.5% (w/v) Saponin (Sigma) in PBA
Permeabilization buffer (TUNEL)	1% sodium citrate, 1% Triton X-100 (Promega)
YT medium (Bio101)	16 g/L tryptone, 5 g/L yeast extract, 5 g/L NaCl
YT agar	YT-Medium + 15 g/L Selekt Agar (Sigma)

3.3 Consumables supplies

Consumables	Source of supply
Centrifuge tubes	50, 15 mL (Corning)
Imject Alum	(Pierce)
Microtome blades	SEC35 (Microm)
Mini lancets	(Braun)
Petri dishes	∅ 10 cm (Greiner)
Reaction tubes	0.5, 1.0, 2.0 mL (Eppendorf)
Superfrost Plus slides	(Roth)
Cover slips	(Roth)
Cryomolds	(Sakura)
Paint brushes	

3.4 Mice, antigen and immunization

BALB/c mice were bread and maintained in the facilities of the BgVV Marienfelde and used between the age of 6-10 weeks. Immunization was performed by a single intraperitoneal (i.p.) injection of 100 μg alum precipitated 2-phenyloxazolone (Sigma) coupled to chicken serum albumin (phOx-CSA) in a ratio of 10:1 [91].

3.5 Tissue collection and cell preparation

Mice were sacrificed by cervical dislocation and subsequently the spleens were dissected. For immunohistology purposes spleens were embedded in cryoprotective Tissue-Tek OCT compound (Sakura), cautiously frozen in liquid nitrogen and stored at -70° C until cryosectioning. By default spleens were bisected giving rise to two cryopreserved tissue specimens except for the spleen tissue intended for the three dimensional reconstruction experiments.
Spleen sections of NZB and (NZB/W)xF1 mice were kindly provided by Katrin Moser and Daniel Panne (Research Groups Humoral Immunology and Autoimmunology, DRFZ, Berlin).

For flow cytometry, single cell suspensions were prepared from dissected spleens. Spleens were mechanically disaggregated by pressing through 70 μm cell strainers (Becton Dickinson) using flattened pestles and the cell strainers were subsequently washed with PBA. Thereafter, the cell suspensions were filled-up with PBA to a volume of 50 mL and centrifuged at 400 x g for ten minutes. The supernatant was discarded and the cell pellet was resuspended in 5 mL erythrocyte lysis buffer. Lysis of erythrocytes was stopped after one minute by addition of 10 mL PBA. Afterwards, the cell suspensions were centrifuged at 400 x g for ten minutes, the supernatant was discarded and the cell pellet was resuspended and washed in PBA. The cell pellet was again collected by centrifugation at 400 x g for ten minutes and discarding the supernatant. The cell count was determined by using the Casy Cell Counter. The pellet was finally resuspended in PBA to a cell concentration of 10^6 cells per mL.

3.6 Immunohistology

A major part of this thesis deals with high-throughput immunofluorescence staining and subsequent evaluation of cryopreserved spleen sections for different purposes. On this account, the applied protocols differ in order to serve the respective purpose. A comprehensible representation of this protocols is given by first introducing the standard protocol and afterwards specifying the modifications for each application.

3.6.1 Cryosectioning of spleen tissue

Cryosectioning was performed applying a Microm HM 500 OM cryostat adjusted to a box temperature of -20°C and an object temperature of -17°C. Frozen tissue samples were first allowed to adjust to the box temperature by leaving them untouched in the box for about fifteen minutes. Cryosections of a thickness of 8 μm - corresponding to one cell layer - were cut and picked up onto Superfrost Plus glass slides (Roth). For the three dimensional reconstruction experiments sections of 25 μm thickness were cut. Tissue sections were air-dried for about one hour at room temperature and subsequently fixed in fresh cold acetone for ten minutes. After complete evaporation of acetone, slides were stored at -70°C.

3.6.2 Standard protocol for immunofluorescence staining

Splenic cryosections were allowed to thaw at room temperature for about five to ten minutes before they were encircled with a grease pen (Dako pen, Dako). Prior to staining with various antibody combinations (Table 3.1), unspecific binding was prevented by blocking the sections in PBS/3% BSA. Likewise, all antibodies were diluted in PBS/3% BSA. For direct immunofluorescence staining sections were incubated with diluted fluorescent dye conjugated primary antibodies for about thirty minutes, extensively washed in PBS and then mounted with FluoromountG (Southern Biotech). In case of indirect immunofluorescence staining, unconjugated antibodies were detected using fluorescent dye conjugated secondary antibodies (Table 3.1) and incubated in the dark for another thirty minutes. Sections were washed in PBS and coverslips were mounted with FluoromountG (Southern Biotech). Before examination mounted sections were allowed to air-dry for at least two hours.

Specificity	Source	Dilution
α-B220:bio	rat, clone RA3.6B2 (DRFZ)$^{\checkmark}$	1:100
α-B220:Cy5	rat, clone RA3.6B2 (DRFZ)$^{\checkmark}$	1:100
α-CD3:A488	rat, clone KT3 (Serotec)	1:10
α-CD4:Cy5	clone GK1.5 (DRFZ)$^{\checkmark}$	1:100
α-CD4:FITC	clone GK1.5 (DRFZ)$^{\checkmark}$	1:50
α-CD68:A488	rat, clone FA-11 (Serotec)	1:100
α-F4/80:Cy5	rat, clone F4/80 (DRFZ)$^{\checkmark}$	1:100
α-FDC-M2:bio	rat, clone FDC-M2 (ImmunoK)	1:250
α-Ki67	rat, clone TEK3 (DAKO)	1:50
α-MOMA-2	rat, clone MOMA-2 (Southern Biotech)	1:100
PNA:bio(*)	5 mg/mL, B-1075 Vector	1:200
PNA:FITC(*)	5 mg/mL, FL-1071, (Vector)	1:500
PNA:Rho(*)	5 mg/mL, RL-1072 Vector	1:500
α-rat IgG:A647	goat, 2 mg/mL, A21247 (Molecular Probes)	1:800
α-A488	rabbit, 1 mg/mL, A11094 (Molecular Probes)	1:100
α-rabbit IgG:A594	goat, 2 mg/mL, A11012 (Molecular Probes)	1:400
SA:A546(*)	2 mg/mL, S11225 (Molecular Probes)	1:250
SA:A555(*)	2 mg/mL, S32355 (Molecular Probes)	1:250
SA:A647(*)	2 mg/mL, S32357 (Molecular Probes)	1:800

Table 3.1: Survey of antibodies applied for immunofluorescence staining. All listed antibodies are α-mouse antibodies unless otherwise noted. (*) labeled items represent non-antibody proteins that are used for detection. $^{\checkmark}$ labeled antibodies were purified from B-cell hybridoma culture supernatants and conjugated to fluorescent dyes in the DRFZ.

3.6.3 Detection of apoptotic cells applying TUNEL technology

In situ detection of apoptotic cells in splenic tissue sections was performed applying TUNEL technology (TdT-mediated dUTP nick-end labeling) [92]. The TUNEL technology is based on the enzymatic labeling of free 3'-OH ends of fragmented DNA, that accounts for a hallmark of apoptosis. The enzyme TdT catalyzes the incorporation of either directly fluorescent dye coupled (*In situ* cell death detection kit, Roche) or biotinylated nucleotides (DeadEnd Colorimetric TUNEL System, Promega). The latter are detected in a further step by binding of streptavidin conjugated to a fluorescent dye.

The TUNEL assay requires pretreatment of the tissue sections by fixation and permeabilization that lead to accessibility of the fragmented DNA for the TdT enzyme. An unrequested side effect of this pretreatment is the degradation of other epitopes resulting at the best in poor staining of the same tissue section with additional antibodies. By testing different fixation and permeabilization conditions a protocol that ensures consistent detection of apoptotic cells applying TUNEL in combination with high quality immunofluorescence staining of further epitopes was established, that is specified in the following.

Cryosections were directly encircled with a grease pen (Dako pen, Dako) and fixed in 1% PFA for thirty minutes. Afterwards sections were washed three times three minutes with PBS and subsequently permeabilized in 1% sodium citrate/1% Triton X-100 at 4°C for two minutes. The sections were washed in PBS again, in the mean time the TUNEL reaction mixture was prepared (Tables 3.2 and 3.3). Applying the *In situ* cell death detection kit the TUNEL reaction mixture was directly added to the sections, the DeadEnd colorimetric TUNEL system required a preceding equilibration step carried out by incubating the sections with provided equilibration buffer for five to ten minutes at room temperature. After addition of the TUNEL reaction mixture sections were covererd with plastic coverslips to ensure even distribution of the reagent and to minimize evaporative loss. The slides were incubated at 37°C for one hour inside a humified chamber. Afterwards, sections were either directly washed in PBS (*In situ* cell death detection kit) or first immersed in 2x SSC buffer for ten minutes to terminate the reaction and then washed in PBS (DeadEnd colorimetric TUNEL system). Staining of the same tissue sections with additional antibodies was performed following the standard protocol (see Section 3.6.2). In case of the DeadEnd colorimetric TUNEL system, incorporated biotinylated nucleotides were detected using streptaviding conjugates SA:A546 or SA:A647 (Molecular Probes), respectively.

Component	Volume per reaction [μL]
Labeling solution	45
Enzyme solution	5

Table 3.2: Composition of the TUNEL reaction mixture applying the *In situ* cell death detection kit provided by Roche.

Component	Volume per reaction [μL]
Equilibration buffer	98
Biotinylated nucleotide mix	1
rTdT enzyme	1

Table 3.3: Composition of the TUNEL reaction mixture applying the DeadEnd colorimetric TUNEL system provided by Promega.

3.6.4 Improvement of Ki-67 staining

The Ki-67 antigen is a large nuclear protein (about 350 kDa) present only in the nuclei of cycling cells. Detection of this antigen by the α-Ki67 antibody could be dramatically enhanced by pretreatment of tissue sections by fixation and permeabilization as described for TUNEL technology (Section 3.6.3). Most likely, the accessibility of the nuclear Ki67 antigen is likewise improved.

3.6.5 Immunofluorescence staining of thick spleen sections

The 25 μm thick spleen sections were fixed and permeabilized prior to staining as described for TUNEL technology (section 3.6.3). This pretreatment improved the depth of penetration of antibodies into the tissue and reduced incubation times. All antibodies were applied in a two times higher concentration compared to the standard immunofluorescence staining protocol and the incubation time was extended to one hour. Additionally, the washing steps were prolonged to ten minutes. To avoid squashing of tissue section during the mounting process, sellotape was affixed to the slides serving as a spacer.

3.6.6 Establishment of four color immunofluorescence staining of macrophages, T cells, proliferating cells and FDC networks

In order to reduce time and effort of data acquisition, a four color immunofluorescence staining protocol was established for three dimensional reconstruction experiments. The chosen dye combination was A488, A555, A594 and A647, the absorption and emission spectra of these dyes are listed in the appendix (A.1).
The initial problem was the unavailability of any of the applied antibodies conjugated to A594, even worse the antibodies detecting macrophages (α-CD68) and T cells (α-CD3) both were conjugated to A488. Therefore, we chose an unorthodox "recolor" approach by first labeling T cells with the α-CD3:A488 antibody and directly afterwards quenching the fluorescence by addition of a rabbit α-Alexa488 antibody that is finally detected by a α-rabbit IgG:A594 antibody. Macrophages, proliferating cells and FDC network could then be labeled as usual. The chronology of the staining is given below.

1. rat α-Ki67
2. α-rat:A647
3. α-CD3:A488
4. rabbitα-A488 + α-FDC-M2:bio
5. α-rabbit IgG:A594 + SA:A555 + α-CD68:A488

3.7 Confocal microscopy

Immunofluorescence stained tissue sections were typically analyzed applying the Leica DM Ire2 confocal laser scanning microscope provided by the DRFZ. Data acquisition, processing and analysis are specified in Section 3.7.1 and 3.7.2. The sole exception was the acquisition of images for the three dimensional reconstruction experiments that were performed using the Leica TCS SP2 with IRBE2 of the group of Werner Zuschratter at the Leibnitz Institute for Neurobiology (IFN) in Magdeburg. The latter microscope was additionally equipped with a motorized xy-stage (Merzhäuser), allowing the implementation of meander scans. Because data acquisition, processing and analysis was much more complex in this case it is described in a discrete section (Section 3.7.3).
The basics of confocal microscopy are not explained here in detail, for interested readers the book *Confocal Laser Scanning Microscopy* is recommended [93].

3.7.1 Image acquisition Leica DM Ire2

All images were acquired using the LEICA LCS software, applied settings are summarized in the appendix (Table A.2). Images were scanned in sequential mode, that is each channel was scanned separately. In the following, channel 0 (ch0) always corresponds to stainings with FITC or A488, channel 1 (ch1) to A546 and channel 2 (ch2) to Cy5, APC or A647. Each channel was assigned a RGB pseudocolor: ch0=green, ch1=red, ch2=blue). Images of individual GC were typically acquired at x400 magnification. In rare cases, images were also acquired at x100 for overview purposes or at x630 magnification for detailed inspection of cellular interactions. For the analysis of macrophage morphology images were additionally magnified beyond x630 applying an electrical zoom factor.

3.7.2 Image processing and quantitative analysis

The first step of image processing comprised merging of the images obtained separately for each channel to one image, henceforth referred to as overlay image. Automated batch RGB merge of images as well as subsequent quantitative analysis of GC overlay images were implemented with the support of ImageJ based macros, that are listed in the appendix (Table A.4). ImageJ macros were developed with the help of Anke Klein, an undergraduate student of the Systems Immunology Group group. Macro source codes are available on request (n.wittenbrink@biologie.hu-berlin.de).

3.7.3 Image acquisition, processing and analysis for three dimensional reconstruction of murine spleens

Images of serial whole spleen sections were acquired using the Leica TCS SP2 confocal microscope operated by the group of Werner Zuschratter (IFN, Magdeburg). The settings for image acquisition are listed in the appendix (Table A.3). Images of whole spleen sections were obtained by performing meander scans (more precisely comb scans) at x100 magnification. The meander scan technology facilitates scanning of regions that are much larger than the optical field specified through the chosen objective by segmentation of the defined region into overlapping tiles. Each tile is scanned individually and afterwards, the images of overlapping tiles are aligned to one assembly image. The Leica TCS SP2 microscope was equipped with a motorized xy-stage (Merzhäuser) that was automatically actuated by the Arivis browser software. This software was also used to configure the settings of the meander scans as overlap and alignment of tiles (appendix, Table A.3). Serial images of whole spleen sections obtained for each analyzed tissue were integrated as separated layers into a Photoshop file. Within the first layer of the Photoshop file the entirety of follicular niches (FDC networks) was marked by consecutive numbering and the status of each follicular niche - either empty or occupied by a GC - was recorded. The mask containing the consecutive numbering was projected onto the next layer and newly arising follicular niches were added to the mask. Again the status of each follicular niche was recorded. This procedure was repeated for all layers of the photoshop file.

3.8 3-D reconstruction

Following a manual segmentation (ImageJ) of the GC as defined by the Ki-67 staining and a binarization of the segmented outline (ImageJ based macro *MacroROIVolumes*, developed by Armin Weiser, a fellow member of the Systems immunology group, for further details see Appendix A.4), the individual GC have been slice wise aligned according to their center of mass, both with and without allowing rotation. After the alignment a principal component analysis (Matlab) was performed on the filled outlines, resulting in three orthogonal eigenvectors, ensuring a right hand system. The length and angles (yaw, pitch, roll) of the eigenvectors were visualized (Amira) as ellipsoids, using the volume of the manual segmented data as constraint. 3-D reconstructions of murine spleens were assisted by Dr. Michael Sibila, University of Technology, Berlin, Institute for Software Engineering and Theoretical Computer Science and Armin Weiser, a fellow member of the Systems Immunology Group.

3.9 Flow cytometry

For FACS (fluorescence activated cell sorting) analysis single cell suspensions were stained for surface and intracellular markers applying fluorochrome conjugated antibodies (Table 3.4) and measured employing a BD FACS Calibur flow cytometer. In the flow cytometer, single cells move past an excitation source (laser) and the light hitting the cells is either scattered or absorbed and then re-emitted (fluorescence). This scattered or re-emitted light is collected by a detector. The pattern of light-scattering is dependent on the size and shape of cells and thereby gives a relative measure of the cellular characteristics. Fluorescence-based detection relies on the capacity of fluorescent dyes to adsorb light of an appropriate wavelength and subsequently re-emit light of a different wavelength. Detection of the intensity of the emitted wavelength is used as an indicator of the presence of a fluorescent dye on the cell and therefore the component it is labeling.

Specificity	Source	Dilution
surface markers		
α-B220:PE	rat, clone RA3.6B2 (DRFZ)✓	1:200
α-F4/80:Cy5	rat, clone F4/80 (DRFZ)✓	1:200
PNA:FITC(*)	5 mg/mL, FL-1071, (Vector)	1:2000
rat IgG2a:FITC	clone R35-95, isotype control, (Becton Dickinson)	1:100
intracellular markers		
α-CD68:A488	rat, clone KT3 (Serotec)	1:5

Table 3.4: Survey of antibodies applied in flow cytometry. All listed antibodies are α-mouse antibodies unless otherwise noted. (*) labeled items represent non-antibody proteins that are used for detection. ✓ labeled antibodies were purified from B-cell hybridoma culture supernatants and conjugated to fluorescent dyes in the DRFZ.

3.9.1 Extracellular staining of cells for analysis by flow cytometry

For each staining a volume of the single cell suspensions (Section 3.5) equally to 10^6 cells was transferred to a 1.5 ml reaction tube and cells were collected by centrifugation at 400 x g at 4°C. The supernatant was discarded, pelleted cells were resuspended in 100 μL of the respective antibodies diluted in FACS buffer followed by a twenty minute incubation at 4°C in the dark. The staining was stopped by addition of 1 mL FACS buffer and centrifugation at 400 x g for ten minutes. The supernatant was discarded, cells were washed and finally resuspended in 500 μL FASC buffer. Just prior to analysis 1 μL of propidium iodide (PI, 1 mg/mL, Sigma) was added to allow exclusion of dead/necrotic cells.

3.9.2 Intracellular staining of cells for analysis by flow cytometry

In case of cells that were stained for both, surface and intracellular markers, the extracellular staining was carried out first in order to prevent disintegration of membrane-bound molecules due to fixation and permeabilization. The latter are required for the intracellular staining. For intracellular staining cells were first fixed in 500 μL 2% PFA for twenty minutes at room temperature. Fixation was stopped by addition of 1 mL PBA and centrifugation at 400 x g for ten minutes. The supernatant was discarded and cells were permeabilized in 50 μl PBA/0.5% Saponin at 4°C. After twenty minutes 50 μL of antibody diluted in PBA/0.5% Saponin was added and incubated for another twenty minutes at 4°C. Staining was stopped by addition of 1 mL PBA/0.5% Saponin and centrifugation at 400 x g for ten minutes. The supernatant was discarded and the cells were repeatedly washed in PBA/0.5% Saponin at 4°C before they were finally resuspended in 500 μL FACS buffer.

3.9.3 FACS sorting of germinal center B cells and follicular Mϕ

Splenic single cell suspensions were prepared as described in Section 3.5. B cells were rapidly isolated from these preparations by magnetic negative depletion. Therefore, B cells were first stained with α-B220:PE and afterwards, magnetically labeled using α-PE MicroBeads (diluted 1:5) provided by Miltenyi Biotec. Separation of B cells was carried out applying the "DeplS" program of the autoMACS separator (Miltenyi Biotec). After autoMACS separation the cell counts of the B220$^+$ and B220$^-$ fractions were determined using the Casy cell counter (Schärfe System). Aliquots of both fractions were taken (about 10^5 cells) and their purity was checked by FACS analysis. For identification of GC B cells, the B220$^+$ fraction was counterstained with PNA:FITC. The B220$^-$ fraction was first stained with α-F4/80:Cy5 and was afterwards stained intracellulary with α-CD68:A488. Both fractions were finally resuspended in FACS buffer adjusted to a concentration of 5×10^7-1×10^8 cells/mL. Within the B220$^+$ fraction germinal center B cells were identified as B220$^+$ PNA^{high}. Follicular macrophages were identified within the B220$^-$ fraction as CD68$^+$ F4/80$^-$ B220$^-$, the latter to exclude any remaining B cell contamination. GC B cells and follicular macrophages were collected separately following multicolor cell sorting using a FACSAria cell-sorting system (Becton Dickinson). The RNA of collected GC B cells and follicular macrophages was isolated directly after cell sorting (Section 3.10.1).

3.10 Molecularbiology

3.10.1 Isolation of RNA

Isolation of RNA from sorted cells was performed in a RNAse-free environment using the PicoPure RNA isolation kit (Arcturus, Biozym). To avoid RNAse contamination certified RNAse-free buffers and reagents were used. Lab benchtops, tube racks and pipettors were routinely treated with the RNAse decontamination reagent RNAseZap (Ambion) and gloves were changed frequently during the isolation process. FACS sorted cells were first resuspended in 100 μL extraction buffer and incubated for thirty minutes in a heatblock adjusted to 42°C. Afterwards RNA was isolated according to the manufacturers' instructions. During isolation an optional DNAse treatment was performed in order to remove DNA from the preparations (RNAse-free DNAse Set, Qiagen). The isolated RNA was immediately stored at -70°C. RNA concentrations were determined using the Nanodrop ND-1000 spectrophotometer (Witec).

3.10.2 Amplification of Ig light chain rearrangements

Primers

All primers were synthesized by TIBMolBiol. The supplied lyophilisates were resuspended in DEPC H_2O (Roth) to a final concentration of 100 pmol per μl. Overall IgL chain rearrangements (IgL) were amplified using a primer set that was originally set up for the assembly of a mouse derived phage display library at the MRC Centre for Protein Engineering (for further information see http://www.mrc-cpe.cam.ac.uk/). These primers were designed to amplify the whole spectrum of variable region rearrangements of murine IgL. To simplify the working procedure and to save time, three primer mixes were prepared: V_L-mix, J_L-mix and C_L-mix, respectively. These mixes contained the primers listed below in a final concentration of 10 pmol per μL each (Table 3.5). The first round RT-PCR used the primer combination V_L-mix, C_L-mix. In case of follicular macrophage derived RNA, a second round PCR was carried out, using the semi-nested primer combination V_L-mix, J_L-mix.

PhOx specific IGKV4-59 (VκOx1) IgL rearrangements were amplified by RT-PCR using the primer combination Vκ77, C_L-mix (Table 3.5). The binding site of the Vκ77 primer is interrupted by a long intron sequence on the DNA level. Therefore, the Vκ77 primer cannot bind to and amplify genomic DNA. On RNA level the intron is missing due to splicing of mRNA. Again, the amplification of follicular macrophage derived RNA required a second round of PCR, that was carried out using the primer combination Vκ77, J_L-mix.

The optimal annealing temperature of primer mixes (62^{o}C) was determined in temperature gradient PCRs (data not shown). For a map off the used primers see Figure 3.1.

1. V_L-mix: Vκ-1 to 8 and Vλ-1
2. J_L-mix: Jκ-1/2, 4, 5 and Jλ-1, 2/3
3. C_L-mix: Cκ and Cλ

Primer	Sequence	Length [nt]	T_m [^{o}C]
Vκ-1	gatattgtgatgacBcagDc	20	58
Vκ-2	gatRttKtgatgacccaRac	20	57
Vκ-3	gaaaatgtgctcacccagtc	20	60
Vκ-4	gaYattgtgatgacacagtc	20	57
Vκ-5	gacatccagatgacacagac	20	60
Vκ-6	gaYattgtgctSacYcaRtc	20	59
Vκ-7	gacatccagatgacYcartc	20	60
Vκ-8	caaattgttctcacccagtc	20	58
Vλ-1	gctgttgtgactcaggaatc	20	60
Jκ-1/2	gtttKatttccagcttggtgc	21	62
Jκ-4	gttttatttccaactttgtc	20	52
Jκ5	ccagcttggtcccagcaccg	20	68
Jλ-1	ggacagtcagtttggttc	18	54
Jλ-2/3	ggacagtgaccttggttc	18	56
Cκ	gttcactgccatcaatcttc	20	58
Cλ	ggaaggtggaaacaBggtg	19	60
Vκ77	gctaatcagtgcctcagtcataata	25	63

Table 3.5: Primers used in amplification of Ig light chain rearrangements.

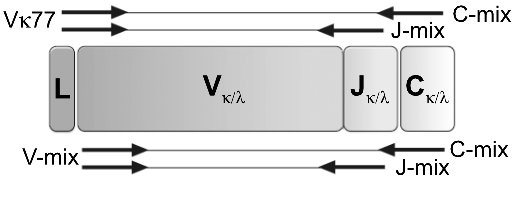

Figure 3.1: Primer map. Illustrated are the locations of primers used for amplification of overall IgL (V_L-mix, C_L-mix, J_L-mix) and IGKV4-59 (VκOx1) (Vκ77, C_L, J_L-mix).

OneStep RT-PCR and second round PCR

The reverse transcription of RNA and subsequent amplification of the resulting cDNA was performed applying the OneStep RT-PCR kit (Quiagen). This kit features the primer-specific transcription of RNA into cDNA, that is not the whole RNA but only RNA matching the used primer(s) is transcribed into cDNA. By virtue of the specially formulated enzyme blend provided with the kit reverse transcription and subsequent PCR amplification are feasible in one step i.e. in one reaction tube. The composition of RT-PCR samples is depicted in Table 3.6. RT-PCRs were performed in Biometra thermocyclers, according to the following temperature profile: *reverse transcription*, 50°C, 30 minutes $\longmapsto$ *initial denaturation*, 95°C, 15 minutes $\longmapsto$ *40 cycles of PCR amplification*: denaturation, 94°C, 1 minute $\mapsto$ annealing, 62°C, 1 minute $\mapsto$ elongation, 72°C, 1 minute $\longmapsto$ *final elongation*, 72°C, 10 minutes $\longmapsto$ *Cool off*, 4°C, ∞.
Second round PCRs were performed using Amplitaq Gold DNA Polymerase provided by Applied Biosystems, the composition of samples is given in Table 3.7. PCRs were performed in Biometra thermocyclers, according to the following temperature profile: *initial denaturation*, 94°C, 9 minutes $\longmapsto$ *40 cycles of PCR amplification*: denaturation, 94°C, 1 minute $\mapsto$ annealing, 62°C, 1 minute $\mapsto$ elongation, 72°C, 1 minute $\longmapsto$ *final elongation*, 72°C, 10 minutes $\longmapsto$ *Cool off*, 4°C, ∞.

Component	Volume per reaction [μL]
Mastermix	
RNAse-free water	19
5x RT-PCR buffer	10
5x Q-Solution	10
dNTP mix (10 mM of each dNTP)	2
Enzyme mix	2
Primer	
3’Primer (10 pmol/μl)	3
5’Primer (10 pmol/μl)	3
Template	
RNA template (5-50 ng/μl)	1
Total volume	50

Table 3.6: Composition of RT-PCR samples applying the OneStep RT-PCR kit provided by Qiagen.

3.10.3 Analytical and preparative agarose gel electrophoresis

For visualization and separation of DNA amplificates analytical and preparative submarine horizontal agarose gel electrophoresis was conducted. For analytical purposes gels made from standard agarose were prepared (Roth), for preparative purposes NuSieve GTG agarose (FMC) featuring a low melting temperature was used. In general, 100 mL agarose gels (1.5-2% in TAE) containing 1 μL ethidiumbromide (1 mg/mL, Biorad) were poured. The added ethidiumbromide intercalates into the DNA double helices and can be later on vizualized by UV-illumination (λ=302 nm).

Component	Volume per reaction [μL]
Mastermix	
DNAse-free water	34.75
10x PCR Gold buffer	5
dNTP mix (10 mM of each dNTP)	2
$MgCl_2$ (25 mM)	4
AmplitaqGold DNA polymerase	1.25
Primer	
3'Primer (10 pmol/μl)	1
5'Primer (10 pmol/μl)	1
Template	
First round RT-PCR sample	1
Total volume	50

Table 3.7: Composition of second round PCRs samples, AmpliTaq Gold DNA Polymerase, Applied Biosystems.

In case of each sample 18 μL were mixed with 2 μL of loading buffer (Invitrogen) that contained the tracking dyes bromphenol blue and xylene xyanole. The electrophoresis was performed in 1xTAE buffer applying a constant voltage of 100-120 V. The size dependent separation of DNA fragments is based on the migration of DNA after conducting an electric field. Positively charged DNA migrates towards the negative pole with a velocity that is reciprocally proportional to the $\log_{10}$ of its size. A molecular size weight marker (Track-It 100 bp DNA Ladder, Invitrogen) was used to identify the size of amplificates run on the agarose gel. After electrophoresis gels were photographed applying an UV-illuminator and fragments of interest were dissected using disposable micro lancets (Braun). Single bands at 350 bp and 290 bp were expected for first round RT-PCRs and second round PCRs, respectively.

3.10.4 Extraction of DNA from agarose gels

Following preparative agarose gel electrophoresis, fragments of interest were excised from the gel using mini lancets (Braun). The DNA of excised amplificates was then extracted applying the QIAQuick gel extraction kit (Qiagen) according to the manufacturers' instructions. The QIAQuick system is based on the combination of spin-column technology and selective binding of DNA to silica-gel membranes in the presence of high salt concentrations while contaminants pass through. Extracted DNA was finally eluted with 50 μl DEPC H_2O (Roth) and was stored at 4°C.

3.10.5 Cloning of IgL amplificates

Cloning of Ig light chain amplificates was performed applying the TOPO TA Cloning Kit (with pCR2.1-TOPO vector) with One Shot TOP10F' Chemically Competent E. coli cells (Invitrogen). TOPO TA cloning provides a one-step cloning strategy for *Taq* polymerase-amplified PCR fragments by taking advantage of the nontemplate-dependent terminal transferase activity of the enzyme that results in the addition of single deoxyadenosines (A) to the 3' ends of PCR amplificates. Such amplificates ligate with the linearized pCR2.1 vector, that bears overhanging 3' single deoxythymidine (T) residues. Identification of successfully transformed cells resulted from using ampicillin resistance as selection marker. Insert carrying vectors were detected by blue/white screening of recombinant bacterial clones that is based on the insertional inactivation of the enzyme β-galactosidase (LacZ). Functional β-galactosidase converts the substrate X-Gal into a colored product resulting in blue colonies. Cloning inserts disrupt the β-galactosidase activity and yield in white bacterial colonies.

Ligation

The composition of the ligation mixture is displayed in Table 3.8. After gentle mixing, the ligation mixture was incubated for five to ten minutes at room temperature and placed on ice until transformation.

Component	Volume per reaction [μL]
DEPC H_2O	3
Salt solution	1
PCR amplificate (20 ng/μL)	1
TOPO pCR2.1 vector	1
Total volume	6

Table 3.8: Composition of the ligation mixture applying the TOPO TA Cloning kit provided by Qiagen.

Transformation

Competent cells were allowed to thaw by incubating for about ten minutes on ice. Precautiously, 2 μL of the ligation mixture were added to the competent cells and mixed gently by stirring with the pipet tip. Then, competent cells were incubated on ice for thirty minutes and thereafter, uptake of vector DNA was launched by heat-shock (42°C, thirty seconds). Afterwards competent cells were placed on ice, supplemented with 250 μL S.O.C medium and shaken horizontally (200 rpm) at 37°C for one hour. 25 to 50 μL of each transformation were spread on prewarmed selective agar plates (see Table 3.9) and incubated overnight at 37°C. Transformants were then isolated from agar plates and incubated overnight in 2 mL LB medium containing 50 μg/mL ampicillin.

Component	Quantity
LB medium (Bio101)	8 capsules
Select agar (Roth)	4.5 g
H_2O	300 [μL]
autoclaving	
Ampicillin [100 mg/mL] (Roth)	150 μL
IPTG [1 M] (Roth)	80 μL
X-Gal [20 mg/mL Dimethylformamide] (Roth)	700 μL

Table 3.9: Composition and preparation of selective agar plates.

3.10.6 Plasmid minpreparation

Plasmid minipreparations were performed using the NucleoSpin Plasmid kit according to the manufacturers' instructions (Macherey-Nagel). The kit is based on SDS/alkaline lysis of harvested bacteria, followed by DNA binding to a silica membrane and removal of contaminants by employing spin column technology. The plasmid DNA was finally eluted with 50-100 μl DEPC H_2O (Roth) and was afterwards stored at 4°C.

3.10.7 Sequencing of IgL amplificates

Sequences of cloned IgL rearrangements were obtained using the DNA sequencing service offered by MWG Biotech (for further information see the website of the company http://www.mwg-biotech.com/html/all/index.php). For sequencing, a volume equivalent to 1 μg of the isolated plasmid DNA was transferred to a new 1.5 ml reaction tube, vacuum dried and then send to MWG Biotech.
Sequence analysis was performed using the IMGT database and IMGT/V-Quest. Sequence alignments were done in CLC Free Workbench.

3.11 Mathematical simulations

All mathematical simulations presented in this thesis were compiled using the R software (http://www.r-project.org/). Specifications and explanations of simulations are given directly in the text of the results part. Simulations were assisted by my supervisor Dr. Michal Or-Guil and Dr. Johannes Schuchhardt (MicroDiscovery GmbH, Berlin, Germany).

3.12 Statistical analysis

Statistical analysis was performed using the Analyze-It software add-in for Microsoft Excel. Statistical significance was assessed using Student's t test, Wilcoxon rang sum test (Mann-Whitney U test) or χ^2 test unless otherwise noted. Values of p were considered statistically significant at $p<0.05$. Linear and power regressions were calculated in Sigmaplot.

Revising the kinetics of germinal center growth

Chapter 4

Revising the kinetics of germinal center growth

The current state of knowledge on the kinetics of GC growth following immunization with hapten-carrier conjugates is basically attributed to a series of distinguished articles, published by the groups of I.C. MacLennan [24], G. Kelsoe [70] and A.K. Szakal, J.G. Tew [45] in 1991. Nevertheless, just this kinetics became a major challenge for the present thesis, as initial results revealed a much more complex picture than anticipated so far.

4.1 Assessing the kinetics of GC growth by 2-D cross-sectional evaluation

The kinetics of GC growth was assessed by studying the *de novo* formation of GC within the murine spleen following intraperitoneal (i.p.) immunization of BALB/c mice with 2-phenyloxazolone (phOx) coupled to chicken serum albumin (CSA). Spleens of challenged mice were collected at frequent intervals of two to three days over a period of three weeks and were subsequently subjected to cross-sectional immunohistological analysis.

4.1.1 2-D cross-sectional evaluation of GC size and geometry

To save time and effort, the cross-sectional size of GC was not recorded separately but by means of triple immunofluorescent stainings that were carried out to assess either kinetics of GC T cells (Section 5.1) or GC macrophages (Section 5.2). Since these stainings were performed on consecutive sections, the resultant kinetics of GC growth turned out to be identical. In the following, the kinetics of GC growth is given according to the evaluation of stainings performed for recording the kinetics of GC T cells. GC were identified as Ki-67 positive cell clusters and by anatomical location in triple immunofluorescence stainings of proliferating cells (Ki-67), T cells (CD3) and FDC networks (FDC-M2) (Figure 4.1, A). For the quantitative analysis, GC boundaries, referred to as regions of interest (ROIs), were first manually assigned to all acquired images. Subsequently, the size of cross-sectional GC was recorded by measuring the areas of assigned ROIs [μm^2]. In addition, the geometry of cross-sectional GC was captured by parameterization of ROIs applying an ellipse-fitting algorithm that outputs the major (r1) and minor radii (r2) of fitted ellipses (Figure 4.1). As a further indicator for GC size, the number of Ki-67^+ proliferating cells per cross-sectional GC was determined by automated batch processing of image stacks applying an adapted version of the Nucleus Counter Plugin of the ImageJ software (Figure 4.1, B).

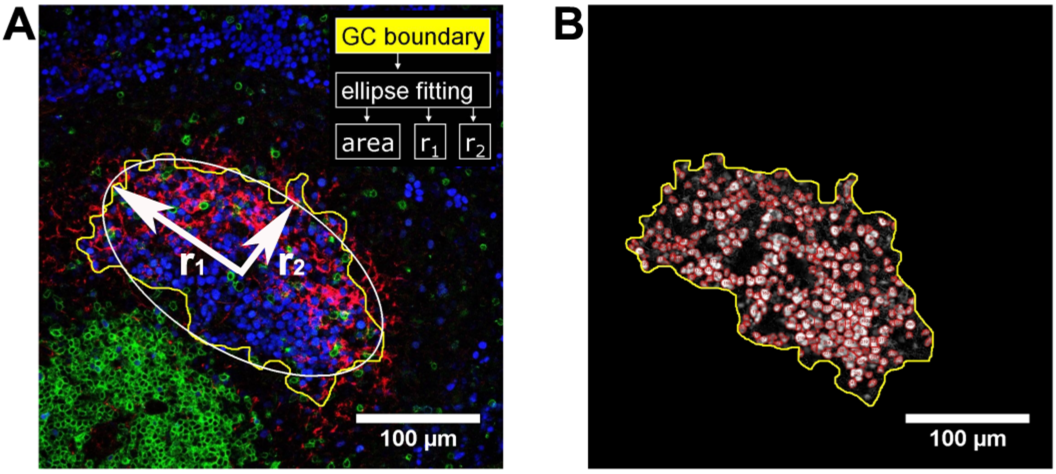

Figure 4.1: Quantitative analysis of acquired GC images exemplified by representative images of a GC at day 12 after immunization. (A) GC were identified by reactivity to Ki-67 and anatomical location in triple stainings of proliferating cells (Ki-67, blue), T cells (CD3, green) and FDC (FDC-M2, red). GC boundaries were manually assigned (yellow) and saved as regions of interest (ROI). ROIs were parametrized by an ellipse fitting algorithm and resultant areas of ROIs as well as major (r1) and minor radii (r2) of the fitted ellipses (white) were recorded. (B) Automated detection and measurement of Ki-67^+ proliferating cells for the GC depicted in (A) applying an adapted version of the Nucleus Counter plugin of the ImageJ software. Scale bar 100 μm.

The work of Camacho et al. [67] first pointed out a less pronounced subcompartimentalization of murine splenic GC by means of Ki-67 staining compared to human tonsillar GC. This observation was further confirmed by others, revealing a rather phenotypically homogeneous proliferating GC B cell population throughout the response. In spite of that, Ki-67 was affirmed as convenient marker for identification and measurement of GC in an initial experiment. This was realized by comparison of measurements of GC that were identified by reactivity to Ki-67 to GC visualized in adjacent sections using PNA. Such analysis reveals a strict concordance of recorded cross-sectional GC areas assessed by Ki-67 and PNA reactivity at all tested time points (Figure 4.2). For the large scale analysis Ki-67 was preferred to PNA because it both facilitates the manual assignment of ROIs due to a more distinct contour of GC and potentiates automated detection and counting of Ki-67^+ cells within assigned ROIs. The number of Ki-67^+ cells is further shown to strictly correlate with the cross-sectional area of GC (Figure 4.3), therefore both modes of measuring GC size can be employed interchangeable.

Accordingly, the mutual dependence of cross-sectional GC size and numbers of Ki-67^+ cells can be inferred from the data set. As a result, 1 μm^2 cross-sectional GC area is equivalent to 0.0116 Ki-67^+ cells, respectively one Ki-67^+ cell corresponds to 86 μm^2 cross-sectional GC area.

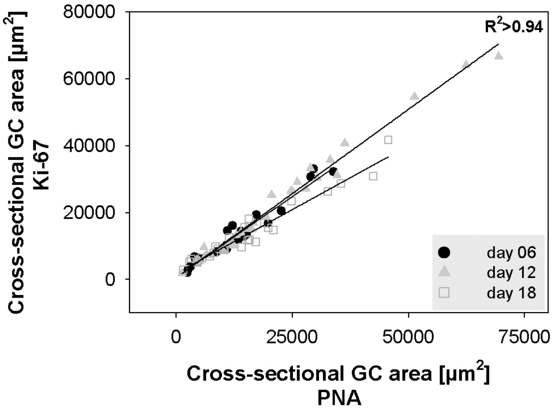

Figure 4.2: Verification of Ki-67 as consistent marker for detection and measurement of GC. The scatter plot demonstrates the strict correlation of cross-sectional areas recorded by means of reactivity to Ki-67 (vertical axis) and PNA (horizontal axis). GC were stained with PNA on adjacent sections (not shown) and acquired images were processed as illustrated in Figure 4.1 for Ki-67. Data is representative of in each case one splenic tissue section at day 6, 12 and 18 post immunization. Regression lines and correlation coefficients (R^2) are specified for the scatter plots.

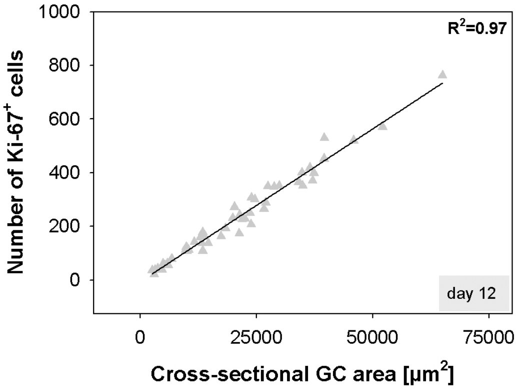

Figure 4.3: The number of Ki-67^+ cells within cross-sectional GC is determinated by the size of GC. Vertical axis represents the number of Ki-67^+ cells of cross-sectional GC plotted against the cross-sectional area of these GC. Data is representative of a splenic tissue section at day 12 post immunization. Regression line and correlation coefficient (R^2) are specified for the scatter plot.

4.1.2 Robust overall GC growth kinetics is based upon notable size distribution of GC within individual sections

The kinetics of GC growth was assessed by quantitative analysis of GC size and geometry as described above. In total, 1136 GC out of 45 sections derived from 23 mice were evaluated, a detailed survey of all analyzed sections and evaluated GC is given in Section 5.1, Table 5.1. The resultant kinetics of the average size of GC by means of recorded cross-sectional GC areas is resumed in Figure 4.4. Well-established GC, typically of very small size, are first detectable at day 4 after immunization. The average size of GC afterwards steeply increases and reaches its maximum at day 10, thereafter, it gradually declines. The deviation of mean values, both for sections of the same and different individuals, turns out to be rather moderate (Figure 4.4, A).

Converse to the fairly robust kinetics of the mean size of GC, discrete mean values are shown to be representative of a notable size distribution of GC within the individual spleen sections, reflected by substantial intra-section standard deviations (Figure 4.4, B). The kinetics of GC growth, given by the numbers of Ki-67$^+$ cells per cross-sectional GC, leads to conforming results. Moreover, displaying the entirety of recorded values for each time point demonstrates that the size distribution of cross-sectional GC emerges as early as day 6 and becomes most pronounced between day 8 to 12 after immunization. A striking feature of the broad size distribution of GC is the sustained high frequency of cross-sectional GC of rather small size (Figure 4.5).

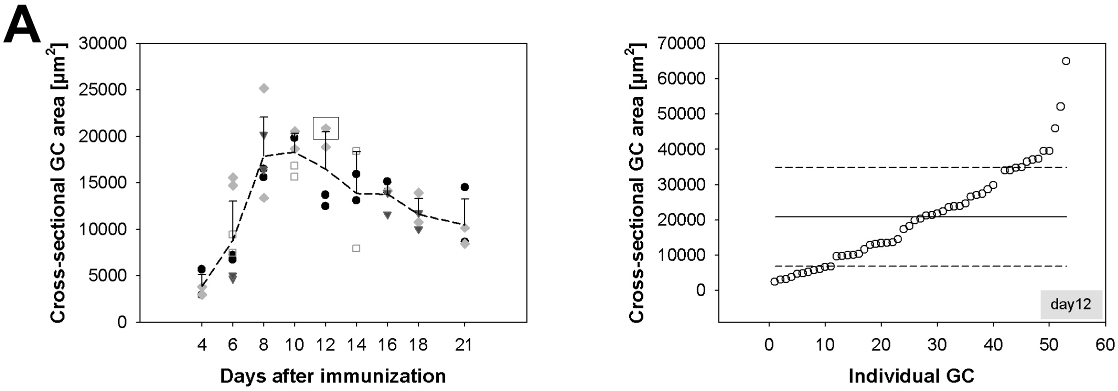

Figure 4.4: Kinetics of GC growth in spleens of phOx-CSA immunized mice. GC were identified and measured as illustrated in Figure 4.1. (A) Mean kinetics and inter-section variance of GC size. Vertical axis represents the slope of the mean area of GC with the standard deviation plotted against the time after immunization. The data were obtained from two sections per mouse (n=2-4) that were at least 50 sections apart. The two values obtained per mouse are each depicted by the same symbol. The analysis reveals low inter-section variation within and between individual mice. (B) High intra-section variance of GC size. Data is representative of the splenic tissue section at day 12 post immunization highlighted by a box in (A). The scatter plot represents recorded GC areas (vertical axis) for all detected GC, sorted by their size (horizontal axis). The solid line depicts the intra-section mean, dashed lines indicate the range of the intra-section standard deviation.

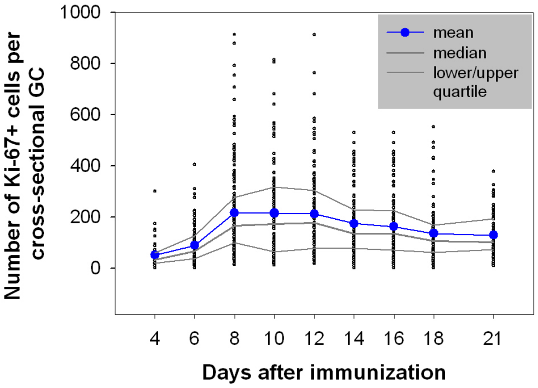

Figure 4.5: Kinetics of GC growth displayed as numbers of Ki-67^+ cells per cross-sectional GC. The depicted values are representative of the entirety for measured GC for each time point. The course of the mean is given by the blue curve, gray curves illustrate the median (thick line) as well as lower and upper quartile (thin lines).

4.1.3 Mathematical simulation of virtual random sectioning fails to explain the high intra-section variance of GC size.

The broad size distribution of cross-sectional GC within individual spleen sections most likely reflects random sectioning of GC. Nevertheless, it can also be indicative of a real size distribution of GC in the original 3-D spleen sample or even attributes to both. The problem of anticipating the distribution and extension of objects in the original 3-D space based on cross-sectional profiling is a general one, referred to as Wicksell's corpuscle problem (schematically illustrated in Figure 4.6). To assess the influence of random sectioning on the obtained data, R-based mathematical simulations of virtual random sectioning of various shaped ellipsoids were performed (Figure 4.7). Briefly, ellipsoids were allowed to freely rotate in the 3-D space and virtually random sectioned 20,000 times. The resultant radii (r1, r2) as well as the frequencies (f) of areas and radius ratios (r1/r2) of cross-sectional ellipses were plotted and compared to the experimentally obtained data. Such analysis explicitly rules out that random sectioning of spheres (Figure 4.7, A) accounts for the experimentally recorded cross-sectional profiles of GC (exemplified for day 10 after immunization in Figure 4.7, C). Likewise, neither of the further tested ellipsoids succeeds in reproducing the experimentally obtained data. Figure 4.7, B illustrates the simulation of random sectioning of an oblong shaped ellipsoid that bears the closest resemblance to the experimental data. The most striking divergence of simulations occurs at the level of recorded cross-sectional GC areas, as all simulations failed to reproduce the experimentally recorded high frequencies of rather small cross-sectional GC areas.

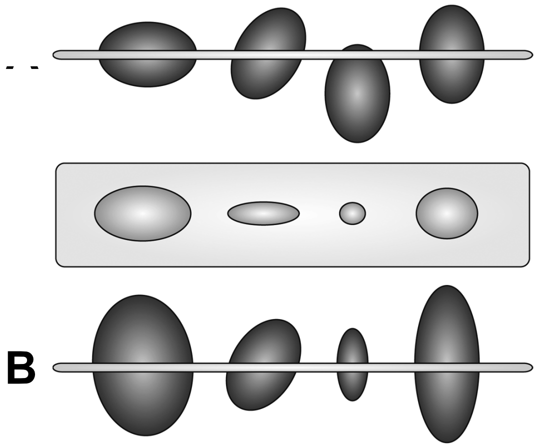

Figure 4.6: Schematic illustration of Wicksell's corpuscle problem. The Wicksell's corpuscle problem deals with the dilemma of inferring the volume distribution of a population of particles, using a lower dimensional sampling probe. As illustrated, rather different populations of particles (A and B) give rise to the very same cross-sectional profile.

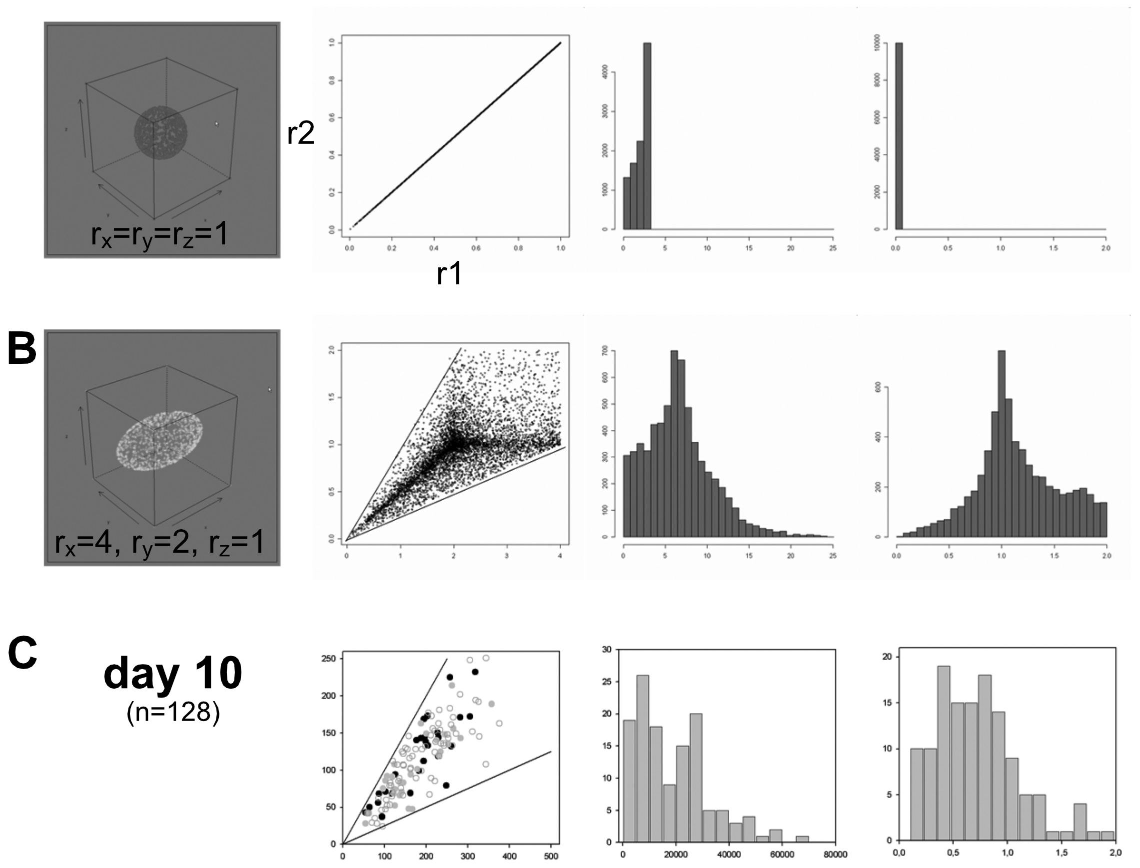

Figure 4.7: Random sectioning fails to explain the high intra-section variance of GC size. Various shaped ellipsoids were virtually sectioned in R-based mathematical simulations. Briefly, ellipsoids were allowed to freely rotate in the 3-D space and randomly sectioned 20,000 times. The resultant radii (r1, r2) as well as the frequencies (f) of areas and radius ratios (r1/r2) of cross-sectional ellipses were plotted and compared to experimentally obtained data. (A) Simulation of random sectioning of a sphere (r_x=r_y=r_z=1). (B) Simulation of random sectioning of an oblong ellipsoid (r_x=4, r_y=2, r_z=1). (C) Experimentally obtained data exemplified for the total number of cross-sectional GC recorded at day 10 after immunization (see Table 5.1), symbols indicate individual mice (n=3). *Simulations were assisted by Dr. Michal Or-Guil and Dr. Johannes Schuchhardt.*

4.2 A theoretical approach to GC ensemble kinetics

The finding that the broad size distribution of cross-sectional GC does not solely attribute to random sectioning of GC (Section 4.1.3) but potentially also reflects a real size or volume distribution of GC has some major implications for the interpretation of GC growth kinetics. According to the current notion, the growth behavior of individual GC obeys the average kinetics of the ensemble of GC within the observed lymphatic tissue. The existence of a real size distribution of GC challenges this view, since it allows for non-uniform growth of individual GC within an ensemble. To check if others than the established ensemble kinetics are consistent with the experimental data, different predefined GC ensembles were therefore subjected to simulation-based random sectioning.

4.2.1 Formulation of hypothetical growth kinetics of individual GC

As a first step, hypothetical growth kinetics of individual GC, that later serve as templates for the composition of GC ensembles, are formulated according to the mathematical model given below. In the model scenario, a fraction of proliferating GC B cells halts proliferation and is subjected to selection as given by the selection rate. Selected GC B cells do not further take part in the GC reaction but disappear from the system by either undergoing apoptosis or emigration. Due to this lack of internal iteration, the modeled kinetics is independent of affinity of the B cell receptor. Therefore, the time course and lifetime of an individual GC solely rely on the chosen rates of proliferation and selection. Two examples of hypothetical growth kinetics of individual GC that substantially differ with regard to their lifetimes are illustrated in Figure 4.8. In the former case, the life time of individual GC is equivalent to the established life span of the GC ensemble of about 3 weeks (Figure 4.8, A), whereas the latter case features a significantly shorter lifetime of individual GC of about 6 days (Figure 4.8, B). In the following, these two cases are referred to as the *long-lived* and *short-lived* kinetics, respectively.

Model equations

The model scenario outlined above is specified by the following set of ordinary differential equations:

$$\dot{b} = p \cdot b(t) - r(t) \cdot b(t) \tag{4.1}$$

$$\dot{c} = r(t) \cdot b(t) - \delta \cdot c(t) \tag{4.2}$$

$$r(t) = \frac{r_0}{2} \cdot (1 + \tanh((t - t_0)/\tau)) \tag{4.3}$$

A population GC B cells (b) proliferates with the rate constant p. A fraction of this population then halts proliferation and is subjected to selection according to the selection rate function *r(t)*. The GC B cells undergoing selection (**c**) disappear from the system with the rate constant δ. The chosen selection rate function *r(t)* fulfills the premise of a gradually increasing selection rate, starting from zero and finally reaching its maximum rate constant r_0.

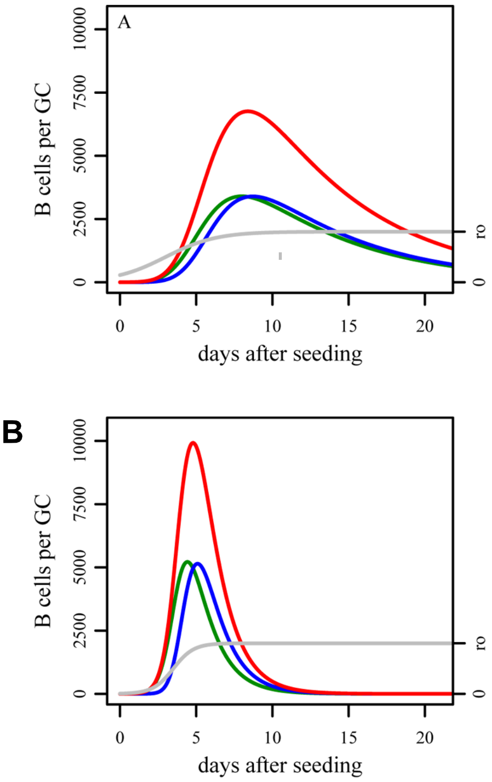

Figure 4.8: Formulation of hypothetical long-lived (A) and short-lived (B) growth kinetics of individual GC according to the mathematical model described in Section 4.2.1. Illustrated are the simulated time plots of the populations of proliferating B cells (b), B cells undergoing selection (c), total B cells (b+c) and the selection rate function (r). Applied parameter values and initial conditions are depicted for each plot. *Modeling was assisted by Dr. Michal Or-Guil and Dr. Johannes Schuchhardt.*

4.2.2 Simulation of random sectioning of different GC ensemble kinetics

The *long-lived* and *short-lived* growth kinetics of individual GC now serve as templates for composition of kinetics of ensembles of many individual GC of which 500 are allowed to coexist. Albeit there is no limit to conceivable ensemble scenarios, the consideration is first confined to the 3 rather "simple" instances represented in the left panel of Figure 4.9. With respect to the ensemble kinetics illustrated in Figure 4.9, A and B the time course of individual GC is given by the *long-lived* kinetics. Since GC are unlikely to be launched all at exactly the same time, these ensemble kinetics additionally allow for a small variation in the seeding time point. Nevertheless, seeding of GC is restricted to a short period of time, in which the maximum seeding rate is reached within 1.5 days and afterwards rapidly decays. Since seeding of GC is virtually absent from day 4 after immunization onwards, the ensembles of GC are seeded "almost" simultaneously, thereby promoting virtually synchronous

GC growth progression. The ensemble kinetics represented in Figure 4.9, A and B finally diverge in that the latter additionally allows for pronounced variation of maximal attained GC size. Regarding the ensemble kinetics illustrated in Figure 4.9, C, each individual GC obeys the *short-lived* kinetics. Moreover, compared to the afore described ensemble kinetics, the maximum seeding rate is attained at a later time point (day 4 after immunization) and only decays slowly afterwards. Since seeding is confined to a extended period of time, it provides for asynchronous seeding and progression of GC.

To facilitate comparison of the hypothetical ensemble kinetics represented in Figure 4.9, A, B and C with the experimentally recorded ensemble kinetics of cross-sectional GC size (Figure 4.5), simulations of planar random sectioning were performed. To this end, the generic shape of GC is specified as oblong ellipsoid (diameter ratios 4:1:1), and GC are assumed to possess no preferential orientation but to be distributed randomly within the spleen. During simulations, sectioning of GC ellipsoids occurs according to their individual probability of being cut at all, which strictly depends on their size. The resultant cross-sectional profiles are depicted in the right panel of Figure 4.9. Strikingly, the simulation of random sectioning of any of the three highly divergent ensemble kinetics results in the very same cross-sectional profile that in turn closely resembles the experimentally attained data (Figure 4.5). Therefore, cross-sectional evaluation of GC size just suffices to infer the average kinetics of the ensemble but does not allow for inference of the underlying kinetics of individual GC. In conclusion, the accepted notion of GC growth including synchronous seeding and progression of long-lived GC (Figure 4.9, A) turns out to be not the only conceivable scenario.

4.3 Assessing the kinetics of GC growth by 3-D volumetric evaluation

The cross-sectional evaluation of GC size has proven insufficient for inferring the kinetics of individual GC. Moreover, simulation-based random sectioning revealed that others than the accepted notion of GC ensemble kinetics are consistent with the experimental data, allowing for asynchronous formation and progression of GC and a lifetime of individual GC that is much shorter than previously thought. To further elucidate the growth kinetics of individual GC, the evaluation was upgraded from cross-sectional to volumetric profiles of splenic GC. The 3-D evaluation of splenic volumes shall be capable of distinguishing the introduced hypothetical GC ensemble kinetics (Section 4.2.2, Figure 4.9), by means of two measures:

1. Time course of occupation of follicular niches by GC
   Regarding the two ensemble kinetics featuring synchronous GC formation and progression (Figure 4.9, A and B), the number of follicular niches occupied by GC do not increase from day 4-6 onwards, since seeding of GC is merely restricted to a short period of time. By contrast, the asynchronous ensemble kinetics of short-lived GC (Figure 4.9, C) is characterized by increasing numbers of follicular niches occupied by GC even after day 6, since the period of seeding is extended.

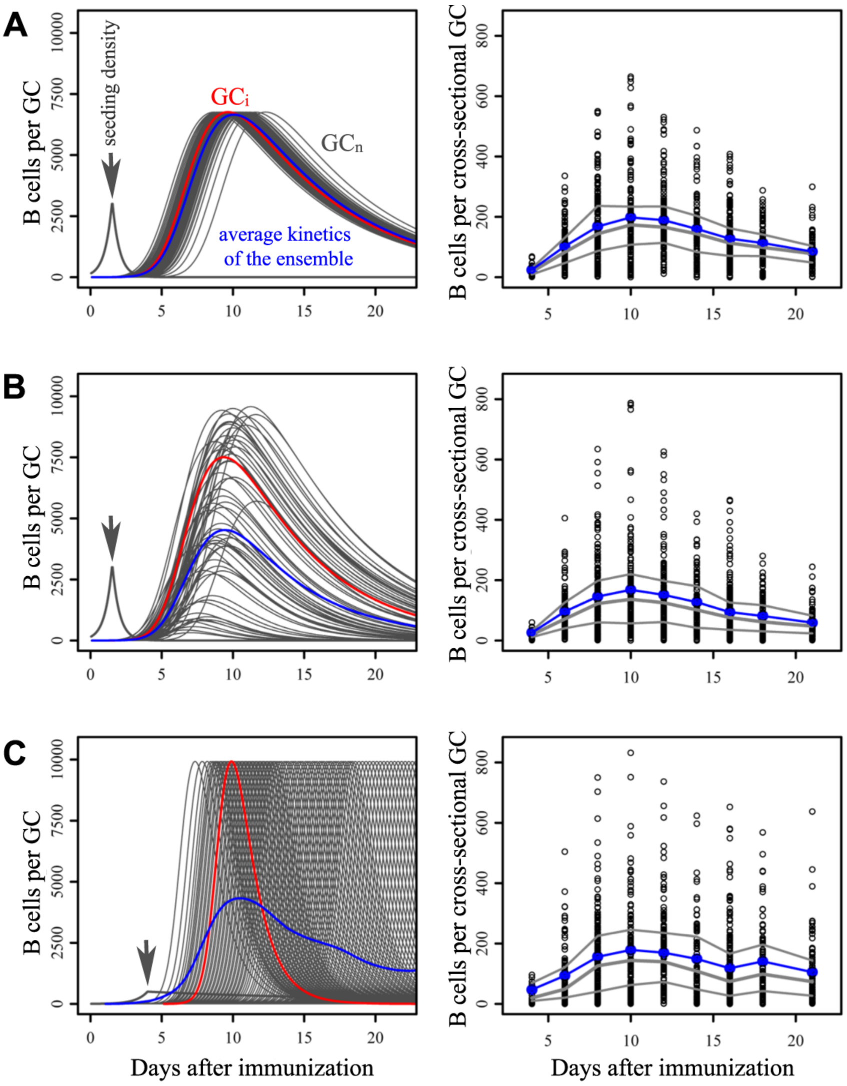

Figure 4.9: Simulation of random sectioning of different GC ensemble kinetics. *Left panel*: GC ensembles kinetics were compiled using the hypothetical growth kinetics of individual GC shown in Figure 4.8 as templates. Each ensemble is composed out of many individual GC of which 500 are allowed to coexist (GC$_n$, gray curves). For readability, only every tenth individual GC kinetics is illustrated, in which one is highlighted (GC$_i$, red curve). The distribution of GC seeding events is given by the seeding density, that follows a cusp like shape (dark gray curve, arbitrary units). The illustrated ensemble kinetics (A), (B) and (C) represent combinations of different individual GC growth kinetics and seeding events. The resultant average kinetics of each ensemble is indicated by the blue curve. *Right panel*: Simulated cross-sectional profiles of the respective ensemble kinetics. Simulations were performed assuming that GC are distributed randomly, have the shape of oblong ellipsoids (r$_x$=4, r$_y$=1, r$_z$=1), and that ellipsoids are sectioned by a plane cut, in which their individual probability of being cut at all, is dependent on their size. Cross-sectional profiles are displayed as numbers of B cells per cross-sectional GC (open circles), the mean size of cross-sectional GC (blue circles) as well as the median lower and upper quartile (gray curves) of the simulated size distribution are highlighted. (A) Synchronous ensemble kinetics of long-lived GC. The maximum seeding rate is reached within 1.5 days and decays rapidly within half a day. (B) Ensemble kinetics of long-lived GC featuring high variation in attained maximum size. The seeding rate is the same as in (A). (C) Asynchronous ensemble kinetics of short-lived GC. The seeding rate increases for four days and decays only slowly afterwards, implementing an ongoing series of seeding events. *Simulations were assisted by Dr. Michal Or-Guil and Dr. Johannes Schuchhardt.*

2. Volume distribution of GC
   In contrast to the synchronous ensemble kinetics of long-lived GC of fixed maximal size (Figure 4.9, A), both the ensemble kinetics of long-lived GC featuring high variation in maximal attained size (Figure 4.9, B) and the asynchronous ensemble kinetics of short-lived GC (Figure 4.9, C) are characterized by a profound volume distribution of GC.

4.3.1 3-D volumetric evaluation of GC growth kinetics

The approach to 3-D evaluation of GC growth kinetics is graphically illustrated in Figure 4.10, a detailed survey of analyzed spleen specimens is given in Table 4.1. Briefly, spleens of cohorts of BALB/c mice (n=3) were analyzed at day 6, 10 and 14 after phOx-CSA challenge. With respect to each spleen specimen, 7 serial tissue sections (s01-s07), spaced at intervals of 50 μm, spanning a total thickness of 300 μm were quadruple stained for proliferating cells (mAb Ki-67), FDC-networks (mAb FDC-M2), T cells (mAb CD3) and macrophages (mAb CD68). Images of entire spleen sections were afterwards obtained by performing meander scans at x100 magnification (exemplary depicted for a spleen specimen obtained at day 10 after immunization in Figure 4.10, A.

Evaluation of spleen specimens was performed both separately for each individual section (2-D cross-sectional evaluation) and integratively for the whole series of sections (3-D volumetric evaluation). The results of the 2-D cross-sectional evaluation are summarized in Table 4.1. Both the recorded total number of follicular niches and the number of follicular niches occupied by GC show only little variation among each series of serial sections. The mean area of the analyzed sets of serial sections ranges from 30.8 to 49.5 mm^2, correspondingly the estimated volume ranges from 9.2 to 14.9 mm^3.

The 3-D volumetric evaluation was accomplished by tracing follicular niches throughout the analyzed splenic volume or the series of images sections, respectively. During tracing, follicular niches were denoted as either empty or occupied by virtue of concomitant existence or absence of GC. The tracing of follicular niches is exemplary illustrated for one empty and three occupied niches at day 10 after immunization in Figure 4.10, B. Notably, the numbers of sections spanned by occupied follicular niches show pronounced variation. Regarding empty follicular niches, this variation turns out to be rather moderate since their range generally tends to be smaller (Figure A.3).

4.3.2 The 3-D volumetric evaluation of occupation of follicular niches indicates continuous new formation of GC throughout the immune response

The time courses of the numbers of total, occupied and empty follicular niches - as revealed by 3-D volumetric evaluation - are graphically illustrated in Figure 4.11. Values are quoted as numbers of follicular niches per 12 mm^3, corresponding to the average volume comprised by the series of 7 serial sections analyzed per spleen specimen (see Table 4.1). Notably, the total number of follicular niches per splenic volume is fixed in BALB/c mice and does not change during the progression of the immune response in these mice (231±13, 234±35, 225±24 at days 6, 10 and

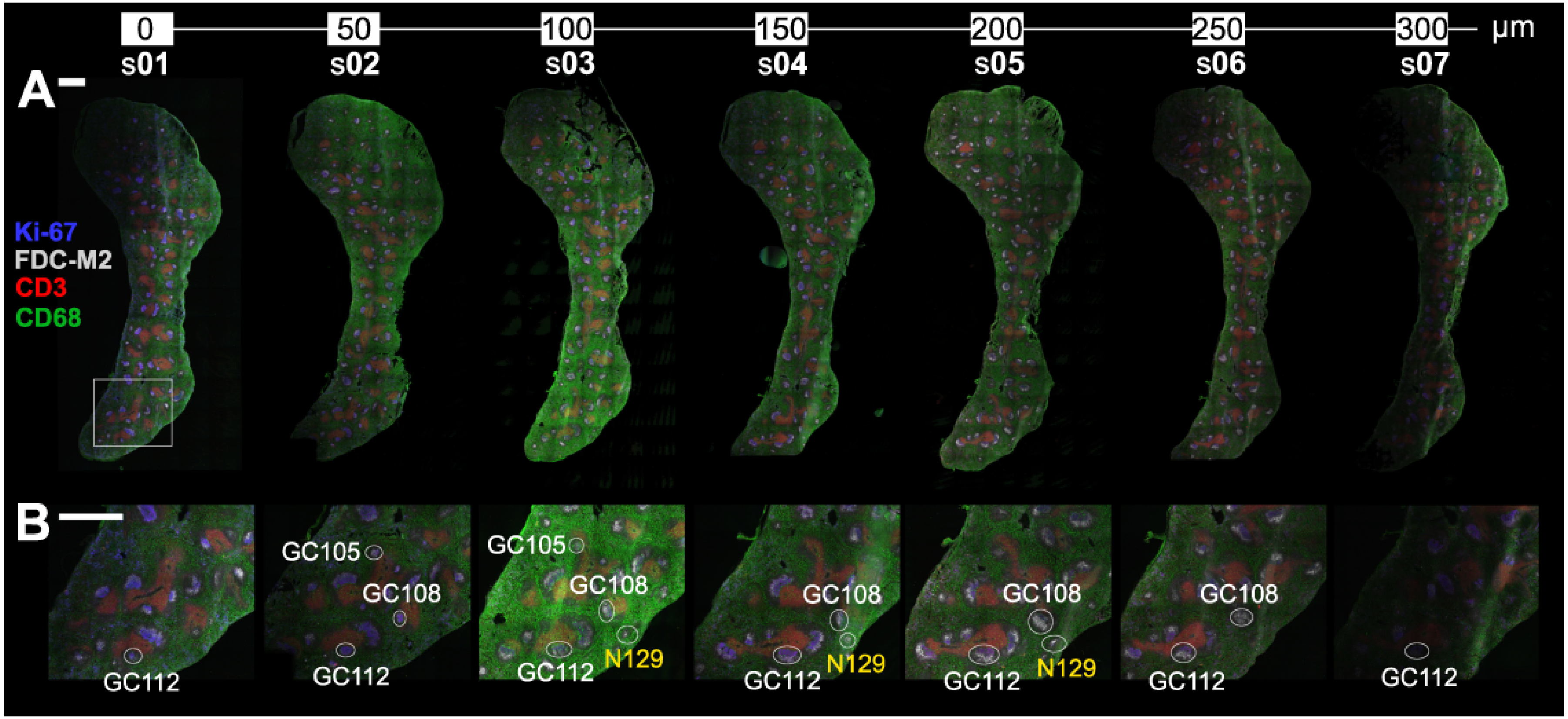

Figure 4.10: 3-D evaluation of the kinetics of GC growth in spleens of phOx-CSA challenged mice. (A) Serial spleen sections (s01-s07) spaced at intervals of 50 μm, spanning a total thickness of 300 μm, were quadruple stained for proliferating cells (mAb Ki-67), FDC-networks (mAb FDC-M2), T cells (mAb CD3) and macrophages (mAb CD68). Entire areas of spleen sections were imaged by meander scans performed at x100 magnification. Follicular niches as identified by FDC-M2 reactivity and anatomical location were numbered serially and each niche was traced throughout the series of imaged spleen sections. During tracing, follicular niches were marked as either occupied or empty by virtue of concomitant existence or absence of GC. (B) Exemplary illustration of tracing of follicular niches for the region boxed in (A). Highlighted are three occupied niches (GC105, 108 and 112) and one empty niche (N129). Both occupied and empty niches are consistently found to span quite different numbers of spleen sections. Image series are representative of a spleen at day 10 after immunization. Scale bar 1 mm.

Number of follicular niches occupied by GC/total number of follicular niches$^{a)}$									
	day 06			day 10			day 14		
	⊙	⊛	⊚	⊞	⊠	⊟	⊕	⊗	⊖
s01	33/119	49/128	100/162	75/90	97/126	89/112	80/90	68/94	56/106
s02	38/124	60/140	96/158	80/106	88/117	100/125	90/101	73/104	79/102
s03	26/127	49/148	80/161	80/108	87/110	97/129	90/112	81/101	80/122
s04	32/130	40/122	98/166	84/116	89/110	90/123	92/112	74/89	77/117
s05	38/121	48/111	95/178	80/113	85/117	92/135	89/119	74/99	83/148
s06	27/118	37/105	99/165	86/115	92/117	92/125	84/99	81/118	82/145
s07	21/89	48/106	97/164	90/112	88/130	90/130	88/113	77/97	81/136
Mean area of spleen sections [mm^2]									
	35.8	44.4	49.5	30.8	46.9	45.1	37.7	34.7	45.9
Estimated volume [mm^3]$^{b)}$									
	10.8	13.3	14.9	9.2	14.1	13.5	11.3	10.4	13.8

Table 4.1: Survey of spleen specimens analyzed for 3-D evaluation of GC growth kinetics. Specified are both the number of follicular niches occupied by GC and the total number of follicular niches detected within each of the serial sections (s01-s07) analyzed per spleen. Additionally, the mean area of each series of serial sections and the estimated volume comprised by the very sections are indicated. Three spleens were analyzed at each time point (day 6, 10 and 14), and different symbols refer to individual mice. ^{a} Listed values refer to the independent evaluation of single sections. ^{b}The volume comprised by the analyzed sections was estimated through multiplying their mean area by the total thickness spanned by them (300 μm).

14, respectively) (Figure 4.11). With regard to follicular niches occupied by GC, numbers significantly increase from 128±25 at day 6 to 189±27 at day 10 (p=0.04 in Student's t test). Naturally, the numbers of empty follicular niches decrease to that effect, from initially 103±32 at day 6 to 45±9 at day 10. Thereafter, the numbers of occupied niches only slightly decrease to finally 177±29 at day 14, accordingly the numbers of empty niches increase to 48±17. Since the frequency of occupied follicular niches significantly increases from day 6 (55%) to day 10 (81%) and is rather stable until day 14 (79%), the 3-D volumetric evaluation indicates continious new formation of GC, even after day 6, thus favoring asynchronous GC ensemble kinetics. Noteworthy, the frequeny of empty follicular niches is unexpectedly high even at day 10 and 14 (19% and 21%, respectively) (Figure 4.11).

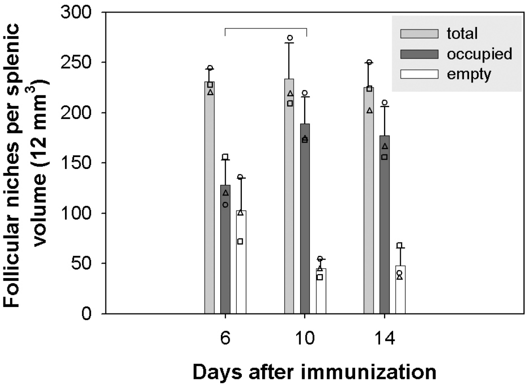

Figure 4.11: 3-D evaluation of occupation of follicular niches indicates continuous formation of new GC throughout the response. Follicular niches were identified and traced as described in Figure 4.10. The bar graphs illustrate the mean numbers of total (light gray), occupied (dark gray) and empty follicular niches (white) per splenic volume recorded at each time point. Values of individual mice (n=3 for each time point) are further indicated by different symbols. In order to improve interpretability values are quoted as numbers of niches per 12 mm^3, corresponding to the mean estimated volume analyzed per spleen (see Table 4.1). Significant differences as calculated by Student's *t* test are indicated.

4.3.3 3-D reconstructions reveal that GC possess an ellipsoid shape and cover a wide range of volumes

3-D reconstructions were performed on serial sections of each 3 spleen specimens at day 6, 10 and 14 after immunization (see Table 4.1) as described in the materials and methods Section 3.8. For reasons of feasibility and facility of inspection, 3-D reconstructions were in either case confined to those GC that were wholly contained within the serial sections. Lateral views, detail enlargements of lateral views and top views of 3-D reconstructions of each one representative spleen specimen at day 6, 10 and 14 are showcased in Figure 4.12, A, B and C, respectively. As an aside, the 3-D reconstruction shown for day 10 after immunization pertains to the series of meander scans illustrated in Figure 4.10, A. The actual numbers of wholly contained GC as well as their mean, range and total volume are summarized for all spleen specimens in Table 4.2. The numbers of wholly contained GC are fluctuating with respect to the three spleen specimens analyzed per time point (e.g. 23, 27 and 42 at day 10) (Table 4.2). However, no striking differences are detected regarding the different time points analyzed. As a matter of course, the fluctuation of numbers of wholly contained GC is reflected by the total volume comprised by the very GC (e.g. 55.0, 80.8 and 112.9 $\times 10^6$ μm^3 at day 10), though the total volume at day 6 (21.2, 23.1 and 41.1$\times 10^6$ μm^3) is evidently lower compared to day 10 and 14. Likewise, the mean volume is minor for day 6 GC (0.5±0.6, 0.6±0.8, 1.4± 1.8 $\times 10^6$ μm^3) compared to day 10 (2.4±3.5, 3.0±4.4, 2.7± 3.7 $\times 10^6$ μm^3) and day 14 GC (2.6±2.8, 2.0±2.1, 1.6±1.9 $\times 10^6$ μm^3). The particularly high standard deviations of mean GC volumes are due to the omnipresent wide range of GC volumes. The smallest and largest GC differ by a maximal factor of 220 at day 6, 1180 (!) at day 10 and 555 at day 14 (Table 4.2). But whereas the lower value limit of GC volumes is rather retained during the progression of the immune response (0.01, 0.01, 0.02 $\times 10^6$ μm^3 at days 6, 10 and 14), the upper value limit increases from day 6 to day 10 and 14, respectively (4.0, 11.8, 11.1 $\times 10^6$ μm^3) (Table 4.2). Hence, GC of rather small volume are not restricted to the early phase but are also found at the peak of the immune response. In contrast, the existence of GC of large volumes is confined to the peak (day 10) and early decay phase (day 14).

The concomitance of different sized GC is subsidiary spotlighted in Figure 4.13 by focusing on 3-D reconstruction of the detail enlargement shown for tracing of follicular niches throughout series of serial sections at day 10 after immunization in Figure 4.10, B. The positions of the occupied follicular niches GC105, GC108 and GC112 are marked in the 3-D reconstruction image by arrows. Not only that the very GC span different numbers of serial sections (1, 5 and 7 respectively), but they are of quite different volume, as the largest (GC112, 10.0 $\times 10^6$ μm^3) differs from the smallest (GC105, 0.5 $\times 10^6$ μm^3) by the factor of 20. By using the previously recorded density of Ki-67$^+$ cells per cross-sectional GC area (0.0116/μm^2, see Section 4.1.1) the numbers of cells comprised by the very GC are estimated as 12,500 (GC112) and 630 (GC105). Albeit the highlighted GC show a pronounced variation in size, their geometrical shape - as given by the radius ratios of fitted GC ellipsoids - turns out to be rather uniform. 3-D reconstruction confirms the results of virtual random sectioning (Section 4.1.3) in that GC do not possess a spherical but ellipsoid shape.

The 3-D reconstructions only constrictively allow for predication of the orientation of GC within spleen because the chosen alignment mode (slicewise alignment of individual GC due to their center of mass, Section 3.8) causes straightening of GC. The impression of perpendicular stringed GC therefore, at least partially, attributes to a bias generated during alignment. However, comparison of 3-D reconstructions performed with and without alignment suggest that GC may possess a preferential spatial orientation in the spleen (Figure 4.14). GC appear to be predominately positioned upright (vertical) within the spleen, in which the axis of their major extension is quasi-perpendicular to the longitudinal section plane. Horizontal or "lying" GC (axis of major extension parallels the section plane) are observed rather occasionally.

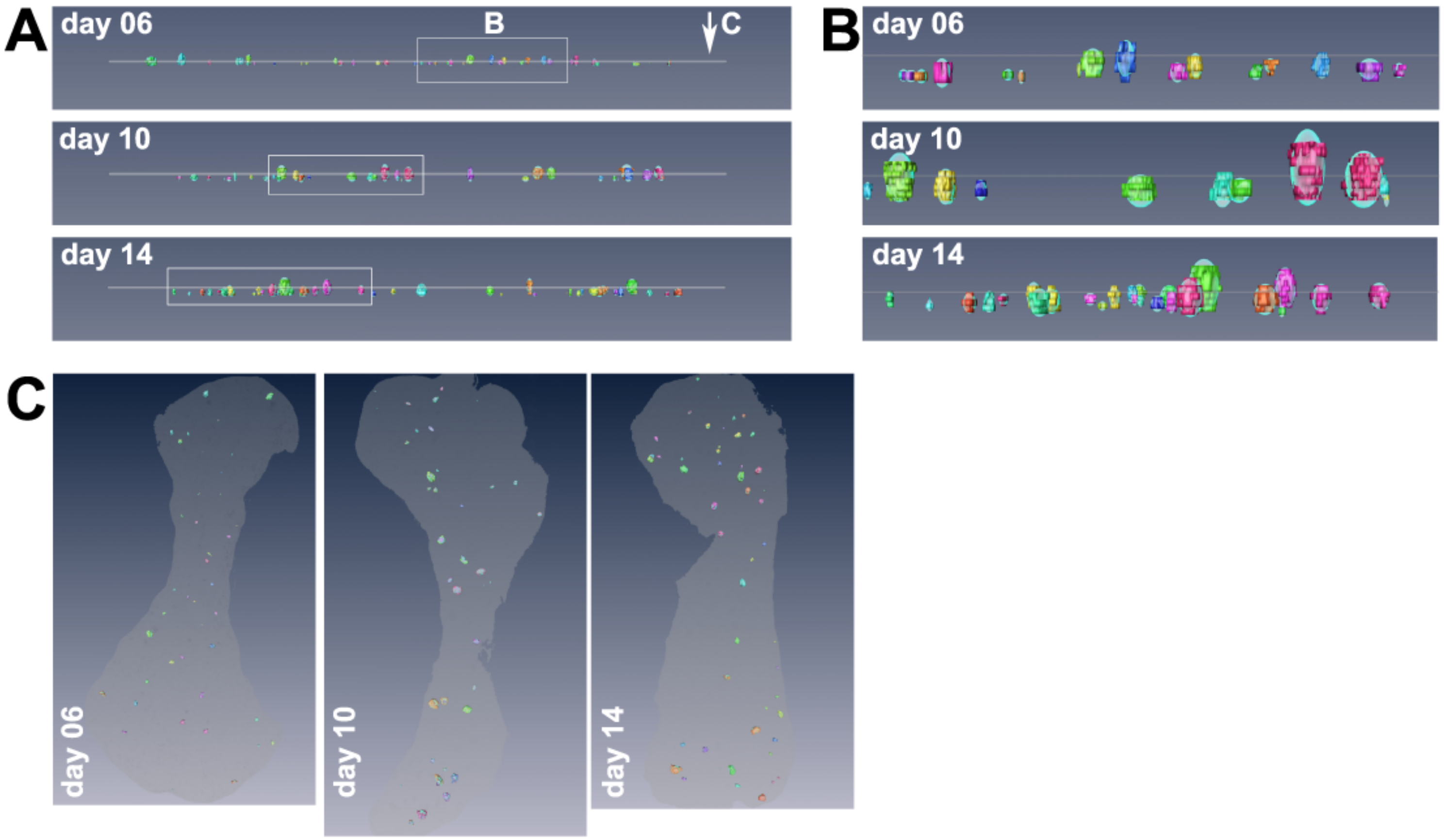

Figure 4.12: 3-D reconstructions of splenic volumes depicting GC at days 6, 10 and 14 after immunization. For each reconstruction serial spleen sections (s01-07) that were quadruple stained for proliferating cells (mAb Ki-67), FDC-networks (mAb FDC-M2), T cells (mAb CD3) and macrophages (mAb CD68) were imaged by meander scans performed at x100 magnification (Figure 4.10). 3-D reconstruction was performed for the fraction of GC that were wholly contained within the analyzed splenic volume. Briefly, GC outlines were segmented and individual GC were aligned slice wise according to their center of mass. To facilitate geometrical analysis, ellipsoids were fitted to aligned GC applying principal component analysis (PCA). (A) Lateral view of reconstructed splenic volumes representative of mice challenged 6 (*top panel*), 10 (*middle panel*) and 14 days earlier (*bottom panel*). (B) Detail enlargements of regions framed in (A). (C) Top view of reconstructed splenic volumes shown in (A). The dimensions of underlying spleen sections are superimposed. Data is each representative of three spleens analyzed per time point.

Spleen specimen		Number of GC (wholly contained)	Volume of GC [10^6 μm^3]		
			mean ± SD	range	$\sum$
day 06	⊙	43	0.5 ± 0.6	0.01-2.2	21.2
	⊛	37	0.6 ± 0.8	0.03-3.7	23.1
	◎	30	1.4 ± 1.8	0.06-4.0	41.1
day 10	⊞	23	2.4 ± 3.5	0.02-11.7	55.0
	⊠	27	3.0 ± 4.4	0.01-20.7	80.8
	⊟	42	2.7 ± 3.7	0.01-11.8	112.9
day 14	⊕	41	2.6 ± 2.8	0.02-11.1	107.4
	⊗	20	2.0 ± 2.1	0.04-9.4	40.8
	⊖	50	1.6 ± 1.9	0.02-8.1	80.9

Table 4.2: Survey of numbers and volumes of GC resulting from 3-D reconstructions. Specified are the number, mean volume, range of volumes and total volume ($\sum$) of GC wholly contained within the reconstructed splenic volumes specified in Table 4.1. Different symbols refer to individual mice.

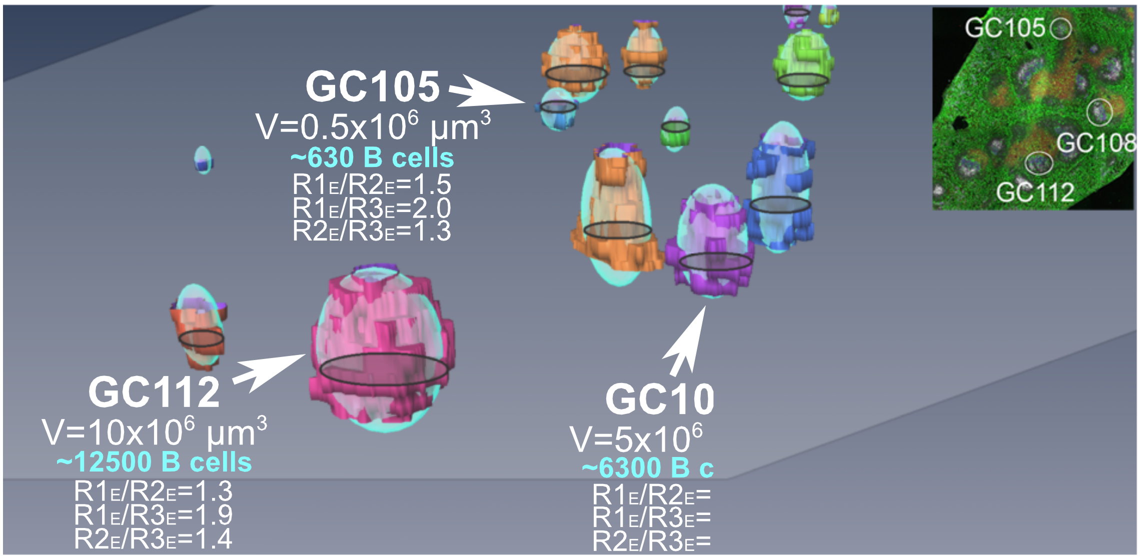

Figure 4.13: 3-D reconstruction of splenic volumes reveals a broad volume distribution of geometrically uniform GC. Detail enlargement of the 3-D reconstruction of the splenic volume depicting day 10 GC illustrated in Figures 4.10 and 4.12, (*middle panels*). The staining of the respective region of serial section s03 is superimposed (upper right corner), for orientation purposes the position of s03 is likewise displayed in the 3-D reconstruction. The positions of the occupied niches GC105, 108 and 112 are indicated with arrows. The volumes and estimated numbers of B cells comprised by reconstructed GC are each quoted. The geometry of GC is pointed out by specifying the ratios of the radii of fitted ellipsoids, in which $R1_E$, $R2_E$ and $R3_E$ always refer to the largest, medial and smallest radius, respectively. Staining, imaging and 3-D reconstruction were carried out as described in Figure 4.12.

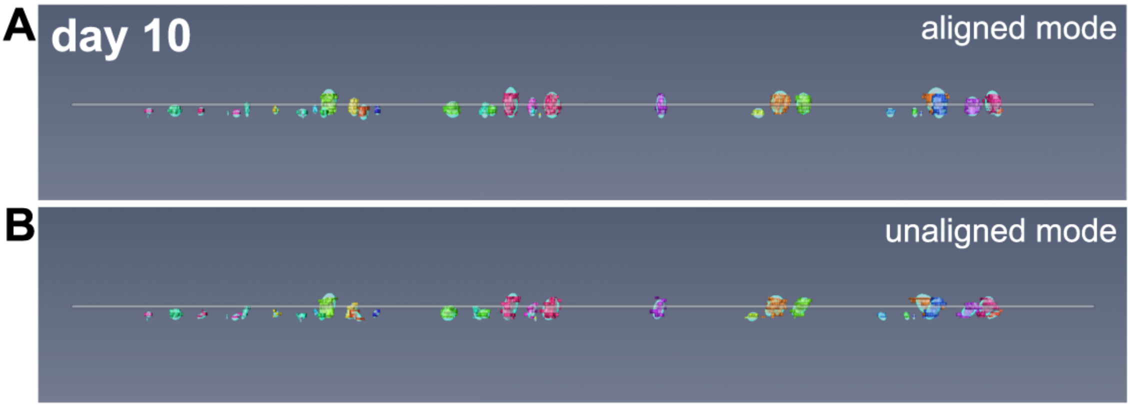

Figure 4.14: Spatial orientation of GC within the spleen. Albeit the straightening bias due to slicewise alignment of individual GC during 3-D reconstruction, GC turn out to possess a preferential spatial orientation within the spleen. Within spleen, ellipsoid GC appear to be predominately positioned upright, in which the the axis of their major extension is quasi-perpendicular to the section plane. (A) Lateral view of 3-D reconstruction of a splenic volume representative for day 10 after immunization. 3-D reconstruction was performed by slicewise alignment of individual GC as described in Figure 4.12 (*aligned mode*). (B) The same as in (A), except for 3-D reconstruction was performed without the slicewise alignment of individual GC (*unaligned mode*).

4.3.4 GC possess an uniform ellipsoid shape that is preserved upon GC growth and progression

As aforementioned, the pure inspection of 3-D reconstructions give the impression that GC possess a rather uniform ellipsoid shape. To further elucidate the shape of GC and in particular its variation over the time course of the immune response, the geometrical data on fitted GC ellipsoids are subjected to closer examination. On that account, the recorded radii of fitted GC ellipsoids ($R1_E$, $R2_E$, $R3_E$) are separately plotted versus each other for each of the time points analyzed (days 6, 10 and 14), in which $R1_E$, $R2_E$ and $R3_E$ always refer to the largest, medial and smallest radius, respectively. The plots thus obtained show a settled linear dependency between $R1_E$ and $R2_E$, $R1_E$ and $R3_E$ as well as $R2_E$ and $R3_E$ (Figure 4.15). As a tendency, the largest radius ($R1_E$) appears to be most susceptible to variations as indicated by lower squared correlation coefficients (R^2). The variation seen in ($R1_E$) most likely attributes to straightening of GC during 3-D reconstruction (Section 4.3.3, Figure 4.14), that effectuates compression of the very radius. Furthermore, the inter-individual variation of the linear dependency of radii of fitted GC ellipsoids is low, since linear regression lines of individual mice almost coincide at either of the time points.

In order to disclose potential dependencies with respect to shape and size, radii of fitted GC ellipsoids are separately plotted against the underlying volume of the very GC (Figure 4.16). Since the inter-individual variation turns out to be low (see above and Figure 4.15), data obtained for individual mice (n=3) are each merged for days 6, 10 and 14, respectively. Such analysis reveals strict dependencies of either of the radii (R_E) and the underlying volume (V) (Figure 4.16). These dependencies are specified by best-fit curves resulting from power regressions that obey to the formula

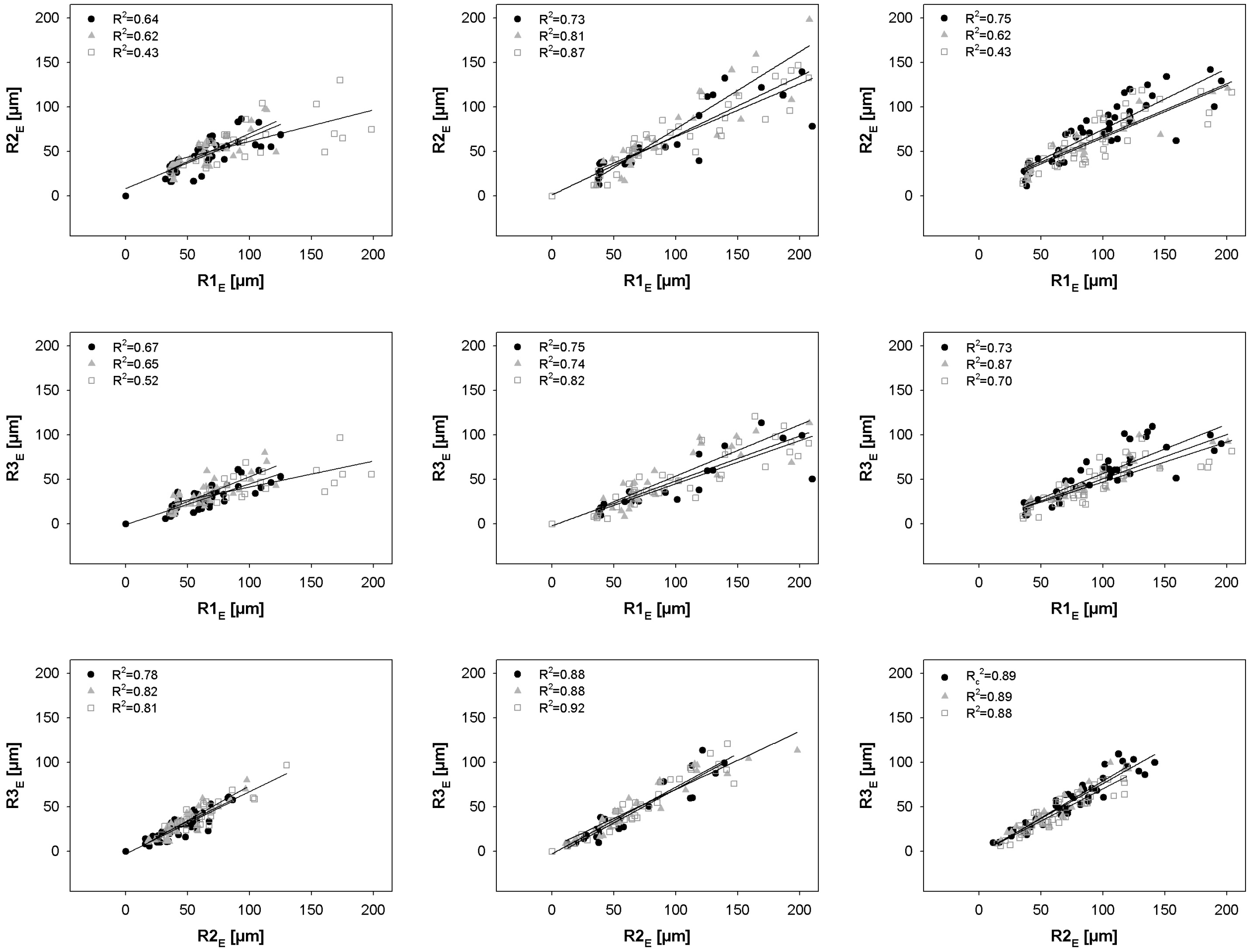

Figure 4.15: Low inter-individual variation of GC 3-D geometry. Scatter plots illustrate the correlations of the radii of fitted GC ellipsoids (R1$_E$, R2$_E$ and R3$_E$) at day 6 (*left panel*), 10 (*middle panel*) and 14 after immunization (*right panel*). R1$_E$, R2$_E$ and R3$_E$ always refer to the largest, medial and smallest radius, respectively. Values of individual mice (n=3 per time point) are represented as different symbols. The corresponding linear regression curves are displayed as solid lines. Staining, imaging and 3-D reconstruction were carried out as described in Figure 4.12.

$R_E = a \cdot V^b$. All three radii of fitted GC ellipsoids virtually show cube root dependency on the volume as indicated by the calculated values for the exponent b (e.g. $b=0.33$, 0.30, 0.36 for $R1_E$, $R2_E$, $R3_E$ at day 6). Noteworthy, the formal dependency of either of the radii on the volume is almost invariable with respect to days 6, 10 and 14 (e.g. $R2_E = 63 \cdot V^{0.30}$ at day 6, $R2_E = 62 \cdot V^{0.33}$ at days 10 and 14). The high squared correlation coefficients ($R^2 \geq 0.80$ for $R1_E$, $R^2 \geq 0.90$ for $R2_E$ and $R^2 \geq 0.91$ for $R3_E$) furthermore substantiate the visual impression of uniformly shaped GC. Consequently, GC turn out to possess a uniform shape that is notedly preserved upon GC growth and progression of the immune response (Figure 4.16). In synopsis, the radii of GC ellipsoids roughly obey to the following formulas: $R1_E = 91 \cdot \sqrt[3]{V}$, $R2_E = 62 \cdot \sqrt[3]{V}$, $R3_E = 44 \cdot \sqrt[3]{V}$. Accordingly, the approximate shape of GC is given by the radii ratios $R1_E : R2_E : R3_E$ that are 2.1 : 1.4 : 1.

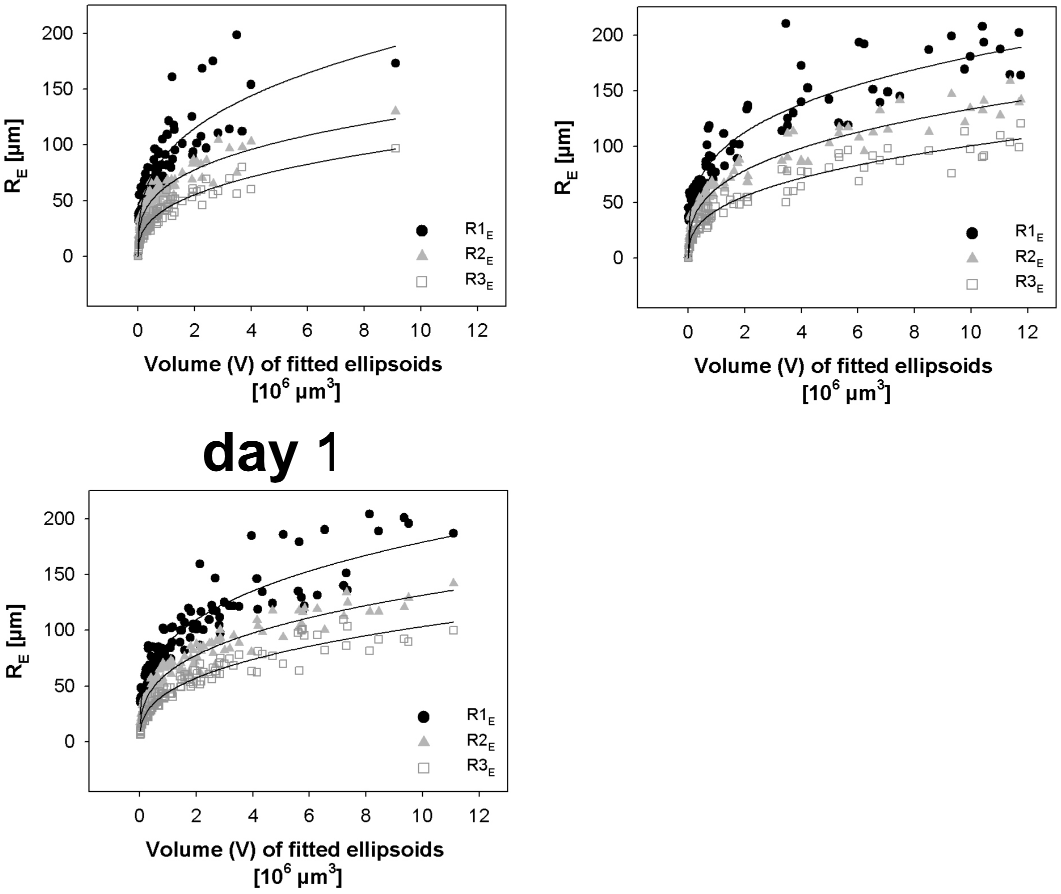

Figure 4.16: The 3-D shape of GC is preserved upon GC growth and progression of the immune response. Illustrated is the interrelation of shape and size of GC as revealed by 3-D reconstruction of in each case three spleens at day 6, 10 and 14 after immunization (see Figure 4.12). The radii of fitted GC ellipsoids ($R1_E$, $R2_E$ and $R3_E$) are plotted separately against the underlying volumes of the very GC. Best-fit curves resulting from power regression analysis ($R_E = a \cdot V^b$) are depicted as solid lines. The respective values of constants (a), exponents (b) and squared correlation coefficients (R^2) are shown next to the curves.

4.3.5 The 3-D evaluation of GC size reveals a considerable volume distribution that is not consistent with the accepted notion of GC growth kinetics

As argued before, the volume distribution of GC - and in particular its time course - shall be capable of providing insight into the ensemble kinetics of GC growth. Since 3-D reconstructions were confined to GC that are wholly contained within the set of 7 serial sections (s01-s07), volume distributions are initially biased towards GC of small size. To correct for this bias, volume distributions were further restricted to GC intersecting the central section (s04), in which the probability is higher for large compared to small sized GC. When displayed as linear histograms of the frequencies of GC belonging to binned size classes, data thus corrected indicate the existence of a distribution of GC volumes at days 6, 10 and 14 (Figure 4.17, A). Nonetheless, the volume distribution of GC at day 6 is rather narrow, in that 91.1% of all GC belong to the smallest linear binned size class (between 0.01 and 3.5 $\times 10^6$ μm^3 or 15 and 4.400 GC B cells, respectively). At day 10 after immunization the volume distribution broadens and shifts towards larger size GC. But, the frequency of GC assigned to the smallest linear binned size is still high, albeit decreased (58.6%). To gain better resolution of the very GC comprising up to 4.400 GC B cells, the data are additionally displayed as semi-logarithmic histograms, in which logarithmic binned size classes are plotted versus their frequencies (Figure 4.17, B). Consequential plots emphasize the shift towards larger GC between days 6 and 10. Finally, the volume distribution of day 14 GC resembles the data obtained at day 10 after immunization, albeit it slightly tends to shift back towards small sized GC (71.4% of GC fall into the smallest linear binned size class).

Taken together, the data indicate a volume or size distribution of GC that becomes most pronounced at day 10 after immunization. This volume distribution is profound, since it reveals the concomitance of GC within the spleen that differ by a maximal factor of about 1,000 (Section 4.3.3). The existence of a such defined volume distribution is not consistent with the accepted notion of synchronous ensemble kinetics of long-lived GC, that is characterized by a rather constricted volume distribution of GC (see Figure 4.9, A). Besides refuting the accepted notion, the volume distribution is not sufficient to provide unambiguous predicates on the ensemble kinetics of GC, as it may attribute to either variation of maximal attained size of GC (see Figure 4.9, B), asynchronous ensemble kinetics (see Figure 4.9, C) or even both or scenarios just more complex.

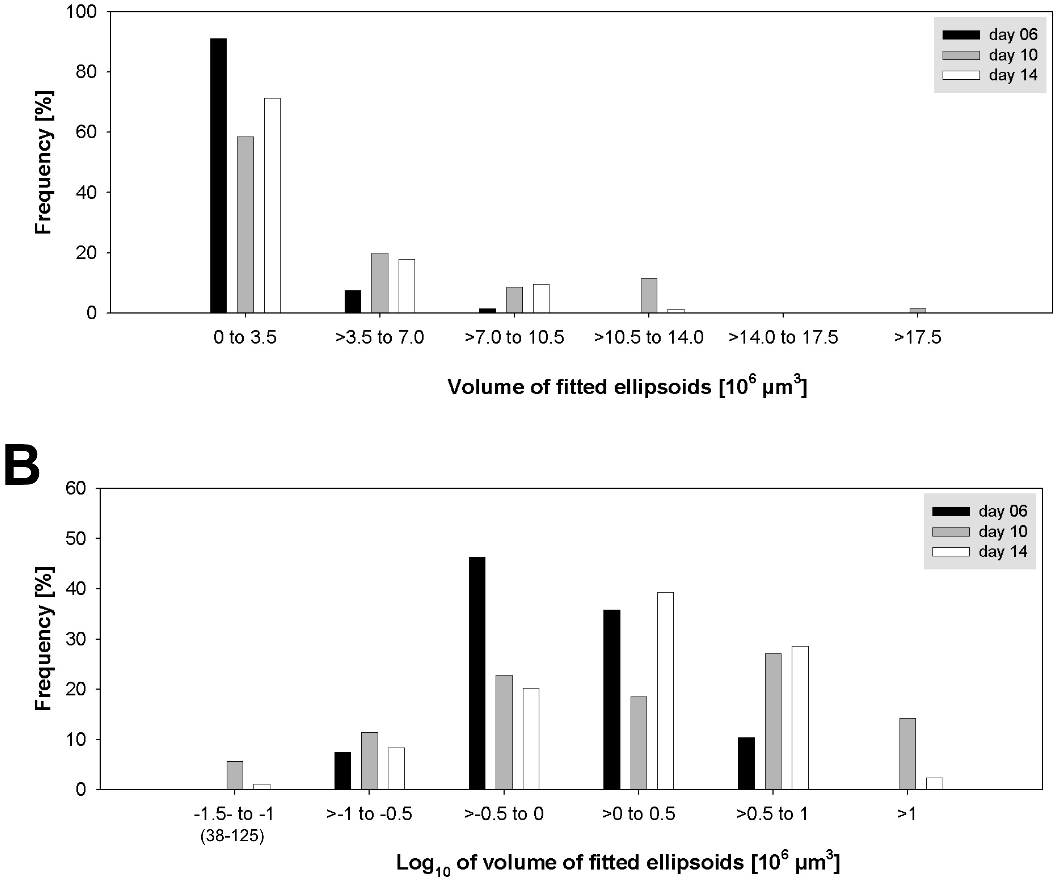

Figure 4.17: The 3-D evaluation of GC size reveals a considerable volume distribution that is not consistent with the accepted notion of GC growth kinetics. (A) Depicted are the size distributions of fitted GC ellipsoids at day 6, 10 and 14 after immunization as revealed by 3-D reconstruction of splenic volumes. 3-D reconstructions were performed by means of in each case seven serial spleen sections (s01-07), spaced at intervals of 50 μm as illustrated in Figures 4.10 and 4.12. The frequencies of GC sizes refer to merged data sets of three mice at each time point and include all GC that cross the central section (s04) and are wholly contained within the analyzed splenic volumes. GC sizes are represented as volumes and estimated numbers of B cells comprised by these volumes. The underlying total numbers of GC are indicated ($\sum$), in which values of individual mice are given in parentheses. (B) Semi-logarithmic application of the volume distribution specified in (A) featuring improved separation of small GC volumes.

4.4 Discussion

A major part of the investigations presented in this thesis involves the in-depth contemplation of the kinetics of GC growth within spleen. This effort is motivated by two major circumstances: (i) the enduring lack of understanding of some rather basic aspects of affinity maturation, in particular with respect to the tempo-spatial organization and regulation of the implied processes, namely expansion, SHM and selection [94] and ii) the increasing number of experimental findings reported in the primary literature that may challenge the prevailing notion of GC growth kinetics. The assessment of GC growth kinetics is generally hampered by shortcomings in feasibility of real-time observation of GC, as modern imaging techniques do not allow for observation of time scales longer than a few hours. Furthermore, as yet an adequate in vitro system mimicking spleen or lymph node is still missing [95]. Thus, the current standard of knowledge is a combined result of direct *ex vivo* flow cytometric [96, 97] and immunohistological monitoring of GC cell populations [70, 24, 45]. Albeit lacking any experimental validation, the core statement of the consequently established or traditional conception of GC growth kinetics (Section 1.4.4) implies that all GC within an ensemble behave rather uniformly synchronous. The investigation of GC growth in phOx-CSA challenged BALB/c mice refutes this prevailing notion by negating this "uniformity presumption" (Figures 4.11-4.13, 4.17, Table 4.2). Cross-sectional profiling reveals a robust average kinetics of GC growth that is based upon a notable size distribution of GC within individual spleen sections (Figures 4.4-4.5) that is farther shown not to solely attribute to random sectioning (Figure 4.7). Moreover, the recorded cross-sectional profile turns out to be consistent with both the established and unfamiliar conceptions of GC growth (Figure 4.9), the latter including variegation in terms of seeding (synchronous/asynchronous), life-time (long-lived/short-lived) and maximum size of GC (fixed/variable). Finally, 3-D volumetric evaluation lends support to non-uniform, asynchronous growth of GC, given that seeding of GC is an ongoing process (Figure 4.11), and GC display a profound volume distribution (Figures 4.12-4.13, 4.17, Table 4.2). Together theses results allow the proposal of a revised model of affinity maturation in such way as depicted in Figure 4.18.

4.4.1 2-D cross-sectional evaluation of GC growth kinetics

Due to facilitation of manual assignment of GC boundaries and determination of actual cell counts, GC were generally identified by using the proliferation marker Ki-67 that stains cells during all active phases of the cell cycle (G1/S/G2/M) but not resting cells (G0) [98]. Ki-67 was initially reported to reveal a far-less striking subcompartimentalization of murine GC than is typical of human GC [67], a finding that was yet sharpened by Rahman et al. [69], claiming that Ki-67 is ubiquitously expressed by murine GC B cells as identified by GL-7 reactivity. Nevertheless, since the staining patterns of GL-7 and PNA slightly differ [99, 68, 96], Ki-67 remained a controversial marker for measurement of GC. Therefore, potential distortion of results owing to the use of Ki-67 was excluded at the outset of experiments (Section 4.1.1) by demonstrating that cross-sectional areas of GC as revealed by Ki-67 reactivity are consistently equivalent to those obtained by PNA-reactivity (Figure 4.2). Consequently, proliferation is not restricted to any subcompartment of murine GC, and the majority of GC B cells is in an active phase of the cell cycle and does not enter the resting state. These findings were just recently confirmed by real-time *in vivo* imaging of GC [100, 101].

The available data on growth kinetics of GC are not standardized as they are derived from differently immunized mice (NP-CGG, SRBC, HSA) or rats (DNP-MSH), refer to different lymphoid tissues (lymph node, spleen) and include different measures for GC size that usually represent either indirect or extrapolated quantities (number of GC, volume estimated by cross-sectional diameter of GC, relative volume) [102, 70, 24, 69, 103, 68, 45]. Despite direct data comparison is impeded by the divergence of applied protocols, the identified mean time course of GC is surprisingly similar to the above cited works. Since the growth kinetics of splenic GC following phOx-CSA challenge (Figures 4.4-4.5) shows the very mean time course, it is considered representative. Moreover, categorizing recorded GC into three size classes (small, medium, large) following the convention introduced by the group of T. Manser [104, 69, 68], leads to consistent results (data not shown). Consequently, the observed profound size distribution of GC (Figure 4.5) is not exceptional to phOx-CSA challenged BALB/c mice but constitutes a general phenomenon. Together these result prove a robust induction of GC responses following phOx-CSA challenge.

Simulations of random sectioning of various shaped ellipsoids (Figure 4.7) first suggested that the observed size distribution of GC does not solely attribute to random sectioning but may reflect a real size distribution of GC. By then, a stereological approach to estimate the volumes of GC by means of their cross-sectional profiles turns out to be impracticable, since building of fair assumptions are impeded by the unknown 3-D shape and shape distribution of GC. Stereology (from greek *stereos*=solid) is an interdisciplinary research field devoted to the three-dimensional interpretation of planar sections of either tissues or materials [105]. Initially defined as the "spatial interpretation of sections", stereology is recently referred to as the science of estimating higher dimensional information from lower dimensional samples. Albeit their steady advancement, stereological techniques do not apply to all problems as they commonly share the need to make certain assumptions about the object of interest that is to be estimated [106]. As by now, the 3-D volumetric evaluation has revealed that splenic GC possess a preserved uniform shape that is specified as ellipsoid with diameter ratios 2.1 : 1.4 : 1 (Section 4.3.4, Figure 4.15-4.16), it shall be worthwhile to resume and advance a stereological approach.

4.4.2 Theoretical approach to GC ensemble kinetics

The simulation of random sectioning of hypothetical ensemble kinetics of GC is an inverse approach to overcome the "deadlock situation" arising from cross-sectional evaluation and stereology, that is, the volume distribution/ensemble of GC cannot be inferred by means of cross-sectional profiles (Section 4.4). The idea behind was to simulate cross-sectional profiles of conceivable kinetics of ensembles of GC and to subsequently identify the best-fit to the experimentally obtained profile (Figure 4.5). In these premises, the inverse approach fails, as it demonstrates that the kinetics of the experimentally obtained cross-sectional profile is consistent with various ensemble kinetics of strikingly different nature (Figure 4.9). This finding is unlikely to attribute to configuration of simulations, since involved assumptions were as well fixed and experimentally supported: (i) each ensemble is composed of 500 randomly distributed individual GC [70], (ii) the generic shape of GC was specified as prolate ellipsoid (Figure 4.7, 4.16, Section 4.1.3, 4.3.4) and (iii) the probability of sectioning through an individual GC is defined by its size.

To aid subsequent discussion of internal GC processes, the kinetics of individual GC are gathered from a purposely simply-kept mathematical model (Figure 4.8, Section 4.2.1), that is similar to models established by Iber and Maini [107] and Meyer-Hermann et al. [75]. Following a proposition of Oprea et al. [108], the model omits iteration in that once selected cells do not further take part in the progression of the respective GC. Due to the lack of internal iteration (recycling), the modeled kinetics is independent of BCR affinity and both time course and lifetime of individual GC solely rely on the rates of proliferation and selection. The recycling hypothesis was proposed by Kepler and Perelson [109] as **one** implementation of an optimal mutation schedule in which periods of rapid mutation alternate with periods of mutation-free growth, hence referred to as *phasic mutation schedule*. Recycling is generally committed to the conception of cell migration within two-compartmental GC (proliferation and mutation act on centroblasts in the dark zone, whereas centrocytes are subjected to selection in the light zone of GC) [109, 110]. Actually, migration of GC B cells in both directions was recently shown by real-time *in vivo* observation of GC [100, 101]. However, whether spatial separation of processes applies to murine GC remains to be rigorously addressed. Anyhow, proliferation is observed in both dark and light zones (Section 4.4.1) [100, 101], and it seems that selection rather affects a phenotypically homogeneous population of proliferating GC B cells [69, 68]. Since recycling remains rather speculative it is not included within the current model of individual GC growth kinetics. However, non-consideration of recycling does not affect the outcome of simulations, as yet appointing the geometrical shape of growth curves is sufficient for the current purpose.

In the first instance, the simulation-based inverse approach demonstrates that cross-sectional profiling of GC does not allow for categorical inference of neither the kinetics of the ensemble nor the underlying kinetics of individual GC (Figure 4.9, Section 4.2.2). Furthermore, by signifying that rather unfamiliar hypothetical ensemble kinetics that forgo the "uniformity presumption" are consistent with the cross-sectional data, it compels reconsideration of the conception of GC growth kinetics. In fact, hypothetical ensemble kinetics were composed in an nonarbitrary fashion but by taking into account some rather novel experimental findings:

(i) There is increasing evidence that the initial phase of GC formation is rather similar to all GC [111], whereas the further progression of GC is susceptible to factors as the presence of accessory T cells [37], FDC [112] and the fitness of seeder cells [113, 114]. Consequently, within an ensemble, GC may as well differ in their maximum attained size and individual lifetimes, or even both (Figure 4.9, C). According to this conception, the time course and outcome of individual GC may signify their quality or efficiency, respectively. Interestingly enough, the lifetime of individual GC might differ from the persistence of the ensemble of GC, in that it is much shorter. (Whether the volume distribution of GC observed at the peak of the immune response (Figure 4.17) attributes to "differently successful" GC is under current investigation by the help of Atijeh Valai. Briefly, light chain V genes are PCR amplified and cloned from microdissected GC of different but known volumes).

(ii) *In vivo* imaging reveals that GC are dynamic open structures, continually visited by naive follicular B cells, thus indicating germinal center seeding is an ongoing process [101]. Continual recruitment of B cells into the GC reaction is further substantiated by the identification of a stable population of splenic B cells displaying a GC founder phenotype following immunization [96, 97]. It is easily conceivable that such recruitment is not only confined to already existing GC but may also apply for yet empty follicular niches, thus leading to sustained new formation of GC. Accordingly, seeding of GC might indeed constitute a process of marked asynchronicity (Figure 4.9, C).

4.4.3 3-D volumetric evaluation of GC growth kinetics

The motive force to proceed to volumetric evaluation (Section 4.3.1) was the accumulating evidence that GC growth kinetics might be quite different than previously accepted. The data presented here, are the first time that GC growth has been directly assessed by monitoring the real size of GC, to wit their volume. Prior to the actual analysis determined efforts were made to establish optimal cryosectioning and staining protocols that both ensure constant quality and ideal 3-D alignment of serial whole spleen images (this work was assisted by a student assistant of the Systems Immunology group, Anke Klein, who gives a full record of these pilot experiments in her student research thesis [115]). Briefly, in order to facilitate identification and especially tracing of follicular niches throughout serial sections, a complex quadruple staining of proliferating cells, FDC, T cells and macrophages was established (Section 3.6.6, Figure 4.10). The effectivity of manual tracing of follicular niches was further improved ($\geq$95%) by using sections of 25 μm thickness that turned out to least susceptible to tissue ruptures and wrinkles [115].

Based upon tracing of follicular niches throughout serially sectioned splenic tissues at days 6, 10 and 14, the number of follicular niches estimates to about 600-800 per spleen, irrespective of the time point analyzed, thereby reconfirming the formation of primary follicles including the FDC reticulum prior to antigenic stimulation [116]. However, as a consequence of GC formation, FDC networks seem to expand, most probably reflecting "maturation" of FDC [117, 118, 68]. It is hard to know, whether FDC networks are passively stretched by growing GC or if FDC even actively proliferate. At the height of the immune response to phOx-CSA no more than 450-650 GC are estimated to be present in the spleen. This estimate is slightly higher than previously quoted for NP-CGG challenged C57BL/56 mice (300-500 GC) [70]. This disparity between the two studies may be related to either different immunogenicity of phOx-CSA and NP-CGG and the higher challenging dosage of antigen (100 μg phOx-CSA vs. 50 NP-CGG μg) [45, 119, 120] or different detection of GC (quadruple immunofluorescent staining vs. single immunoenzymatic staining with PNA). Moreover, GC account for as much as 0.2-0.4%, 0.6-1.0% and 0.4-1.0% of the total splenic volume at days 6, 10 and 14 after phOx-CSA challenge, which is consistent with the relative volumes of GC during the primary DNP-MSH response in rats reported by Liu et al. [24]. Likewise, the course of the mean volume of GC (Table 4.2) is in agreement with previously described extrapolated GC volumes in lymph nodes [45]. Taken together, these results signalize very robust average kinetics of the volume comprised by splenic GC. Noteworthy, such behaviour was already predicted by simulations of hypothetical ensemble kinetics that are, albeit strikingly differing in underlying time courses of individual GC, reflected by the very same average kinetics of GC volumes (Figure 4.9).

By means of 3-D reconstructions GC are shown to be randomly distributed throughout the spleen, irrespective of their size, that is GC related to individual PALS regions vary in volumes (Figures 4.12, 4.13). Thus, neighboring GC rather seem to represent discretely acting entities, a finding further supported by genetic non-relatedness of neighboring GC [121]. As argued before, it is difficult to assess the spatial orientation of GC, since slicewise alignment of individual GC during 3-D reconstruction causes an artifact, to wit, the impression of perpendicular stringed GC. Likewise, the informative value of 3-D reconstructions obtained by alignment of whole spleen sections is limited, as yet minimal wrinkles and fissures within sections heavily interfere with the spatial orientation of individual GC. Nevertheless, GC tend to be arranged "upright" (vertical) with respect to the section plane, lying (horizontal) GC are observed rather occasionally (Figure 4.14).
In terms of geometry, GC are found to possess marked ellipsoid shape, as emphasized by accurate ellipsoid fitting results (Section 4.3.4, Figures 4.12, 4.13, 4.16). In fact, the general belief in spherical GC - routinely used to extrapolate the volume of GC - certainly does not apply to the herein well-studied splenic GC. Perfectly unexpected, GC are shown to not only possess ellipsoid but indeed an *uniform* ellipsoid shape that is fairly specified by the radius ratios 2.1:1.4:1 (Figure 4.16). Substantial distortion of this result owing to straightening of GC during slicewise alignment is finally ruled out by the data obtained when alignment was performed for whole sections rather than individual GC (radius ratios turn out as 2.65:1.45:1, appendix Figure A.2).

Perhaps the most thrilling conclusion to 3-D volumetric evaluation is that it explicitly refutes the central proposition of the traditional conception of GC growth kinetics, that is the "uniformity" presumption. The finding that numbers of GC significantly increase from day 6 to day 10 after antigenic challenge (about 30%) (Section 4.3.2, Figure 4.11) attests continual "birth" of new GC, that is, formation of GC is not confined to an initial phase limited in time, as generally believed. The observed increase does not attribute to "overlooking" day 6 GC that tend to be smaller, and therefore have a lower probability of being cut compared to day 10 GC, since (i) imaged splenic volumes are spaced at close intervals (the non-imaged interspace each accounts for one section) and (ii) the frequency of day 6 GC intersecting only one section is low (5%), and rather decreased compared to day 10 GC (10%) (appendix Figure A.3).

Based upon *in vivo* imaging of GC, Schwickert et al. [101] propose ongoing seeding of pre-existing GC by naive follicular B cells that contributes to the stringency of affinity maturation. Indeed, the data presented here point out that ongoing seeding is not solely restricted to pre-existing GC but additionally entails continual "birth" of new GC. Sustained new formation of GC provides a rational explanation for the substantial proportion of late GC showing little or even no evidence of somatic mutation [122] in particular, and the well-documented high frequency of unmutated sequences comprised by GC B cell populations (25-30%, Table 6.1) in general [123, 124, 125]. Asynchrononous formation of GC is also consistent with the very broad range of GC volumes observed at all sampled time points (Section 4.3.5, Figure 4.17, Table 4.2). It is tempting to speculate that small volumes account for "young" GC, only recently formed, whereas large volumes signify already fully established "old" GC. However, a direct link between volume and age of GC is rather unlikely, since the size of GC is probably influenced by other factors such as efficiency and lifetime of individual GC (discussed in Section 4.4.2). Affinity maturation based upon somatic hypermutation is generally considered a game with few winners and many losers, since most mutations are deleterious [126]. Kepler and Perelson [109] point out that, given the actual rate of somatic hypermutation, accumulation of random mutations is likely to render B cells incapable of binding the antigen, thereby compromising affinity maturation. Nevertheless, affinity maturation is efficient as revealed by recurring key mutations that increase the affinity of the antibody for its antigen by a factor of 10 [127, 32, 128]. To solve such ambivalence, concepts as the phasic mutation schedule and recycling were introduced [109, 110]. Asynchronous formation of GC alleviates the seriousness of deleterious mutations in that failing of individual GC may not compromise overall affinity maturation, because the very GC are likely to "die fast" thereby vacating follicular niches for a "next round" of GC. In this scenario, the lifetime of GC is not fixed but may vary among individual GC. The presented results also have implications for molecularbiological approaches to study affinity maturation and in particular its underlying selection process. In all probability, the crux of evaluation of GC growth kinetics also applies for exploration of selection within GC by means of sequence analysis of B cells. Albeit such sequencing data provide insights into global selection, they presumably fail to specify the local selection process operating within individual GC. This may explain why there is still uncertainity about how B cells are selected on the mechanistical level [94, 129]. To put in a nutshell: the presented data reveal that we are comparing apples to oranges, even when examining GC comprised by one spleen. But there is more to it than that: Who are the apples? Who are the oranges? The missing link to this dilemma is an adequate GC-age marker.

4.4.4 Revised model of affinity maturation

The essence of the presented results is that the GC reaction turns out to be of likewise robust and variable nature. In an imposing review on *textbook GC*, Manser [50] emphasized that one hallmark of GC responses is their inherent plasticity. So far, myriads of intervening approaches to the function of GC were applied, for the most part targeting factors that are attributed to play a role for the operation of GC, to name but a few: bcl-2, bcl-xl, BAFF/BAFF-R, CD19, CD40/CD40-L, CXCR-4, Fas, FcgammaRIIB, Msh-2, T cells [130, 102, 113, 69, 103, 68, 131, 132, 37, 104, 129]. Strikingly, such interventions hardly ever fully abrogate but result in an "altered version" of the GC response. By all means, it is beyond the power of the linear, uniform textbook conception of the GC response to explain such plasticity. The results presented in this thesis best support a new concept of affinity maturation (Figure 4.18) that is based upon three principal components: i) formation of splenic GC is both, **asynchronous** and **sustained** over the overall response, ii) GC continuously generate emigrant B cells released into the periphery, a fraction of whom **recirculate** to the splenic white pulp, and iii) GC are **open structures** that continuously **recruit** B cells from the pools of recirculating and naive follicular B cells.

In this conception, once established GC instantly start to produce emigrant B cells that are released into the circulation, in which the requisite step to become an emigrant B cell is to succeed in the local selection process operating in GC. This idea is consistent with the early appearance of antigen specific [133] B cells in the blood that display a post-GC memory-like phenotype, that is isotype switched and shows V region mutation [133]. Since it is not clear if these cells are true memory B cells [134], they are referred to as recirculating emigrant B cells in the following. As recirculating emigrant B cells apparently do not accumulate in the blood, and their population is continuously renewed over the time course [133], it is tempting to speculate what happens to the surplus cells. One possibility is that they differentiate to AFC that subsequently settle in the bone marrow. Nevertheless, this is unlikely to attribute to all of the surplus cells for two reasons: i) the frequency of AFC in blood is low compared to bone marrow and ii) this would generate an excess of AFC [133]. Additionally, a fraction of the emigrant B cells may differentiate to the recently identified B220$^-$ memory population that is found in the splenic red pulp and bone marrow [135]. The other options, if not differentiation, are death or re-entrance into GC. The revised model favors a combination of the latter by proposing a global selection process that acts on the level of re-entrance into follicular niches. In this scenario, recirculating short-lived emigrant B cells [133, 134] compete for recruitment into already established GC, since otherwise they will die. Indeed, recirculating emigrant B cells are shown to be responsive to the chemokine CXCL-13, strongly suggesting a migratory pathway that returns these cells to follicular niches. Moreover, transfer experiments performed by Schwickert et al. [101] reveal that pre-existing GC recruit antigen-specific B cells, as far as the transferred cells possess an competitive advantage in antigen-binding affinity. Recirculation of GC emigrant cells and global selection are further supported by the analysis of mice that feature improved B cell survival due to the transgenic expression of the anti-apoptotic protein bcl-2. The immune response in these mice is characterized by accumulation of B cells displaying a post-GC memory-like phenotype in the spleen, including an excessive number of low-affinity B cells [136]. Such abundance of low affinity B cells likely attributes to curtailment of the global selection process, in that competition for reentrance into GC is strongly reduced. Expression of the bcl-2 transgene prevents cell death of the low affinity variants and thereby distorts affinity maturation. Strikingly, bcl-2 transgene expression does not impede the generation of high affinity key mutation bearing B cells, but rather averts their propagation [136]. Besides recirculating cells, also naive follicular B cells may interfere in the global selection step, as they are shown to represent incessant visitors to pre-existing GC [101]. Naive follicular B cells are long-lived [137], which may compensate for their disadvantage in competition with recirculating cells. Since GC formation is an ongoing process, recirculating B cells as well as naive follicular B cells may additionally continuously give rise to new GC within empty or recently vacated follicular niches, an event hereinafter referred to as launching or relaunching, respectively. Whether recirculating B cells are capable to induce formation of GC or if (re)launching solely attributes to naive follicular B cells remains to be elucidated.

Albeit not explicitly depicted in the graphical illustration of the proposed model (Figure 4.18), soluble antigen presumably plays a pivotal role in adjusting recirculation of emigrant B cells. The phenomenon of soluble antigen induced cell death of antigen-specific GC B cell is well-known and thought to reflect clonal deletion of self-reactive B cells emerging within GC [138, 139, 140]. Interestingly, reduction in the spleen is preceded by rapid elimination of antigen specific B cells from the blood [140]. Therefore, soluble antigen may not only affect GC in a local but also in a global fashion, in that it prevents recirculation of emigrant B cells by "killing" them. Noteworthy, whereas single injections of soluble antigen do not significantly affect cross-sectional numbers and size of GC, repeated injections cause a four- to fivefold in size within 20 hours [138]. Consequently, recirculation of emigrant B cells may contribute or even be required for the maintenance of GC. This circumstance might also provide an explanation for the inconsistency of T cell independent (TI) GC responses. The generation of GC emigrant B cells is likely to rely on CD40-CD40L interactions in the presence of GC T cells, since blocking of this interaction grossly impairs establishment of the memory compartment [141, 142, 143]. Since CD40-CD40L signaling is not required for the initial induction of GC [142], TI antigens can elicit the formation of GC - even in the absence of CD40L providing GC T cells. Nevertheless, they presumably fail to maintain these GC since they are incapable to generate emigrant B cells, which might explain the rapid disappearance of GC. Taken together, adjusting the recirculation of emigrant B cells provides a potential tool to affect the growth kinetics of GC. In this scenario, the onset and height of GC responses are controlled by the amount of soluble antigen that defines the pool of recirculating emigrant B cells. This idea is consistent with the delayed formation of GC in response to *Salmonella*, in that GC become first detectable after the spread of *Salmonella* is impeded by production of sufficient amounts of antibodies in an extensive extrafollicular response (unpublished, data were presented in a contributed talk given by A.F. Cunningham at the BSI congress 2007).

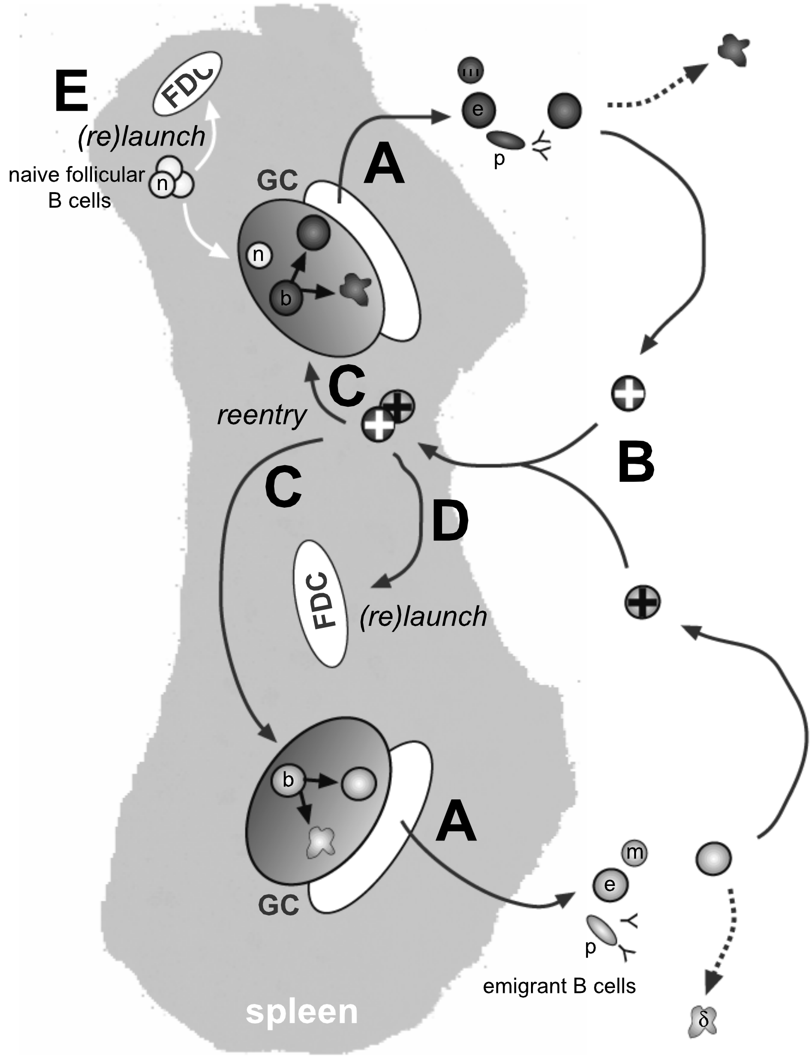

Figure 4.18: A revised model of affinity maturation. The proposed events involved in GC formation and progression during affinity maturation are illustrated in a sketch of the spleen. **A.** B cells (b) within already established GC undergo SHM and selection. **B.** B cells succeeding to pass this local selection step leave GC as emigrant B cells (e), including memory B cells (m) and AFC (p). The size of the emigrant pool is finite, hence survival is competitive and may lead to additional cell death of emigrant B cells (δ). A fraction of surviving emigrant B cells becomes recirculating B cells (+) that are permitted to reenter the spleen. **C.** Recirculating B cells can join already established GC reactions (reentry) or **D.** occupy vacant follicular niches giving rise to new GC ((re)launch). Access to follicular niches involves a global selection step, including competition among recirculating B cells and **E.** naive follicular B cells that may also continuously join pre-existing or even (re)launch new GC.

The crux of recirculation: oligoclonality of GC

The efficiency of affinity maturation is generally believed to attribute to the implementation of an iterative process, in that phases of diversification repeatedly alternate with phases of selection. Briefly, if diversification is not interposed by multiple rounds of selection, B cells are considered to loose their capability to bind antigen on account of accumulation of deleterious mutations in their V genes. Although iteration is reasonable, it lacks experimental validation, since tracing succession of selection and subsequent resumption of diversification for individual B cells is, as yet, unfeasible from the experimentally point of view. Nevertheless, two concepts of implementation of iteration subsist, namely i) recycling within GC, also referred to as internal iteration and ii) recirculation or external iteration, respectively. In contrast to recycling, recirculation has been treaten as an orphant over the past years, somehow fallen into oblivion. So why? - Because GC are oligoclonal! Assuming recirculation of GC B cells immediately prompts the audience to point out that recirculation is implausible because GC are oligoclonal (well-funded personal experience). The oligoclonal composition (1-5 clones) of GC is well-documented by two kinds of experiments including sequence analysis of individual GC [118, 121] and immunohistological evaluation after seeding of GC with either two antigens or two defined B cell populations [118, 121, 144, 24, 101]. While oligoclonality does certainly attribute to established GC, initial seeding of GC is likely to be multiclonal [121, 145] and clonal failures are rather common and inherent to the GC reaction [145]. Consequently, only the minor (oligoclonal) population of clones that survive the interclonal competition within GC at all become emigrant B cells, thereby giving rise to a selected repertoire [133]. The interclonal diversity is supposed to even further decline in case the very emigrant B cells recirculate, since reentry into GC is linked to an additional global selection process. In this scenario, the B cells that previously came off victorious of each individual GC ("locally selected") now have to compete globally with each other. This global selection process is likely to be again accompanied by marked clonal failures.

One might argue that reentry should increase the local interclonal diversity of individual GC assessed in experiments, just because this process may add cells that are quite unrelated to the currently propagating cells. That this is not necessarily the case, is best reflected by naive follicular B cells that are recently shown to represent frequent visitors to pre-established GC [101] but strikingly never perturbed oligoclonality in forerun studies. This phenomenon most likely attributes to the transient nature of these visits, in that the retention time of naive follicular B cells is low as indicated by higher motility and velocity compared to the physically restricted GC B cells [101]. The minor proportion of naive follicular B cells [101] further indicates that the rate of influx is rather low compared to the proliferation rate of GC B cells. If such behavior also accounts for recirculating emigrant B cells, they are very unlikely to increase the interclonal diversity of GC, especially as they also represent a restricted pre-selected pool of cells. Therefore, reentry of recirculating emigrant B cells does not necessarily contradict oligoclonality.

Kinetics of the cellular players of germinal centers

Chapter 5

Kinetics of the cellular players of germinal centers

5.1 Kinetics of germinal center T cells

For assessing the kinetics of GC T cells serial spleen sections of phOx-CSA immunized mice, derived at different time points after immunization, were triple stained for proliferating cells (mAb Ki-67), FDC-networks (mAb FDC-M2) and T cells (mAb CD3). In the following, stained sections were analyzed by confocal microscopy for the presence of GC that were identified as cell clusters of Ki-67^+ proliferating cells in the context of FDC-networks. The collectivity of all GC within individual sections was subsequently recorded by image acquisition (x400 magnification). Image evaluation was performed as exemplary depicted for a GC image obtained at day 8 after immunization in Figure 5.1. In total, 1136 GC out of 45 sections derived from 23 mice were evaluated, a detailed survey of all analyzed sections and evaluated GC is given in Table 5.1, the recorded parameters (direct and derived quantities) are listed in Table 5.2.

days p.i.					Σ (GC)/○
4	⊙(14) ⊙(17)		⊖(4) ⊖(11)		(46)/4
6	⊙(12) ⊙(16)	⊗(19) ⊗(15)	⊖(16) ⊖(35)	⊘(15) ⊘(11)	(139)/8
8	⊙(18) ⊙(31)		⊖(35) ⊖(45)	⊘(27) ⊘(37)	(193)/6
10	⊙(27)	⊗(10) ⊗(19)	⊖(31) ⊖(41)		(128)/5
12	⊙(22) ⊙(16)		⊖(37) ⊖(52)		(127)/4
14	⊙(27) ⊙(25)	⊗(44) ⊗(12)			(108)/4
16	⊙(34) ⊙(26)		⊖(50) ⊖(38)	⊘(26) ⊘(25)	(199)/6
18			⊖(21) ⊖(20)	⊘(30) ⊘(39)	(110)/4
21	⊙(17) ⊙(22)		⊖(19) ⊖(28)		(86)/4
					(**1136**)/45

Table 5.1: Survey of spleen sections analyzed for tracing the kinetics of GC T cells. Each ○ represents one analyzed spleen section at the given time point after immunization, identical ○ patterns (⊙ ⊗ ⊖⊘) reflect sections (interspace>500 μm) derived from the same animal. The number of evaluated GC for each section is given in parentheses.

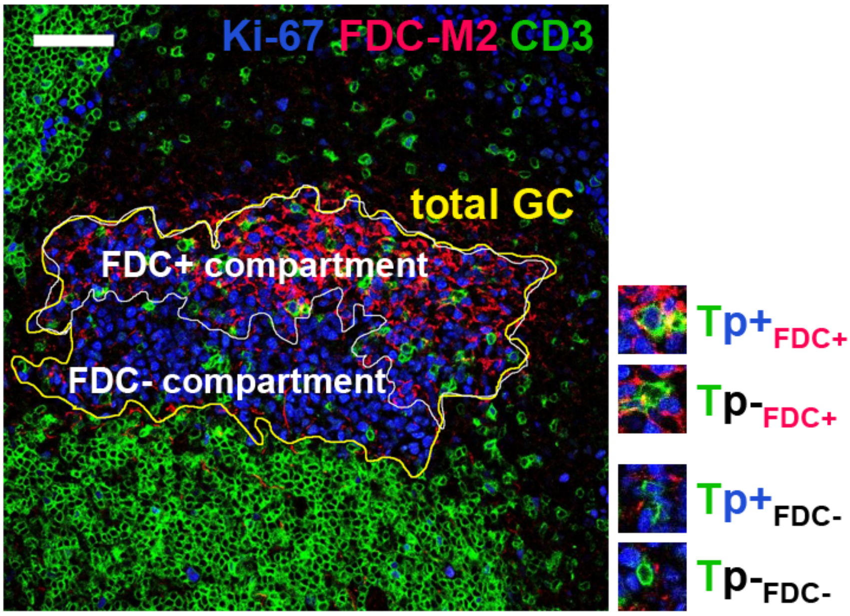

Figure 5.1: Data acquisition for assessing the kinetics of GC T cells exemplified by an image of a GC obtained at day 8 after immunization. GC were identified as clusters of proliferating cells (mAb Ki-67) within the context of FDC networks (mAb FDC-M2). GC T cells (T) were specified as CD3$^+$ cells within the manually assigned boundaries of GC (ROIs), by further discriminating between the FDC-rich light zone (FDC+) and the FDC-poor dark zone (FDC-) of GC. The subpopulation of proliferating GC T cells (p+) was identified as CD3$^+$ Ki-67$^+$, accordingly non-proliferating T cells (p-) were identified as CD3$^+$ Ki-67$^-$. Scale bar 50 μm.

Parameter	Parameter description	Calculation formula
(D) area$_t$	total area of GC	
(D) area$_{FDC+}$	area of FDC-rich light zone	
(D) nKi$_t$	total number of Ki-67$^+$ cells	
(D) nKi$_{FDC+}$	number of Ki-67$^+$ cells within FDC-rich light zone	
(D) nTp+$_{FDC+}$	number of proliferating T cells within FDC-rich light zone	
(D) nTp+$_{FDC-}$	number of proliferating T cells within FDC-poor dark zone	
(D) nTp-$_{FDC+}$	number of non-proliferating T cells within FDC-rich light zone	
(D) nTp-$_{FDC-}$	number of non-proliferating T cells within FDC-poor dark zone	
(d) area$_{FDC-}$	area of FDC-poor dark zone	=area$_t$ - area$_{FDC+}$
(d) nKi$_{FDC-}$	number of Ki-67$^+$ cells within FDC-poor dark zone	=nKi$_t$ - nKi$_{FDC+}$
(d) nTp+$_t$	total number of proliferating T cells	=nTp+$_{FDC+}$ + nTp+$_{FDC-}$
(d) nTp-$_t$	total number of non-proliferating T cells	=nTp-$_{FDC+}$ + nTp-$_{FDC-}$
(d) nT$_{FDC+,t}$	total number of T cells within FDC-rich light zone	=nTp+$_{FDC+}$ + nTp-$_{FDC+}$
(d) nT$_{FDC-,t}$	total number of T cells within FDC-poor dark zone	=nTp+$_{FDC-}$ + nTp-$_{FDC-}$
(d) nT$_t$	total number of T cells	=nT$_{FDC+,t}$ + nT$_{FDC-,t}$

Table 5.2: Survey of recorded parameters for assessing the kinetics of GC T cells. Listed are the recorded direct (D) and derived quantities (d).

5.1.1 The number of GC T cells reflects cross-sectional GC size

The numbers of GC T cells detected per cross-sectional GC show pronounced inner-section variation, thereby reflecting the already stated broad size distribution of cross-sectional GC. Both, the total number of GC T cells and the numbers of GC T cells in the two analyzed GC compartments (FDC-rich light zone and FDC-poor dark zone) correlate with the corresponding cross-sectional GC areas throughout all sampled time points. The left panels of Figure 5.2, A and B illustrate the correlation of numbers of GC T cells and GC area for the peak (day 10) and the decay phase (day 16) of the GC response, respectively. Correlations were rated by performing simple linear regression. As demonstrated previously (Section 4.1.1), the size of GC can be specified by either quoting cross-sectional GC areas or numbers of Ki67$^+$ cells of cross-sectional GC. Therefore, the recorded numbers of GC T cells not only correlate with the cross-sectional GC area, but as well with the numbers of Ki67$^+$ cells per cross-sectional GC (right panel of Figure, 5.2, A and B). However, in-between day 8 to 21 after immunization, the correlation of GC T cells within the FDC-rich light zone, tend to be more pronounced (R^2=0.77-0.90), than the correlation of numbers of GC T cells within the FDC-poor dark zone (R^2=0.70-0.80). As an aside, correlation coefficients obtained for the very early phase of GC formation (day 4 to 6) have unsteady and lower values (R^2=0.40-0.90). This is most probably due to both, the low number and relatively small size of cross-sectional GC, detected in the very period.

5.1.2 Very different correlation of proliferating and non-proliferating GC T cells with cross-sectional GC size

The separation of the overall GC T cell population into proliferating and non-proliferating GC T cells indicates divergent behavior of the two GC T cell subsets. Whereas the recorded numbers of non-proliferating GC T cells feature distinctive correlation with cross-sectional GC size (R^2=0.8-0.9), proliferating GC T cells do not correlate well (R^2=0.3-0.6) (Figure 5.3, A). Likewise, the numbers of proliferating GC T cells are not governed by the dimensions of either of the two GC compartments or dark and light zone, respectively (Figure 5.3, B). Noteworthy, the recorded numbers of proliferating cells show high variability with respect to GC of equivalent cross-sectional size (Figure 5.3, B). Symptomatically, rather large GC harboring no or only low numbers of proliferating GC T cells, are frequently observed from day 10 onwards, whereas very small GC often comprise unexpectedly high numbers of proliferating T cells at about the same time (highlighted by merged day 10 data in Figure 5.4). However, the numbers of proliferating T cells are rather nominal and thereby prone to manual counting errors and statistical fluctuations. Therefore, functional relevance of this finding is questionable.

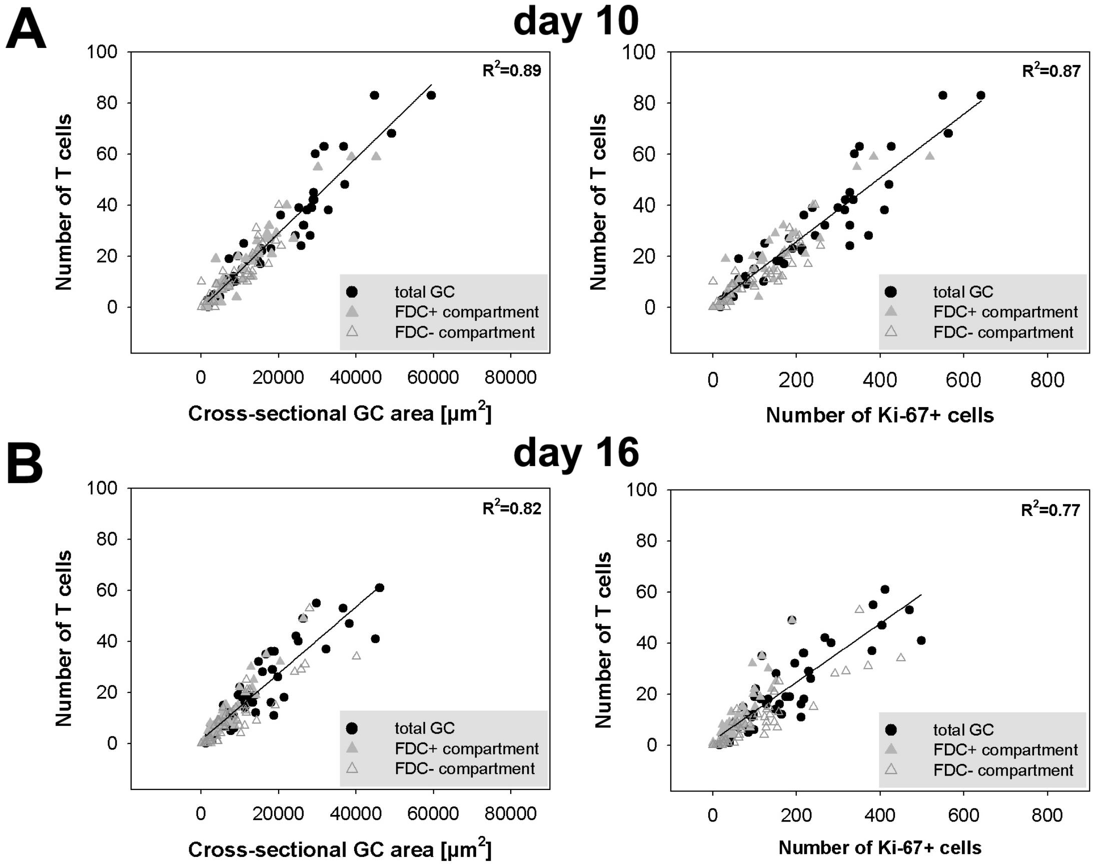

Figure 5.2: Inner-section correlation of numbers of GC T cells and cross-sectional GC size exemplary depicted for spleen sections obtained at day 10 (A) and day 16 (B) after immunization. The cross-sectional size of GC is given as both, cross-sectional GC area (left panel) and number of Ki-67$^+$ cells per cross-sectional GC (right panel). Correlations are rated applying simple linear regression. Regression line (black) for total numbers of GC T cells and correlation coefficient (R^2) are specified for each scatter plot.

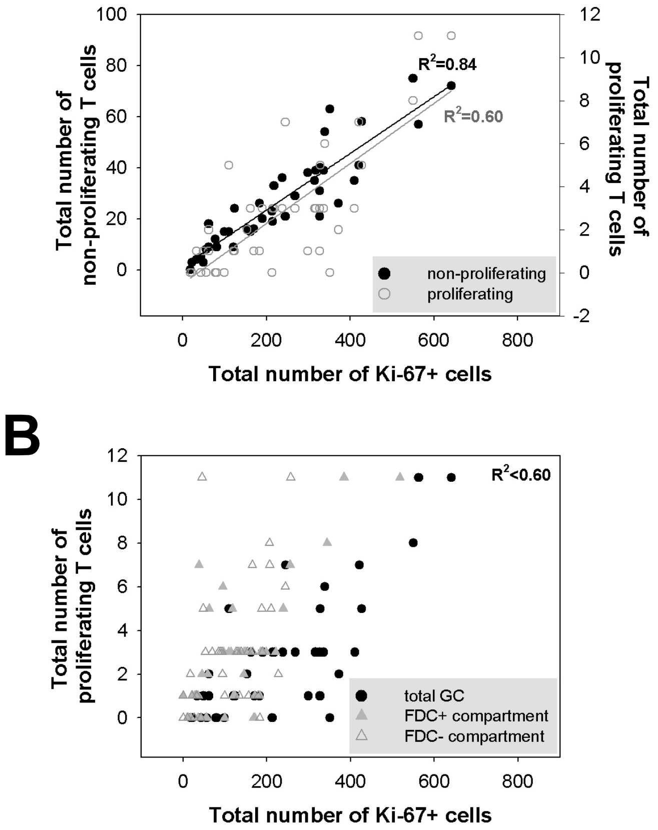

Figure 5.3: Interrelation of GC T cell proliferation and cross-sectional GC size exemplary shown for a spleen section obtained at day 10 after immunization. (A) The numbers of non-proliferating GC T cells correlate with the total cross-sectional GC size, but numbers of proliferating GC T cells do not. (B) The numbers of proliferating GC T cells are likewise not governed by the size of either of the two GC compartments. Correlations are rated applying simple linear regression. The regression lines for non-proliferating (black) and proliferating GC T cells (gray) as well as appendant squared correlation coefficients (R^2) are specified for each scatter plot.

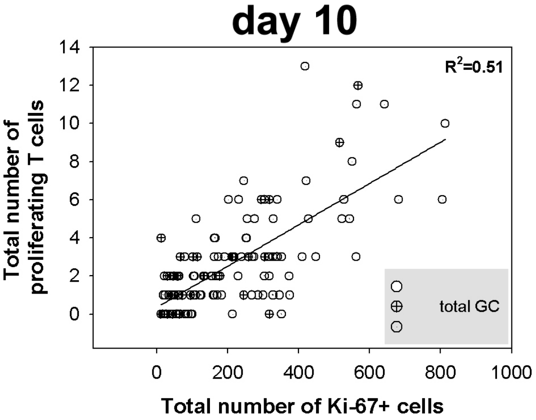

Figure 5.4: Illustration of highly variable numbers of proliferating GC T cells recorded for GC of equivalent cross-sectional size. Data is representative of merged data obtained for day 10 after immunization (128 GC out of 5 spleen sections). Note: GC of equivalent cross-sectional size harbor variational numbers of proliferating GC T cells. Correlation is rated applying simple linear regression. The regression line (black) and the squared correlation coefficient (R^2) are specified for the scatter plot.

5.1.3 Mean kinetics of GC T cells

The mean number of total GC T cells steeply increases from day 4 onwards and reaches its maximum at day 8 after immunization. After peaking at day 8, the mean number of total GC T cells marginally declines featuring an almost "steady state level" from day 10 to 21 (Figure 5.5, A). The mean kinetics of total GC T cells therefore resembles the overall growth kinetics of GC. The same applies to the kinetics of GC T cells within the two GC compartments, in which the mean number of GC T cells in the FDC rich light zone is constantly higher compared to the FDC poor dark zone (Figure 5.5, A). The comparison of images of B cell zones of naive and immunized mice further indicates an antigen-driven influx of T cells into follicular niches, in that accumulation of T cells in B cell zones is not observed until the induction of GC formation (Figure 5.6).

The mean frequency of GC T cells in relation to numbers of Ki-67$^+$ proliferating cells ranges between 10-16% (Figure 5.7, A). Therefore, GC T cells constitute a minor fraction of the total GC cell population. The kinetics of the mean frequency of GC T cells is characterized by two maxima (day 6 and days 16-21) seperated by an intermediate minimum (day 12 after immunization) (Figure 5.7, A) . The chronologically early maximum most probably reflects the strong influx of T cells observed at the onset of GC formation, whereas the successional minimum and rather late maximum are most likely due to a rather sustained mean number of T cells but increasing/decreasing mean cross-sectional GC size. The kinetics of frequencies of GC T cells with respect to dark and light zone - calculated as mean ratio of GC T cells per number of Ki-67$^+$ cells covered by the respective compartment - resemble the overall kinetics (Figure 5.7, A). However, the density of GC T cells is increased in the light zone compared to the dark zone about a factor of 1.5 between days 10 to 16 after immunization.

Albeit the recorded mean numbers of proliferating GC T cells per GC are low (0.4-4), an apparent peak is observed at day 8 after antigenic challenge (Figure 5.5, B). The mean frequency of proliferating GC T cells in reference to total numbers of GC T cells is characterized by a striking maximum at day 6 (16%) (Figure 5.7, B). Taken together, the recorded data imply that proliferation of GC T cells is a feature of the early phase of GC formation and becomes marginal thereafter. In this scenario, rather stable mean numbers of GC T cells are attained in the early phase of GC formation by migration and proliferation of T cells. Afterwards, the mean number of GC T cells is sustained by either "long-term" residing or continuous circulation of GC T cells.

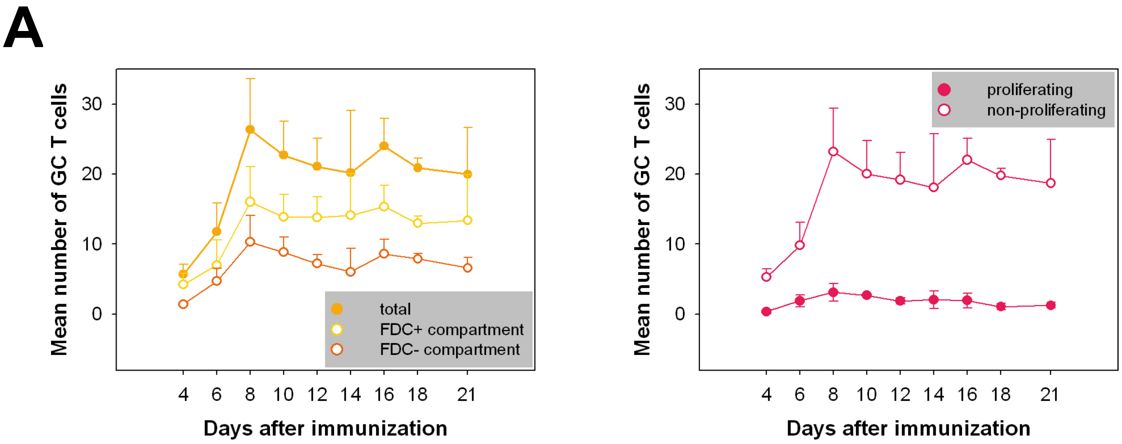

Figure 5.5: Mean kinetics of GC T cells. Illustrated are the mean numbers and standard deviations of GC T cells per cross-sectional GC. Each mean is representative of the entirety of analyzed sections at the given time point (see Table 5.1). (A) Mean kinetics of the overall number of GC T cells and numbers of GC T cells in the FDC- and FDC+ GC compartment (dark and light zone). (B) Mean kinetics of non-proliferating and proliferating GC T cells.

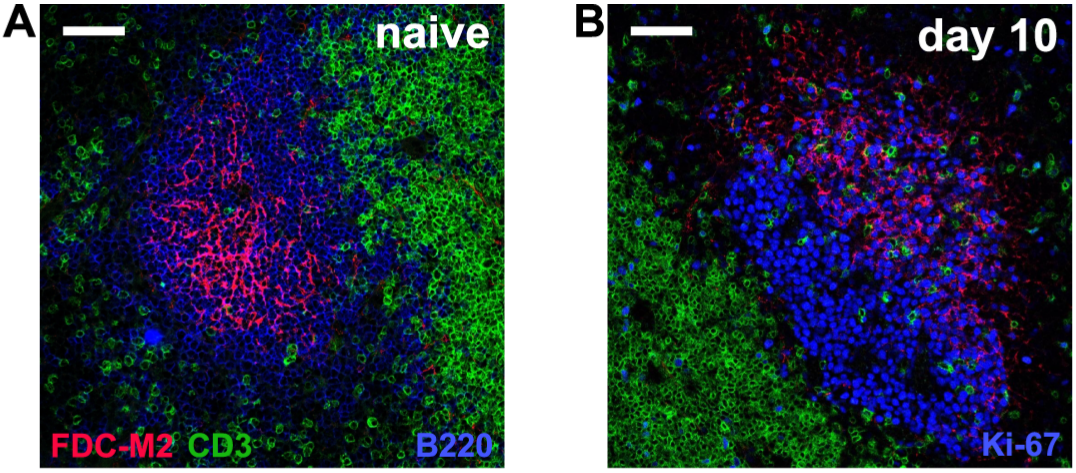

Figure 5.6: Antigen-driven influx of T cells into follicular niches due to GC formation. Whereas follicular niches of naive mice typically lack notable numbers of T cells, GC show accumulation of T cells, in particular within the FDC-rich light zone. Images are representative of triple immunofluorescent stainings of T cells (mAb CD3), FDC networks (mAb FDC-M2) and either B cell zones of naive (A) or GC of immunized mice at day 10 after immunization (B). B cell zones of naive mice were visualized applying mAb B220, GC of immunized mice were identified as clusters of Ki-67^+ cells within the context of FDC networks. Scale bar 50 μm.

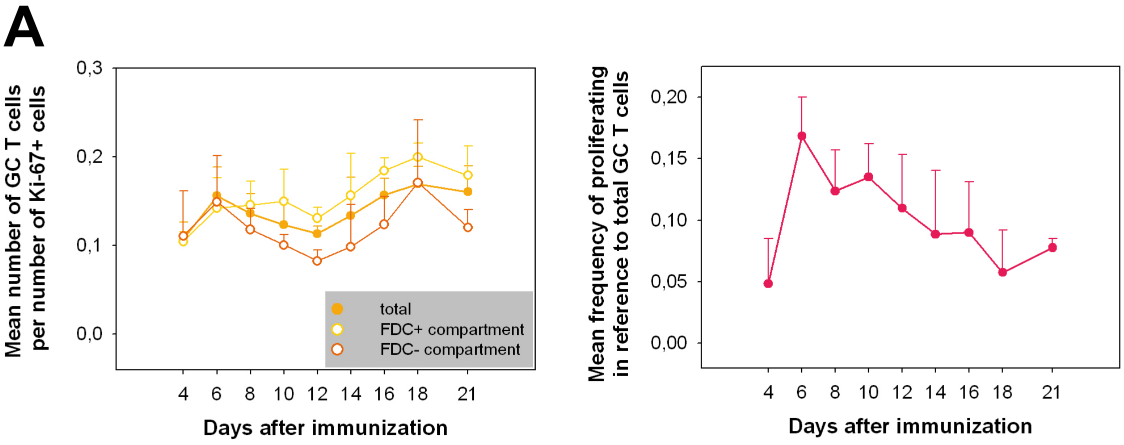

Figure 5.7: Kinetics of frequencies of GC T cells. (A) Mean frequencies of GC T cells in relation to Ki-67^+ cells per cross-sectional GC. Illustrated are the frequencies of total GC T cells and GC T cells within the FDC- and FDC+ GC compartment (dark and light zone). (B) Mean frequency of proliferating GC T cells with regard to the total number of GC T cells. Data are each representative of the entirety of evaluated GC at a given time point (see Table 5.1).

5.2 Kinetics of germinal center Mϕ

For assessing the kinetics of GC macrophages (Mϕ) serial spleen sections of phOx-CSA immunized mice, derived at different time points after immunization, were triple stained for proliferating cells (mAb Ki-67), FDC-networks (mAb FDC-M2) and Mϕ (mAb CD68). In the following, stained sections were analyzed by confocal microscopy for the presence of GC that were identified as cell clusters of Ki-67$^+$ proliferating cells in the context of FDC-networks. The collectivity of all GC within individual sections was subsequently recorded by image acquisition (x400 magnification). Image evaluation was performed as exemplary depicted for a GC image obtained at day 10 after immunization in Figure 5.8. In total, 1290 GC out of 52 sections derived from 26 mice were evaluated. A detailed survey of all analyzed sections and evaluated GC is given in Table 5.3, the recorded parameters (direct and derived quantities) are listed in Table 5.4.

days p.i.					Σ (GC)/○
4	⊙(15) ⊙(18)		⊖(6) ⊖(5)		(44)/4
6	⊙(11) ⊙(18)	⊗(13) ⊗(8)	⊖(14) ⊖(23)	⊘(15) ⊘(12)	(114)/8
8	⊙(25) ⊙(30)		⊖(31) ⊖(51)	⊘(32) ⊘(36)	(205)/6
10	⊙(23) ⊙(29)	⊗(16) ⊗(8)	⊖(32) ⊖(45)		(153)/6
12	⊙(18) ⊙(19)	⊗(13) ⊗(32)	⊖(41) ⊖(55)		(178)/6
14	⊙(23) ⊙(21)	⊗(41) ⊗(29)	⊖(21 ⊖(12)		(147)/6
16	⊙(26) ⊙(27)		⊖(46) ⊖(38)	⊘(28) ⊘(28)	(193)/6
18		⊗(14) ⊗(47)	⊖(23) ⊖(23)	⊘(25) ⊘(46)	(178)/6
21	⊙(15) ⊙(20)		⊖(16) ⊖(27)		(78)/4
					(**1290**)/52

Table 5.3: Survey of spleen sections analyzed for tracing the kinetics of GC Mϕ. Each ○ represents one analyzed spleen section at the given time point after immunization. Identical ○ patterns (⊙ ⊗ ⊖⊘) reflect sections (interspace>500 μm) derived from the same animal. The number of evaluated GC for each section is given in parentheses.

Parameter	Parameter description	Calculation formula
(D) area$_t$	total area of GC	
(D) area$_{FDC+}$	area of FDC-rich light zone	
(D) nKi$_t$	total number of Ki-67$^+$ cells	
(D) nKi$_{FDC+}$	number of Ki-67$^+$ cells within FDC-rich light zone	
(D) nM$_{FDC+}$	number of Mϕ within FDC-rich light zone	
(D) nM$_{FDC-}$	number of Mϕ FDC-poor dark zone	
(d) area$_{FDC-}$	area of FDC-poor dark zone	=area$_t$ - area$_{FDC+}$
(d) nKi$_{FDC-}$	number of Ki-67$^+$ cells within FDC-poor dark zone	=nKi$_t$ - nKi$_{FDC+}$
(d) nM$_t$	total number Mϕ	=nM$_{FDC+}$ + nM$_{FDC-}$

Table 5.4: Survey of recorded parameters for assessing the kinetics of GC Mϕ. Listed are the recorded direct (D) and derived quantities (d).

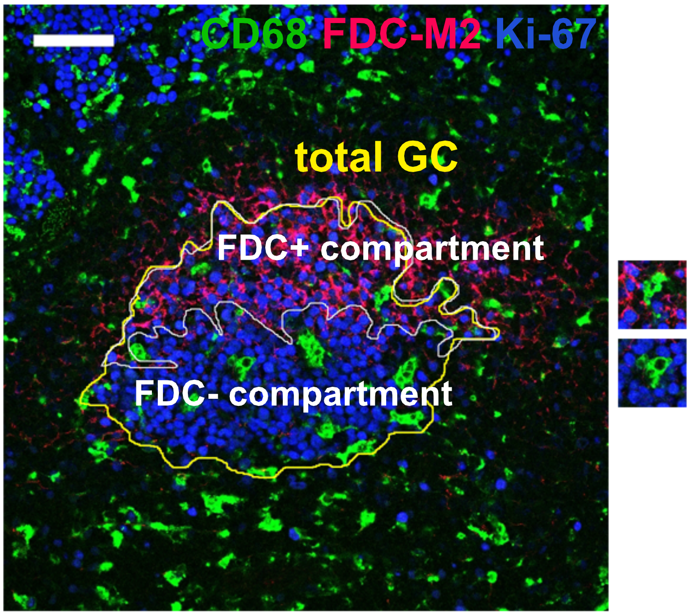

Figure 5.8: Data acquisition for assessing the kinetics of GC Mϕ exemplified by an image of a GC obtained at day 10 after immunization. GC were identified as clusters of proliferating cells (mAb Ki-67) within the context of FDC networks (mAb FDC-M2). GC Mϕ (M) were specified as CD68$^+$ cells within the manually assigned boundaries of GC (ROIs), by further discriminating between the FDC-rich light zone (FDC+) and the FDC-poor dark zone (FDC-) of GC. Scale bar 50 μm.

days p.i.		Σ (B cell zones)/○
naive (0)	⊙(69) ⊙(60) ⊗(53) ⊗(46)	(228)/4
4	⊙(39) ⊙(62)	(101)/2
6	⊙(52) ⊙(57)	(109)/2
10	⊙(36) ⊙(54)	(90)/2
21	⊙(43) ⊙(53)	(96)/2
x	⊙(68) ⊙(79)	(147)/2
		(771)/14

Table 5.5: Survey of spleen sections analyzed for assessing the frequency of Mϕ within B cell zones of naive and immunized BALB/c. Each ○ represents one analyzed spleen section at the given time point after immunization. Identical ○ patterns (⊙⊗) reflect sections (interspace>500 μm) derived from the same animal. The number of evaluated B cell zones for each section is given in parentheses.

5.2.1 The number of GC Mϕ reflects cross-sectional GC size

Likewise to GC T cells, the recorded numbers of Mϕ per cross-sectional GC feature prominent inner-section variation based on the underlying broad size distribution of cross-sectional GC. The total numbers as well as the numbers of Mϕ within dark and light zone of GC appear to be dependent on the size of the appendant compartments (Figure 5.9). The strict correlation of numbers of Mϕ and cross-sectional GC size is observed throughout all sampled time points, irrespective of the delineation of cross-sectional GC size in terms of either areas or numbers of Ki-67$^+$ cells (Figure 5.9, A and B). Notably, the regulation of numbers of macrophages appears to be very tight, as the vast majority of evaluated spleen sections feature squared correlation coefficients (R^2) substantially above 0.9.

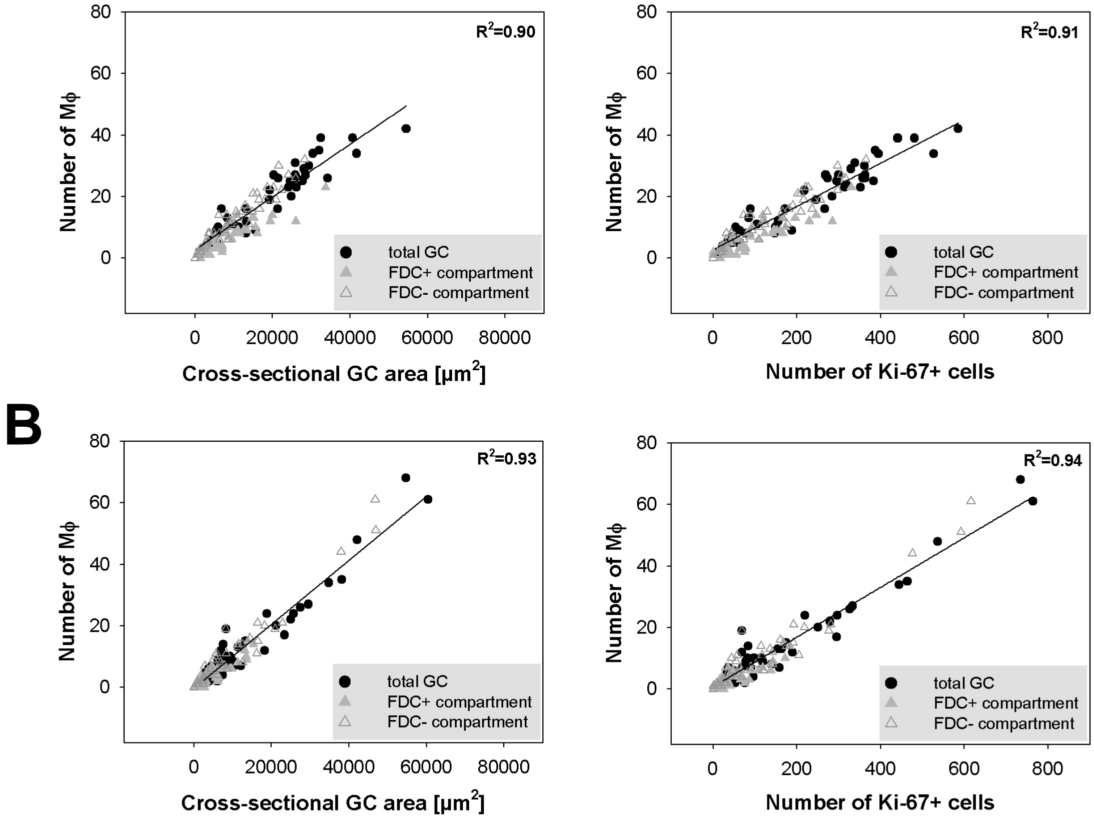

Figure 5.9: Inner-section correlation of numbers of GC Mϕ and cross-sectional GC size exemplarily depicted for spleen sections obtained at day 10 (A) and day 16 (B) after immunization. The cross-sectional size of GC is given as both cross-sectional GC area (left panel) and number of Ki-67$^+$ cells per cross-sectional GC (right panel). Correlations are rated applying simple linear regression. Regression line (black) for total numbers of macrophages and squared correlation coefficient (R^2) are specified for each scatter plot.

5.2.2 Mean kinetics of GC Mϕ

The mean kinetics of GC Mϕ follows the overall GC growth kinetics, marked by an increment of mean numbers of GC Mϕ in the early phase of GC formation up to the peak (day 4 to 10 after immunization), followed by a gradually but moderate decline until the last sampled time point (day 21 after immunization). The herein described kinetics holds true for both, the total numbers of GC Mϕ and the numbers of GC Mϕ in the two differentiated GC compartments (Figure 5.10, A). The mean numbers of GC Mϕ in the FDC-rich light zone and FDC-poor dark zone do not differ significantly, at the utmost a trend towards slightly elevated numbers GC of Mϕ in the FDC devoid compartment can be anticipated.

The frequency of GC Mϕ in relation to Ki-67$^+$ cells ranges between 8-11% (Figure 5.10, B). Hence GC Mϕ constitute a rather small GC cell population, if not the smallest, given the recorded frequency of GC T cells (10-16%). As a hallmark, the frequency of GC Mϕ in relation to Ki-67$^+$ cells additionally turns out to be sustained in an almost fabulous fashion throughout the immune response, displaying pronounced robustness (Figure 5.10, B). Taken together, the recorded, rather invariant mean frequency of numbers of GC Mϕ per Ki-67$^+$ cells and virtually absent standard deviations with regard to the total GC as well as the two GC compartments, indicate a very tight regulation.

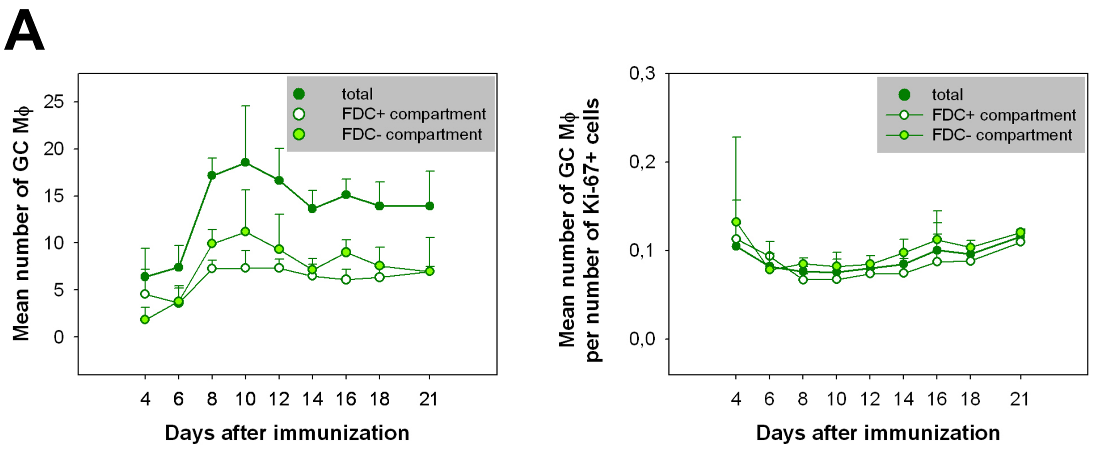

Figure 5.10: Mean kinetics of GC Mϕ. Illustrated are the mean numbers and standard deviations of GC Mϕ per cross-sectional GC. Each mean is representative of the entirety of analyzed spleen sections at the given time point (see Table 5.3). (A) Mean kinetics of the overall number of GC Mϕ and numbers of GC Mϕ in the FDC- and FDC+ GC compartment (dark and light zone) (B) Mean frequencies of GC Mϕ in relation to Ki-67$^+$ cells per cross-sectional GC. Depicted are the frequencies of total GC Mϕ and GC Mϕ within the FDC+ and FDC- GC compartment (dark and light zone).

5.2.3 GC Mϕ do not invade B cell zones due to GC formation but are already detectable in B cell zones of naive mice

The course of the mean kinetics of numbers and frequencies GC Mϕ highly suggests an influx of GC Mϕ into B cell zones due to the onset of GC formation, as do T cells (Section 5.1.3). Indeed, influx of Mϕ only as a consequence of GC formation (simplified: first comes the GC, then the Mϕ follow) is a current doctrine that is taken up to allege that GC Mϕ cannot play a role for initiation and the early phase of GC development at all [45]. Astonishingly, juxtaposing images of follicular niches of naive to follicular niches of immunized mice explicitly refutes the "Mϕ influx doctrine". In contrary to T cells, Mϕ are already frequently detected in B cell zones of naive mice (Figure 5.11, A). The presence of Mϕ in B cell zones was repeatedly verified in naive mice that were checked for the absence of GC by PNA staining. Based on this finding, Mϕ have to be understood as a component of the primary follicular niche that is a prerequisite for GC formation (simplified: first comes the Mϕ, then GC follow).

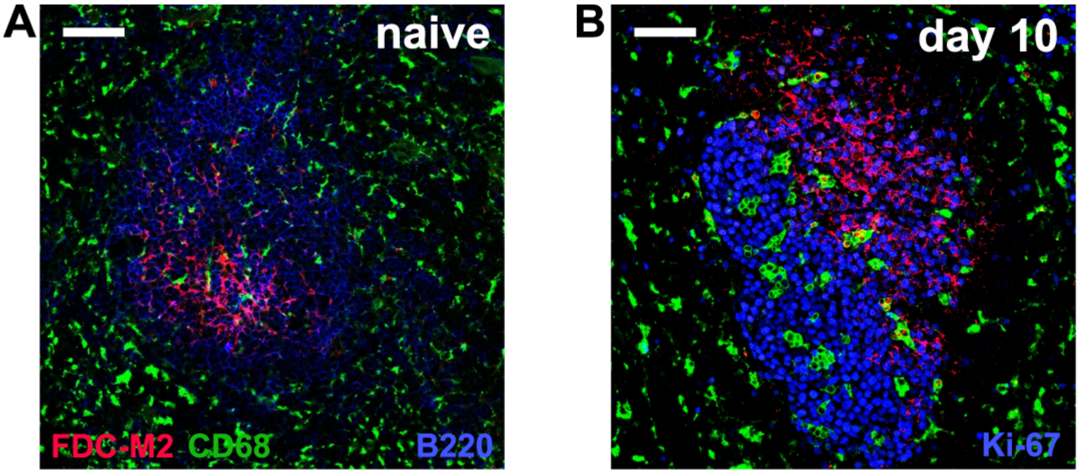

Figure 5.11: Mϕ do not invade B cell zones due to GC formation but are already detectable in B cell zones of naive mice. Images are representative of triple immunofluorescent stainings of B cell zones of naive (A) and immunized mice at day 10 after immunization (B). B cell zones of naive mice were visualized applying mAb B220, GC of immunized mice were identified as clusters of Ki-67^+ cells within the context of FDC networks (mAb FDC-M2). Scale bar 50 μm. Note: Images are representative of both the same B cell zone and GC as shown for GC T cells (figure 5.6).

5.2.4 The frequency of Mϕ per cross-sectional GC is regulated in a superordinate fashion by the overall B cell zone size

The comparison of images of follicular niches of naive to immunized mice gives the impression that the frequencies of Mϕ in the corresponding B cell zones are quite equivalent (Figure 5.11). To further elucidate the regulation of numbers of Mϕ, the frequencies of Mϕ per cross-sectional B cell zone size was assessed in naive and immunized mice. For this purpose spleen sections were triple stained for B cells (mAb B220), T cells (mAb CD4) and macrophages (mAb CD68) and both the size of cross-sectional B cell zones and associated numbers of Mϕ were recorded (Figure 5.12, A). Within individual sections the number of Mϕ strictly correlates with cross-sectional B cell zone size ($R^2 \geq 0.9$) (Figure 5.12, B). The quantitative analysis verifies the prementioned qualitative impression. As illustrated in Figure 5.12, C, the frequencies of Mϕ within B cell zones of naive (35±6 Mϕ/25,000 μm^2) and immunized mice (30±3 Mϕ/25,000 μm^2) are rather steady. The overall average frequency of Mϕ within follicles of BALB/c mice, ultimately adds up to 31±5 Mϕ/25,000 μm^2.

Besides affirming the involvement of Mϕ in formation of primary follicular niches (Section 5.2.3) this finding further implies that the frequency of Mϕ is governed by the overall B cell zone size. Therefore, the executing regulation mechanism does not take charge of GC B cells in particular, but of B cells in general. Figuratively, GC formation and growth lead to an expansion of the overall B cell zone that is accompanied by an influx of Mϕ because the number of B cells increases, not by reason that there are "specialized" GC B cells. As an aside, the superordinate regulation of the frequency of Mϕ is not confined to naive and immunized BALB/c mice but is also valid for other mouse strains, as well as its perturbation is potentially associated with autoimmunity (Section 5.4.2).

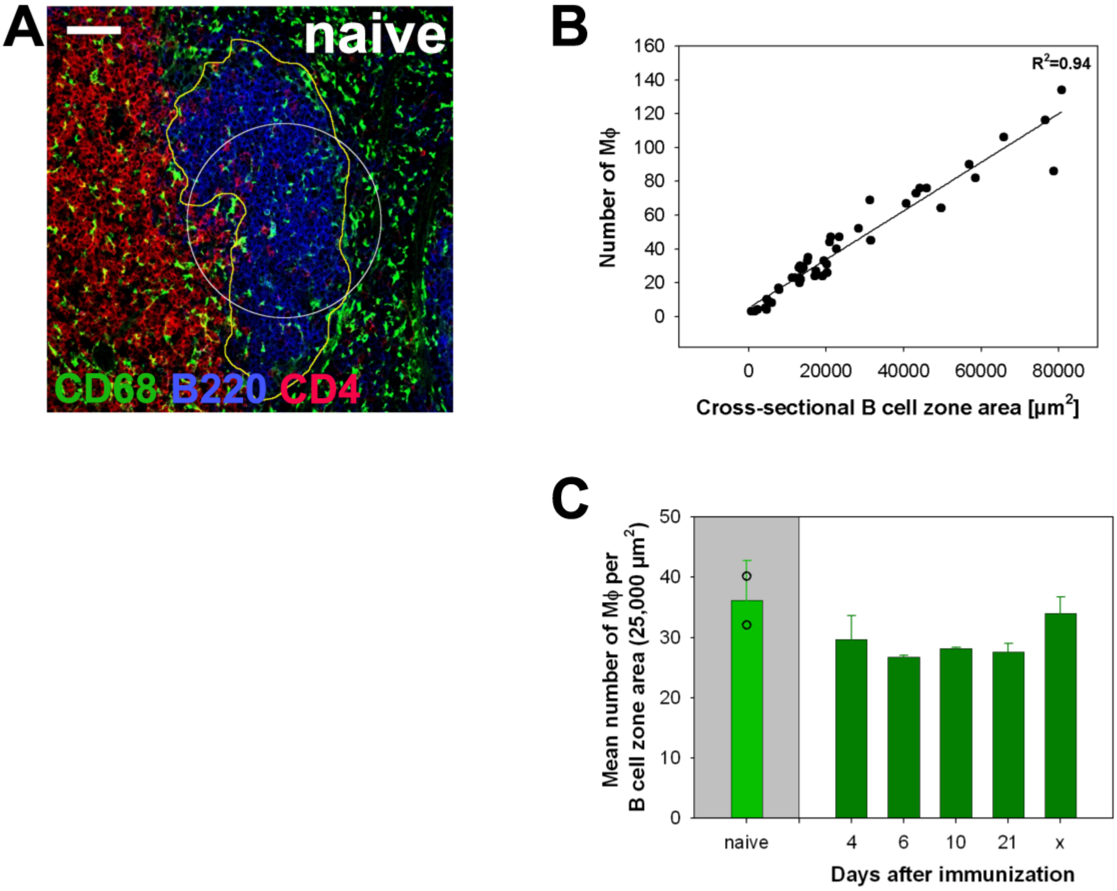

Figure 5.12: Steady frequencies of Mϕ within B cell zones of naive and immunized mice. (A) Evaluation of the frequency of Mϕ within B cell zones exemplarily shown for a spleen section derived from a naive mouse. B cell zones were identified as B220$^+$ areas (ROI, highlighted in yellow) adjacent to T cell zones (mAb CD4). Mϕ within B cell zones were identified and counted by CD68 reactivity. Scale bar 50 μm. (B) The number of Mϕ strictly correlates with cross-sectional size of the B cell zone. Data is representative of a spleen section derived from a naive BALB/c mouse. Correlation is rated applying simple linear regression. Regression line (black) and squared correlation coefficient (R^2) are specified for the scatter plot. (C) The frequency of Mϕ within B cell zones remains sustained upon immunization. Illustrated are the mean frequencies of Mϕ within B cell zones of two naive and five immunized mice at different time points after immunization. Data is each representative of two evaluated sections per mouse. In order to improve interpretability, frequencies are quoted as numbers of Mϕ per 25,000 μm^2, corresponding to the area comprised by the white selection in (A).

5.3 Kinetics of cell death and uptake of apoptotic cells within germinal centers

For assessing the kinetics of apoptotic cells within GC, serial spleen sections of phOx-CSA immunized mice were triple stained for GC B cells (PNA), macrophages (mAb CD68) and apoptotic nuclei (TUNEL). In the following, stained sections were analyzed by confocal microscopy for the presence of GC that were identified as cell clusters of PNA^+ cells. The collectivity of all GC within individual sections was subsequently recorded by image acquisition (x400 magnification). Image evaluation was performed as exemplary depicted for a GC image obtained at day 10 after immunization in Figure 5.13. In total, 1038 GC out of 42 sections derived from 21 mice were evaluated, a detailed survey of all analyzed sections and evaluated GC is given in Table 5.6.

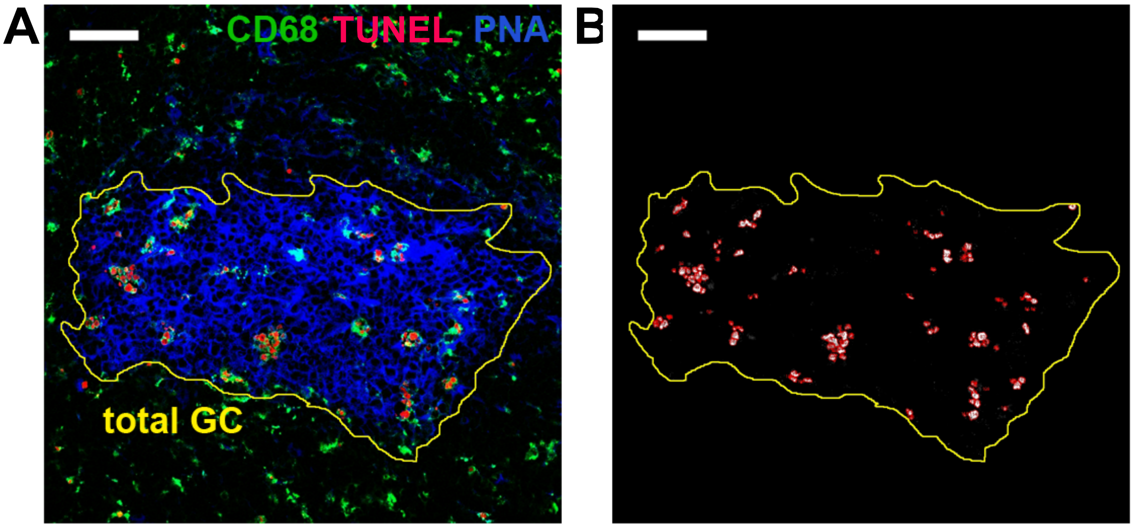

Figure 5.13: Data acquisition for assessing the kinetics of cell death within GC exemplified by an image of a GC obtained at day 8 after immunization. (A) GC were identified by PNA-reactivity and apoptotic nuclei were specified as $TUNEL^+$ signals within the manually assigned boundaries of GC (ROIs). Scale bar 50 μm. (B) Automated detection and measurement of $TUNEL^+$ nuclei for the GC depicted in (A) applying an adapted version of the Nucleus Counter plugin of the ImageJ software. Scale bar 50 μm.

5.3.1 Less pronounced inner-section correlation of numbers of apoptotic nuclei and cross-sectional GC size

As expected by the underlying broad size distribution of cross-sectional GC, the recorded numbers of apoptotic nuclei per cross-sectional GC show distinctive inner-section variation. But whereas the numbers of GC T cells and in particular GC macrophages turn out to well correlate with the underlying cross-sectional size of GC, this dependency appears to be less pronounced with respect to the numbers of apoptotic nuclei, reflected by lessened squared correlations coefficients ($R^2 \leq 0.76$). The inner-section correlation is exemplarily depicted for day 10 and 16 in Figure 5.14.

days p.i.				Σ (GC)/○
4	⊙(13) ⊙(12)	⊖(7) ⊖(5)		(37)/4
6	⊙(11) ⊙(17)	⊖(11) ⊖(17)	⊘(16) ⊘(8)	(80)/6
8	⊙(24) ⊙(36)	⊖(34) ⊖(48)	⊘(30) ⊘(42)	(214)/6
10	⊙(28) ⊙(31)	⊖(31) ⊖(37)		(127)/4
12	⊙(26) ⊙(22)	⊖(7) ⊖(20)	⊘(38) ⊘(57)	(170)/6
14	⊙(21) ⊙(18)			(39)/2
16	⊙(24) ⊙(29)	⊖(50) ⊖(22)	⊘(18) ⊘(29)	(172)/6
18		⊖(20) ⊖(23)	⊘(34) ⊘(36)	(113)/4
21	⊙(20) ⊙(17)	⊖(21) ⊖(28)		(86)/4
				(**1038**)/42

Table 5.6: Survey of spleen sections analyzed for tracing the kinetics of apoptotic nuclei within GC. Each ○ represents one analyzed spleen section at the given time point after immunization. Identical ○ patterns (⊙⊗⊖⊘) reflect sections (interspace>500 μm) derived from the same animal. The number of evaluated GC for each section is given in parentheses.

5.3.2 The number of apoptotic nuclei does not reflect cross-sectional GC size

The aforementioned less-stringent correlation of numbers of apoptotic nuclei and cross-sectional GC size becomes even more apparent by merging all data recorded at a given time point. Noteworthy, GC of the same cross-sectional size harbor arbitrary numbers of apoptotic cells, as exemplary illustrated for day 8 after immunization in Figure 5.15, A. At that time for instance, the numbers of apoptotic nuclei, corresponding to a cross-sectional GC area of 27,000 μm^2 (marked by the gray dashed line in Figure 5.15, A), cover a range from 25 to 109. Figure 5.15, B illustrates the automatic detection and measurement of apoptotic nuclei within three GC of the very cross-sectional size. Besides differing in the actual number, those GC also vary in the appearance of apoptotic nuclei, as increasing numbers effectuate a shift from initially discrete to cumulative clusters of of apoptotic nuclei. The formation of clusters of apoptotic nuclei indicates multiple uptake by GC macrophages as specified in Section 5.3.4. The high variance is not attributed to variation between mice but constitute a decisive trait.

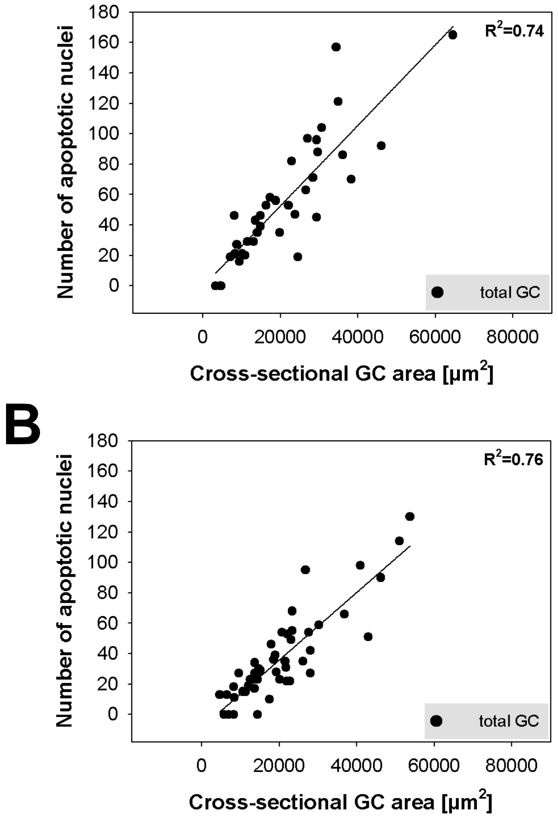

Figure 5.14: Inner-section correlation of numbers of apoptotic nuclei and cross-sectional GC size exemplary depicted for sections obtained at day 10 (A) and day 16 (B) after immunization. The cross-sectional size of GC is given as cross-sectional GC area, as revealed by PNA-reactivity. Apoptotic nuclei were visualized applying TUNEL.

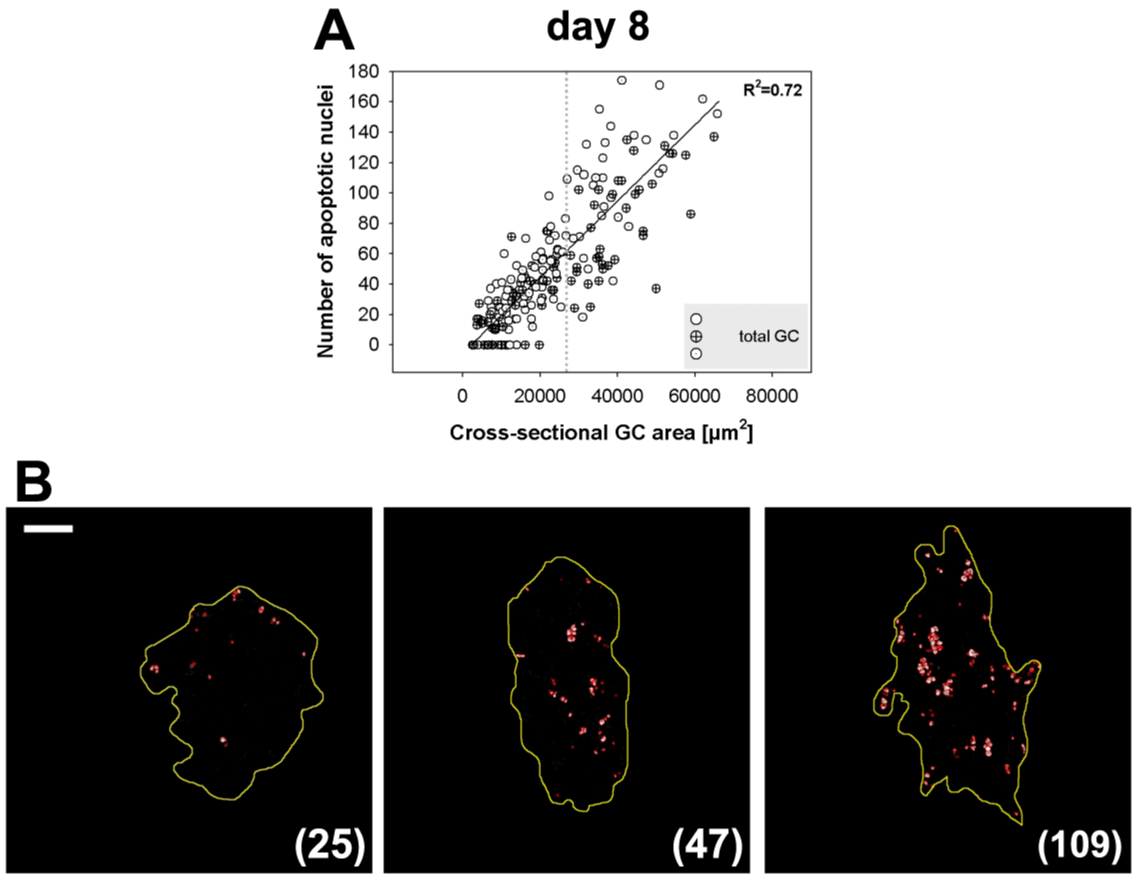

Figure 5.15: The number of apoptotic nuclei does not reflect cross-sectional GC size. (A) Less-stringent correlation of numbers of apoptotic nuclei and cross-sectional GC size. Note: GC of the same cross-sectional size harbor arbitrary numbers of apoptotic nuclei. Data is representative of merged data obtained for day 8 after immunization (214 GC out of 6 spleen sections). GC were identified by PNA-reactivity and apoptotic nuclei were visualized applying TUNEL. Correlation is rated applying linear regression. The regression line (black) and the squared correlation coefficient (R^2) are specified for the scatter plot. (B) Automated detection and measurement of apoptotic nuclei exemplified by a series of GC of the same cross-sectional size (27,000 μm^2, highlighted by the gray dashed line in (A)). Increasing numbers of apoptotic nuclei are reflected by a shift from initially discrete (*left panel*) to cumulative clusters of signals (*middle* to *right panel*). GC boundaries (yellow) were each assigned according to the source images.

5.3.3 Mean kinetics of apoptotic nuclei

The time course of the mean number of apoptotic nuclei per cross-sectional GC follows the overall growth kinetics of GC (Figure 5.16, A). Whereas apoptotic nuclei are rather infrequently observed within follicles of naive mice (Figure 5.17, A), and are only detected occasionally at the onset of GC formation (day 4), their mean number steadily increases afterwards, reaching a maximum at day 10 after immunization. At that time, also huge clusters of apoptotic nuclei are abound in cross-sectional GC (Figure 5.17, B). After peaking at day 10, the mean number of apoptotic nuclei per cross-sectional GC moderately decays.
The time course of the mean frequency of apoptotic nuclei relative to cross-sectional GC area is characterized by a steep increase at the outset up to day 8 after im-

munization. From day 8 to 21 after immunization, the mean frequency is retained at a quasi steady state level. Nevertheless, it tends to slightly decrease between day 10 to 16, giving rise to a less apparent second maximum at at day 18 after immunization (Figure 5.16, B). Albeit not directly recorded, the mean frequency of apoptotic nuclei with respect to the numbers of Ki-67$^+$ cells was extrapolated using the already assessed density of Ki-67$^+$ cells per cross-sectional GC area (1 cell/86 μm^2, Section 4.1.1). Expression of the mean frequency of apoptotic nuclei in relation to the number of Ki-67$^+$ cells facilitates its comparison to frequencies of GC T cells and macrophages. As aforementioned, starting from 0%, the frequency of apoptotic nuclei in relation to Ki-67$^+$ cells first increases and averages to 21 % at its peak at day 10 after immunization. In the following, the mean frequency ranges between 17-21 % (Figure 5.16, B, *dashed line*). Taken together, whereas apoptotic nuclei represent a minor cellular constituent at the onset of GC formation, they subsequently evolve to a major cellular constituent of GC (17-21%), as revealed by comparison to frequencies of GC T cells (10-16%) and macrophages (8-11%).

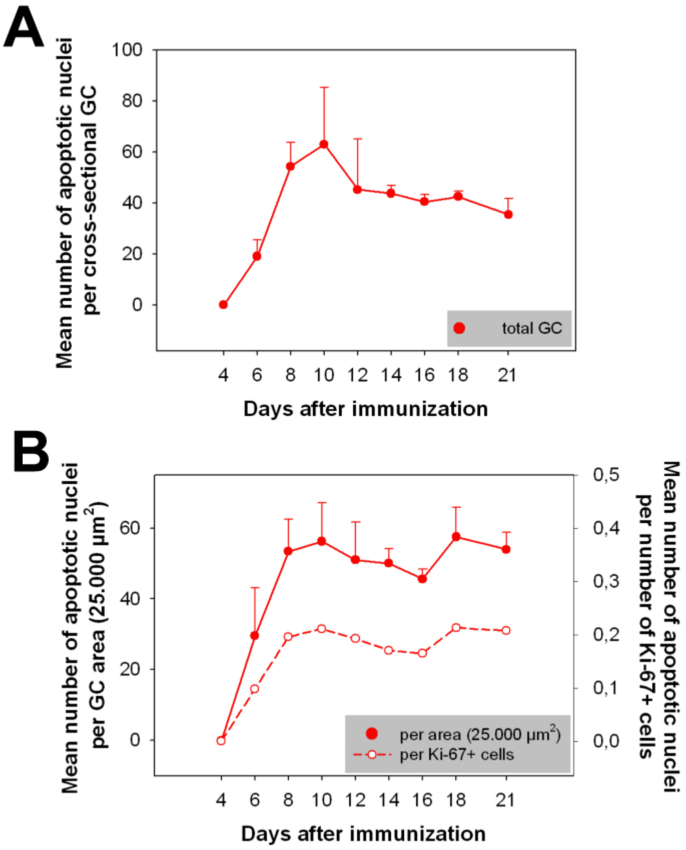

Figure 5.16: Mean kinetics of apoptotic nuclei within GC. (A) Time course of the mean number of apoptotic nuclei per cross-sectional GC. (B) Mean frequencies of apoptotic nuclei with respect to cross-sectional GC area (solid line) and numbers of Ki-67$^+$ cells (dashed line). Mean values and standard deviations are each representative of the entirety of analyzed sections at the given time point (see Table 5.6). The mean frequency of apoptotic nuclei in relation to Ki-67$^+$ cells is an extrapolated quantity, taking into account that one Ki-67$^+$ cell corresponds to 86 μm^2 cross-sectional GC area (specified in Section 4.1.1).

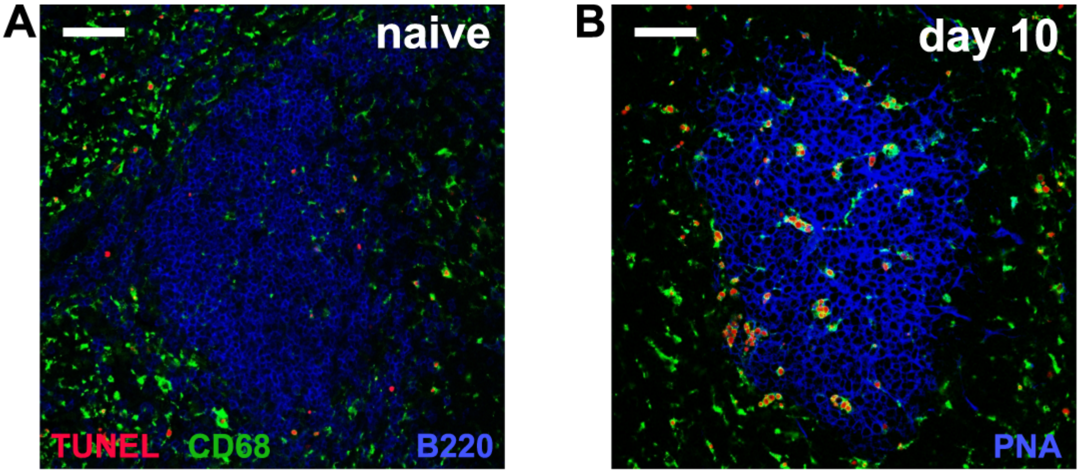

Figure 5.17: Apoptotic nuclei become a major cellular constituent of GC and entail the formation of abundant clusters during the immune response. Whereas apoptotic nuclei are basically absent from follicles of naive mice (A), they accumulate in GC and give rise to the formation of huge clusters due to their multiple uptake by GC macrophages (B). Images are representative of triple immunofluorescent stainings of apoptotic nuclei (TUNEL), macrophages (mAb 68) and B cell zones of naive (A) and GC of immunized mice at day 10 after immunization (B), respectively. B cell zones of naive mice were visualized applying mAb B220, GC of immunized mice were identified by PNA-reactivity. Scale bar 50 μm.

5.3.4 Uptake of apoptotic cells by GC Mϕ

The non-inflammatory removal of apoptotic cells generally requires their efficient recognition and uptake by macrophages, since impaired clearance of dying cells apparently involves the development of autoimmunity [146]. Among the individual kinetics of apoptotic nuclei and GC macrophages, just the kinetics of uptake is a matter of particular interest. Visually, the uptake of apoptotic cells by GC macrophages is reflected by colocalization of TUNEL$^+$ nuclei and CD68$^+$ macrophages in immunofluorescent stainings. Notably, within GC of immunized BALB/c the occurrence of TUNEL$^+$ signals turns out to be exclusively restricted to macrophages, as they were never detected in the absence of a dedicated macrophage. Moreover, the observed formation of clusters of apoptotic nuclei attributes to multiple uptake by macrophages, as illustrated in Figure 5.18. Noteworthy, multiple uptake of apoptotic nuclei by GC macrophages accounts for profound changes regarding the macrophage size. Hence, the number of apoptotic nuclei ingested by a macrophage determine its size.

The uptake of apoptotic cells is first rated by examining the time course of the mean number of apoptotic nuclei per GC Mϕ. Since the frequency of GC Mϕ per cross-sectional GC area is fixed (see Section 5.2.4), and the kinetics of GC Mϕ is already known (Section 5.2.2), the numbers of GC Mϕ are extrapolated from cross-sectional GC areas for this purpose. Accordingly, the resultant time course of the mean number of apoptotic nuclei per GC Mϕ mimics the kinetics of the mean frequency of apoptotic nuclei per cross-sectional GC area, albeit the ordinate scale differs. The mean number of apoptotic nuclei per GC Mϕ steeply increases until day 8 to 10 after immunization (1.8±0.3) but subsequently hardly decays (1.5±0.4, day 21) (Figure 5.19, A). After all, the mean number of apoptotic nuclei per GC Mϕ is a less informative measure of uptake of apoptotic cells within GC, because it misleadingly implies that apoptotic nuclei are evenly distributed among GC, solely dependent on their cross-sectional size. To factor in the given disparity in numbers of apoptotic nuclei within GC of the same cross-sectional size, GC are first classified according to their respective mean number of apoptotic nuclei per Mϕ. Since the number of inclosed apoptotic nuclei determines the size of Mϕ, data thus obtained figuratively qualify GC according to their mean size of Mϕ, as exemplified in figure 5.18. Plotting the distribution of GC comprising either small, medium, large or very large Mϕ - in the following referred to as the Mϕ size distribution - reveals radical changes over the observed time course (Figure 5.19, B). Whereas small Mϕ prevail at the onset of the formation of GC (100%, day 4), the Mϕ size distribution afterwards incrementally shifts towards larger Mϕ till day 10 after immunization. At that time, the bulk of GC comprises either medium (42%), large (34%) or even very large Mϕ (9%). Hence the once prevalent small Mϕ (15%) just account for a small fraction of GC. Subsequently, the frequencies of GC containing large and very large Mϕ successively decline. Thus, GC comprising very large Mϕ are virtually absent at day 14 (2%) and the vast majority of GC feature medium sized Mϕ (74%). Noteworthy, albeit the mean number of apoptotic nuclei per GC Mϕ at day 12 and 14 stays equal to 1.6, the underlying Mϕ size distributions are disparate (Figure 5.19, B). After day 14 the Mϕ size distribution again shifts towards larger Mϕ, wherein this second shift strikingy resembles the already specified preceding shift between days 6 to 10 with respect to both general progression and attained frequencies. In conclusion, the Mϕ size distribution constitutes a key element for cross-sectional evaluation of GC growth kinetics, as its particular shape may serve as an excellent marker for the stage of the immune response. Moreover, it turns out to be the sole parameter that succeeds in reflecting the underlying volume distribution of GC (Section 4.3.5).

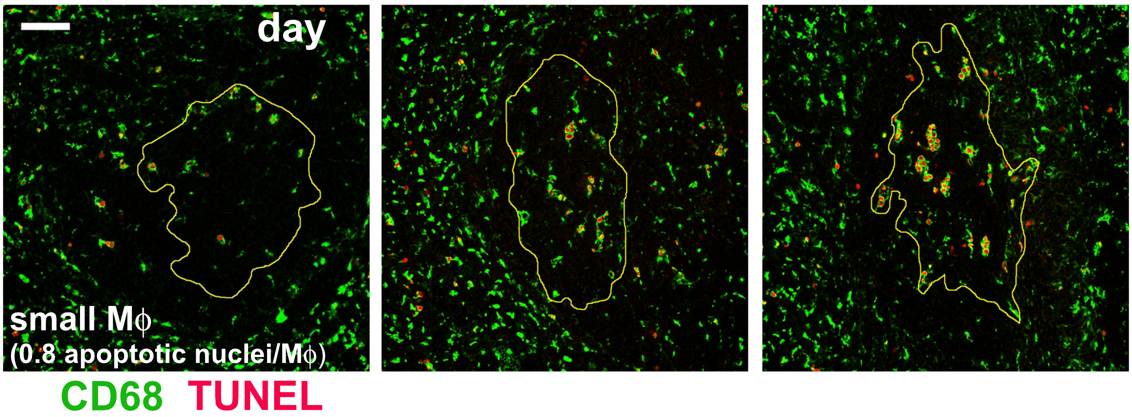

Figure 5.18: The disparity in numbers of apoptotic nuclei within GC of the same cross-sectional size is reflected by the varying size of macrophages. Multiple uptake of apoptotic nuclei by GC macrophages involves profound changes with respect to macrophage size. The mean size of GC macrophages is equivalent to the ratio of numbers of apoptotic nuclei to numbers of macrophages within an individual GC. Therefore, it allows for rating of uptake of dying cells within GC. To facilitate evaluation, the mean size of macrophages of individual GC is confined to the provision of four size classes: small (0-1), medium (1-2), large (2-3) and very large (>3 apoptotic nuclei per macrophage). The frequencies of GC belonging to the four size classes give rise to a distribution that is referred to as macrophage size distribution (Figure 5.19, B). Images illustrate the colocalization of apoptotic nuclei (TUNEL) and GC macrophages (mAb CD68) for the same series of GC as depicted in Figure 5.15. GC boundaries (yellow selection) were assigned according to PNA-reactivity (hidden, in order to facilitate inspection). Scale bar 50 μm.

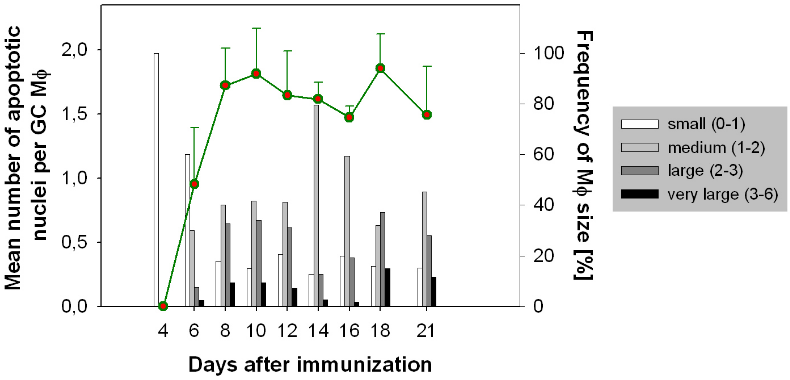

Figure 5.19: Mean kinetics of uptake of apoptotic cells by GC macrophages and underlying macrophage size distribution. The macrophage size distribution is subjected to radical changes over the time course that are not necessarily reflected by the mean kinetics. (A) Time course of the mean number of apoptotic nuclei per GC Mϕ (green solid line). (B) Time course of the macrophage size distribution that was acquired as illustrated in Figure 5.18. Data is representative of the entirety of analyzed sections at a given time point (see Table 5.6). The mean number of apoptotic nuclei per GC Mϕ is an extrapolated quantity, allowing for the absolute frequency of GC Mϕ per cross-sectional GC area (31±5 Mϕ/25,000 μm^2, as specified in Section 5.2.4).

5.3.5 The shape of the Mϕ size distribution potentially acts as an regulatory element - Implications of a phenomenological mathematical model

The cell kinetics in germinal centers are remarkably fast, as for instance GC B cells have been shown to divide every 6 to 10 hours [144, 147]. But despite this high proliferation rate, the total number of GC B cells grows much slower than expected. So far, the mechanisms that control the growth behavior of GC are still ill-defined. Apparently, the high proliferation rate has to be counterbalanced by a comparably high apoptosis rate, but besides, GC macrophages are thought to play an important role in the regulation of GC growth [45, 46]. The evaluation of the kinetics of GC macrophages and uptake of apoptotic cells by GC macrophages suggests that instead of the number, rather the size of GC macrophages might represent a regulatory element. This working hypothesis was tested by devising a mathematical model that assumes simple feedback mechanisms for the interaction between GC B cells and macrophages. *Mathematical modeling was assisted by Dr. Michal Or-Guil and Dr. Johannes Schuchhardt.*

The model

The model describes the kinetics of individual GC as illustrated in Figure 5.20 and as translated into a mathematical model (given below). The formation of GC is accompanied by a brisk expansion phase characterized by pronounced GC B cell proliferation. Consequently, the number of follicular B cells increases and macrophages are attracted to the B cell follicles, respectively GC (superordinate regulation, Section 5.2.4). Due to selection and competition for survival signals within GC, a fraction of GC B cells becomes apoptotic. Apoptotic GC B cells are immediately recognized and phagocytozed by GC macrophages. The size of GC macrophages is influenced by two counteracting processes: uptake of apoptotic cells and degradation of the very cells within macrophages. Whereas uptake of apoptotic cells increases the size, the degradation of apoptotic material decreases the size of a macrophage. The kinetics of GC B cells and macrophages are coupled by a negative feedback mechanism that implies inhibition of GC B cell proliferation by large macrophages loaded with several apoptotic cells.

Model equations

The interactions described in the *Model* section and in Figure 5.20 are specified by the following set of ordinary differential equations:

$$\dot{b} = p_t \cdot b - \phi \sum_{k=0}^{n-1} m_k \cdot b \tag{5.1}$$

$$\dot{m}_0 = \alpha \cdot b - \delta \cdot m_0 - \phi \cdot m_0 \cdot b + \theta \cdot m_1 \tag{5.2a}$$

$$\dot{m}_k = \phi \cdot m_{k-1} \cdot b - \phi \cdot m_k \cdot b + \theta \cdot m_{k+1} - \theta \cdot m_k \tag{5.2b}$$

$$\dot{m}_n = \phi \cdot m_{n-1} \cdot b - \theta \cdot m_n \tag{5.2c}$$

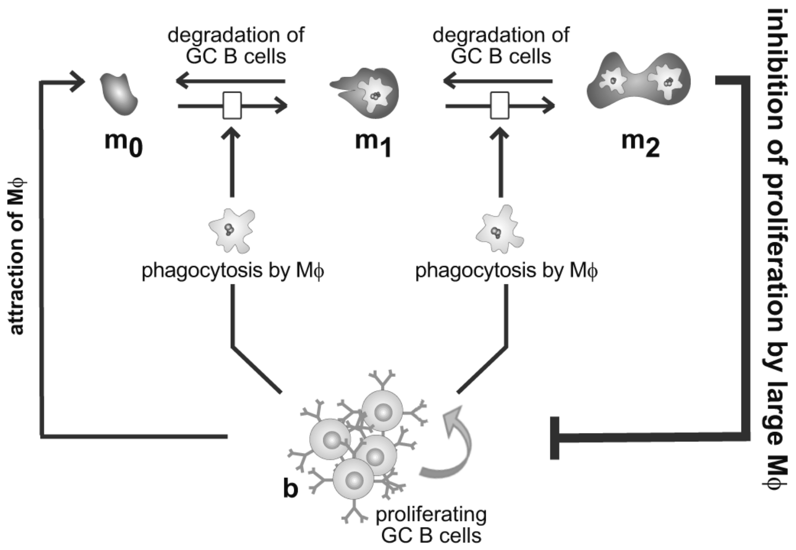

Figure 5.20: Model interactions of GC B cells and macrophages. The simulation starts with the formation and expansion of GC by swiftly proliferating GC B cells (b). As the proliferation of GC B cells increases the total number of B cells, macrophages (m) are attracted to B cell follicles and thus to GC. The subscript of m indicates the number of engulfed apoptotic cells and thereby reflects the size of GC macrophages. Due to selection within GC, a fraction of GC B cells becomes apoptotic and is immediately engulfed and phagocytozed by GC macrophages. Uptake of apoptotic cells gradually increases the size of GC macrophages, whereas the degradation of apoptotic cells within GC macrophages decreases their size. On account of a simple feedback mechanism, GC macrophages counteractively influence the expansion of GC B cell as large GC macrophages suppress GC B cell proliferation.

GC B cells (b) proliferate with the actual proliferation rate p_t but disappear with rate ϕ due to apoptosis and uptake by GC macrophages (m) (Equation 5.1). The size of macrophages is reflected by the index k that indicates the number of engulfed apoptotic cells. The kinetics of macrophages belonging to any size class m_k are specified by each two influx and efflux terms (Equation 5.2b). Influx to m_k is given by either uptake of apoptotic cells by macrophages of size *k-1* or by degradation of apoptotic cells within macrophages of size *k+1* that occurs at rate θ. Accordingly, the efflux from m_k is defined by either uptake or degradation of apoptotic cells by macrophages of size k. In the particular case of macrophages that harbor no apoptotic cells at all (m_0) (Equation 5.2a), the influx is given by the initial attraction of macrophages by B cells with rate α and the degradation of apoptotic cells within macrophages of size *k=1*. The efflux from m_0 is determined by the death rate δ of macrophages and uptake of apoptotic cells by macrophages of size *k=0*. Consequently, the kinetics of macrophages belonging to the maximal size class m_n (Equation 5.2c) comprise only each one influx (uptake of apoptotic cells by macrophages of size *n-1*) and efflux term (degradation of apoptotic cells within macrophages of size n).

The influence of the macrophage size distribution on the actual proliferation rate p_t is implemented as:

$$p_t = \frac{p_{max}}{1 + f\sum_{k=0}^{n} k \cdot m_k} \tag{5.3}$$

In the absence of GC B cell apoptosis and uptake (k=0) proliferation occurs at maximal rate p_{max}. Uptake of apoptotic cells leads to a decline of the actual proliferation rate p_t, where the decline is proportional to the general negative feedback potency of macrophages (f) and their actual size distribution.

Parameter and initial conditions	Value	Reference
Maximum proliferation rate of GC B cells (p_{max})	2.75 day^{-1}	[144, 147]
Rate of uptake of apoptotic cells by GC macrophages (ϕ)	0.001 day^{-1}	
Degradation rate of apoptotic cells ingested by GC macrophages (θ)	0.7 day^{-1}	[148]
Initial rate of attraction of GC macrophages by B cells (α)	0.015 day^{-1}	
Death rate of GC macrophages (δ)	0.5 day^{-1}	
Negative feedback potency rate of GC macrophages (f)	0.01	

Table 5.7: Parameter values and initial conditions.

The model succeeds in reproducing major characteristics of GC cell kinetics

The behavior of the model resembles the major characteristics of the experimentally recorded cell kinetics of GC. In the simulation, GC first become detectable at around day 4 and last for about three weeks. The maximum size of GC is attained at day 8 after immunization when the total population size of GC B cells amounts to about 12,000 cells. Thereafter, GC gradually vanish (Figure 5.21, *top panel*). Moreover, the simulated time course of GC macrophages parallels GC growth as the numbers of GC macrophages increase during the expansion but consequently decrease in the decay phase of GC. The peak number of GC macrophages is detected at day 12 after immunization. At this time, the population size of GC macrophages is about 750 cells (Figure 5.21, *bottom panel*).

The simulation additionally succeeds in reproducing the kinetics of uptake of apoptotic cells within GC, since the size of macrophages - reflected by the number of apoptotic nuclei per GC macrophage - steeply increases up to day 10 and thereafter slowly decays (Figure 5.22, *left panel*). Noteworthy, the simulation also provides a fair prediction of the macrophage size distribution as exemplarily illustrated for day 4, 6 and 10 in Figure 5.22, *middle panel.* It accurately predicts that virtually all GC macrophages are of small size at the onset of GC formation (day 4), but then gradually shift towards larger size (day 6), finally resulting in a predominance of large-sized GC macrophages at the peak of GC growth (day 10).

The herein outlined model has to be considered rather phenomenologically, since several parameter values are not yet established experimentally (Table 5.7) and were therefore tuned within reasonable limits to achieve a realistic behavior of the simulation. Nevertheless, it provides strong evidence that the size distribution of macrophages acts as a regulatory element with regard to GC growth kinetics.

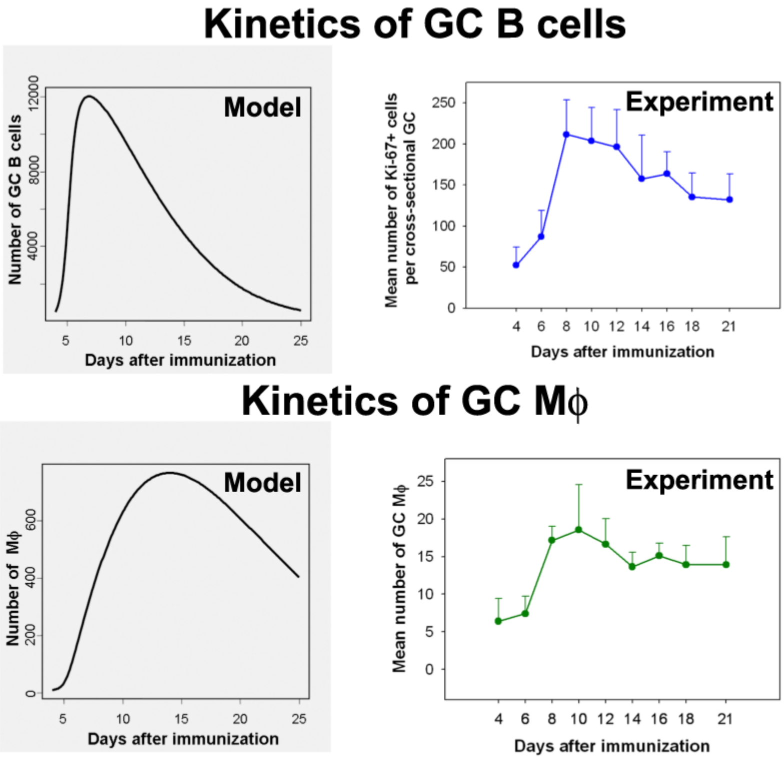

Figure 5.21: The model phenomenologically reproduces the experimentally recorded kinetics of GC B cells and macrophages. The simulated time plots of GC B cells and macrophages (gray-shaded) are each opposed to the experimentally recorded kinetics. Parameter values and initial conditions of the simulation were applied according to Table 5.7. The ordinate scales of simulations and experimental data differ, as simulations are performed on GC volumes but experimental data are derived from cross-sectional evaluation.

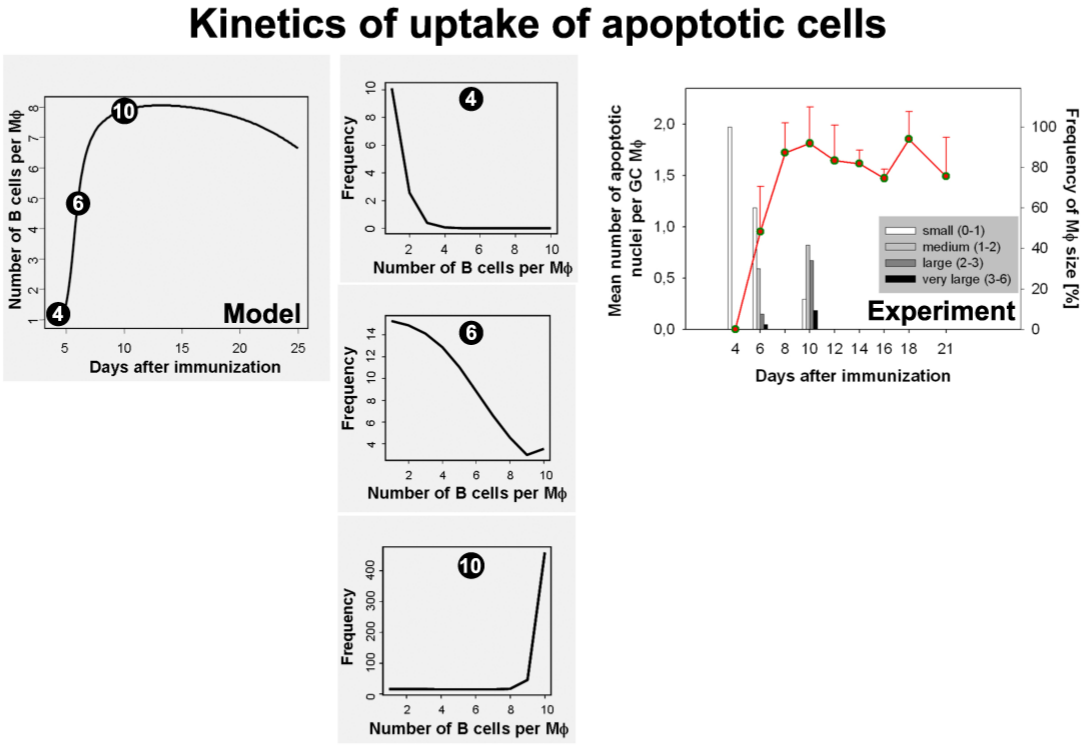

Figure 5.22: The model reproduces the experimentally recorded kinetics of uptake of apoptotic cells and predicts the macrophage size distribution. The simulated time plot of the uptake of apoptotic GC B cells by macrophages as well as the resultant macrophage size distributions at day 4, 6 and 10 (gray-shaded) are opposed to the experimentally recorded data. Parameter values and initial conditions of the simulation were applied according to Table 5.7.

5.4 Excursus: Perturbed GC Mϕ compartment in autoimmune NZB/W mice

The immunohistological detection of apoptotic cells applying the TUNEL technology was established in a series of pilot experiments using cryosections of spleen tissue derived from lupus-prone (NZB/W)xF1 mice. The NZB/W strain exhibits spontaneous GC formation in the spleen in the absence of purposeful immunization and adventitious infection. The cells of these spontaneously developing GC were reported to be phenotypically similar with respect to cell-surface markers to GC that arise in response to immunization [149]. As an initially unanticipated result of the pilot experiments, the morphology of GC Mϕ and associated apoptotic cells of NZB/W mice turned out to be obviously peculiar. Because the generation of high titers of anti-DNA antibodies in autoimmune mice is generally ascribed to malfunction of GC and in particular to clearing defects of Mϕ within GC [150], the NZB/W model emerged as an eligible candidate to complement the analysis of the kinetics of apoptotic cells and their uptake by Mϕ assessed in BALB/c mice. Therefore, the follicular Mϕ of NZB/W mice were subjected to further analysis. The frequency of Mϕ within B cell zones was recorded for naive NZB/W of different age as described before for naive and immunized BALB/c mice (Section 5.2.4). Naive NZB and BALB/c mice served as controls and standards, respectively. A survey of all analyzed tissue specimens is depicted in Table 5.8.

Specimen					Σ (B cell zones)/○
NZB (6-8 w)	⊙(41)	⊙(40)	⊗(43)	⊗(41)	(165)/4
NZB/W (6-8 w)	⊙(40)	⊙(49)	⊗(43)	⊗(43)	(175)/4
NZB/W (14 w)	⊙(62)	⊙(53)	⊗(53)		(168)/3
					(**508**)/10

Table 5.8: Survey of spleen sections analyzed for assessing the frequency of Mϕ within B cell zones of NZB/W and NZB mice. Each ○ represents one analyzed spleen section at the given time point after immunization, identical ○ patterns (⊙⊗) reflect sections (interspace>500 μm) derived from the same animal. The number of evaluated B cell zones for each section is given in parentheses.

5.4.1 Aberrant morphology of GC Mϕ in NZB/W mice

As mentioned in the preface of this section, confocal imaging of fluorescence stained GC Mϕ and apoptotic cells discloses differences of NZB/W compared to BALB/c mice with respect to morphology. These differences strikingly unveil by performing z-scans accounting for the third dimension of Mϕ (Figure 5.23, A and B, middle left panel). Unlike z-scans, default xy-scans do not expose these alterations (Figure 5.23, A and B, left panel). A great many of GC Mϕ of NZB/W mice feature clear signs of disintegration. The cell membrane of these Mϕ ceases to exist as a whole framework, but is fractionated into myriads of membrane particles (blebs, vesicles) (Figure 5.23, A, middle right panel). As a concomitant feature, the accumulation of loads of apoptotic nuclear debris is detected in conjunction with these Mϕ (Figure 5.23, A, right panel). This "exaggerated" morphology of NZB/W Mϕ can be interpreted as a decomposition phenomenon due to Mϕ hyperactivity - finally resulting in Mϕ death.

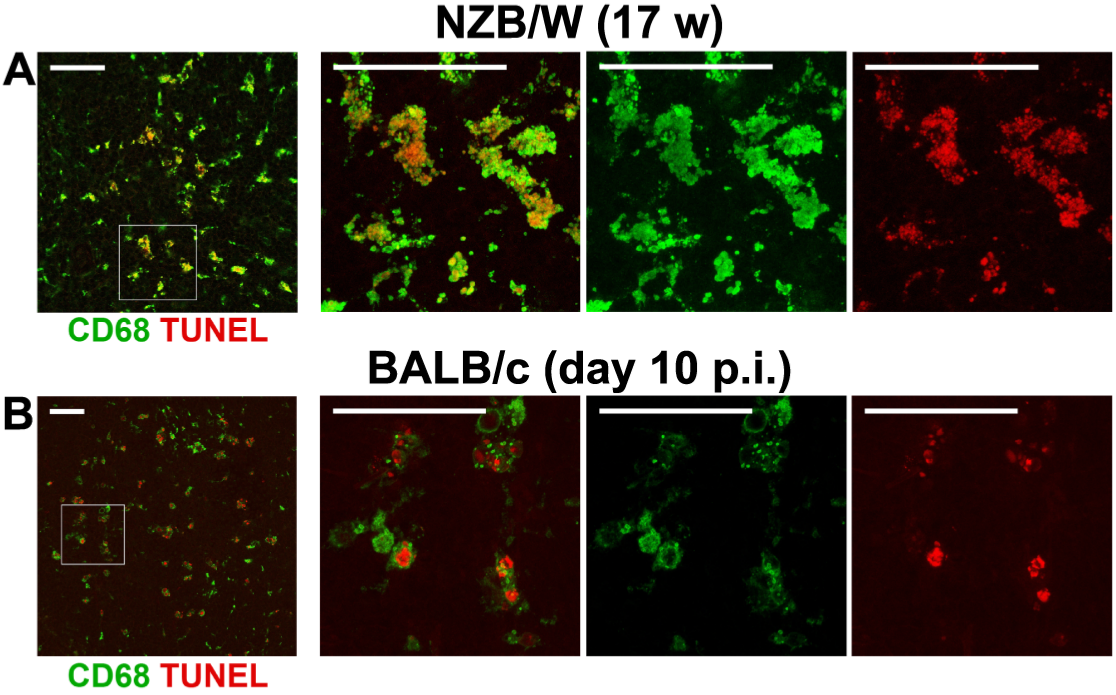

Figure 5.23: Aberrant morphology of GC Mϕ in NZB/W mice. Illustrated are stainings of GC Mϕ (mAb CD68) and apoptotic cells (TUNEL) of a 17 weeks old unimmunized NZB/W mouse (A) and an immunized BALB/c mouse at day 10 after immunization (B). Whereas GC Mϕ of NZB/W and immunized BALB/c mice look rather similar in xy-scans at lower magnification (*left panel*), maximum projections of z-scans at higher magnification reveal striking differences regarding the morphology of GC Mϕ (*middle left panel*). GC Mϕ of NZB/W show clear signs of disintegration of the cell membrane (*middle right panel*) accompanied by pronounced accumulation of loads of apoptotic nuclear debris (*right panel*). Scale bar 50 μm.

5.4.2 Decreased frequencies of follicular Mϕ in NZB/W mice due to disease progression

Decomposing "dying" GC Mϕ do not emerge occasionally but rather habitually in NZB/W mice. Assuming progressional death of GC Mϕ in NZB/W mice, the tightly regulated equilibrium between follicular Mϕ and B cells should get affected by the time. In fine, the frequency of Mϕ in B cell zones of NZB/W mice would drop along disease progression. To verify this hypothesis, the frequency of Mϕ within B cell zones of NZB/W mice of different age was recorded and compared to frequencies obtained for parental NZB and naive BALB/c mice.
Likewise BALB/c, NZB/W and parental NZB mice show stringent inner-section correlation of numbers of Mϕ and cross-sectional B cell zone size ($R^2 \geq 0.9$) (Figure 5.24). Moreover, the mean frequency of Mϕ of young 6-8 weeks old NZB/W mice ($35 \pm 3/25{,}000\ \mu m^2$) is the same as established for naive BALB/c mice ($35 \pm 6/25{,}000\ \mu m^2$), once more emphasizing the tight superordinate regulation of numbers of Mϕ by the overall B cell zone size (Section 5.2.4). In fact, the frequency of Mϕ decreases along disease progression, as it is significantly reduced of about one third in 14 weeks old compared to 6-8 weeks old NZB/W mice ($21 \pm 1/25{,}000\ \mu m^2$) (Figure 5.25, A); ($p=0.0001$, independent samples t-test). The decline in numbers of Mϕ becomes even more striking by opposing the distributions of frequencies of Mϕ within B cell zones. Whereas the distribution of frequencies of 6-8 weeks old NZB/W mice is indistinguishable compared to naive BALB/c mice, it radically shifts towards lower frequencies in 14 weeks old NZB/W mice (Figure 5.25, B). Recapitulating, the herein described results indicate an acquired imbalance of frequencies of follicular Mϕ and B cells due to disease progression in lupus-prone NZB/W mice.

In addition, the frequencies of Mϕ within B cell zones of 6-8 weeks old parental NZB ($29 \pm 3/25{,}000\ \mu m^2$) turn out to be slightly decreased compared to naive BALB/c mice ($35 \pm 6/25{,}000\ \mu m^2$) (Figure 5.25). NZB mice are reported to develop autoimmunity, but of a different kind and at a different age compared to NZB/W mice [151]. If impairment of the follicular Mϕ compartment also contributes to disease progression in NZB mice has to be elucidated in follow-up experiments.

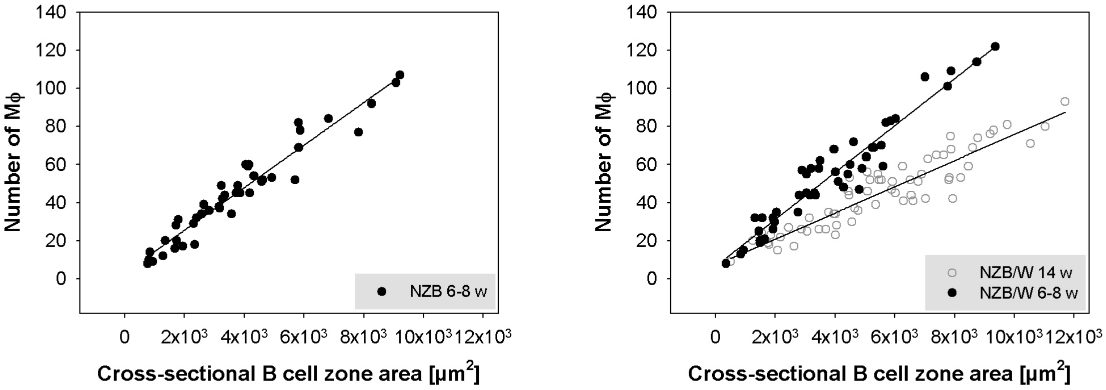

Figure 5.24: Inner-section correlation of numbers of GC Mϕ and cross-sectional B cell zone size in NZB and NZB/W mice. Data is representative of each one spleen section derived from 6-8 weeks old NZB, NZB/W and 14 weeks old NZB/W. The cross-sectional size of B cell zones is given as cross-sectional area. Correlations are rated applying simple linear regression. Regression lines and squared correlation coefficients (R^2) are specified for each scatter plot.

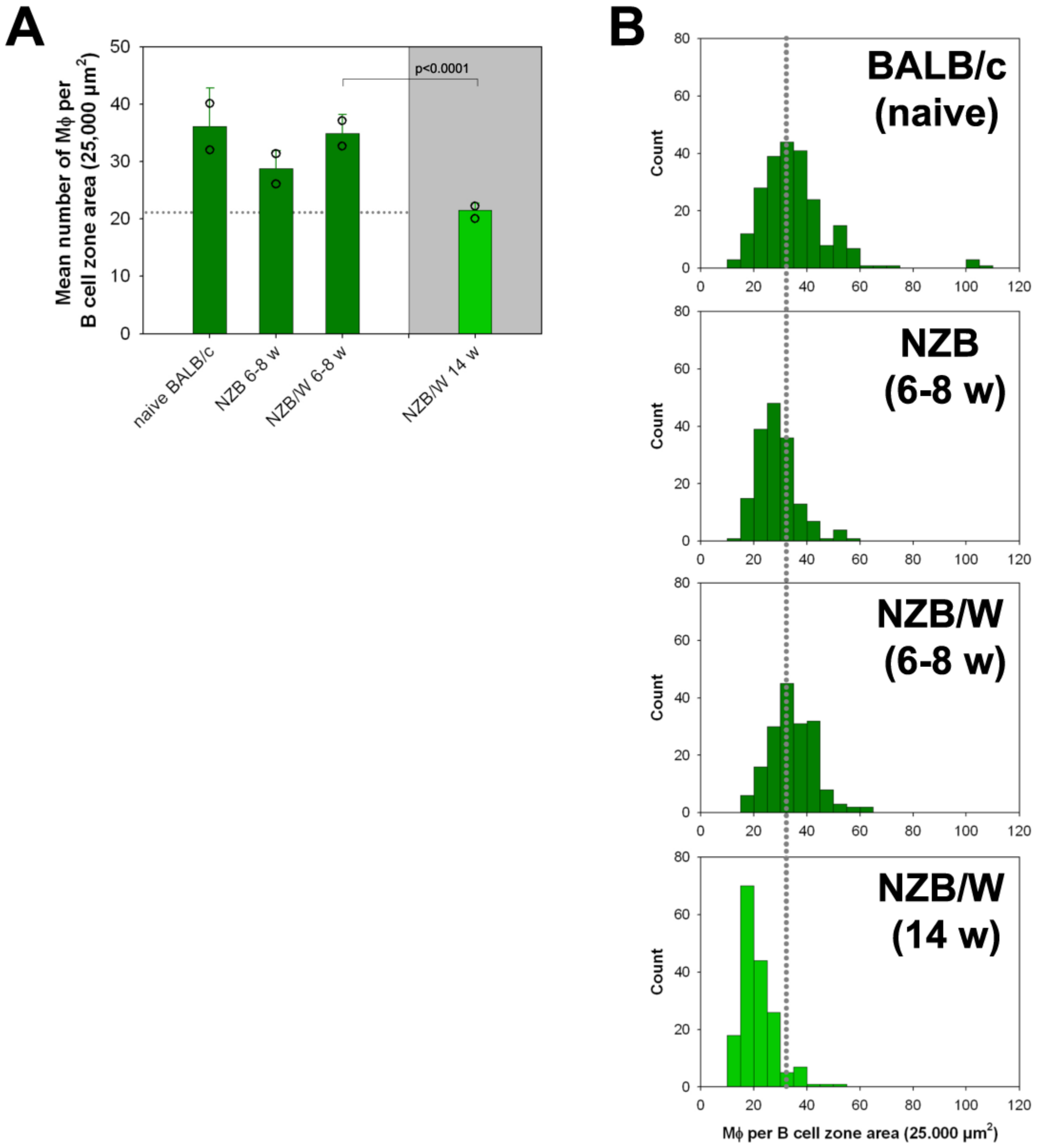

Figure 5.25: Age-dependent decline in numbers of follicular Mϕ in NZB/W. The number of Mϕ per B cell zone area was determined as described previously (Section 5.2.4). (A) Illustration of mean frequencies of Mϕ within B cell zones of in each case two naive BALB/c, 6-8 weeks old parental NZB as well as 6-8 and 14 weeks old NZB/W mice. Data is representative of two evaluated spleen sections per mouse, values of individual mice are depicted as open circles. The frequency of Mϕ of 6-8 weeks old NZB/W is in par with steady frequencies reported for naive and immunized BALB/c mice, but explicitly drops in 14 weeks old NZB/W mice. Significant differences as calculated by Student's *t* test are indicated. (B) Striking shift towards lower frequencies of Mϕ within B cell zones of NZB/W mice due to disease progression. Displayed are the distributions of frequencies of Mϕ within B cell zones of the same mice as depicted in (A). Data is representative of all sections analyzed per mouse strain and time point.

5.5 Discussion

5.5.1 Kinetics of GC T cells

GC T cells are thought to represent an unique subset of antigen specific T cells [152], also referred to as follicular helper T cells [41, 42, 27, 153], that plays a pivotal role in affinity maturation, in that it is linked to proliferation, differentiation and in particular memory formation [141, 142, 154, 143]. Only recently, *in vivo* imaging of GC provided evidence that GC T cells may also drive the selection of high affinity GC B cells [100]. Studies performed in this thesis for the first time address the kinetics of this unique subset during the primary immune response.

In contrast to macrophages, T cells first selectively colonize B cell follicles upon antigenic challenge but are practically absent in primary follicles of naive mice (Figure 5.6). Although assessment of proliferating GC T cells is hampered by their generally low frequency within the GC cell population ($\leq$1%), the obtained results indicate that proliferation of GC T cells is certainly not governed by the size of GC or one of its compartments (Figure 5.3), but rather by the stage or age of the immune response, respectively (Section 5.1.2). Marked GC T cell proliferation is restricted to a short period of time following the migration and entry of T cells into follicular niches, reaching its peak at day 6 (17 % of GC T cells are proliferating, Figure 5.7, B). Thereafter, proliferation of T cells is straight off reduced to a marginal level (Figure 5.7, B). Together with the finding that initial colonization of B cell follicles by T cells is not directed by B cells but rather controlled by dendritic cells (DC) [155], these results suggest that the presence of T cells within the early phase of GC formation is not soleley for the purpose of providing B cell help but may also indicate regular T cell differentiation pathways as for instance clonal expansion [156, 157] and formation of CD4 memory [158, 159]. Given the fact that the early phase of GC formation also takes place in the absence of T cells [113, 37], B cells and T cells are likely to act independently at this stage. Moreover, this early stage of initial GC formation may serve to procreate pools of both, B cells and T cells whose interaction becomes a prerequisite for affinity maturation only afterwards. In the light of the revised model of affinity maturation (Section 4.4.4, Figure 4.18), it is tempting to speculate that the very interaction involves a shift from local to global acting processes in that it triggers mobilization of both, GC B cells and T cells, in which the latter are already shown to extensively travel among white pulp regions when GC are fully established [153].

After the initial phase of formation of GC, proliferating T cells are not absent but rather sporadically detected within individual GC, in which the actual numbers are highly variable for GC of equivalent cross-sectional size (Figure 5.4). Whether this finding attributes to the ongoing new formation of GC (Section 4.3.2, Figure 4.11) and thus reflects the age distribution of GC cannot be gathered from the present data.

The kinetics of total numbers of GC T cells follows the time course of the overall size kinetics of GC peaking at day 8 after antigenic challenge, as do the numbers of GC T cells within dark and light zone of GC (Figure 5.5). Consistent to previous reports, the numbers of GC T cells are always higher for the FDC rich compartment of GC, indicating preferential localization of GC T cells in the light zone [100, 154, 147]. GC T cells constitute a minor fraction of the GC cell population (10-16%) (Figure 5.7, A), although recorded frequencies are slightly increased compared to previous reports (5-10%) [155, 153], which most probably attributes to differences in studied mouse models as well as antibodies used for detection of GC T cells. Notably, the variable numbers of GC T cells among individual GC turn out to reflect the underlying size distribution of GC, in that numbers are strictly governed by the cross-sectional GC size (Figure 5.2). The strong correlation of numbers of GC T cells with GC size further suggests that T cell retention within GC is regulated by factors intrinsic to GC, most likely delivered by B cells or stromal cells such as FDC and DC [155]. Nevertheless, the observations that T cells are often found in close proximity to macrophages (not shown) and also carry apoptotic blebs [100], may indicate a complex feedback system of GC cell homeostasis including GC B cells, T cells and macrophages. With regard to the selection model proposed by Allen et al. [100], the take over from macrophage derived apoptotic material to T cells may not only drive selection by limiting T cell help but may concomitantly promote GC B cell proliferation by effecting the suggested regulatory propensity of macrophages (Section 5.3.5).

5.5.2 GC Mϕ and uptake of apoptotic cells

The presence of characteristic macrophages within GC is recognized for about 125 years and was already described when GC were first discovered by Flemming [28]. Early light and electron microscopical studies revealed that these macrophages contain many phagocytozed lymphocytes in their cytoplasm and thus specified them as tingible body macrophages (TBM) [28, 160, 43]. Due to the observation that the definition of TBM does not account for the collectivity, but rather describes a marked subset of large macrophages (Figure 5.8, 5.17), macrophages within follicles or GC are referred to as follicular and GC macrophages, respectively, in the current thesis. The analysis of (GC) macrophages challenge the prevailing view, in that their role turns out to be not restricted to sole removal of apoptotic cells but is likely to also involve induction, homeostasis and regulation of GC. The study of uptake of apoptotic cells within GC indicates that selection of BC B cells is not confined to the the light zone but is likely to occur also in the dark zone of GC. Moreover, it lends support to asynchronous growth and ongoing seeding of GC.

Presence and functions of Mϕ within B cell follicles

In striking contrast to the work of Smith et al. [45], macrophages are shown not to require antigenic stimulation to colonize follicles but already represent a constituent cell population of B cell zones of naive mice (Figure 5.11), in which their actual number strictly correlates with the underlying size of the B cell zone (35 ± 6 Mϕ/25.000 μm^2 or 9 ± 1 Mϕ/100 B cells) (Figure 5.12). The differences between Smith et al. [45] and the results presented here, attribute to the antibodies used for detection of follicular macrophages (mAb Mac-2, mAb CD68) and underline the uniqueness and adaptability of this particular subset of macrophages. Since the macrophage antigen Mac-2 has been reported to be expressed by mature macrophages [161], its absence from macrophages of primary follicles [45] strongly suggests maturation or differentiation of follicular macrophages upon antigenic stimulation. Whether this maturation attributes to GC formation *per se* or intense uptake of apoptotic cells within GC remains to be rigorously addressed, yet the latter is supported by the propensity of mAb Mac-2 to stain very large (TBM-like) macrophages [45]. Noteworthy, the Mac-2 staining pattern is resembled by a further mature macrophage marker, MOMA-2 (not shown). Besides their unknown ontogeny [162], there is still controversy whether GC macrophages are resident [163] or migratory macrophages [45], in which the former is recently encouraged by *in vivo* imaging of GC. Nevertheless, the abundance of phenotypically indifferent macrophages within T and B zones of primary follicles (Figure 5.11) suggest a common origin of these macrophages, thereby favoring ongoing replenishment of GC macrophages by macrophages from the T zone. The presence of macrophages in B zones of naive mice further indicates that they may be involved in or even be required for the induction of GC responses. However, albeit GC macrophages were reported to possess two requisite characteristics [44, 164], they are rather unlikely to contribute to the induction of GC by functioning as critical antigen presenting cells [46].

As a hallmark, the strict correlation of numbers of macrophages in B cell zones with the size of the B cell zone is even preserved upon antigenic challenge and germinal center development (30 ± 3 Mϕ/25,000 μm^2 or 8 ± 1 Mϕ/100 B cells) (Figure 5.12). This tight balance most likely reflects an integral homeostatic interdependency of follicular B cells and macrophages. Peripheral B cell homeostasis was recently shown to primarily rely on B cell activation factor (BAFF) production by radiation-resistant stromal cells [165]. Nevertheless, macrophages have been shown to produce BAFF *in vitro* [166, 167, 168] and reconstitution of BAFF-deficient mice with wild type bone marrow containing macrophages was proven to be sufficient to induce maturation of some newly formed B cells to mature follicular B cells [165]. The close proximity of macrophages and B cells further suggests that locally high concentrations of macrophage-derived BAFF may affect the homeostasis of B cell zones by mediating B cell survival.

The importance of the 8:100 macrophage to B cell ratio for macrophage-B cell interactions within B cell follicles is withal supported in that young NZB/W show the same ratio (Figure 5.25). Noteworthy, the imbalance of this ratio (5:100) in older NZB/W mice (Figure 5.25) coincides with the progression of autoimmune disease in these mice, characterized by spontaneous formation of GC and elevated autoantibody titers [169, 149, 170].

GC Mϕ and uptake of apoptotic cells indicate that selection takes place in the dark zone and light zone of GC

As expected, the number of GC macrophages turns out to be strictly dependent on the underlying size of GC (Figure 5.9), as indicated by marked inner-section correlations and the almost invariable 1:10 GC macrophage to B cell ratio (Figure 5.10, B). The striking difference of the macrophage to B cell ratio reported here and the one previously assessed by Smith et al. [45] (1:350) attributes to the incomplete coverage of GC macrophages by means of Mac-2 reactivity, as discussed above.

The time course of total numbers of GC macrophages follows the overall size kinetics of GC and macrophages are found evenly distributed within both GC compartments throughout the response (Figure 5.10, A). Mentionably, GC macrophages are often found at both, the transition of dark and light zone and the very the basal part of GC adjoining to the T cell zone (Figure 5.8). Nevertheless, costaining of apoptotic cells reveals that cell death occurs throughout GC, showing no preferential bias towards the very macrophages or either of the two GC compartments (Figure 5.13, 5.18). Taken together, this results strongly suggest that selection of GC B cells is not restricted to the FDC rich light zone as generally believed [147], but does also take place in the dark zone of GC. Selection of GC B cells within the dark zone is also supported by sequence analysis of single GC performed by Camacho [118], that revealed low inter- and intraclonal diversity of GC B cells within the dark zone. However, because the irreversible steps of apoptosis, namely caspase-3 activation and DNA-fragmentation, first occur only when GC B cells are attached to macrophages [171], it cannot be excluded that the decisive death signal is delivered exclusively within the light zone of GC.

Although GC are detectable as early as day 4 after antigenic challenge, GC B cell apoptosis is hardly detectable until day 6, but afterwards phenomenally increases up to day 8-10 (Figure 5.16, A), causing apoptotic cells to henceforth become a major population of GC as reflected by a 1:5 apoptotic nuclei to GC B cell ratio (Figure 5.16, B, Figure 5.17). The skyrocketing time course of cell death most probably reflects the transition of GC from an initial formation phase to a "function phase", in which the transition is characterized by massive cell death of GC B cells due to the onset of SHM between days 7 to 8 [121] and subsequent failures in selection.

Evaluation of cell death within GC supports asynchronous GC growth and ongoing seeding of GC

Unanticipated, cross-sectional evaluation of uptake of apoptotic cells within GC supports the proposition of asynchronous GC growth and ongoing seeding of GC (Section 4.3.2). In striking contrast to GC T cells (Figure 5.2) and GC macrophages (Figure 5.9), the number of apoptotic nuclei per GC obviously does not well correlate with the underlying size of GC (Figures 5.14-5.15, A), as GC of equivalent size are constantly shown to comprise arbitrary numbers of apoptotic nuclei within a broad range (e.g. 0-100), (Figure 5.15, B). Since the observed disparity in numbers of apoptotic nuclei is also well reflected on the level of macrophage size (Figure 5.18) it is considered a relevant finding, most likely reflecting the coexistence of GC of different age or volume, respectively. Indeed, quantification of the disparity by grading GC into 4 classes by means of their mean size of macrophages (referred to as macrophage size distribution) (Section 5.3.4, Figures 5.18-5.19) leads to a picture that resembles the kinetics of the volume distribution of GC (Figure 4.17).

Regulation of the GC reaction by shifts in GC Mϕ phenotypes

As discussed above, the analysis of GC macrophages performed by [45] was incomplete in that they only detected a particular subpopulation, namely Mac-2$^+$ GC macrophages which are typically large due to multiple uptake of apoptotic cells and follow the traditional definition of TBM [28, 160, 43]. The data presented in this thesis, however, show that the actual number of GC macrophages is much higher, and thereby indicate the existence of at least one more subpopulation of GC macrophages, that are Mac-2$^-$ and smaller in size. Indeed, this is a finding of importance, since shifts in phenotypes of macrophages subpopulations (Mac-1, Mac-2, Mac-3) are associated with immunosuppressive activity [172]. In this context, macrophages expressing the Mac-2 antigen are suggested to possess suppressive activity due to the production of prostaglandin E2 (PGE2), that can be counteracted by Mac-2$^-$ macrophages [172, 173]. Prostaglandins, in particular PGE2, are capable to repress lymphokine production by T cells and are also believed to mediate local suppressive activity directly on B cells [174, 175]. The presence of Mac-2$^+$ and Mac-2$^-$ macrophages within GC and the observation that Mac-2$^+$ GC macrophages (TBM) are actually rich in PGE2 [46], therefore gave rise to the hypothesis that shifts between macrophage phenotypes may apply for the homeostasis, longevity or intensity of the GC reaction. The hypothesis was approached by a mathematical model (Section 5.3.5, Figure 5.20) that has to be considered rather phenomenologically, since several parameter values are not yet established experimentally and were therefore tuned within reasonable limits to achieve a realistic behavior of the simulation (Table 5.7). The central proposition of the model is that the phenotype of each macrophage is specified by the number of engulfed apoptotic cells and thereby by its size at a given time, in which large macrophages (TBM) act suppressive by repressing proliferation of GC B cells. The model succeeded in reproducing major characteristics of the GC reaction, such as recorded mean time courses of GC B cells, GC macrophages and uptake of apoptotic cells (Figure 5.21-5.22). Noteworthy, it also fairly predicted the experimentally recorded macrophage size distribution (Figure 5.22). Taken together, the model provides strong evidence that the shift between macrophage phenotypes or sizes, respectively, may indeed account for a central regulatory element of GC reactions.

5.5.3 An acquired imbalance of follicular Mϕ and B cells contributes to progression of autoimmunity in NZB/W mice

The literature provides profound evidence for a strong link between impaired clearance of apoptotic cells within GC and the pathogenesis of autoimmunity in mice [85, 86, 176, 177] and men [83, 178, 82, 87, 179]. According to an elegant model proposed by Gaipl et al. [82], that has become the general conception, clearing defects of macrophages within GC lead to the accumulation of apoptotic cells that undergo secondary necrosis and thereby release autoantigens that afterwards become accessible due to binding to FDC. In the following, presentation of autoantigens on FDCs, promotes positive selection of autoreactive B cells that may exit GC and become autoantibody secreting plasma cells. Nevertheless, the nature of the triggering clearance defect remains ambiguous, in that it is not clear whether it attributes to an intrinsic/acquired macrophage defect or is serum dependent, i.e. associated with decreased levels of complement [180, 181, 85, 86, 182]. Based on the analysis of macrophages from different SLE patients Gaipl et al. [82] even suggest heterogeneous clearance defects.

However, the results of the current thesis indicate that the disease progression in lupus-prone NZB/W mice not necessarily implies a "qualitative" clearance defect of macrophages, but rather correlates with an acquired "quantitative" imbalance of follicular macrophages and B cells due to marked macrophage death (Figures 5.23, 5.25). These findings further lead to the proposal of a revised model for the pathogenesis of autoantibodies in NZB/W mice, that is illustrated in Figure 5.26. In this scenario, an increased apoptotic load within GC, most likely due to hyperactive B cells [183, 184, 185] and/or accelerated apoptosis rates of NZB/W spleen cells [186], jeopardizes the ability of local macrophages to efficiently clear cell corpses. The high apoptotic load involves increased phagocytic activity of local macrophages, that are thus subjected to sustained stress. If the apoptotic load finally exceeds the local capacity of macrophages for clearance, macrophages collapse and undergo cell death, most probably in form of apoptosis (Figures 5.23). Phagocytosis-induced apoptosis of macrophages has already been shown to occur in the course of intracellular destruction of bacteria and is assumed to constitute a mechanism for the disposal of terminally differentiated macrophages [187]. As discussed before, uptake and digestion of apoptotic cells within GC most likely involves differentiation of macrophages (Section 5.5.2), which lends support to the proposition that phagocytosis-induced apoptosis of macrophages may represent a general phenomenon during GC reactions. Whereas such macrophage death may be modest and balanced by attraction of new macrophages under normal "healthy" conditions, the sustained high apoptotic load within GC of NZB/W mice is likely to prevent compensation of macrophage death, thereby causing the experimentally observed imbalance of follicular macrophages and B cells (Figure 5.25). Noteworthy, unbalanced macrophage death within GC creates a vicious circle scenario in that dropping numbers of macrophages act as an feedback amplifier by further increasing the apoptotic load.

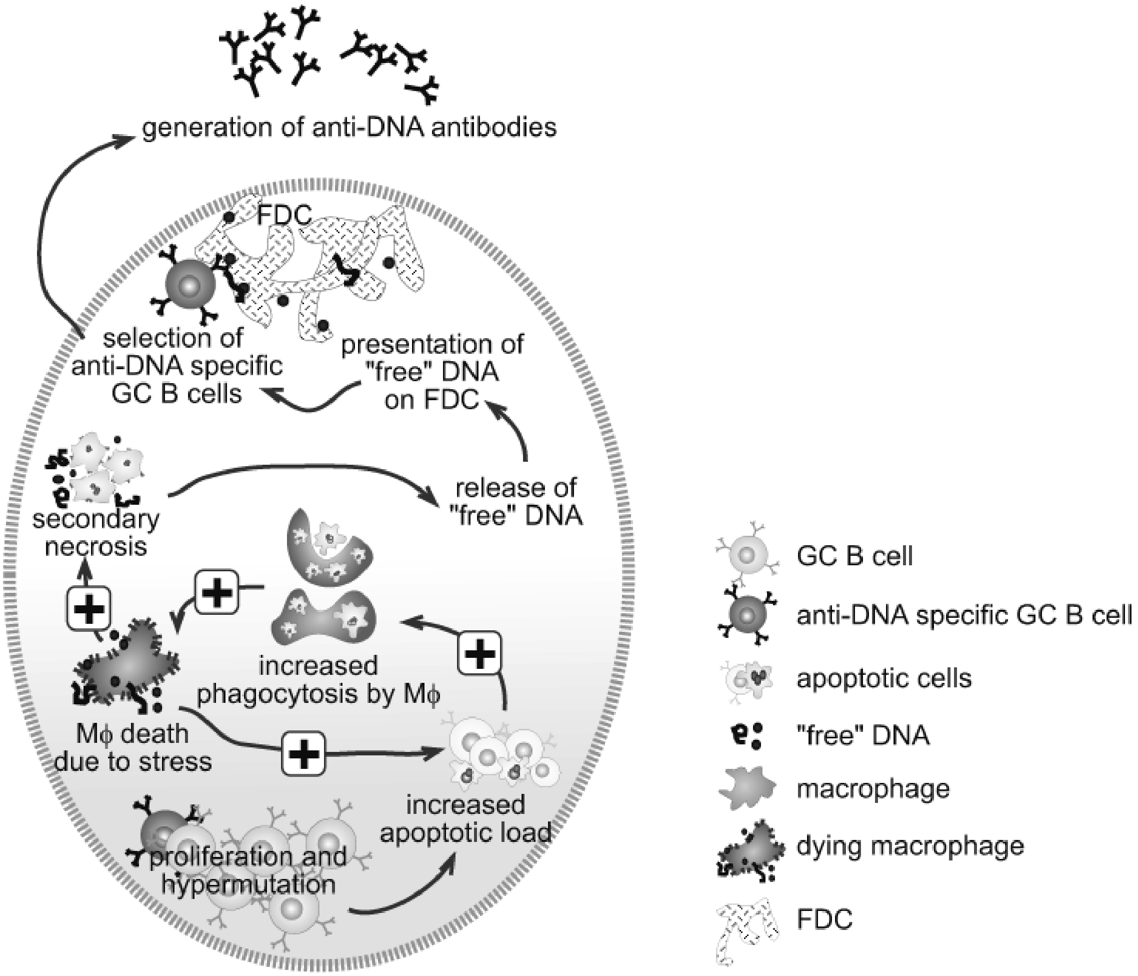

Figure 5.26: Model for the pathogenesis of autoantibodies in GC of NZB/W mice. Hyperactivity and/or an accelerated apoptosis rate of GC B cells causes an increased apoptotic load within GC of NZB/W mice. The high apoptotic load effects increased phagocytic activity of local macrophages that are thereby subjected to sustained stress. When the apoptotic load exceeds the local capacity of macrophages for clearance, macrophages collapse and undergo cell death. In the following, unbalanced macrophage death acts as an feedback amplifier in that it further increases the apoptotic load within GC. [1]Apoptotic cells accumulate, enter the state of secondary necrosis and release modified autoantigens, that become accessible by presentation on FDC. Autoreactive GC B cells are positively selected due to engagement of their BCR and autoantigen bound to FDC. Finally, positively selected autoreactive GC B cells exit GC and become autoantibody secreting plasma cells. [1]This part of the model is adopted from Gaipl et al. [82].

Comparison of B cell receptor light chain sequences derived from living and apoptotic germinal center B cells

Chapter 6

Comparison of B cell receptor light chain sequences derived from living and apoptotic germinal center B cells

Peripheral selection within GC is generally believed to occur in a B cell receptor dependent fashion. The fate of individual GC B cells is assumed to rely on their antigen binding properties and competence to interact with accessory cells, including FDC and GC T cells. Consequently, the primary sequence of B cell receptor variable regions (BCR V region) should act as an indicator of survival fate of GC B cells. To test this hypothesis, B cell receptor sequences derived from either living or apoptotic GC B cells were compared to each other. Since the comparison was performed at different time points after immunization, this type of analysis further aimed at revealing dynamical aspects of selection.

6.1 Strategy for identification and recovery of living and apoptotic GC B cells

Prior to actual isolation, an approach strategy for identification of living and dying GC B cells was mapped out. Whereas living GC B cells are easily identified as B220$^+$ PNA^{high} cells among viable lymphocytes [96] (example shown in Figure 6.1), detection of dying GC B cells is much more complex. At first, dying GC B cells were assessed applying Annexin V (AnV) as primary cell death marker. Albeit AnV has been reported to permit reproducible identification of early apoptotic GC B cells (B220$^+$ PNA^{high} AnV$^+$ PI$^-$) [188, 189], this approach was subsequently rejected for the following reasons: i) low frequency of early apoptotic GC B cells ($\sim$ 5% of GC B cells and $\sim$ 0.2% of total lymphocytes, respectively, data not shown), ii) ambiguous origin, as AnV reactivity is not neccessarily due to the *in situ* GC microenvironment but is as well likely to be acquired during cell preparation.
Since direct detection of GC B cells that are unequivocally undergoing apoptosis is currently unrealizable, the initial strategy was revised as to indirect recovery of

rather late apoptotic GC B cells from macrophages. Therefore, splenic macrophages were stained with an antibody to CD68 (macrosialin) and subsequently analyzed by flow cytometry. As macrosialin is only exposed at low levels on the cell surface but is abundant within cells, extracellular staining of CD68 was compared to intracellular staining following permeabilization of cells using saponin. Such analysis reveals that permeabilization of cells and intracellular staining of CD68 explicitly improve the identification of splenic macrophages, as regards recorded frequencies and separation of stained cells (Figure 6.2). However, CD68 staining results in the detection of the entirety of splenic macrophages, including red pulp and marginal zone macrophages. As in particular red pulp macrophages are not involved in the clearance of apoptotic GC B cells but are rather likely to engulf dying plasma cells, additional macrophage markers were screened in order to further restrict the macrophage population identified by CD68. Immunohistological staining reveals that, whereas the macrophage marker F4/80 is ubiquitously expressed by red pulp macrophages, macrophages of the white pulp completely lack F4/80 expression (Figure 6.3). Therefore, additional staining of macrophages with an antibody to F4/80 allows the identification of the subset of macrophages restricted to the splenic white pulp (CD68$^+$ F4/80$^-$), in the following referred to as follicular macrophages (example shown in Figure 6.4).

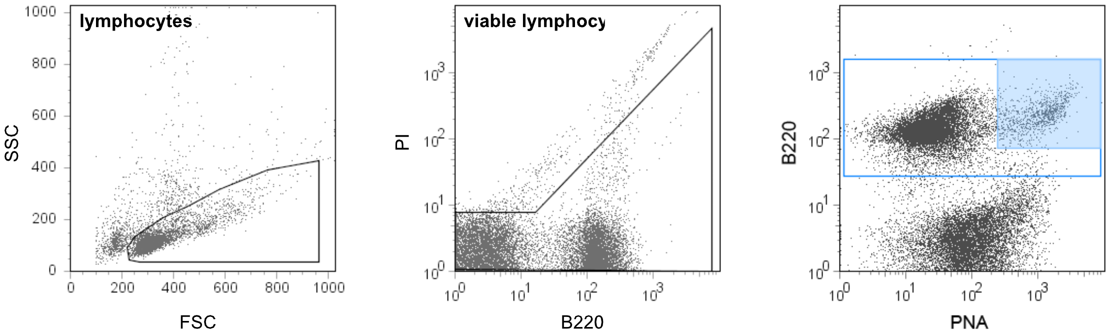

Figure 6.1: Identification of GC B cells by flow cytometry. Splenocytes from phOx-CSA challenged BALB/c were isolated 12 days after immunization, stained with B220:PE and PNA:FITC and were subsequently analyzed by flow cytometry. Splenocytes are gated first on lymphocytes (*left panel*) and then on viable cells (PI$^-$) (*middle panel*). GC B cells are identified as the B220$^+$ PNA^{high} subpopulation (blue tinted box) of total B cells (blue box, *right panel*). Flow cytometry profiles are given as dot plots, numbers within the dot plot specify the frequencies [%] of B cells and GC B cells within viable lymphocytes, respectively.

6.2 Isolation of GC B cells and follicular Mϕ

For the comparative analysis of BCR sequences of living and apoptotic GC B cells, both GC B cell and follicular macrophage populations were collected at days 8 and 12 following phOx-CSA challenge using a FACSAria cell sorter. To ensure recovery of sufficient numbers of GC B cells and follicular macrophages, splenocytes from two immunized mice were pooled for each time point. In order to prevent continual uptake of apoptotic B cells by macrophages during cell handling, B cells and macro-

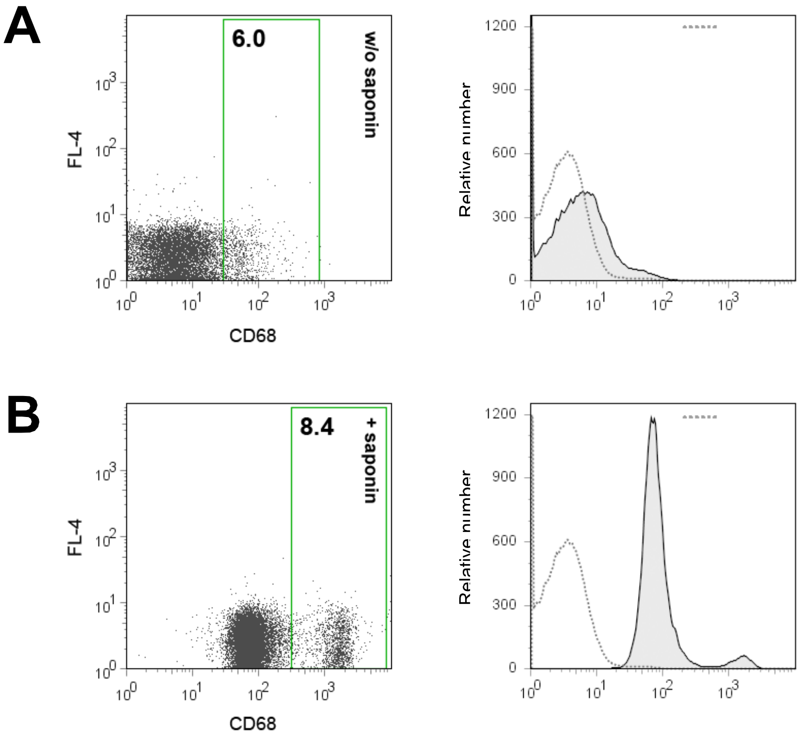

Figure 6.2: Implications of intracellular staining of CD68. As the CD68 transmembrane protein (macrosialin) is predominantly located within the cells, permeabilization of cells improves staining in respect of recorded frequencies and separation of stained cells. (A) Extracellular staining of CD68 (w/o saponin). (B) Intracellular staining of CD68 after saponin treatment. Flow cytometry profiles are given as dot plots (*left panel*) and histograms (*right panel*). In histograms, filled curves illustrate CD68 detection, dotted curves show the isotype control. Data illustrates the analysis of splenocytes (gated on lymphocytes) of a representative immunized BALB/c at day 12 after immunization.

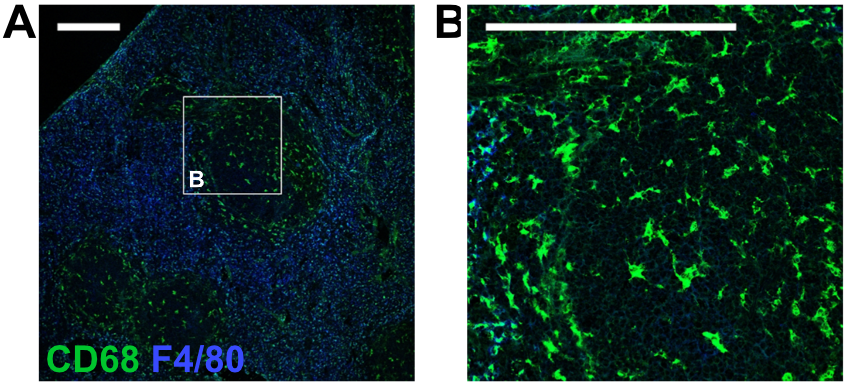

Figure 6.3: Follicular macrophages are distinguished from splenic macrophages by absence of the macrophage marker F4/80. (A) Double immunofluorescence labeling of splenic macrophages reveals colocalization of CD68 (green) and F4/80 (blue) staining regarding red pulp macrophages, whereas F4/80 expression is absent from macrophages located in T and B cell zones of the white pulp. (B) Higher magnification view of the detail boxed in (A). Image is representative of a stained spleen section at day 10 after immunization. Scale bar 250 μm.

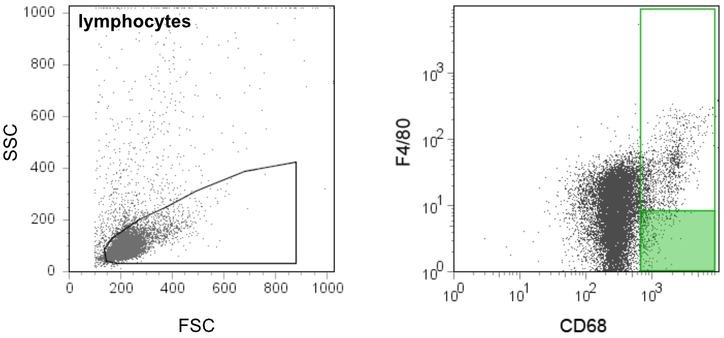

Figure 6.4: Identification of follicular macrophages by flow cytometry. Splenocytes from phOx-CSA challenged BALB/c were isolated 12 days after immunization, stained with F4/80:Cy5 and CD68:A488 and were subsequently analyzed by flow cytometry. Splenocytes are gated on lymphocytes (*left panel*) and follicular macrophages are identified as the CD68$^+$ F4/80$^-$ subpopulation (green tinted box) of total splenic macrophages (green box, *right panel*). Flow cytometry profiles are given as dot plots, numbers within the dot plot specify the frequency [%] of total splenic macrophages and follicular macrophages (fol. Mϕ), respectively, within the lymphocyte gate.

phages were henceforth rapidly separated by magnetic negative depletion of B cells from spleen cell suspensions. Subsequently, GC B cells and follicular macrophages were identified within the B cell fraction and B cell depleted fraction, respectively (exemplary depicted for day 12 after immunization in Figure 6.5, A and B). The initial frequency of B cells within spleen cell suspensions was about 50% at all sampled time points. After MACS seperation, B cells were enriched up to 96% in the B cell fraction and the frequency of B220$^+$ PNA^{high} GC B cells for each time point was as follows: day 8 (7.8%), day 12 (7.7%) (Figure 6.5, A). By contrast, B cells and thus also GC B cells were virtually absent from the B cell depleted fraction (Figure 6.5, B).

CD68$^+$ macrophages constituted of about 6 to 8% of total splenocytes at all sampled time points. As a consequence of passive enrichment due to B cell depletion their frequency increased up 11%, whereas CD68$^+$ F4/80$^-$ follicular macrophages accounted for about 1.5 to 7% of splenocytes within the B cell depleted fraction (Figure 6.5, B). Nevertheless, macrophages were not strictly confined to the B cell depleted fraction but were also detected with minor frequencies within the B cell enriched fraction (Figure 6.5, A). Macrophages within the B cell fraction account for CD68$^+$ B220$^+$ double positive macrophages that gained B220 reactivity due to partially engulfed B cells. However, the depletion of CD68$^+$ B220$^+$ double positive macrophages during MACS seperation does not interfere with the strategy for recovery of apoptotic cells. To ensure the isolation of B cells that are unequivocally undergoing apoptosis, sorting was restricted to follicular macrophages that stain negative for extracellular B cell markers (B220$^-$ F4/80$^-$ CD68$^+$). The number of collected cells was about 10^6 in case of GC B cell samples and 10^5 for the samples of follicular macrophages, respectively.

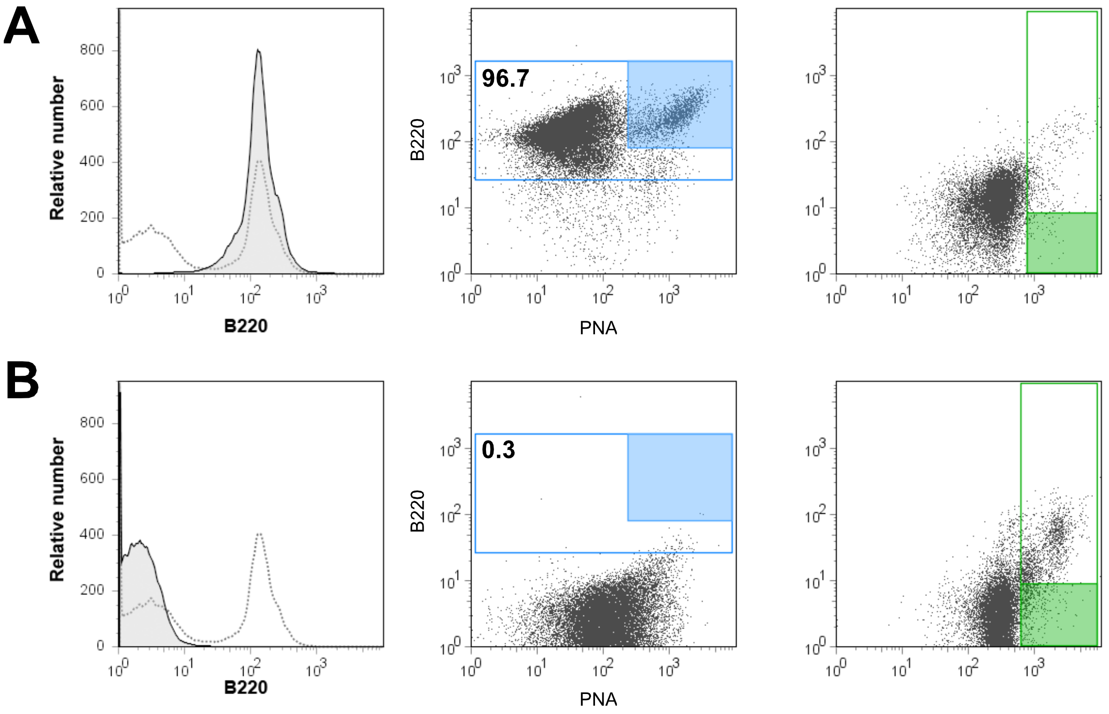

Figure 6.5: Isolation of GC B cells and follicular Mϕ exemplarily illustrated for phOx-CSA challenged BALB/c following day 12 after immunization. First, B cells and macrophages were separated by magnetic negative depletion of B cells from spleen cell suspensions. (A) Identification of GC B cells and splenic macrophages within the B cell enriched fraction. (B) Identification of follicular macrophages in the B cell depleted fraction. Flow cytometry profiles are given as histograms or dot plots. Numbers within dot plots specify the frequencies [%] of the respective cell populations. In histograms, the dotted and filled curves indicate B220 detection before and after MACS seperation, respectively.

6.3 IgL repertoire analysis of live and phagocytozed B cell fractions

GC B cells and follicular macrophages were sorted from spleens of phOx-CSA immunized BALB/c mice at days 8 and 12 using the gating scheme shown in Figure 6.5. IgL chains of live and phagocytozed B cells were amplified by RT-PCR from total RNA of sorted populations using a primer mix covering the whole spectrum of κ and λ light chain gene families (Section 3.10.2). Transcripts of the VκOx1 gene (IGKV4-59 according to the new IMGT nomenclature), that dominates the phOx response, were amplified in separate RT-PCR reactions using gene specific primers (Section 3.10.2). For identification of Vκ and Jκ genes as well as mutation analysis, amplificates were directly sequenced after cloning and compared against the IMGT database (http://imgt.cines.fr/IMGT_vquest/vquest) [90]. Clones that were identical on the cDNA level were counted once. Potential clonal relatedness of sequences was determined by means of shared V_L and J_L gene segment use and identical VJ joins (LCDR3s). Rather occasionally, out of frame LCDR3s are observed among both, overall and phOx specific IgL sequences of phagocytozed B cell fractions. These out of frame LCDR3s are unlikely to represent *a priori* unproductive IgL rearrangements, but rather seem to be a byproduct of somatic hypermutation (deletion/insertion) [190], since i) amplifications were performed on RNA preparations, in which a priori unproductive IgL rearrangements are unlikely to be transcribed into mRNA, ii) the appearance of such out of frame LCDR3s correlates with the increasing average mutation frequency from day 8 to 12 after immunization, iii) the belonging V genes show additional mutations (ranging from 2 to 7). On this accounts, phOx specific sequences featuring out of frame LCDR3s are included in the analyses, but are specially indicated ($\oslash$) in sequence alignments.

6.3.1 Equivalent V gene family and J gene segment use among IgL of live and phagocytozed B cell fractions

IgL chain diversity in the mouse mainly attributes to the Igκ locus in that the observed Igκ:Igλ ratio of B cells is as high as 95:5 [191]. Whereas the Igκ locus comprises 91 functional Vκ genes belonging to 19 subgroups (V_L gene families) [90], the Igλ locus is thought to include only three functional Vλ genes. Although the murine Igκ locus is well explored, data regarding the adult functional repertoire of mice is both fragmentary and contradictory. Nevertheless, Vκ gene family use is considered to be non-random, showing predominance of the Vκ families IGKV1, IGKV4 and IGKV6 [192].

The frequencies of V_L gene family expression in live and phagocytozed B cell fractions were quantitatively compared using the χ^2 test. For both time points analyzed the frequencies of V_L gene family expression in live and phagocytozed B cell fractions are found to be statistically equivalent ($p>0.10$). Thus, the level of expression of a given V_L gene family within the live B cell fraction seems to directly affect the level of expression within the corresponding phagocytozed B cell fraction. The overall hierarchical pattern of V_L gene family expression (IGKV10, 12>IGKV4>IGKV1>IGKV6, 8, 9 and IGKL1) does not correlate to genomic complexity and remains unchanged between day 8 to 12 after phOx-CSA challenge (Figure 6.6). The obvious dominance of IGKV10, IGKV12 and IGKV4 expression is very unlikely to be due to a primer bias since the adapted primer mix was shown to amplify the here missing V_L gene families (e.g. IGKV7) - when subjected to RNA of total splenic B cells (data not shown). In addition, members of gene families known to be rather slightly expressed, are occasionally identified, as for instance IKVL-1. Identified Vκ genes are scattered about the entire Igκ locus (Appendix A.1). The overall response to phOx-CSA is predominated by B cells bearing the Igκ V genes IGKV10-94, 10-96, 12-41, 12-44, 12-46 and 4-59 (appendix Figure A.4). Whereas the prevalence of IGKV4-59 (VκOx1) may be readily explained by its major role in the phOx response, the reason for overrepresentation of IGKV10 and IGKV12 genes is currently unclear.

J_L gene segment use by live and phagocytozed B cells was quantitatively compared as described above. At day 12 post immunization, J_L usage is both equivalent in the live and phagocytozed B cell fraction ($p>0.20$) (Figure 6.6) and its hierarchical pattern (Jκ1, Jκ2»Jκ5>Jκ4>Jλ1) reflects previously reported J_L usage of splenic murine B cells [193]. Jκ1 and Jκ2 are the predominant genes segments, each accounting for about 35 to 50% of IgL rearrangements. By contrast, J_L usage is significantly different in the live and phagocytozed B cell fraction at day 8 after phOx-CSA challenge ($p\leq0.001$). Whereas J_L usage in the live B cell fraction resembles the hierarchical pattern observed at day 12, J_L usage in the phagocytozed B cell fraction is characterized by a marked overrepresentation of Jκ5 (50%) and underrepresentation of Jκ2. The reason for the deviant Jκ use in the phagocytozed B cell fraction is unclear.

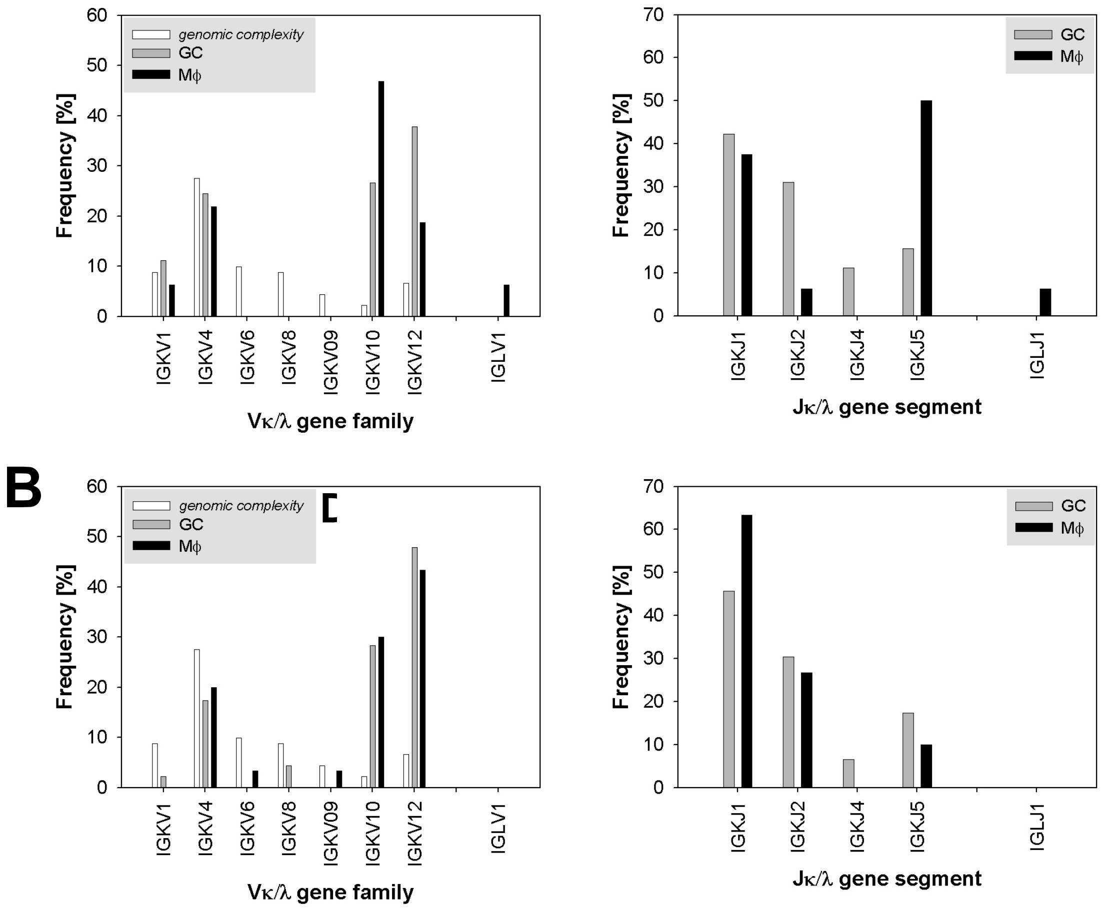

Figure 6.6: IgL repertoire analysis among live and phagocytozed B cell fractions. Illustrated are the distributions of V_L gene family and J_L gene segment use for live (GC, gray) and phagocytozed B cell (Mϕ, black) fractions derived from phOx-CSA challenged BALB/c mice at days 8 (A) and 12 (B). V_L gene families and J_L gene segments were identified using the IMGT/V-Quest database [90]. V_L gene family usage is additionally compared to expected frequencies according to the genomic complexity of V_L gene families.

6.3.2 Variational kappa J gene segment use among phOx specific IgL of live and phagocytozed B cell fractions

In addition to IGK4-59 (VκOx1) rearrangements, five IGKV4-74 (128.con) rearrangements and one rearrangement of IGKV4-78 (H1) were observed among the pool of analyzed sequences. Since IGKV4-74 and IGKV4-78 most likely represent additional phOx specific gene segments in that they have been previously isolated from phOx specific GC [118] and share high sequence homology to IGKV4-59 (>94%), they were included in the analysis. For transparency reasons, IGKV4-74 and IGKV4-78 rearrangements are each identified by respective labels. Integration of IGKV4-74 and IGKV4-78 rearrangements did not interfere with the analysis, since their exclusion did not alter the results.

The analysis of J_L gene segment use phOx specific rearrangements reveals highly significant differences regarding live and phagocytozed B cell fractions at days 8 and 12 ($p<0.001$) (Figure 6.7). The live B cell fraction features marked overrepresentation of Jκ5 (>50%) that is counteracted by complete absence of Jκ1 expression. In turn, phagocytozed B cell fractions are highly enriched for Jκ1 expression (60-80%) but nearly lack Jκ2 and Jκ5 rearrangements. For one, this result affirms the dominance of IGKV4-59/Jκ5 rearrangements in the immune response against phOx [124], but most interestingly, it reveals that such dominance goes at the expense of Jκ1 usage. The strict absence of Jκ1 rearrangements from live B cell fractions further suggests that such rearrangements hold features that categorically cause negative selection, which might explain their overrepresentation in phagocytozed B cell fractions.

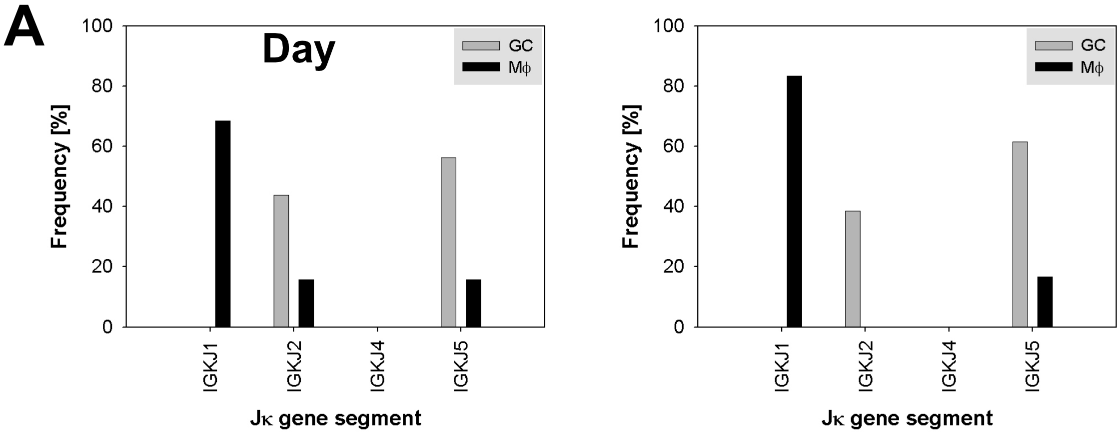

Figure 6.7: J_κ gene segment use of phOx-specific IgL among live and phagocytozed B cell fractions. Illustrated are the distributions of J_κ gene segment use among phOx specific IgL sequences of live (GC, gray) and phagocytozed (Mϕ, black) B cell fractions at days 8 (A) and 12 (B). J_κ gene segments were identified using the IMGT/V-Quest database [90].

6.3.3 Differences in interclonal diversity of phOx specific IgL between live and phagocytozed B cell fractions

The interclonal diversity of phOx specific IGK4-59 (VκOx1), IGKV4-74 (128.con) and IGKV4-78 (H1) rearrangements among live and phagocytozed B cell fractions was determined based on shared Vκ gene segments and identical nucleotide sequences of VJ joins and LCDR3s, respectively. At both time points analyzed, the interclonal diversity among the phagocytozed B cell fraction exceeds the diversity of the live B cell fraction (Table 6.2). Noteworthy, LCDR3s that are different on the nucleotide level but become identical when translated into protein, are repeatedly observed among phOx specific IgL sequences of live B cell fractions during analysis, thus suggesting that interclonal diversity is even more diminished on the translated or protein level. On this account, LCDR3s of live and phagocytozed B cell fractions were compared by multiple alignment of their amino acid sequences (Figure 6.8). In the first instance, amino acid sequence alignments of phOx specific IgL reveal differences regarding the spectrum of LCDR3s detected among live and phagocytozed B cell fractions. Whereas live B cell fraction appear to be interclonally restricted (6-8 different LCDR3s), interclonal diversity is markedly pronounced in the phagocytozed B cell fractions (15-20 different LCDR3s). The overall interclonal diversity (live+phagocytozed) of phOx specific IgL is the same at day 8 and 12 (26 and 23 different LCDR3s, respectively).

The comparison of LCDR3s of live and phagocytozed B cell fractions furthermore suggests that the texture of the LCDR3 is substantially important to the outcome of selection of phOx specific GC B cells, in that even key mutation bearing Igκ rearrangements are found in the phagocytozed fraction at both time points analyzed (Figure 6.8). Among phOx specific IgL sequences of phagocytozed B cell fractions, a group of "odd-looking" LCDR3s leaps to the eye which is rather phenomenologically characterized by an increased occurrence of histidine (H), arginine (R) and tryptophan residues (W) (Figure 6.8). The observation that this group primarily consists of Jκ1 rearrangements suggests that use of Jκ1 is prone to formation of LCDR3s that are detrimental to phOx binding, which might explain the aforementioned strict absence of of Jκ1 rearrangements from live B cell fractions (Figure 6.7).

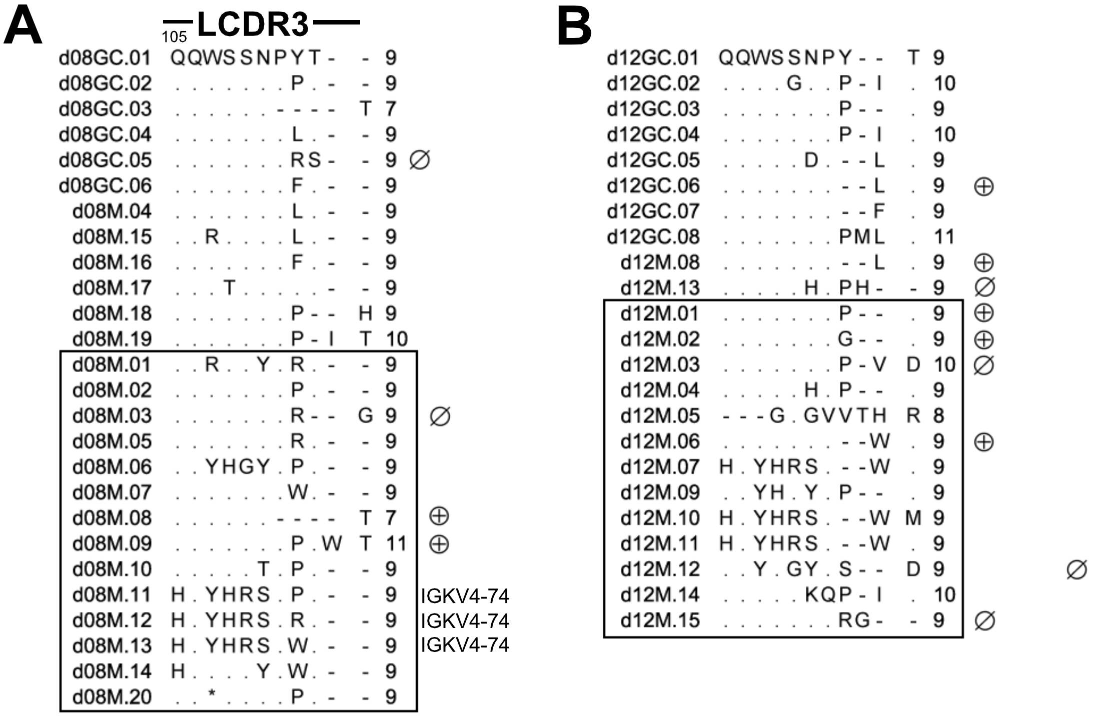

Figure 6.8: Comparison of LCDR3s of phOx specific IgL sequences among live and phagocytozed B cell fractions. The amino acid sequence spectrum of observed κ light chain rearrangements among live (GC) and phagocytozed (M) phOx-specific B cell fractions obtained at days 8 (A) and 12 (B) is illustrated. Boxed sequences refer to κ light chain rearrangements that were exclusively found in context of Jκ1 usage. ⊕ indicate rearrangements of key mutation ($H_{34}Q/N$) bearing κ light chains. Alignments include LCDR3s that become out of frame (∅) due to deletions/insertions in the cause of somatic hypermutation (discussed in Section 6.3).

6.3.4 Phagocytozed B cell fractions are generally not enriched in LCDR3s showing characteristics related to autoreactivity

Autoreactivity and, in particular, anti-DNA reactivity of antibodies is generally ascribed to the emergence of long, positively charged HCDR3s which are otherwise negatively selected in normal "healthy" circumstances [194, 195]. However, studies by Park et al. [196] indicate that positive charged LCDR3s also contribute to DNA binding. To account for this, LCDR3s of live and phagocytozed B cell fractions were compared in order to assess whether nonstandard lengths and positive charge are enriched among the latter fraction. The average length of LCDR3 is 8.9±0.3 aa. This value is similar for live and phagocytozed B cell fractions at day 8 (8.9±0.4 aa vs. 8.9±0.3 aa) and day 12 (8.9±0.3 aa vs. 9.0±0.4 aa) (data not shown). Alike, the average length of LCDR3 of phOx specific B cells (9.1±0.5 aa) is invariant with respect to live and phagocytozed fractions at day 8 (8.9±0.5 aa vs. 9.0±0.5 aa) and day 12 (9.3±0.6 aa vs. 9.1±0.5 aa), respectively (data not shown). Potential signs of autoreactivity owing to LCDR3 charge were assessed by quantifying the incidence of positively charged amino acid residues (R, K, H) in this region. Overall IgL sequences of live and phagocytozed B cell fractions do not significantly differ with respect to LCDR3 charge at either of the time points analyzed (p>0.20) (Figure 6.9). Between 75 to 90% of all LCDR3s bear either one (50-75%) or no positively charged amino acid residue (15-30%). In fact, the frequency of LCDR3s with 3 or more positively charged residues never exceeds 3.3%. Thus, phagocytozed B cell fractions are generally not enriched in LCDR3s showing characteristics related to autoreactivity.

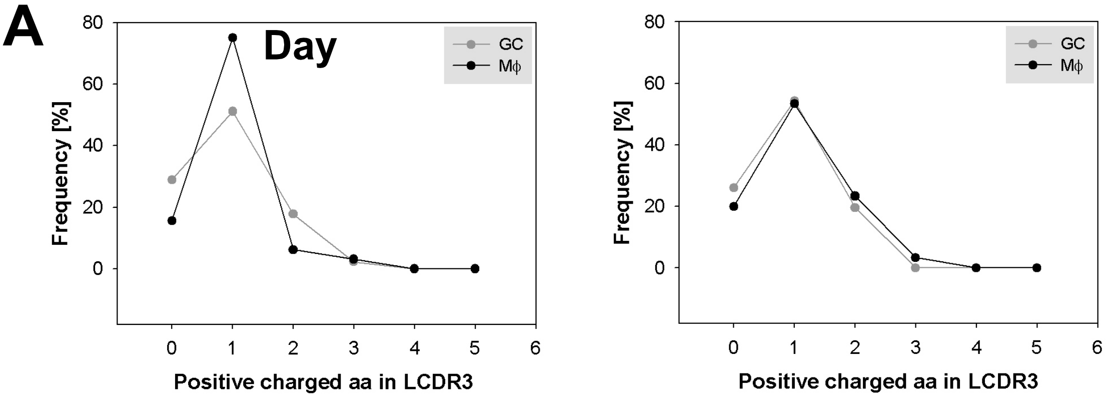

Figure 6.9: Frequency of overall clones bearing positively charged amino acids (aa) within their LCDR3. The frequency of clones bearing a given number of positively charged amino acids (R, K, H) within their LCDR3 is graphically illustrated for live (GC, gray) and phagocytozed (Mϕ, black) B cell fractions derived from phOx-challenged BALB/c mice at days 8 (A) and 12 (B).

6.3.5 Accumulation of positively charged LCDR3s among phOx specific IgL sequences of phagocytozed B cells

The quantification of charged amino acid residues in LCDR3s of phOx specific rearrangements reveals striking differences in relation to overall IgL sequences, in that the live B cell fractions are nearly void of positively charged residues (>95% in phOx specific vs. 15-30% in overall LCDR3s) (Figure 6.10). Accordingly, charged phOx specific LCDR3s accumulate within phagogytosed B cell fractions as already phenomenologically observed during sequence alignment (Figure 6.8). PhOx specific IgL rearrangements of live and phagocytozed B cell fractions cannot directly be compared statistically with each other, since the formers each comprise only one single charged LCDR3 and thereby fall beneath the minimum frequency threshold required for the statistical test. However, since charged phOx specific LCDR3s are virtually absent from live B cell fractions, the observed differences are highly probable significant. Coupled with the observation that positively charged LCDR3 are usually not enriched among phagocytozed B cell fractions (Section 6.3.4, Figure 6.9), LCDR3 charge appears to have crucial impact on predicting survival fate of phOx specific B cells.

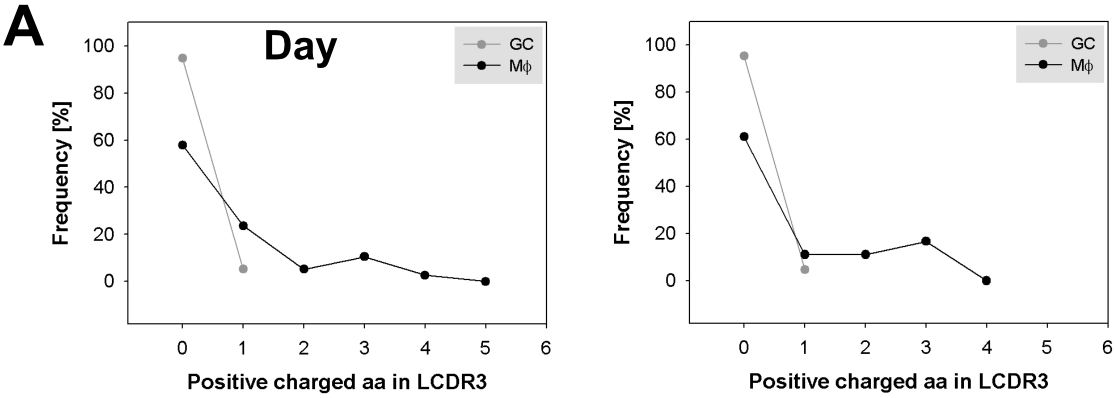

Figure 6.10: Frequency of phOx-specific clones bearing positively charged amino acids (aa) within their LCDR3. The frequency of phOx-specific clones bearing a given number of positively charged amino acids (R, K, H) within their LCDR3 is graphically illustrated for live (GC, gray) and phagocytozed (Mϕ, black) B cell fractions at days 8 (A) and 12 (B).

6.4 Hypermutation among live and phagocytozed B cell fractions

The frequency of somatic hypermutation was determined for overall and phOx specific IgL sequences amplified from live and phagocytozed B cells by comparison against the IMGT database [90]. Sequences that were identical on the cDNA level were only counted once. Potential clonal relatedness did not compromise mutation analysis as clonally related groups principally contained sequences that were different in their mutation pattern, thereby indicating that they were derived from distinct B cells (see sequence alignments in the appendix). The results of mutation analyses of overall IgL and phOx specific IgL sequences are summarized in Table 6.1 and Table 6.2, respectively.

6.4.1 Hypermutation of overall IgL sequences from live and phagocytozed B cell fractions

Live and phagocytozed B cell fractions always include germline sequences, though the proportion of unmutated sequences is consistently reduced about a factor of 2-3 among phagocytozed B cells (Table 6.1). The proportion of germline sequences among live B cell fractions decreases from day 8 (35.6%) to day 12 (21.7%), thereby indicating the progression of affinity maturation. On the other hand, the proportion of unmutated sequences among phagocytozed B cell fractions turns out to be rather stable over time ($9.4 \mapsto 10.0\%$) (Table 6.1). Since variational proportions of germline sequences have an biasing effect on the calculation of average mutation frequencies and statistical analyses, germline sequences were excluded for this parts of the analysis. For transparency reasons, average mutation frequencies resulting from calculations when unmutated sequences were included, are additionally quoted in Table 6.1. Mutation frequencies were statistically compared using Wilcoxon rang sum test. Noteworthy, IgL sequences from live and phagocytozed B cell fractions at day 8 post immunization differ neither in average mutation frequencies (2.83 vs. 2.48) nor the range of detected mutations (0-10 vs. 0-7) (Table 6.1). The distributions of mutations look very similar, except for the proportion of unmuated sequences as stated above (Figure 6.11, A). Statistical comparison using Wilcoxon rank sum test finally approves that live and phagocytozed B cell fractions are not significantly different from each other regarding mutation frequency (p=0.6951) at day 8 post immunization. The picture at day 12 post immunization remains rather unchanged against day 8, in that average mutation frequency (2.97 vs. 2.44), the range of mutations (0-6 vs. 0-7) and the distribution of mutations among IgL of live and phagocytozed B cells look very similar (Table 6.1, Figure 6.11, B). Likewise, differences in mutation frequency at day 12 turn out to be not significant (p=0.0872). The calculated average mutation frequency within live B cell fractions does not increase over time ($2.83 \mapsto 2.97$) and differences are shown to be not significant (p=0.4312). The same applies for the average mutation frequency of phagocytozed B cell fractions ($2.48 \mapsto 2.44$, p=0.5032). The rather fixed average mutation frequencies observed among overall IgL sequences are somewhat surprising considering that the progression of the GC reaction is usually accompanied by the accumulation of mutations. However, since this analysis was performed on overall IgL sequences of GC B cells, it pools different responses, namely the carrier-specific, hapten-specific and mixed hapten-carrier specific responses, thus providing an "average picture" of somatic hypermutation after phOx-CSA challenge. Still more surprising than its constancy, the average mutation frequency is unexpectedly high, even early in the response, which mainly attributes to high numbers of mutations within IgL rearrangements of IGKV10 and IGKV12 genes that dominate the overall response (Section 6.3.1, Figure 6.6, sequence alignments are shown in the appendix). The reason for the increased accumulation of mutations within this particular genes is currently unclear but may reflect differences in the rate of somatic hypermutation in dependence of the initial affinity of GC B cells as suggested by Dal Porto et al. [197].

Day	Sample	No. of cells thru cDNA (% gl)[1]	No. unique LCDR3	Average no. of mut.[2]	Range of mut.	FW R/S	CDR R/S
08	GC	45 (35.6)	35	2.83 (1.82)	0 - 10	3.1	4.3
	Mϕ	32 (9.4)	18	2.48 (2.28)	0 - 7	3.9	13.5
12	GC	46 (21.7)	31	2.97 (2.33)	0 - 6	2.6	5.5
	Mϕ	30 (10.0)	21	2.44 (2.20)	0 - 7	2.6	>23

Table 6.1: Comparison of IgL sequences of live (GC) and phagocytozed B cell fractions (Mϕ) post immunization. [1]Sequences that were identical on the cDNA level were counted once, values in brackets signify the proportion of germline (gl) sequences. [2]Calculated excluding germline sequences, values in brackets indicate average mutation frequency when germline sequences were included.

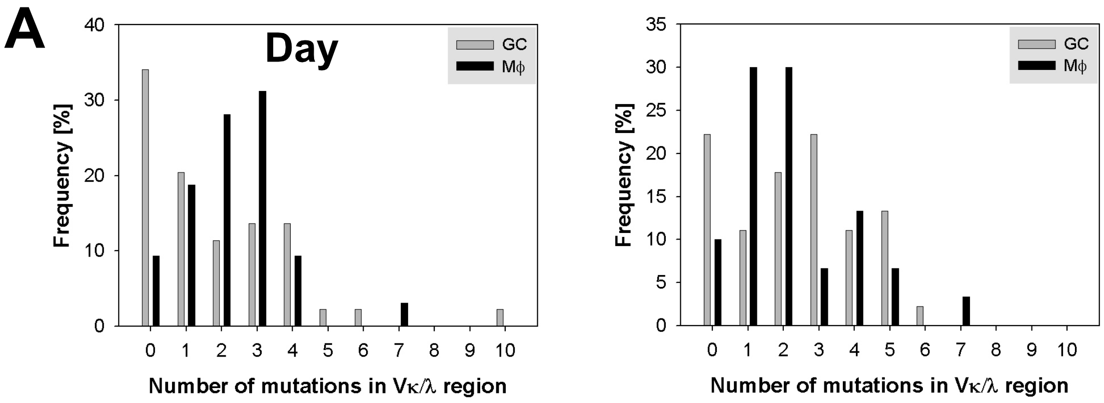

Figure 6.11: Distribution of the frequencies of mutations within IgL sequences of live and phagocytozed B cell fractions. The frequency of clones bearing a given number of mutations in the IgL sequence is graphically illustrated for live (GC, gray) and phagocytozed (Mϕ, black) B cell fractions derived from phOx-challenged BALB/c mice at days 8 (A) and 12 (B).

A further criterion for assessment of somatic hypermutation is the distribution of mutations along V genes, generally referred to as mutation pattern, that provides information on where mutations are located. Under the assumption that somatic hypermutation is random, the distribution of mutations should reflect the size of the respective regions. In case of overall IgL sequences, the size ratio of FR to CDR is rather similar for detected V_L genes, ranging between 79%:21%(IGKV1, IGKV8 and IGLV1 gene family members) and 83%:17% (IGKV4, IGKV10 and IGKV12 gene family members). Likewise, the sizes of individual FR and CDR regions are quite consistent for the identified V_L genes and the mean pattern resembles the pattern of the phOx specific IGKV4-59 gene (FR1:CDR1:FR2:CDR2:FR3:CDR3=27:8:18:3:38:6 [%]). Therefore, observed mutation patterns among overall IgL sequences are compared to the random mutation pattern expected for IGKV4-59, where 83% and 17% of IgL mutations are expected to occur within FR and CDR regions of IgL, respectively. (The difference to previous publications that often quote a 65%:35% ratio is due to the use of the Kabat nomenclature instead of the IMGT nomenclature[90] used in the current thesis.) Traditionally, divergence of experimentally observed from expected mutation patterns were considered an indication of selection [198]. This view is challenged in that mutations pattern were shown to be non-random but intrinsic to the coding sequences of V genes [199, 200].

The overall mutation pattern (FR:CDR) of live (74%:26%) and phagocytozed B cell fractions (60%:40%) isolated at day 8 after immunization looks rather similar, and differences are not significant (p=0.0883 in χ^2 test) (Figure 6.12, A). The same accounts for day 12 after immunization, in that the distribution of mutations is 64%:36% for live and 65%:35% for phagocytozed B cell fractions (p=0.9601) (Figure 6.12, B). Furthermore, neither the overall mutation pattern of live (74%:26% ↦ 64%:36%) nor phagocytozed B cell fractions (60%:40% ↦ 65%:35%) significantly changes over the time course (p=0.1530 and p=0.6760, respectively).

Nevertheless, considering the mutation pattern relevant to the individual FR and CDR regions (segmental mutation pattern), live and phagocytozed B cell fractions show significant differences at day 8 (p=0.0001) (Figure 6.12, A) that mainly attribute to variations in FR1 (31% vs. 12%), CDR1 (7% vs. 27%) and FR3 (18% vs. 33%). The segmental mutation pattern of live B cell fractions at day 8 is additionally significantly different from the one observed at day 12 ($p=0.0001$). Since segmental mutation patterns of live and phagocytozed B cells are indifferent at day 12 ($p=0.6528$) (Figure 6.12, B) and the patterns of phagocytozed B cells do not significantly change over time ($p=0.1325$), the observed difference at day 8 most likely attributes to peculiarities of the live cell fraction.

The analysis of mutation patterns is usually complemented by calculation of replacement to silent mutations ratios (R/S), in which the deviation of experimentally observed from theoretically predicted R/S values is construed as evidence for selection. In this context, CDRs are thought to acquire higher R/S values because they make up the main part of the antigen binding site and replacement mutations therefore should have strong influence on antibody affinity. In contrary, replacement mutations within FRs are believed to be selected against since they are detrimental to antibody structure - resulting in R/S values falling below the expected.

As overall IgL sequences comprise a variety of different V_L genes, distinct values for expected R/S ratios in CDR and FR are not available. Nevertheless, comparison of R/S values of live and phagocytozed B cell fractions should provide some clues regarding selection. Unexpectedly, R/S values of live and phagocytozed B cell fractions turn out to be rather similar in that R/S ratios in CDRs consistently exceeded R/S ratios of FRs at both time points analyzed (Table 6.1). In fact, R/S ratios calculated for CDRs of phagocytozed B cell fractions are strikingly higher as compared to live cells at day 8 (13.5 vs. 4.3) and even further increase up to day 12 (>23 vs. 5.5) after immunization (Table 6.1, Figure 6.12, A and B). The high R/S ratios of overall CDRs of phagocytozed B cell fractions result from high frequencies of replacement mutations in any of the individual CDRs as graphically illustrated by means of the proportions of replacement mutations within CDR1, CDR2 and CDR3 at days 8 and 12 after immunization (Figure 6.12, A and B). Noteworthy, IgL sequences of the phagocytozed B cell fraction isolated at day 12 after immunization show exclusively replacement mutations within CDRs, thus the proportion of replacement mutations is 100% for CDR1, CDR2, CDR3 and overall CDR (Figure 6.12, B).

On the contrary, the R/S ratios calculated for the FR of phagocytozed and live B cell fractions show only minor differences at day 8 (3.9 vs. 3.1) and even further decrease until day 12, in which differences are nullified (2.6 vs. 2.6) (Table 6.1, Figure 6.12, A and B). In addition, replacement mutations apparently do not accumulate within individual FRs of phagocytozed B cell fractions over the time course as given by the proportions of replacement mutations at day 8 and 12 (FR1: $89 \mapsto 50$, FR2: $91 \mapsto 75$, FR3: $71 \mapsto 83$) (Figure 6.12, A and B).

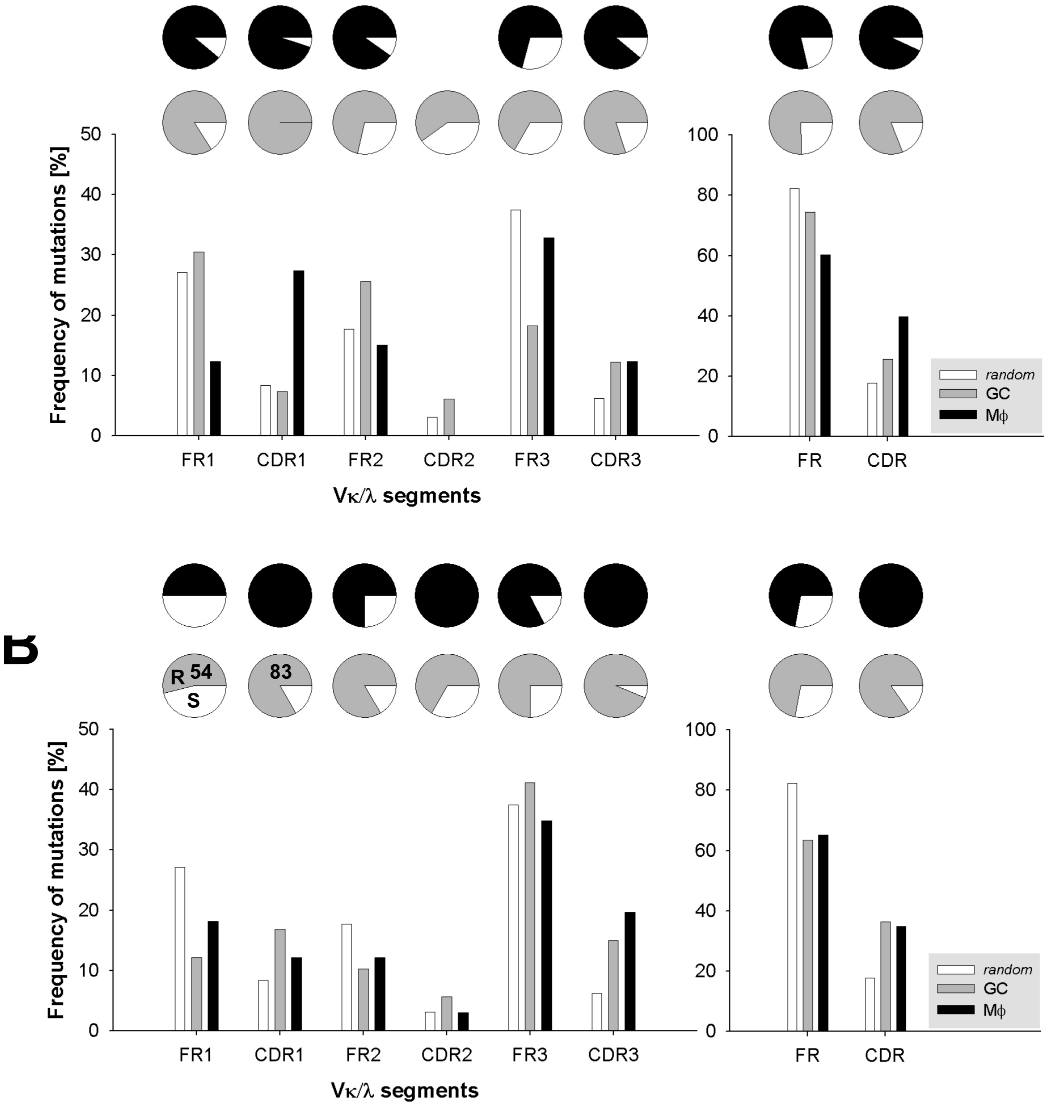

Figure 6.12: Pattern of mutations within IgL sequences of live and phagocytozed B cell fractions. The mean frequencies of mutations within individual FRs and CDRs as well as overall FR and CDR are illustrated for live (GC, gray) and phagocytozed (Mϕ, black) B cell fractions derived from phOx-challenged BALB/c mice at days 8 (A) and 12 (B) after immunization, respectively. The pattern of frequencies expected for equivalent randomly mutated IGKV4-49 (VκOx1) sequences (*random*, white) is shown for comparison. Pie charts signify the proportion of observed replacement to silent mutations, in which the depicted numbers specify the percentage of replacement mutations.

6.4.2 Hypermutation of phOx specific IgL sequences from live and phagocytozed B cell fractions

Similar to overall IgL sequences (Table 6.1), phOx specific IgL sequences of live B cell fractions comprise a considerable proportion of germline sequences, that only slightly decrease from day 8 (36.8%) to day 12 (33.3%) (Table 6.2). Unmutated phOx specific IgL sequences are strikingly less frequent among phagocytozed B cell fractions at day 8 (13.2%) and even decrease over time, in which only one single germline sequence is identified at day 12 (4.5%) (Table 6.2). As argued before (Section 6.4.1), germline sequences were excluded when calculating average mutation frequencies or performing statistical tests. Mutation frequencies were statistically compared using Wilcoxon rang sum test. PhOx specific IgL sequences of live and phagocytozed B cell fractions differ in average number (1.33 vs. 2.39), range (0-3 vs. 0-5) and distribution of mutations at day 8 post immunization (Table 6.2, Figure 6.13, A), in which the differences are shown to be significant (p=0.0171). In contrast, average mutation frequency (3.00 vs. 2.29), range (0-5 vs. 0-7) and distribution of mutations (Table 6.2, Figure 6.13, B) look rather similar for live and phagocytozed B cell fractions at day 12 post immunization and differences turn out to be not significant (p=0.4230). Whereas the increase in the average number of mutations among phOx specific IgL sequences of live B cell fractions from day 8 to 12 (1.33 $\mapsto$ 3.00) is highly significant (p=0.0020), the average mutation frequency observed for phagocytozed B cell fractions is rather invariant (2.39 $\mapsto$ 2.29) and differences are not significant (p=0.6985). Thus, phagocytozed B cell fractions do not necessarily comprise excessively mutated phOx specific IgL sequences.

The overall mutation pattern (FR:CDR) of phOx specific IgL sequences looks rather similar for live (75%:25%) and phagocytozed B cell fractions (85%:15%) at day 8 and differences are shown to be not significant (p=0.5553 in χ^2 test) (Figure 6.14, A). Likewise, live and phagocytozed B cell fractions do not significantly differ in the pattern of mutation within individual FRs and CDRs (p=0.5923) (Figure 6.14, A). The same accounts for phOx specific sequences isolated at day 12, in that live and phagocytozed B cell fractions turn out to be neither significantly different regarding their overall mutation patterns (FR:CDR) (62%:38% vs. 77%:23%) (p=0.1812) nor regarding their pattern of mutations within individual FRs and CDRs (p=0.2880) (Figure 6.14, B). Although, the overall mutation patterns (FR:CDR) of both live and phagocytozed B cell fractions seem to change in favour of higher frequencies of mutations in the CDR of phOx specific IgL over the time course, differences are not significant (p=0.5295 and p=0.3905, respectively). Similarly, the variations observed in the patterns of mutations within individual FRs and CDRs over the time course, are not significant, in case of live as well as phagocytozed B cell fractions (p=0.7618 and p=0.4054, respectively).

In case of the phOx specific IGKV4-59 (VκOx1) gene, expected R/S ratios were calculated in a model of random mutation, resulting in R/S values of 3.4 for the FR and 4.6 for the CDR (expected R/S values for IGKV4-59 according to the IMGT nomenclature were calculated by Armin Weiser, a fellow-member of the Systems

Immunology Group; expected R/S values according to Kabat nomenclature are 3.3 for FR and 3.5 for CDR, respectively [29]). With the sole exception of the live B cell fraction at day 8, all other populations - irrespective of live or phagocytozed - feature the generally contended signs of selected populations, in that R/S values within FRs are lower (1.6-2.7) but R/S values within CDRs are higher (4.5-11.0) than the expected (Table 6.2). However, the scenario is reversed in context of the live B cell fraction at day 8 that shows higher R/S values in FRs (11.0) but lower R/S values in CDRs (3.0) (Table 6.2). The divergence of this live B cell population from both the expected and other B cell populations mainly attributes to the high proportions of replacement mutations in FR1 (100%) and FR3 (100%) (Figure 6.14, A), whose origin is unclear. Whereas R/S ratios in CDRs of live B cells increase over the time course ($3.0 \mapsto 7.0$), the very of phagocytozed B cells decrease ($11.0 \mapsto 4.5$). R/S values within FRs of live B cells decrease from day 8 to day 12, in which the observed decrease is most likely due to the unusually high R/S value at day 8. Similar to overall IgL sequences, phagocytozed B cell fractions show a rather constant R/S ratio over the time course ($2.7 \mapsto 2.7$) (Table 6.2), that even constantly falls below the expected. With respect to replacement mutations in the individual FRs, phagocytozed B cell fractions show rather similar or even lower proportions than live B cells at both time points analyzed (Figure 6.14, A and B). The FR2 may constitute an exception to this, since the proportions of replacement mutations are consistently higher for phagocytozed compared to live B cell fractions (89%:75% and 86%:60% at days 8 and 12, respectively) (Figure 6.14, A and B). Such phenomenon, may attribute to the importance of FR2 for the binding to phOx, in that it comprises both key mutation sites.

Day	Sample	No. of cells thru cDNA (% gl)[1]	No. unique LCDR3	Average no. of mut.[2]	Range of mut.	$H_{34}Q/N$ [%][3]	FW R/S	CDR R/S
08	GC	19 (36.8)	8	1.33 (0.84)	0 - 3	0	11.0	3.0
	Mϕ	38 (13.2)	23	2.39 (2.08)	0 - 5	6.1	2.7	11
12	GC	21 (33.3)	10	3.00 (2.00)	0 - 5	4.8	1.6	7
	Mϕ	22 (4.5)	17	2.29 (2.00)	0 - 7	20.0	2.7	4.5

Table 6.2: Comparison of phOx specific IgL sequences of live (GC) and phagocytozed B cell fractions (Mϕ) post immunization. [1]Sequences that were identical on the cDNA level were counted once, values in brackets signify the proportion of germline (gl) sequences. [2]Calculated excluding germline sequences; values in brackets indicate average mutation frequency when germline sequences were included. [3]The proportion of key mutation ($H_{34}Q/N$) bearing sequences was calculated excluding germline sequences.

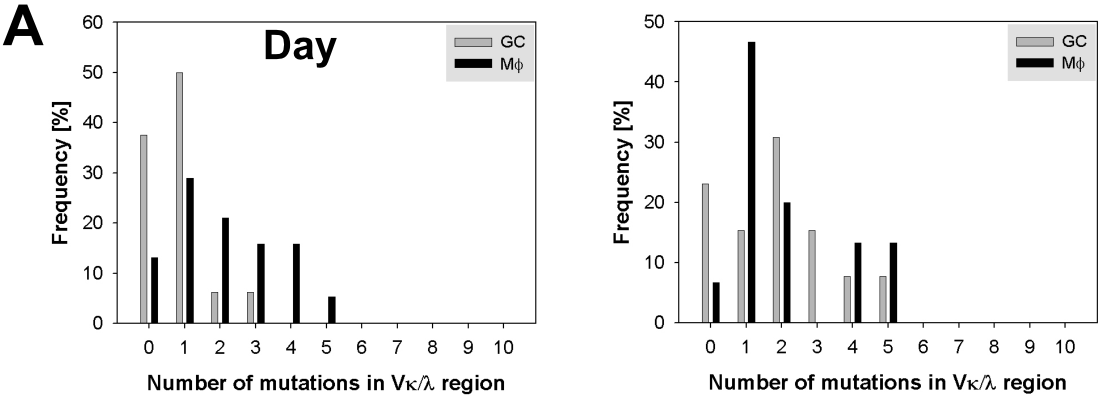

Figure 6.13: Distribution of the frequencies of mutations in phOx specific IgL sequences of live and phagocytozed B cell fractions. The frequency of phOx-specific clones bearing a given number of mutations in the V_L region is graphically illustrated for live (GC, gray) and phagocytozed (Mϕ, black) B cell fractions at days 8 (A) and 12 (B).

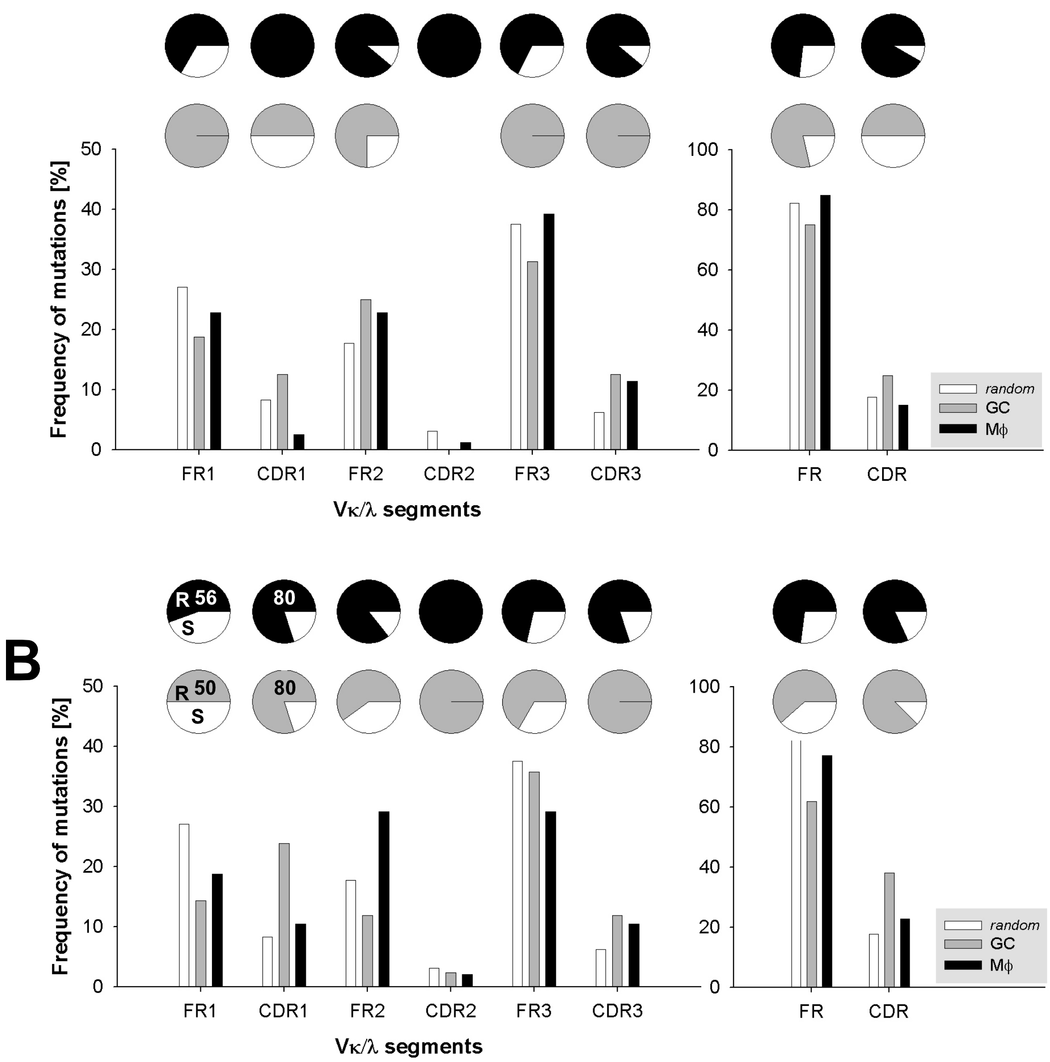

Figure 6.14: Pattern of mutations among phOx specific IgL sequences of live and phagocytozed B cell fractions. The mean frequencies of mutations within individual FRs and CDRs as well as overall FR and CDR are illustrated for phOx specific IgL sequences of live (GC, gray) and phagocytozed (Mϕ, black) B cell fractions at days 8 (A) and 12 (B) after immunization. The pattern of frequencies expected for equivalent randomly mutated IGKV4-49 (VκOx1) sequences (*random*, white) is shown for comparison. Pie charts signify the proportion of observed replacement to silent mutations, in which the depicted numbers specify the percentage of replacement mutations.

6.4.3 Special mutational events: Translational stop codons, frameshifts/deletions and key mutations

The frequencies of special mutational events such as frameshifts/deletions, translational stop codons and key mutations are listed in Table 6.3. Frameshifts/deletions are most frequent in both, overall and phOx specific IgL sequences of phagocytozed B cell fractions at day 12 after immunization (5/30 and 6/22, respectively). With respect to mutation sites, frameshifts/deletions are observed in FR1, FR3 and LCDR3, in which most events rate among the latter. Translational stop codons are found in overall/phOx specific IgL sequences of both live and phagocytozed B cell fractions, though they are commonest in the latter fraction (3/5). True to type, due to the early time points analyzed, the frequency of key mutation bearing phOx specific IgL sequences of live GC B cells is very low, in that only a single out of 21 sequences is detected at day 12 after immunization. As much astonishing, not only the frequency of key mutation bearing phOx specific IgL turns out to be higher in the phagocytozed fraction (4/22 at day 12 after immunization) but the key mutation is even identified among phagocytozed B cell fractions as early as day 8 after immunization.

Sample	No. of cells thru cDNA[1]	Frame shifts/deletions	Translational stop codons	$H_{34}Q/N$
day 08 GC	45	-	1 (FR2)	
day 08 Mϕ	32	-	1 (FR2)	
day 12 GC	46	-	1 (FR2)	
day 12 Mϕ	30	5 (LCDR3)	1 (FR1)	
day 08 phOx GC	19	1 (LCDR3)	1 (FR2)	-
day 08 phOx Mϕ	18	1 (LCDR3)	1 (LCDR3)	2
day 12 phOx GC	21	-	-	1
day 12 phOx Mϕ	22	6 (4 LCDR3, 1 FR1, 1 FR3)	2 (FR1, FR2)	4

Table 6.3: Survey of special mutational events. Illustrated are the numbers of frameshifts/deletions, translational stop codons and key mutations observed in overall/phOx specific IgL sequences of live (GC) and phagocytozed (Mϕ) B cell fractions post immunization. Mutation sites are specified in parentheses. [1]Sequences that were identical on the cDNA level were counted once.

6.5 Discussion

The way of how - and especially by which criteria - B cells are selected within GC is a thrilling question as it is quite fragmentary understood. This is particularly due to the fact that comprehensive assessment of evolutionary processes generally relies on two strands of information, that of survivors **and** losers. Such a demand proves elusive regarding the micro-evolutionary GC reaction, in that loosing B cells just do not fossilize in the fashion of dinosaurs but rapidly disappear. However, a reliable method for recovery of apoptotic "loser" GC B cells could be established during the current thesis that for the first time allowed for tracing of winners and losers during a hapten-carrier elicited immune response.

6.5.1 Reliability of recovery of live and apoptotic GC B cell fractions

To revisit the dinosaur simile, holding the fossile in hands inevitable implies that the belonging dinosaur is dead. Unfortunately, things are not that obvious in case of GC B cells which are fragile and designated to undergo apoptosis [201, 202] unless they receive rescue signals provided by surrounding FDC [203]. Detachment of GC B cells from their microenvironment, as for instance during preparation of cell suspensions, readily actuates the apoptotic machinery and within 5 h about 40-50% of the cells express phospatidylserine (PS), one of the earliest markers of apoptotic cells [66]. Consequently, direct detection of apoptotic GC B cells within cell suspensions (e.g. by annexin V reactivity) is unreliable in that it is not capable to distinguish between cells that died under physiological conditions and cells becoming apoptotic due to cell handling *ex vivo*. Under physiological conditions, externalization of PS on the surface of apoptotic GC B cells leads to their rapid clearance by proximally positioned GC macrophages [204, 205, 85], which makes GC macrophages the most reliable reservoir of apoptotic GC B cells arising *in vivo*. Since there is no marker specific to GC macrophages, a protocol for identification and isolation of follicular or white pulp macrophages ($CD68^{+}$ $F4/80^{-}$), respectively, was developed and established instead (Sections 6.1-6.2, Figures 6.3-6.5). To prevent systemic distortion of the results owing to uptake of *ex vivo* evoked apoptotic GC B cells, B cells were immediately separated from spleen cell suspensions and follicular macrophages showing partially engulfed B cells ($CD68^{+}$ $F4/80^{-}$ $B220^{+}$) were excluded from FACS sorting. The developed protocol turns out a success, since overall IgL sequences of phagocytozed B cell fractions are shown to be related but not identical to live GC B cell fractions (Sections 6.3.1, 6.4, Table 6.1, Figures 6.11-6.12). Moreover, phOx specific IgL sequences of live and phagocytozed B cell fractions are shown to strictly classify according to Jκ gene segment use and differ in interclonal diversity (Figures 6.7-6.8). Noteworthy, the key mutation is identified among phOx specific IgL sequences of phagocytozed B cells as early as day 8 post immunization and its frequency is always higher compared to live GC B cells thereafter (Table 6.2). This lends experimetal support to the blocking model proposed by Kleinstein and Singh [206] that attributes the late occurence and low frequencies of key mutations among live phOx specific GC B cells [118, 122] to the existence of a large number of detrimetal mutations whose presence can prevent the ability of the key mutation to confer high affinity.

6.5.2 Live and phagocytozed GC B cells carry the generally accepted molecular signatures of antigen-driven selection

In previous studies, affinity selection among Ig sequences is often rated by means of the mutation patterns of V genes, in which variation of the distribution of mutations in FR and CDR to the values expected for random mutation is considered evidence for (positive) selection [127, 32, 207]. In this context, affinity maturation is thought to lead to the accumulation of replacement mutations in CDRs (antigen binding sites), thus resulting in R/S ratios exceeding the values expected on the basis of random mutation within CDRs. On the other hand, replacement mutations in the FRs are believed to be (negatively) counterselected as they harm the overall structure of Ig molecules. Consequently, the ratio of R/S substitutions within FRs of positively selected GC B cells should fall below the values expected for random mutation.

However, the here performed comparative IgL sequence analysis of live (positively selected "WINNERS") and phagocytozed (negatively selected "LOSERS") challenges this conception in that both, WINNERS and LOSERS turn out to be in agreement with the abovementioned criteria of positively selected GC B cells. Phagocytozed B cells are shown to not necessarily comprise excessively mutated sequences (Tables 6.1-6.2, Figures 6.11, 6.13) and both, live and phagocytozed B cell fractions show variations of the distribution of mutations in FR and CDR to the expected values for random mutation over the time course, in which mutations usually accumulate in CDRs (summarized in Table 6.4). The fact, that these changes in the overall mutation pattern are rated as not significant in statistical tests most likely attributes to generally low numbers of overall mutations. Since the vast majority of analyzed sequences have a range of 1-4 mutations (Figures 6.11, 6.13), large numbers of sequences may be needed to reach statistical significance. Nevertheless, most importantly, such analysis reveals that there is apparently no difference regarding the distribution of mutations between WINNERS and LOSERS of selection (Figures 6.12 and 6.14).

Likewise, the comparison of R/S ratios among IgL sequences of WINNERS and LOSERS shows that both populations are characterized by accumulation of replacement mutations within CDRs, but not FRs (Tables 6.1, 6.2). Neither phagocytozed overall IgL nor phOx specific IgL sequences are characterized by excessive replacement mutations within FRs as anticipated by the general conception of selection. In fact, R/S ratios among phOx specific IgL sequences of phagocytozed B cells consistently fall below the expected value of 3.4 (Table 6.2). (Expected R/S values for IGKV4-59 according to the IMGT nomenclature were calculated by Armin Weiser, a fellow-member of the Systems Immunology Group. Expected R/S values according to Kabat nomenclature are 3.3 for FR and 3.5 for CDR, respectively [29]). Together

these findings indicate that R/S ratios fail to specify antigen driven selection but rather reflect differences in intrinsic mutability among CDRs and FRs as already argued by Dunn-Walters et al. [208].
In addition, the acquisition of key mutations does not predict the survival fate of GC B cells, as key mutation bearing phOx specific IgL sequences are commonly observed among phagocytozed B cell fractions (Table 6.3). In conclusion, the traditionally proposed molecular signatures fail to demarcate winners and losers and therefore do not allow for determining antigen driven selection.

Sample	Distribution of mutations FR:CDR [%][1] day 8 ↦ day 12
	overall IgL
live	74:**26** ↦ 64:**36**
phagocytozed	61:**39** ↦ 65:**35**
	phOx specific IgL
live	75:**25** ↦ 62:**38**
phagocytozed	85:**15** ↦ 77:**23**

Table 6.4: Survey of changes regarding the distribution of mutations in FRs and CDRs post immunization. [1]Expected proportion for IGKV4-59 (VκOx1) according to IMGT nomenclature is 83%:17%.

6.5.3 Positive selection of GC B cells relies on the absence of adverse mutations within CDRs

The comparative IgL sequence analysis of live and phagocytozed B cells not only emphasizes the failing of previously proposed molecular signatures to determine antigen driven selection (Section 6.5.2), but additionally admits a revised conception of selection, in which the survival of GC B cells particularly relies on the "quality" and cumulative effect of mutations. The high frequencies of replacement mutations within CDRs of phagocytozed B cells (Tables 6.1-6.2), that actually often exceed those of live GC B cells (Figures 6.12 and 6.14), controvert the generally proposed positive or "affinity-enhancing" effects of replacement mutations within CDRs. Indeed, excessive replacement mutations within CDRs rather seem to have a profound negative, deleterious effect. Thus, survival or positive selection of GC B cells seems to be determined by the absence of excess mutations within CDRs that have an adverse effect with respect to antigen binding.

6.5.4 Low interclonal diversity of phOx specific GC B cells is due to continual massive clonal failures

The comparison of phOx specific IgL sequences of live and phagocytozed B cell fractions further reveals striking differences regarding the interclonal diversity between winners and losers. Whereas live GC B cells are interclonally restricted, interclonal diversity turns out to be markedly pronounced among phagocytozed B cell fractions (Section 6.3.3, Figure 6.8). Thus, the generally observed oligoclonality of "live" GC has to be considered only the tip of the iceberg regarding the diversity of the phOx response, just emerging as a consequence of massive clonal failures. The overall interclonal diversity (live+phagocytozed) of phOx-specific GC B cells is shown to remain constant over the time course (Figure 6.8). Consequently, the domination of the GC response by few clones does not attribute to progressive reduction of interclonal diversity due to successive elimination of unfit clones, as both generally believed and taken as the main argument for local antigen-driven selection. In fact, the high interclonal diversity of phagocytozed B cell fractions suggests that interclonal competition is sustained throughout the GC response, most probably incited by ongoing replenishment of the pool of interacting B cells (schematically illustrated in Figure 6.15).

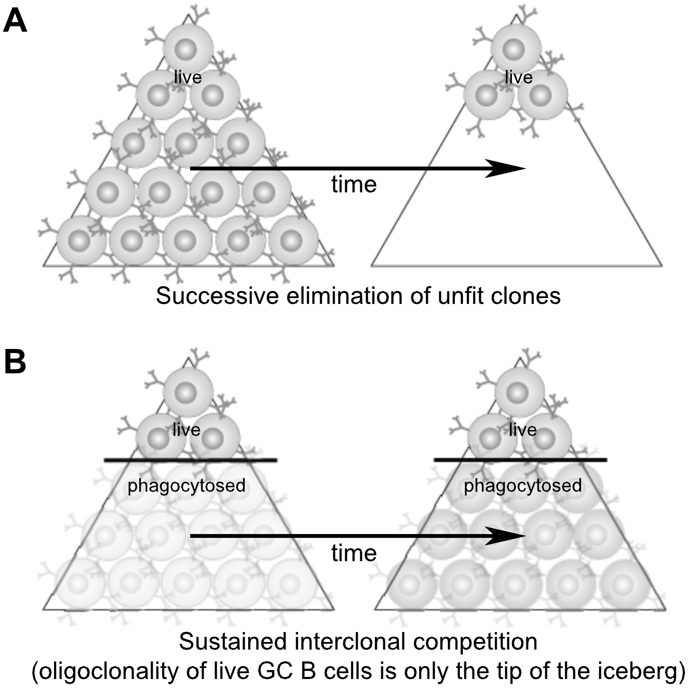

Figure 6.15: Traditional and revised explanation for the domination of GC responses by few clones. (A) Schematic illustration of the traditional conception. The domination of GC responses by few clones is the result of progressive reduction of interclonal diversity due to successive elimination of unfit clones over the time course. (B) Schematic illustration of the revised conception. The domination of GC responses by few clones is the result of sustained interclonal competition that includes massive clonal failures.

6.5.5 Some closing remarks

The comparative analysis of live and phagocytozed B cells presented in the current thesis strongly suggests that the survival fate of GC B cells cannot be predicted by means of **general molecular signatures** of primary BCR sequences, which is partly in line with results reported by Jackson and Capra [209] who followed a similar approach in that they compared IgH sequences of living and dying human tonsillar GC B cells. However, whereas Jackson and Capra [209] do not find consistent differences of living and dying GC B cells at all, the comparative analysis of live and phagocytozed B cell fractions following phOx-CSA challenge performed during this thesis quite does, as for instance variational Jκ gene segment usage (Figure 6.7), LCDR3 charge (Figure 6.10) and interclonal diversity of LCDR3s (Figure 6.8). As highlighted in the opening paragraph, these differences are unlikely to represent generally or universally valid features, respectively, but rather have to be considered special to the GC response to phOx-CSA. Differences between the work of Jackson and Capra [209] and the results presented here, certainly attribute to the circumstance that Jackson and Capra [209] analyze an overall immune response to an unknown mixture of antigens, whereas the analysis reported here is based upon examination of an immune response elicited by a single known antigen (phOx-CSA). Moreover, Jackson and Capra [209] report the repeated identification of identical sequences in both, living and dying B cell fractions, a finding that is not reproduced by the analysis performed here, in that identical sequences in both fractions represent extremely rare exceptional cases. This divergence most likely reflects differences regarding the strategies of recovery of primary BCR sequences of dying GC B cells, in which the study of Jackson and Capra [209] is largely based upon identification of dying GC B cells by Annexin-V reactivity.

Chapter 7

Conclusions and perspectives

The revised model of affinity maturation - emigration, recirculation and global selection

Although this was not the initial intention of the current thesis, the presented results unanimously challenge the general conception of evolution of B cells within GC. This finally lead to the proposal of a revised model of affinity maturation that includes asynchronous formation and ongoing seeding of GC, recirculation of emigrant GC B cells and the implementation of a global selection process. This model strikingly differs from the traditional conception in that it postulates an external (*recirculation*) instead of an internal iterative (*recycling*) process, that is, vital mutation-free phases are not installed by migration of B cells within, but by emigration from GC. Noteworthy, external iteration is indirectly supported by *vivo* imaging of GC, which just recently revealed that recycling within GC is doubtful, because the observed exchange of B cells between dark and light zone of GC falls below the "traffic" required for efficient affinity maturation as predicted by theoretical modeling (Hauser et al., personal communication). However, although the *in vivo* imaging and transfer experiments performed by Schwickert et al. [101] demonstrate that GC are dynamic open structures, and seeding of GC is likely to be ongoing, direct experimental proof for both emigration and recirculation of GC B cells is still missing. Thus far, Schwickert et al. [101] have shown that antigen-specific B cells that are applicated at the height of the GC response can be detected within pre-existing GC afterwards. The next step would be to proof that these B cells do indeed join pre-existing GC reactions, in that they start to hypermutate and are subjected to selection. Interestingly, Schwickert et al. [101] point out that joining of pre-existing GC does rely on a competitive advantage in antigen binding affinity of transfered B cells, thereby lending indirect support to a global selection process acting on the level of reentry into GC. It will be challenging to see what happens after transfer of B cells that have a lower affinity towards the antigen than B cells within pre-existing GC, in particular regarding the following questions: Where do they go and in particular where do they get outcompeted? Do they enter pre-existing GC but then rapidly die within the same GC due to their disadvantage in local competition with B cells of higher affinity? OR Are they excluded from joining pre-existing GC *a priori* due to a globally acting selection process? Regarding the emigration of GC B cells, it does not require a fortune teller to predict that new insights will be available very soon, as it has already drawn the attention of the groups performing in vivo imaging of GC. In this context, the exploration of emigration of GC B cells is particularly incited by 5-bromo, 2'-deoxyuridine (BrdU) pulse labeling experiments that revealed rapid disappearance of BrdU labeled proliferating cells from the light zone of GC (within 2 to 4 h) [100].

Signatures of selection

The herein performed comparative analysis of IgL sequences of live and phagocytozed B cell fractions following phOx-CSA challenge demonstrates the failing of previously proposed molecular signatures to determine antigen driven selection. In addition, it signalizes that selection and therewith survival of GC B cells may be especially determined by the "quality" of mutations (i.e. effected changes on the amino acid level) as well as the cumulative effect of mutations. Thus, the identification of signatures of selection during the response to phOx-CSA may require the comparison of large pools of IGKV4-59 (VκOx1) sequences of both live and phagocytozed B cell fractions on the amino acid level, an approach currently being developed together with Armin Weiser, a fellow member of the Systems Immunology group. Such analysis might reveal patterns of amino acid substitutions that either favor or handicap survival of phOx specific GC B cells, which may contribute to the understanding of their selection process. In addition, further criteria of selection may be attained by assessing the binding properties of antigen-specific BCRs/antibodies of live and phagocytozed GC B cells in ELISAs or BIAcore binding studies, which requires their expression as $(Fab)^2$ fragments first.

Tickling macrophages

Admittedly, macrophages became a personal obsession during the current thesis, very much inspired by the "story of Jekyll and Hyde", a splendid article published by Duffield [210] in 2003, that portrays the dueling personalities of macrophages in inflammation. According to the "Jekyll and Hyde" scenario, engulfment of apoptotic cells leads to a reprogramming of macrophage function, that is once "angry" cell-killing proinflammatory macrophages become calming "anti-inflammatory" healing macrophages. Duffield [210] points out, that the "Jekyll $\rightleftharpoons$ Hyde" transition works in both directions and that the "right amount of Mr Hyde and Dr Jekyll" is vital to the resolution of inflammation. Interestingly, the results presented in the current thesis indicate that such a "Jekyll and Hyde" scenario does also apply to macrophages within GC and may be crucial to the regulation/homeostasis of GC. Moreover, the analysis of macrophages within GC of NZB/W mice suggests that the observed phagocytosis-induced death of macrophages may effect a "Jekyll and Hyde" imbalance, in that the dampening function of Mr Hyde is lost. Thus, the "Jekyll and Hyde" scenario may have to be extended for a third personality e. g. "Jekyll $\rightleftharpoons$ Hyde $\rightarrow$?". It will be of great interest to assess the transitions between macrophage states as they seem to represent a key regulatory element regarding GC homeostasis. As differences in cytokine expression most likely translate into differences in function, a first approach could be to compare the cytokine expression profiles of Mac-2$^+$ and Mac-2$^-$ follicular/GC macrophages, in which the former are likely to represent "Mr Hyde" in that they represent macrophages carrying many engulfed apoptotic cells [45]. Moreover, "macrophage personalities" may be identified and specified by profiling the gene expression of microdissected subsets of follicular/GC macrophages.

Bibliography

[1] A. K. Abbas, H. L. Lichtman, and J. S. Pober. *Cellular and molecular immunology.* W. B. Saunders company, 4th edition, 2000.

[2] C. Martinez-Jean, G. Folch, and M. P. Lefranc. Nomenclature and overview of the mouse (Mus musculus and Mus sp.) immunoglobulin kappa (IGK) genes. *Exp Clin Immunogenet*, 18(4):255–79, 2001.

[3] M. S. Krangel. Gene segment selection in V(D)J recombination: accessibility and beyond. *Nat Immunol*, 4(7):624–30, 2003.

[4] C.A. Janeway, P. Travers, M. Walport, and M. J. Shlomchik. *Immunobiology: The Immune System in Health and Disease.* Garland Publishing, 5th edition, 2001.

[5] I. M. Roitt, M. F. Greaves, G. Torrigiani, J. Brostoff, and J. H. Playfair. The cellular basis of immunological responses. A synthesis of some current views. *Lancet*, 2(7616):367–71, 1969.

[6] B. Glick. *The bursa of Fabricus and antibody production.* PhD thesis, State University, Columbus, 1955.

[7] D. Ribatti, E. Crivellato, and A. Vacca. The contribution of Bruce Glick to the definition of the role played by the bursa of Fabricius in the development of the B cell lineage. *Clin Exp Immunol*, 145(1):1–4, 2006.

[8] F. Melchers, E. ten Boekel, T. Seidl, X. C. Kong, T. Yamagami, K. Onishi, T. Shimizu, A. G. Rolink, and J. Andersson. Repertoire selection by pre-B-cell receptors and B-cell receptors, and genetic control of B-cell development from immature to mature B cells. *Immunol Rev*, 175:33–46, 2000.

[9] A. G. Rolink, C. Schaniel, J. Andersson, and F. Melchers. Selection events operating at various stages in B cell development. *Curr Opin Immunol*, 13(2): 202–7, 2001.

[10] D. Nemazee. Receptor editing in lymphocyte development and central tolerance. *Nat Rev Immunol*, 6(10):728–40, 2006.

[11] A. G. Rolink, J. Andersson, and F. Melchers. Molecular mechanisms guiding late stages of B-cell development. *Immunol Rev*, 197:41–50, 2004.

[12] T. Lopes-Carvalho and J. F. Kearney. Development and selection of marginal zone B cells. *Immunol Rev*, 197:192–205, 2004.

[13] P. Aichele, J. Zinke, L. Grode, R. A. Schwendener, S. H. Kaufmann, and P. Seiler. Macrophages of the splenic marginal zone are essential for trapping of blood-borne particulate antigen but dispensable for induction of specific T cell responses. *J Immunol*, 171(3):1148–55, 2003.

[14] T. A. Banks, B. T. Rouse, M. K. Kerley, P. J. Blair, V. L. Godfrey, N. A. Kuklin, D. M. Bouley, J. Thomas, S. Kanangat, and M. L. Mucenski. Lymphotoxin-alpha-deficient mice. Effects on secondary lymphoid organ development and humoral immune responsiveness. *J Immunol*, 155(4):1685–93, 1995.

[15] H. J. Kim, T. Kammertoens, M. Janke, O. Schmetzer, Z. Qin, C. Berek, and T. Blankenstein. Establishment of early lymphoid organ infrastructure in transplanted tumors mediated by local production of lymphotoxin alpha and in the combined absence of functional B and T cells. *J Immunol*, 172(7): 4037–47, 2004.

[16] M. Gonzalez, F. Mackay, J. L. Browning, M. H. Kosco-Vilbois, and R. J. Noelle. The sequential role of lymphotoxin and B cells in the development of splenic follicles. *J Exp Med*, 187(7):997–1007, 1998.

[17] V. N. Ngo, R. J. Cornall, and J. G. Cyster. Splenic T zone development is B cell dependent. *J Exp Med*, 194(11):1649–60, 2001.

[18] C. G. Lo, T. T. Lu, and J. G. Cyster. Integrin-dependence of lymphocyte entry into the splenic white pulp. *J Exp Med*, 197(3):353–61, 2003.

[19] J. G. Cyster and C. C. Goodnow. Pertussis toxin inhibits migration of B and T lymphocytes into splenic white pulp cords. *J Exp Med*, 182(2):581–6, 1995.

[20] R. Forster, A. E. Mattis, E. Kremmer, E. Wolf, G. Brem, and M. Lipp. A putative chemokine receptor, BLR1, directs B cell migration to defined lymphoid organs and specific anatomic compartments of the spleen. *Cell*, 87(6): 1037–47, 1996.

[21] K. M. Ansel, V. N. Ngo, P. L. Hyman, S. A. Luther, R. Forster, J. D. Sedgwick, J. L. Browning, M. Lipp, and J. G. Cyster. A chemokine-driven positive feedback loop organizes lymphoid follicles. *Nature*, 406(6793):309–14, 2000.

[22] R. Forster, A. Schubel, D. Breitfeld, E. Kremmer, I. Renner-Muller, E. Wolf, and M. Lipp. CCR7 coordinates the primary immune response by establishing functional microenvironments in secondary lymphoid organs. *Cell*, 99(1):23–33, 1999.

[23] L. Ohl, G. Henning, S. Krautwald, M. Lipp, S. Hardtke, G. Bernhardt, O. Pabst, and R. Forster. Cooperating mechanisms of CXCR5 and CCR7 in development and organization of secondary lymphoid organs. *J Exp Med*, 197(9):1199–204, 2003.

[24] Y. J. Liu, J. Zhang, P. J. Lane, E. Y. Chan, and I. C. MacLennan. Sites of specific B cell activation in primary and secondary responses to T cell-dependent and T cell-independent antigens. *Eur J Immunol*, 21(12):2951–62, 1991.

[25] D. M. Sze, K. M. Toellner, C. Garcia de Vinuesa, D. R. Taylor, and I. C. MacLennan. Intrinsic constraint on plasmablast growth and extrinsic limits of plasma cell survival. *J Exp Med*, 192(6):813–21, 2000.

[26] K. A. Pape, V. Kouskoff, D. Nemazee, H. L. Tang, J. G. Cyster, L. E. Tze, K. L. Hippen, T. W. Behrens, and M. K. Jenkins. Visualization of the genesis and fate of isotype-switched B cells during a primary immune response. *J Exp Med*, 197(12):1677–87, 2003.

[27] P. Schaerli, K. Willimann, A. B. Lang, M. Lipp, P. Loetscher, and B. Moser. CXC chemokine receptor 5 expression defines follicular homing T cells with B cell helper function. *J Exp Med*, 192(11):1553–62, 2000.

[28] W. Flemming. Studien über Regeneration der Gewebe. *Arch Mikros Anat*, 24: 355–, 1885.

[29] C. Berek. The development of B cells and the B-cell repertoire in the microenvironment of the germinal center. *Immunol Rev*, 126:5–19, 1992.

[30] G. Kraal, I. L. Weissman, and E. C. Butcher. Germinal centre B cells: antigen specificity and changes in heavy chain class expression. *Nature*, 298(5872): 377–9, 1982.

[31] P. Nieuwenhuis and D. Opstelten. Functional anatomy of germinal centers. *Am J Anat*, 170(3):421–35, 1984.

[32] C. Berek and C. Milstein. Mutation drift and repertoire shift in the maturation of the immune response. *Immunol Rev*, 96:23–41, 1987.

[33] K. Rajewsky, I. Forster, and A. Cumano. Evolutionary and somatic selection of the antibody repertoire in the mouse. *Science*, 238(4830):1088–94, 1987.

[34] J. M. Dal Porto, A. M. Haberman, M. J. Shlomchik, and G. Kelsoe. Antigen drives very low affinity B cells to become plasmacytes and enter germinal centers. *J Immunol*, 161(10):5373–81, 1998.

[35] J. Hasbold, L. M. Corcoran, D. M. Tarlinton, S. G. Tangye, and P. D. Hodgkin. Evidence from the generation of immunoglobulin G-secreting cells that stochastic mechanisms regulate lymphocyte differentiation. *Nat Immunol*, 5(1):55–63, 2004.

[36] D. Paus, T. G. Phan, T. D. Chan, S. Gardam, A. Basten, and R. Brink. Antigen recognition strength regulates the choice between extrafollicular plasma cell and germinal center B cell differentiation. *J Exp Med*, 203(4):1081–91, 2006.

[37] C. G. de Vinuesa, M. C. Cook, J. Ball, M. Drew, Y. Sunners, M. Cascalho, M. Wabl, G. G. Klaus, and I. C. MacLennan. Germinal centers without T cells. *J Exp Med*, 191(3):485–94, 2000.

[38] J. G. Cyster, S. B. Hartley, and C. C. Goodnow. Competition for follicular niches excludes self-reactive cells from the recirculating B-cell repertoire. *Nature*, 371(6496):389–95, 1994.

[39] R. L. Coffman, B. W. Seymour, D. A. Lebman, D. D. Hiraki, J. A. Christiansen, B. Shrader, H. M. Cherwinski, H. F. Savelkoul, F. D. Finkelman, M. W. Bond, and et al. The role of helper T cell products in mouse B cell differentiation and isotype regulation. *Immunol Rev*, 102:5–28, 1988.

[40] A. K. Abbas, K. M. Murphy, and A. Sher. Functional diversity of helper T lymphocytes. *Nature*, 383(6603):787–93, 1996.

[41] D. Breitfeld, L. Ohl, E. Kremmer, J. Ellwart, F. Sallusto, M. Lipp, and R. Forster. Follicular B helper T cells express CXC chemokine receptor 5, localize to B cell follicles, and support immunoglobulin production. *J Exp Med*, 192(11):1545–52, 2000.

[42] C. R. Mackay. Follicular homing T helper (Th) cells and the Th1/Th2 paradigm. *J Exp Med*, 192(11):F31–4, 2000.

[43] D. C. Swartzendruber and C. C. Congdon. Electron Microscope Observations on Tingible Body Macrophages in Mouse Spleen. *J Cell Biol*, 19:641–6, 1963.

[44] J. P. Smith, M. H. Kosco, J. G. Tew, and A. K. Szakal. Thy-1 positive tingible body macrophages (TBM) in mouse lymph nodes. *Anat Rec*, 222(4):380–90, 1988.

[45] J. P. Smith, A. M. Lister, J. G. Tew, and A. K. Szakal. Kinetics of the tingible body macrophage response in mouse germinal center development and its depression with age. *Anat Rec*, 229(4):511–20, 1991.

[46] J. P. Smith, G. F. Burton, J. G. Tew, and A. K. Szakal. Tingible body macrophages in regulation of germinal center reactions. *Dev Immunol*, 6(3-4): 285–94, 1998.

[47] C. Berek and H. J. Kim. B-cell activation and development within chronically inflamed synovium in rheumatoid and reactive arthritis. *Semin Immunol*, 9 (4):261–8, 1997.

[48] I. Voigt, S. A. Camacho, B. A. de Boer, M. Lipp, R. Forster, and C. Berek. CXCR5-deficient mice develop functional germinal centers in the splenic T cell zone. *Eur J Immunol*, 30(2):560–7, 2000.

[49] U. Karrer, C. Lopez-Macias, A. Oxenius, B. Odermatt, M. F. Bachmann, U. Kalinke, H. Bluethmann, H. Hengartner, and R. M. Zinkernagel. Antiviral B cell memory in the absence of mature follicular dendritic cell networks and classical germinal centers in TNFR1-/- mice. *J Immunol*, 164(2):768–78, 2000.

[50] T. Manser. Textbook germinal centers? *J Immunol*, 172(6):3369–75, 2004.

[51] J. G. Tew, M. H. Kosco, G. F. Burton, and A. K. Szakal. Follicular dendritic cells as accessory cells. *Immunol Rev*, 117:185–211, 1990.

[52] M. H. Kosco, E. Pflugfelder, and D. Gray. Follicular dendritic cell-dependent adhesion and proliferation of B cells in vitro. *J Immunol*, 148(8):2331–9, 1992.

[53] J. Lederberg. Genes and antibodies. *Science*, 129(3364):1649–53, 1959.

[54] S. Brenner and C. Milstein. Origin of antibody variation. *Nature*, 211(5046): 242–3, 1966.

[55] M. G. Weigert, I. M. Cesari, S. J. Yonkovich, and M. Cohn. Variability in the lambda light chain sequences of mouse antibody. *Nature*, 228(5276):1045–7, 1970.

[56] M. Muramatsu, K. Kinoshita, S. Fagarasan, S. Yamada, Y. Shinkai, and T. Honjo. Class switch recombination and hypermutation require activation-induced cytidine deaminase (AID), a potential RNA editing enzyme. *Cell*, 102 (5):553–63, 2000.

[57] P. Revy, T. Muto, Y. Levy, F. Geissmann, A. Plebani, O. Sanal, N. Catalan, M. Forveille, R. Dufourcq-Labelouse, A. Gennery, I. Tezcan, F. Ersoy, H. Kayserili, A. G. Ugazio, N. Brousse, M. Muramatsu, L. D. Notarangelo, K. Kinoshita, T. Honjo, A. Fischer, and A. Durandy. Activation-induced cytidine deaminase (AID) deficiency causes the autosomal recessive form of the Hyper-IgM syndrome (HIGM2). *Cell*, 102(5):565–75, 2000.

[58] A. Longacre and U. Storb. A novel cytidine deaminase affects antibody diversity. *Cell*, 102(5):541–4, 2000.

[59] J. Di Noia and M. S. Neuberger. Altering the pathway of immunoglobulin hypermutation by inhibiting uracil-DNA glycosylase. *Nature*, 419(6902):43–8, 2002.

[60] J. C. Weill, B. Bertocci, A. Faili, S. Aoufouchi, S. Frey, A. De Smet, S. Storck, A. Dahan, F. Delbos, S. Weller, E. Flatter, and C. A. Reynaud. Ig gene hypermutation: a mechanism is due. *Adv Immunol*, 80:183–202, 2002.

[61] S. H. Clarke, K. Huppi, D. Ruezinsky, L. Staudt, W. Gerhard, and M. Weigert. Inter- and intraclonal diversity in the antibody response to influenza hemagglutinin. *J Exp Med*, 161(4):687–704, 1985.

[62] G. J. Nossal, G. L. Ada, C. M. Austin, and J. Pye. Antigens in immunity. 8. Localization of 125-I-labelled antigens in the secondary response. *Immunology*, 9(4):349–57, 1965.

[63] L. G. Hannum, A. M. Haberman, S. M. Anderson, and M. J. Shlomchik. Germinal center initiation, variable gene region hypermutation, and mutant B cell selection without detectable immune complexes on follicular dendritic cells. *J Exp Med*, 192(7):931–42, 2000.

[64] K. A. Vora, J. V. Ravetch, and T. Manser. Amplified follicular immune complex deposition in mice lacking the Fc receptor gamma-chain does not alter maturation of the B cell response. *J Immunol*, 159(5):2116–24, 1997.

[65] L. Li and Y. S. Choi. Follicular dendritic cell-signaling molecules required for proliferation and differentiation of GC-B cells. *Semin Immunol*, 14(4):259–66, 2002.

[66] M. van Eijk, J. P. Medema, and C. de Groot. Cutting edge: cellular Fas-associated death domain-like IL-1-converting enzyme-inhibitory protein protects germinal center B cells from apoptosis during germinal center reactions. *J Immunol*, 166(11):6473–6, 2001.

[67] S. A. Camacho, M. H. Kosco-Vilbois, and C. Berek. The dynamic structure of the germinal center. *Immunol Today*, 19(11):511–4, 1998.

[68] S. P. Rao, K. A. Vora, and T. Manser. Differential expression of the inhibitory IgG Fc receptor FcgammaRIIB on germinal center cells: implications for selection of high-affinity B cells. *J Immunol*, 169(4):1859–68, 2002.

[69] Z. S. Rahman, S. P. Rao, S. L. Kalled, and T. Manser. Normal induction but attenuated progression of germinal center responses in BAFF and BAFF-R signaling-deficient mice. *J Exp Med*, 198(8):1157–69, 2003.

[70] J. Jacob, R. Kassir, and G. Kelsoe. In situ studies of the primary immune response to (4-hydroxy-3-nitrophenyl)acetyl. I. The architecture and dynamics of responding cell populations. *J Exp Med*, 173(5):1165–75, 1991.

[71] K. G. Smith, A. Light, G. J. Nossal, and D. M. Tarlinton. The extent of affinity maturation differs between the memory and antibody-forming cell compartments in the primary immune response. *Embo J*, 16(11):2996–3006, 1997.

[72] C. Kesmir and R. J. De Boer. A mathematical model on germinal center kinetics and termination. *J Immunol*, 163(5):2463–9, 1999.

[73] J. G. Tew and T. E. Mandel. Prolonged antigen half-life in the lymphoid follicles of specifically immunized mice. *Immunology*, 37(1):69–76, 1979.

[74] D. M. Tarlinton and K. G. Smith. Dissecting affinity maturation: a model explaining selection of antibody-forming cells and memory B cells in the germinal centre. *Immunol Today*, 21(9):436–41, 2000.

[75] M. Meyer-Hermann, A. Deutsch, and M. Or-Guil. Recycling probability and dynamical properties of germinal center reactions. *J Theor Biol*, 210(3):265–85, 2001.

[76] J. S. Moreira and J. Faro. Modelling two possible mechanisms for the regulation of the germinal center dynamics. *J Immunol*, 177(6):3705–10, 2006.

[77] C. G. Vinuesa and M. C. Cook. The molecular basis of lymphoid architecture and B cell responses: implications for immunodeficiency and immunopathology. *Curr Mol Med*, 1(6):689–725, 2001.

[78] R. Kuppers. Mechanisms of B-cell lymphoma pathogenesis. *Nat Rev Cancer*, 5(4):251–62, 2005.

[79] E. M. Tan. Antinuclear antibodies: diagnostic markers for autoimmune diseases and probes for cell biology. *Adv Immunol*, 44:93–151, 1989.

[80] H. Shan, M. J. Shlomchik, A. Marshak-Rothstein, D. S. Pisetsky, S. Litwin, and M. G. Weigert. The mechanism of autoantibody production in an autoimmune MRL/lpr mouse. *J Immunol*, 153(11):5104–20, 1994.

[81] U. Wellmann, M. Letz, M. Herrmann, S. Angermuller, J. R. Kalden, and T. H. Winkler. The evolution of human anti-double-stranded DNA autoantibodies. *Proc Natl Acad Sci U S A*, 102(26):9258–63, 2005.

[82] U. S. Gaipl, R. E. Voll, A. Sheriff, S. Franz, J. R. Kalden, and M. Herrmann. Impaired clearance of dying cells in systemic lupus erythematosus. *Autoimmun Rev*, 4(4):189–94, 2005.

[83] I. Baumann, W. Kolowos, R. E. Voll, B. Manger, U. Gaipl, W. L. Neuhuber, T. Kirchner, J. R. Kalden, and M. Herrmann. Impaired uptake of apoptotic cells into tingible body macrophages in germinal centers of patients with systemic lupus erythematosus. *Arthritis Rheum*, 46(1):191–201, 2002.

[84] P. S. Hicks, L. Saunero-Nava, T. W. Du Clos, and C. Mold. Serum amyloid P component binds to histones and activates the classical complement pathway. *J Immunol*, 149(11):3689–94, 1992.

[85] R. Hanayama, M. Tanaka, K. Miyasaka, K. Aozasa, M. Koike, Y. Uchiyama, and S. Nagata. Autoimmune disease and impaired uptake of apoptotic cells in MFG-E8-deficient mice. *Science*, 304(5674):1147–50, 2004.

[86] R. Hanayama, K. Miyasaka, M. Nakaya, and S. Nagata. MFG-E8-dependent clearance of apoptotic cells, and autoimmunity caused by its failure. *Curr Dir Autoimmun*, 9:162–72, 2006.

[87] U. S. Gaipl, A. Kuhn, A. Sheriff, L. E. Munoz, S. Franz, R. E. Voll, J. R. Kalden, and M. Herrmann. Clearance of apoptotic cells in human SLE. *Curr Dir Autoimmun*, 9:173–87, 2006.

[88] S. Zullig and M. O. Hengartner. Cell biology. Tickling macrophages, a serious business. *Science*, 304(5674):1123–4, 2004.

[89] J. William, C. Euler, N. Primarolo, and M. J. Shlomchik. B cell tolerance checkpoints that restrict pathways of antigen-driven differentiation. *J Immunol*, 176(4):2142–51, 2006.

[90] V. Giudicelli, D. Chaume, and M. P. Lefranc. IMGT/V-QUEST, an integrated software program for immunoglobulin and T cell receptor V-J and V-D-J rearrangement analysis. *Nucleic Acids Res*, 32(Web Server issue):W435–40, 2004.

[91] C. Berek, G. M. Griffiths, and C. Milstein. Molecular events during maturation of the immune response to oxazolone. *Nature*, 316(6027):412–8, 1985.

[92] C. D. Bortner, N. B. Oldenburg, and J. A. Cidlowski. The role of DNA fragmentation in apoptosis. *Trends Cell Biol*, 5(1):21–6, 1995.

[93] C.J.R. Sheppard and D.M. Shotton. *Confocal Laser Scanning Microscopy*. Microscopy handbooks series. Springer Verlag New York berlin Heidelberg, 1997.

[94] I. C. MacLennan. Germinal centers still hold secrets. *Immunity*, 22(6):656–7, 2005.

[95] Christoph Giese, Christian D. Demmler, Richard Ammer, Stefan Hartmann, Annika Lubitz, Lilja Miller, Riccarda Muller, and Uwe Marx. A Human Lymph Node In Vitro - Challenges and Progress, 2006.

[96] S. M. Shinall, M. Gonzalez-Fernandez, R. J. Noelle, and T. J. Waldschmidt. Identification of murine germinal center B cell subsets defined by the expression of surface isotypes and differentiation antigens. *J Immunol*, 164(11): 5729–38, 2000.

[97] K. L. Wolniak, R. J. Noelle, and T. J. Waldschmidt. Characterization of (4-hydroxy-3-nitrophenyl)acetyl (NP)-specific germinal center B cells and antigen-binding B220- cells after primary NP challenge in mice. *J Immunol*, 177(4):2072–9, 2006.

[98] T. Scholzen and J. Gerdes. The Ki-67 protein: from the known and the unknown. *J Cell Physiol*, 182(3):311–22, 2000.

[99] L. Cervenak, A. Magyar, R. Boja, and G. Laszlo. Differential expression of GL7 activation antigen on bone marrow B cell subpopulations and peripheral B cells. *Immunol Lett*, 78(2):89–96, 2001.

[100] C. D. Allen, T. Okada, H. L. Tang, and J. G. Cyster. Imaging of germinal center selection events during affinity maturation. *Science*, 315(5811):528–31, 2007.

[101] T. A. Schwickert, R. L. Lindquist, G. Shakhar, G. Livshits, D. Skokos, M. H. Kosco-Vilbois, M. L. Dustin, and M. C. Nussenzweig. In vivo imaging of germinal centres reveals a dynamic open structure. *Nature*, 446(7131):83–7, 2007.

[102] B. Alabyev and T. Manser. Bcl-2 rescues the germinal center response but does not alter the V gene somatic hypermutation spectrum in MSH2-deficient mice. *J Immunol*, 169(7):3819–24, 2002.

[103] Z. S. Rahman and T. Manser. B cells expressing Bcl-2 and a signaling-impaired BAFF-specific receptor fail to mature and are deficient in the formation of lymphoid follicles and germinal centers. *J Immunol*, 173(10):6179–88, 2004.

[104] K. A. Vora, K. M. Tumas-Brundage, V. M. Lentz, A. Cranston, R. Fishel, and T. Manser. Severe attenuation of the B cell immune response in Msh2-deficient mice. *J Exp Med*, 189(3):471–82, 1999.

[105] Peter R. Mouton. *Principles and practices of unbiased stereology : an introduction for bioscientists.* Johns Hopkins University Press, Baltimore, 2002.

[106] K. Howell, N. Hopkins, and P. McLoughlin. Combined confocal microscopy and stereology: a highly efficient and unbiased approach to quantitative structural measurement in tissues. *Exp Physiol*, 87(6):747–56, 2002.

[107] D. Iber and P. K. Maini. A mathematical model for germinal centre kinetics and affinity maturation. *J Theor Biol*, 219(2):153–75, 2002.

[108] M. Oprea, E. van Nimwegen, and A. S. Perelson. Dynamics of one-pass germinal center models: implications for affinity maturation. *Bull Math Biol*, 62 (1):121–53, 2000.

[109] T. B. Kepler and A. S. Perelson. Cyclic re-entry of germinal center B cells and the efficiency of affinity maturation. *Immunol Today*, 14(8):412–5, 1993.

[110] M. Oprea and A. S. Perelson. Somatic mutation leads to efficient affinity maturation when centrocytes recycle back to centroblasts. *J Immunol*, 158 (11):5155–62, 1997.

[111] T. A. Shih, E. Meffre, M. Roederer, and M. C. Nussenzweig. Role of BCR affinity in T cell dependent antibody responses in vivo. *Nat Immunol*, 3(6): 570–5, 2002.

[112] P. A. Koni and R. A. Flavell. Lymph node germinal centers form in the absence of follicular dendritic cell networks. *J Exp Med*, 189(5):855–64, 1999.

[113] Vicky M. Lentz and Tim Manser. Cutting Edge: Germinal Centers Can Be Induced in the Absence of T Cells, July 1, 2001 2001.

[114] M. Meyer-Hermann and T. Beyer. The type of seeder cells determines the efficiency of germinal center reactions. *Bull Math Biol*, 66(1):125–41, 2004.

[115] A. Klein. Volumenuntersuchung muriner Keimzentren. Student research thesis, Humboldt University, Institute for Theoretical Biology, Systems Immunology, 2007.

[116] Z. F. Kapasi, G. F. Burton, L. D. Shultz, J. G. Tew, and A. K. Szakal. Induction of functional follicular dendritic cell development in severe combined immunodeficiency mice. Influence of B and T cells. *J Immunol*, 150(7):2648–58, 1993.

[117] P. Balogh, Y. Aydar, J. G. Tew, and A. K. Szakal. Ontogeny of the follicular dendritic cell phenotype and function in the postnatal murine spleen. *Cell Immunol*, 214(1):45–53, 2001.

[118] S. A. Camacho. *Temporal and spatial regulation of the primary immune response*. PhD thesis, Freie Universität Berlin, 1998.

[119] B. Sordat, M. Sordat, M. W. Hess, R. D. Stoner, and H. Cottier. Specific antibody within lymphoid germinal center cells of mice after primary immunization with horseradish peroxidase: a light and electron microscopic study. *J Exp Med*, 131(1):77–91, 1970.

[120] K. Terashima, Y. Imai, T. Kasajima, R. Tsunoda, K. Takahashi, and M. Kojima. An ultrastructure study on antibody production of the lymph nodes of rats with special reference to the role of germinal centers. *Acta Pathol Jpn*, 27(1):1–24, 1977.

[121] J. Jacob, J. Przylepa, C. Miller, and G. Kelsoe. In situ studies of the primary immune response to (4-hydroxy-3-nitrophenyl)acetyl. III. The kinetics of V region mutation and selection in germinal center B cells. *J Exp Med*, 178(4): 1293–307, 1993.

[122] M. Ziegner, G. Steinhauser, and C. Berek. Development of antibody diversity in single germinal centers: selective expansion of high-affinity variants. *Eur J Immunol*, 24(10):2393–400, 1994.

[123] A. Gonzalez-Fernandez, S. K. Gupta, R. Pannell, M. S. Neuberger, and C. Milstein. Somatic mutation of immunoglobulin lambda chains: a segment of the major intron hypermutates as much as the complementarity-determining regions. *Proc Natl Acad Sci U S A*, 91(26):12614–8, 1994.

[124] G. M. Griffiths, C. Berek, M. Kaartinen, and C. Milstein. Somatic mutation and the maturation of immune response to 2-phenyl oxazolone. *Nature*, 312 (5991):271–5, 1984.

[125] M. G. McHeyzer-Williams, M. J. McLean, P. A. Lalor, and G. J. Nossal. Antigen-driven B cell differentiation in vivo. *J Exp Med*, 178(1):295–307, 1993.

[126] C. Berek and M. Ziegner. The maturation of the immune response. *Immunol Today*, 14(8):400–4, 1993.

[127] D. Allen, A. Cumano, R. Dildrop, C. Kocks, K. Rajewsky, N. Rajewsky, J. Roes, F. Sablitzky, and M. Siekevitz. Timing, genetic requirements and functional consequences of somatic hypermutation during B-cell development. *Immunol Rev*, 96:5–22, 1987.

[128] J. Sharon, M. L. Gefter, L. J. Wysocki, and M. N. Margolies. Recurrent somatic mutations in mouse antibodies to p-azophenylarsonate increase affinity for hapten. *J Immunol*, 142(2):596–601, 1989.

[129] Y. Wang and R. H. Carter. CD19 regulates B cell maturation, proliferation, and positive selection in the FDC zone of murine splenic germinal centers. *Immunity*, 22(6):749–61, 2005.

[130] C. D. Allen, K. M. Ansel, C. Low, R. Lesley, H. Tamamura, N. Fujii, and J. G. Cyster. Germinal center dark and light zone organization is mediated by CXCR4 and CXCR5. *Nat Immunol*, 5(9):943–52, 2004.

[131] Y. Takahashi, D. M. Cerasoli, J. M. Dal Porto, M. Shimoda, R. Freund, W. Fang, D. G. Telander, E. N. Malvey, D. L. Mueller, T. W. Behrens, and G. Kelsoe. Relaxed negative selection in germinal centers and impaired affinity maturation in bcl-xL transgenic mice. *J Exp Med*, 190(3):399–410, 1999.

[132] Y. Takahashi, H. Ohta, and T. Takemori. Fas is required for clonal selection in germinal centers and the subsequent establishment of the memory B cell repertoire. *Immunity*, 14(2):181–92, 2001.

[133] E. J. Blink, A. Light, A. Kallies, S. L. Nutt, P. D. Hodgkin, and D. M. Tarlinton. Early appearance of germinal center-derived memory B cells and plasma cells in blood after primary immunization. *J Exp Med*, 201(4):545–54, 2005.

[134] T. Dorner and A. Radbruch. Selecting B cells and plasma cells to memory. *J Exp Med*, 201(4):497–9, 2005.

[135] L. J. McHeyzer-Williams, M. Cool, and M. G. McHeyzer-Williams. Antigen-specific B cell memory: expression and replenishment of a novel B220(-) memory B cell compartment. *J Exp Med*, 191(7):1149–66, 2000.

[136] K. G. Smith, A. Light, L. A. O'Reilly, S. M. Ang, A. Strasser, and D. Tarlinton. bcl-2 transgene expression inhibits apoptosis in the germinal center and reveals differences in the selection of memory B cells and bone marrow antibody-forming cells. *J Exp Med*, 191(3):475–84, 2000.

[137] S. Fossum, M. E. Smith, and W. L. Ford. The recirculation of T and B lymphocytes in the athymic, nude rat. *Scand J Immunol*, 17(6):551–7, 1983.

[138] S. Han, B. Zheng, J. Dal Porto, and G. Kelsoe. In situ studies of the primary immune response to (4-hydroxy-3-nitrophenyl)acetyl. IV. Affinity-dependent, antigen-driven B cell apoptosis in germinal centers as a mechanism for maintaining self-tolerance. *J Exp Med*, 182(6):1635–44, 1995.

[139] B. Pulendran, G. Kannourakis, S. Nouri, K. G. Smith, and G. J. Nossal. Soluble antigen can cause enhanced apoptosis of germinal-centre B cells. *Nature*, 375(6529):331–4, 1995.

[140] K. M. Shokat and C. C. Goodnow. Antigen-induced B-cell death and elimination during germinal-centre immune responses. *Nature*, 375(6529):334–8, 1995.

[141] D. Cosgrove, D. Gray, A. Dierich, J. Kaufman, M. Lemeur, C. Benoist, and D. Mathis. Mice lacking MHC class II molecules. *Cell*, 66(5):1051–66, 1991.

[142] D. Gray, P. Dullforce, and S. Jainandunsing. Memory B cell development but not germinal center formation is impaired by in vivo blockade of CD40-CD40 ligand interaction. *J Exp Med*, 180(1):141–55, 1994.

[143] P. Vieira and K. Rajewsky. Persistence of memory B cells in mice deprived of T cell help. *Int Immunol*, 2(6):487–94, 1990.

[144] F. G. Kroese, A. S. Wubbena, H. G. Seijen, and P. Nieuwenhuis. Germinal centers develop oligoclonally. *Eur J Immunol*, 17(7):1069–72, 1987.

[145] M. J. Shlomchik, P. Watts, M. G. Weigert, and S. Litwin. Clone: a Monte-Carlo computer simulation of B cell clonal expansion, somatic mutation, and antigen-driven selection. *Curr Top Microbiol Immunol*, 229:173–97, 1998.

[146] R. S. Scott, E. J. McMahon, S. M. Pop, E. A. Reap, R. Caricchio, P. L. Cohen, H. S. Earp, and G. K. Matsushima. Phagocytosis and clearance of apoptotic cells is mediated by MER. *Nature*, 411(6834):207–11, 2001.

[147] I. C. MacLennan. Germinal centers. *Annu Rev Immunol*, 12:117–39, 1994.

[148] R. Parnaik, M. C. Raff, and J. Scholes. Differences between the clearance of apoptotic cells by professional and non-professional phagocytes. *Curr Biol*, 10 (14):857–60, 2000.

[149] I. G. Luzina, S. P. Atamas, C. E. Storrer, L. C. daSilva, G. Kelsoe, J. C. Papadimitriou, and B. S. Handwerger. Spontaneous formation of germinal centers in autoimmune mice. *J Leukoc Biol*, 70(4):578–84, 2001.

[150] U. S. Gaipl, A. Sheriff, S. Franz, L. E. Munoz, R. E. Voll, J. R. Kalden, and M. Herrmann. Inefficient clearance of dying cells and autoreactivity. *Curr Top Microbiol Immunol*, 305:161–76, 2006.

[151] A. N. Theofilopoulos, P. J. McConahey, S. Izui, R. A. Eisenberg, A. B. Pereira, and W. D. Creighton. A comparative immunologic analysis of several murine strains with autoimmune manifestations. *Clin Immunol Immunopathol*, 15(3): 258–78, 1980.

[152] K. A. Fuller, O. Kanagawa, and M. H. Nahm. T cells within germinal centers are specific for the immunizing antigen. *J Immunol*, 151(9):4505–12, 1993.

[153] B. Zheng, S. Han, and G. Kelsoe. T helper cells in murine germinal centers are antigen-specific emigrants that downregulate Thy-1. *J Exp Med*, 184(3): 1083–91, 1996.

[154] G. Kelsoe. The germinal center reaction. *Immunol Today*, 16(7):324–6, 1995.

[155] S. Fillatreau and D. Gray. T cell accumulation in B cell follicles is regulated by dendritic cells and is independent of B cell activation. *J Exp Med*, 197(2): 195–206, 2003.

[156] A. Gulbranson-Judge and I. MacLennan. Sequential antigen-specific growth of T cells in the T zones and follicles in response to pigeon cytochrome c. *Eur J Immunol*, 26(8):1830–7, 1996.

[157] B. Zheng, S. Han, Q. Zhu, R. Goldsby, and G. Kelsoe. Alternative pathways for the selection of antigen-specific peripheral T cells. *Nature*, 384(6606):263–6, 1996.

[158] D. van Essen, P. Dullforce, T. Brocker, and D. Gray. Cellular interactions involved in Th cell memory. *J Immunol*, 165(7):3640–6, 2000.

[159] P. J. Linton, J. Harbertson, and L. M. Bradley. A critical role for B cells in the development of memory CD4 cells. *J Immunol*, 165(10):5558–65, 2000.

[160] C. C. Congdon and J. W. Goodman. Changes in lymphatic tissues during foreign tissue transplantation. In A. P. Christoffanini and G. Hoecker, editors, *International Symposium on Tissue Transplantation*, page 181, Universidad de Chile, Santiago, 1961.

[161] T. J. Flotte, T. A. Springer, and G. J. Thorbecke. Dendritic cell and macrophage staining by monoclonal antibodies in tissue sections and epidermal sheets. *Am J Pathol*, 111(1):112–24, 1983.

[162] K. Takahashi. Development and Differentiation of Macrophages and Related Cells : Historical Review and Current Concepts. *Journal of Clinical and Experimental Hematopathology*, 41(1):1–33, 2001.

[163] M. Kotani, K. Okada, H. Fujii, H. Tsuchiya, K. Matsuno, S. Ekino, and S. Fukuda. Lymph macrophages enter the germinal center of lymph nodes of guinea pigs. *Acta Anat (Basel)*, 99(4):391–402, 1977.

[164] A. K. Szakal, M. H. Kosco, and J. G. Tew. A novel in vivo follicular dendritic cell-dependent iccosome-mediated mechanism for delivery of antigen to antigen-processing cells. *J Immunol*, 140(2):341–53, 1988.

[165] L. Gorelik, K. Gilbride, M. Dobles, S. L. Kalled, D. Zandman, and M. L. Scott. Normal b cell homeostasis requires b cell activation factor production by radiation-resistant cells. *J Exp Med*, 198(6):937–45, 2003.

[166] P. A. Moore, O. Belvedere, A. Orr, K. Pieri, D. W. LaFleur, P. Feng, D. Soppet, M. Charters, R. Gentz, D. Parmelee, Y. Li, O. Galperina, J. Giri, V. Roschke, B. Nardelli, J. Carrell, S. Sosnovtseva, W. Greenfield, S. M. Ruben, H. S. Olsen, J. Fikes, and D. M. Hilbert. BLyS: member of the tumor necrosis factor family and B lymphocyte stimulator. *Science*, 285(5425):260–3, 1999.

[167] B. Nardelli, O. Belvedere, V. Roschke, P. A. Moore, H. S. Olsen, T. S. Migone, S. Sosnovtseva, J. A. Carrell, P. Feng, J. G. Giri, and D. M. Hilbert. Synthesis and release of B-lymphocyte stimulator from myeloid cells. *Blood*, 97(1):198–204, 2001.

[168] P. Scapini, B. Nardelli, G. Nadali, F. Calzetti, G. Pizzolo, C. Montecucco, and M. A. Cassatella. G-CSF-stimulated neutrophils are a prominent source of functional BLyS. *J Exp Med*, 197(3):297–302, 2003.

[169] J. B. Howie and B. J. Helyer. The immunology and pathology of NZB mice. *Adv Immunol*, 9:215–66, 1968.

[170] A. N. Theofilopoulos and F. J. Dixon. Murine models of systemic lupus erythematosus. *Adv Immunol*, 37:269–390, 1985.

[171] E. Ninomiya, Y. Ito, M. A. Shibata, K. Kawashima, T. Sakamoto, E. Maruyama, H. Doi, K. Tokitsu, and Y. Otsuki. The activation of caspase-3 and DNA fragmentation in B cells phagocytosed by macrophages. *Med Electron Microsc*, 36(2):87–93, 2003.

[172] R. E. Garner, A. P. Malick, A. D. Yurochko, and K. D. Elgert. Shifts in macrophage (M phi) surface phenotypes during tumor growth: association of Mac-2+ and Mac-3+ M phi with immunosuppressive activity. *Cell Immunol*, 108(2):255–68, 1987.

[173] A. P. Malick, K. D. Elgert, R. E. Garner, and Jr. Adkinson, N. F. Prostaglandin E2 production by Mac-2+ macrophages: tumor-induced population shift. *J Leukoc Biol*, 42(6):673–81, 1987.

[174] Z. Metzger, J. T. Hoffeld, and J. J. Oppenheim. Macrophage-mediated suppression. I. Evidence for participation of both hdyrogen peroxide and prostaglandins in suppression of murine lymphocyte proliferation. *J Immunol*, 124(2):983–8, 1980.

[175] V. C. Schad and R. P. Phipps. Two signals are required for accessory cells to induce B cell unresponsiveness. Tolerogenic Ig and prostaglandin. *J Immunol*, 141(1):79–84, 1988.

[176] B. A. O'Brien, X. Geng, C. H. Orteu, Y. Huang, M. Ghoreishi, Y. Zhang, J. A. Bush, G. Li, D. T. Finegood, and J. P. Dutz. A deficiency in the in vivo clearance of apoptotic cells is a feature of the NOD mouse. *J Autoimmun*, 26 (2):104–15, 2006.

[177] P. K. Potter, J. Cortes-Hernandez, P. Quartier, M. Botto, and M. J. Walport. Lupus-prone mice have an abnormal response to thioglycolate and an impaired clearance of apoptotic cells. *J Immunol*, 170(6):3223–32, 2003.

[178] U. S. Gaipl, S. Franz, R. E. Voll, A. Sheriff, J. R. Kalden, and M. Herrmann. Defects in the disposal of dying cells lead to autoimmunity. *Curr Rheumatol Rep*, 6(6):401–7, 2004.

[179] M. J. Kaplan. Apoptosis in systemic lupus erythematosus. *Clin Immunol*, 112 (3):210–8, 2004.

[180] M. Bijl, E. Reefman, G. Horst, P. C. Limburg, and C. G. Kallenberg. Reduced uptake of apoptotic cells by macrophages in systemic lupus erythematosus: correlates with decreased serum levels of complement. *Ann Rheum Dis*, 65(1): 57–63, 2006.

[181] R. Licht, J. W. Dieker, C. W. Jacobs, W. J. Tax, and J. H. Berden. Decreased phagocytosis of apoptotic cells in diseased SLE mice. *J Autoimmun*, 22(2): 139–45, 2004.

[182] Y. Ren, J. Tang, M. Y. Mok, A. W. Chan, A. Wu, and C. S. Lau. Increased apoptotic neutrophils and macrophages and impaired macrophage phagocytic clearance of apoptotic neutrophils in systemic lupus erythematosus. *Arthritis Rheum*, 48(10):2888–97, 2003.

[183] D. M. Klinman. Polyclonal B cell activation in lupus-prone mice precedes and predicts the development of autoimmune disease. *J Clin Invest*, 86(4): 1249–54, 1990.

[184] R. Merino, M. Iwamoto, L. Fossati, and S. Izui. Polyclonal B cell activation arises from different mechanisms in lupus-prone (NZB x NZW)F1 and MRL/MpJ-lpr/lpr mice. *J Immunol*, 151(11):6509–16, 1993.

[185] U. Wellmann, A. Werner, and T. H. Winkler. Altered selection processes of B lymphocytes in autoimmune NZB/W mice, despite intact central tolerance against DNA. *Eur J Immunol*, 31(9):2800–10, 2001.

[186] S. L. Kalled, A. H. Cutler, and L. C. Burkly. Apoptosis and altered dendritic cell homeostasis in lupus nephritis are limited by anti-CD154 treatment. *J Immunol*, 167(3):1740–7, 2001.

[187] S. Kirschnek, S. Ying, S. F. Fischer, H. Hacker, A. Villunger, H. Hochrein, and G. Hacker. Phagocytosis-induced apoptosis in macrophages is mediated by up-regulation and activation of the Bcl-2 homology domain 3-only protein Bim. *J Immunol*, 174(2):671–9, 2005.

[188] M. van Eijk and C. de Groot. Germinal center B cell apoptosis requires both caspase and cathepsin activity. *J Immunol*, 163(5):2478–82, 1999.

[189] C. Segundo, F. Medina, C. Rodriguez, R. Martinez-Palencia, F. Leyva-Cobian, and J. A. Brieva. Surface molecule loss and bleb formation by human germinal center B cells undergoing apoptosis: role of apoptotic blebs in monocyte chemotaxis. *Blood*, 94(3):1012–20, 1999.

[190] M. Bemark and M. S. Neuberger. By-products of immunoglobulin somatic hypermutation. *Genes Chromosomes Cancer*, 38(1):32–9, 2003.

[191] G. E. Woloschak and C. J. Krco. Regulation of kappa/lambda immunoglobulin light chain expression in normal murine lymphocytes. *Mol Immunol*, 24(7): 751–7, 1987.

[192] J. M. Teale and E. G. Morris. Comparison of V kappa gene family expression in adult and fetal B cells. *J Immunol*, 143(8):2768–72, 1989.

[193] M. Nishi, T. Kataoka, and T. Honjo. Preferential rearrangement of the immunoglobulin kappa chain joining region J kappa 1 and J kappa 2 segments in mouse spleen DNA. *Proc Natl Acad Sci U S A*, 82(19):6399–403, 1985.

[194] M. Z. Radic, J. Mackle, J. Erikson, C. Mol, W. F. Anderson, and M. Weigert. Residues that mediate DNA binding of autoimmune antibodies. *J Immunol*, 150(11):4966–77, 1993.

[195] M. Shlomchik, M. Mascelli, H. Shan, M. Z. Radic, D. Pisetsky, A. Marshak-Rothstein, and M. Weigert. Anti-DNA antibodies from autoimmune mice arise by clonal expansion and somatic mutation. *J Exp Med*, 171(1):265–92, 1990.

[196] J. S. Park, Y. T. Kim, H. Y. Chung, K. Baek, and Y. J. Jang. Primary structures and chain dominance of anti-DNA antibodies. *Mol Cells*, 11(1): 55–63, 2001.

[197] J. M. Dal Porto, A. M. Haberman, G. Kelsoe, and M. J. Shlomchik. Very low affinity B cells form germinal centers, become memory B cells, and participate in secondary immune responses when higher affinity competition is reduced. *J Exp Med*, 195(9):1215–21, 2002.

[198] C. Berek, A. Berger, and M. Apel. Maturation of the immune response in germinal centers. *Cell*, 67(6):1121–9, 1991.

[199] A. G. Betz, M. S. Neuberger, and C. Milstein. Discriminating intrinsic and antigen-selected mutational hotspots in immunoglobulin V genes. *Immunol Today*, 14(8):405–11, 1993.

[200] A. Gonzalez-Fernandez and C. Milstein. Analysis of somatic hypermutation in mouse Peyer's patches using immunoglobulin kappa light-chain transgenes. *Proc Natl Acad Sci U S A*, 90(21):9862–6, 1993.

[201] U. Klein, Y. Tu, G. A. Stolovitzky, J. L. Keller, Jr. Haddad, J., V. Miljkovic, G. Cattoretti, A. Califano, and R. Dalla-Favera. Gene expression dynamics during germinal center transit in B cells. *Ann N Y Acad Sci*, 987:166–72, 2003.

[202] U. Klein, Y. Tu, G. A. Stolovitzky, J. L. Keller, Jr. Haddad, J., V. Miljkovic, G. Cattoretti, A. Califano, and R. Dalla-Favera. Transcriptional analysis of the B cell germinal center reaction. *Proc Natl Acad Sci U S A*, 100(5):2639–44, 2003.

[203] E. Lindhout and C. de Groot. Follicular dendritic cells and apoptosis: life and death in the germinal centre. *Histochem J*, 27(3):167–83, 1995.

[204] K. Asano, M. Miwa, K. Miwa, R. Hanayama, H. Nagase, S. Nagata, and M. Tanaka. Masking of phosphatidylserine inhibits apoptotic cell engulfment and induces autoantibody production in mice. *J Exp Med*, 200(4):459–67, 2004.

[205] R. Hanayama, M. Tanaka, K. Miwa, A. Shinohara, A. Iwamatsu, and S. Nagata. Identification of a factor that links apoptotic cells to phagocytes. *Nature*, 417(6885):182–7, 2002.

[206] S. H. Kleinstein and J. P. Singh. Why are there so few key mutant clones? The influence of stochastic selection and blocking on affinity maturation in the germinal center. *Int Immunol*, 15(7):871–84, 2003.

[207] M. Weigert, editor. *The influence of somatic mutation on the immune response*, volume VI of *Progress in Immunology.* Academic Press,, New York, 1986.

[208] D. K. Dunn-Walters, A. Dogan, L. Boursier, C. M. MacDonald, and J. Spencer. Base-specific sequences that bias somatic hypermutation deduced by analysis of out-of-frame human IgVH genes. *J Immunol*, 160(5):2360–4, 1998.

[209] S. M. Jackson and J. D. Capra. IgH V-region sequence does not predict the survival fate of human germinal center B cells. *J Immunol*, 174(5):2805–13, 2005.

[210] J. S. Duffield. The inflammatory macrophage: a story of Jekyll and Hyde. *Clin Sci (Lond)*, 104(1):27–38, 2003.

Appendix A

Supplemental material

A.1 Absorption and emission maxima of Alexa dyes

Dye	A_{max} [nm]	E_{max} [nm]
A488	494	519
A546	556	573
A555	555	565
A594	590	617
A647	650	668

Table A.1: Absorption and emission maxima (A_{max}, E_{max}) of Alexa dyes.

A.2 Confocal microscope and image acquisition settings

Image acquisition applying Leica DM Ire2 confocal microscope	
Objectives	HC PL APO 10x0.40 IMM UV
	HPX PL APO CS 40x1.25 OIL PH
	HCX PL APO CS 63x1.40 OIL UV
Zoom	1
Pinhole	1 Airy
Format	1024 × 1024 pixel
Frame average	8
Ar (50 mW): 488 nm	(ch0: FITC, A488; green RGB pseudocolor)
GreenHeNe (1.2 mW): 543 nm	(ch1: A546; red RGB pseudocolor)
RedHeNe (10 mW): 633 nm	(ch2: Cy5, APC, A647; blue RGB pseudocolor)
xy-scan	sequential, between frames

Table A.2: Applied settings for image acquisition using the Leica DM Ire2 confocal laser scanning microscope. Listed settings are valid for images if not otherwise annotated.

Image acquisition applying Leica TCS SP2 confocal microscope, IFN Magdeburg	
Objectives	HC PL APO CS 10.0x0.40 UV HPX PL APO CS 40x1.25 OIL PH
Zoom	1.2
Pinhole	1 Airy
Format	512 × 512 pixel
Frame average	4
Ar (50 mW): 488 nm	(A488)
GreenHeNe (1.2 mW): 543 nm	(A555, A594)
RedHeNe (10 mW): 633 nm	(A647)
xy-scan	sequential, between frames
overlap	50 pixel
*alignmen*t	moving block alignment

Table A.3: Applied settings for image acquisition using the Leica TCS SP2 confocal laser scanning microscope, IFN Magdeburg. Listed settings are valid for images if not otherwise annotated.

A.3 Survey of ImageJ based macros

Macro ID	Action	Output
GC area	assignment and measurement of GC boundaries, referred to as regions of interest (ROIs)	areas of ROIs [μm^2]
Count Ki all	automated detection, segmentation and measurement of Ki-67+ cells within assigned ROIs	number of Ki-67+ cells
FitEllipse	parametrization of ROIs by an ellipse fitting algorithm	major and minor radii of fitted ellipses
GC count cells	facilitation of manual counting of GC macrophages and T cells	
MacroROIVolumes	binarization of segmented outlines (ROIs) of GC	aligned and unaligned binary 8-bit images of individual ROIs, coordinates of ROIs

Table A.4: Survey of ImageJ based macros.

A.4 Supplemental figures

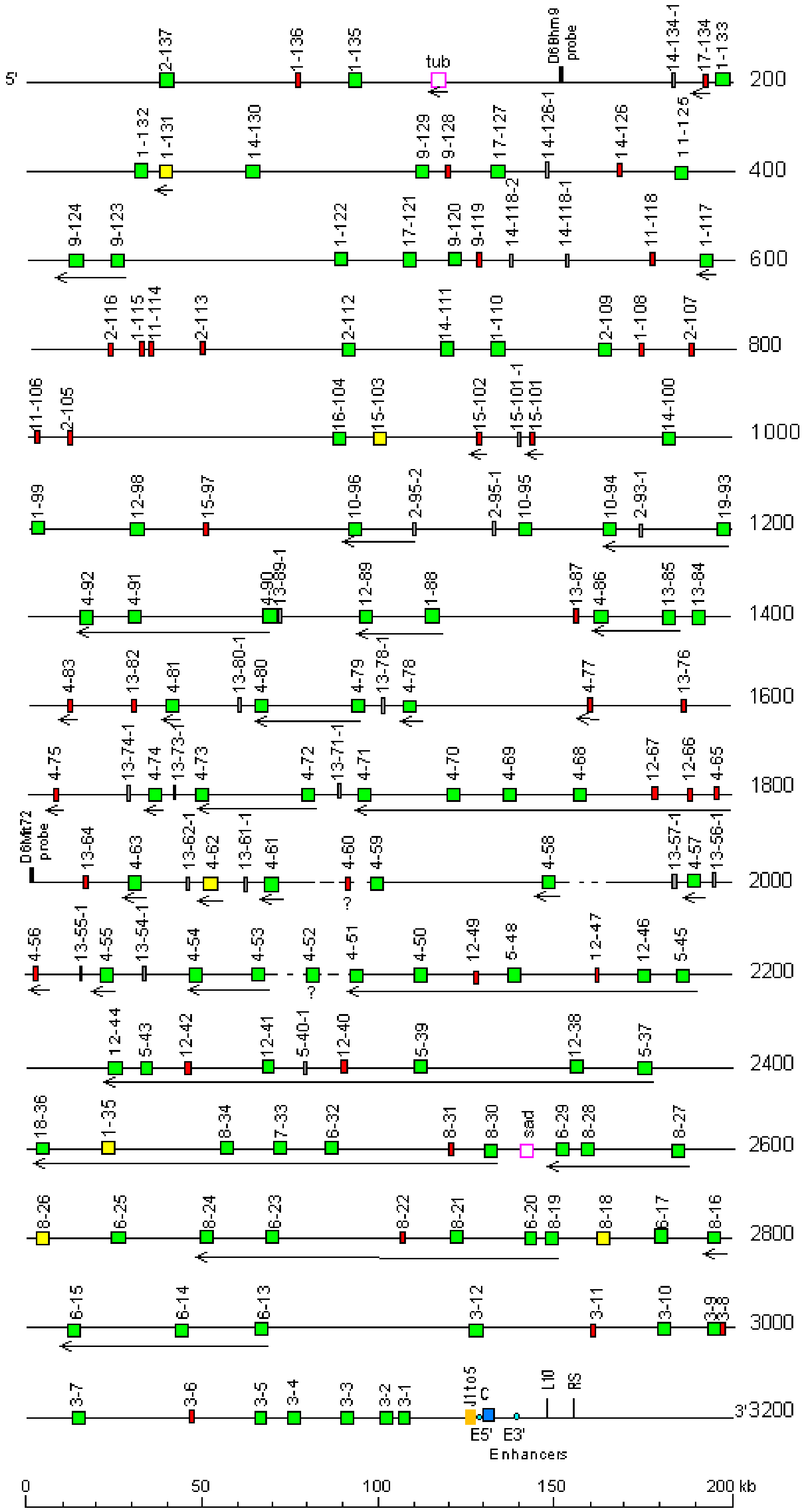

Figure A.1: Murine Igκ locus representation [2].

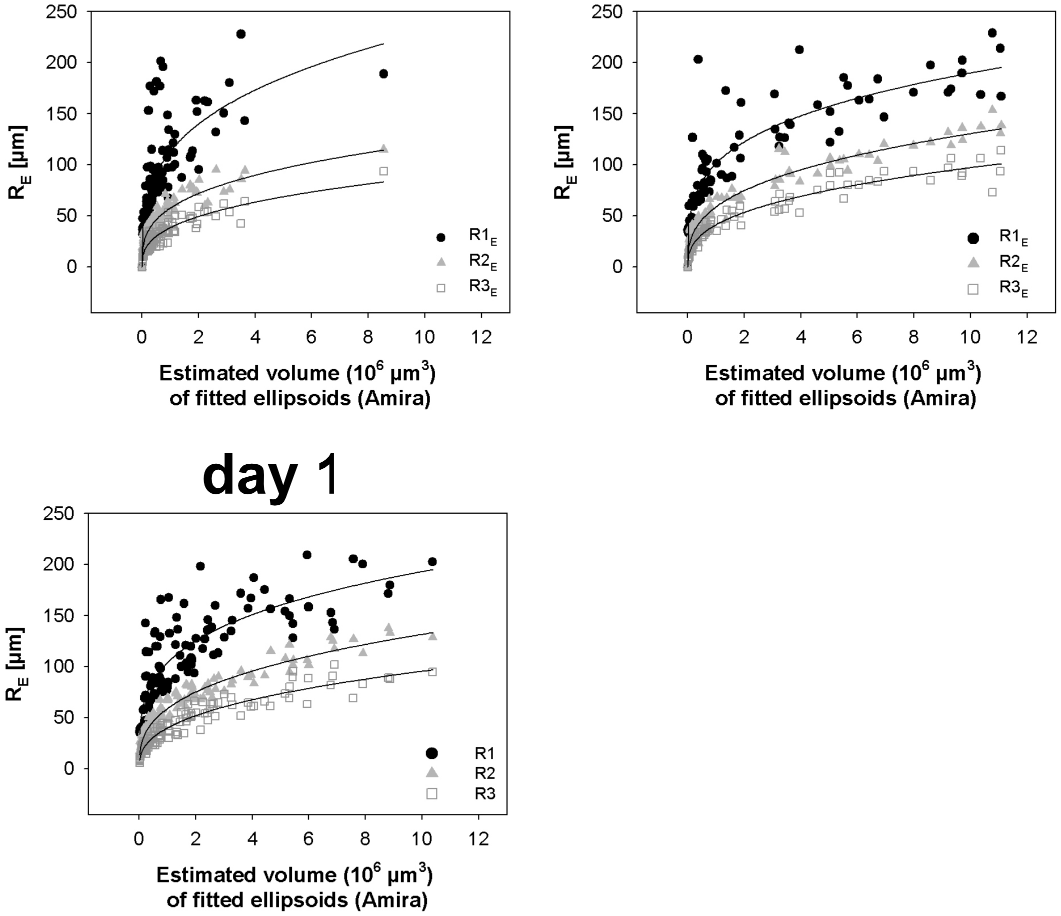

Figure A.2: The 3-D shape of GC as assessed by 3-D alignment of whole spleen sections. Illustrated is the interrelation of shape and size of GC as revealed by 3-D reconstruction of in each case three spleens at day 6, 10 and 14 after immunization. In contrast to figure 4.16 alignment of sections was not performed slicewise for individual GC but for whole sections. The radii of fitted GC ellipsoids ($R1_E$, $R2_E$ and $R3_E$) are plotted separately against the underlying volumes of the very GC. Best-fit curves resulting from power regression analysis ($R_E = a \cdot V^b$) are depicted as solid lines. The respective values of constants (a), exponents (b) and squared correlation coefficients (R^2) are shown next to the curves.

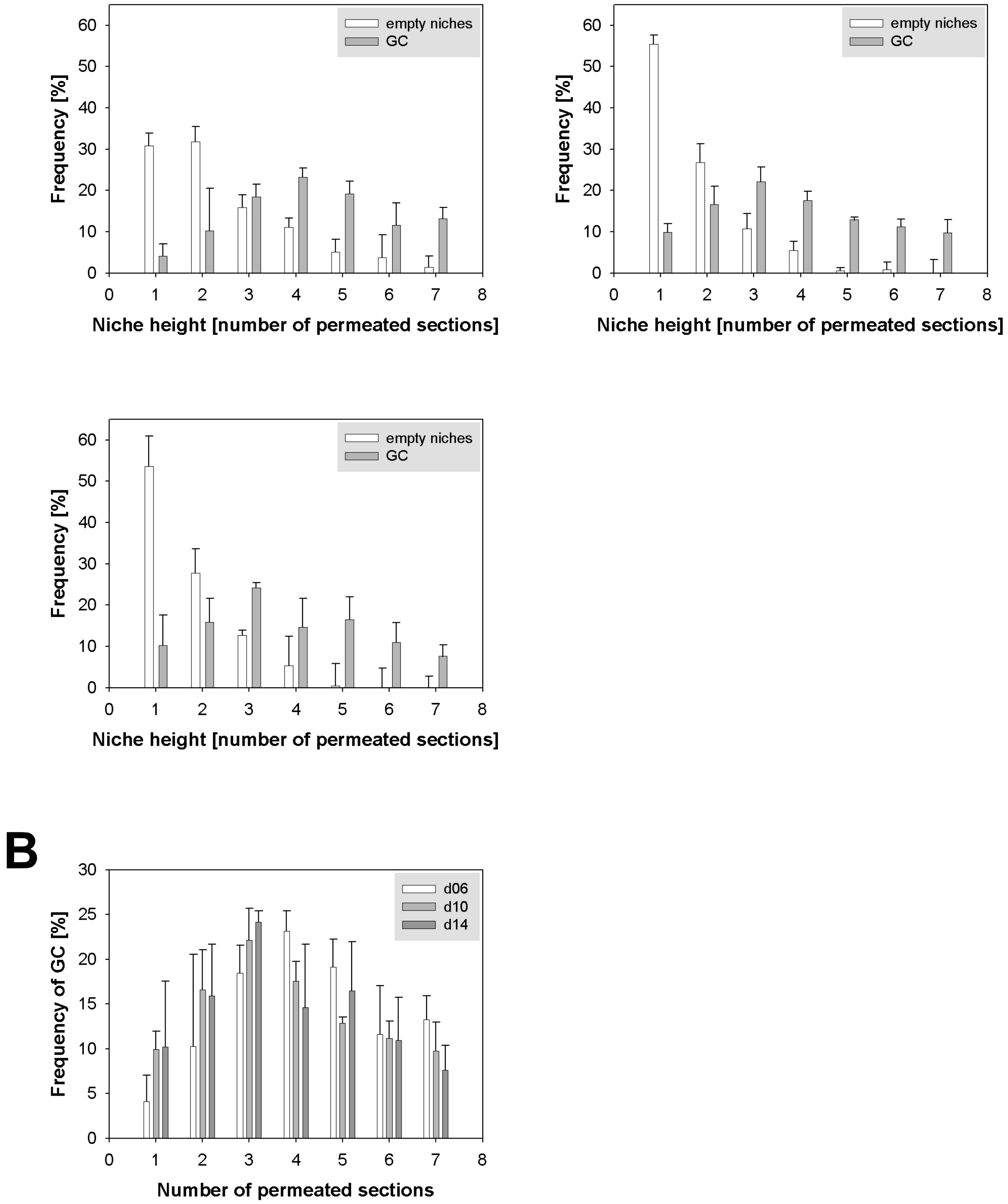

Figure A.3: Penetration depths of follicular niches. (A) Illustrated are the frequencies of empty follicular niches and niches occupied by GC permeating a given number of spleen sections at day 6, 10 and 14 after immunization. (B) Comparative illustration of frequencies of GC permeating a given number of spleen sections at day 6, 10 and 14.

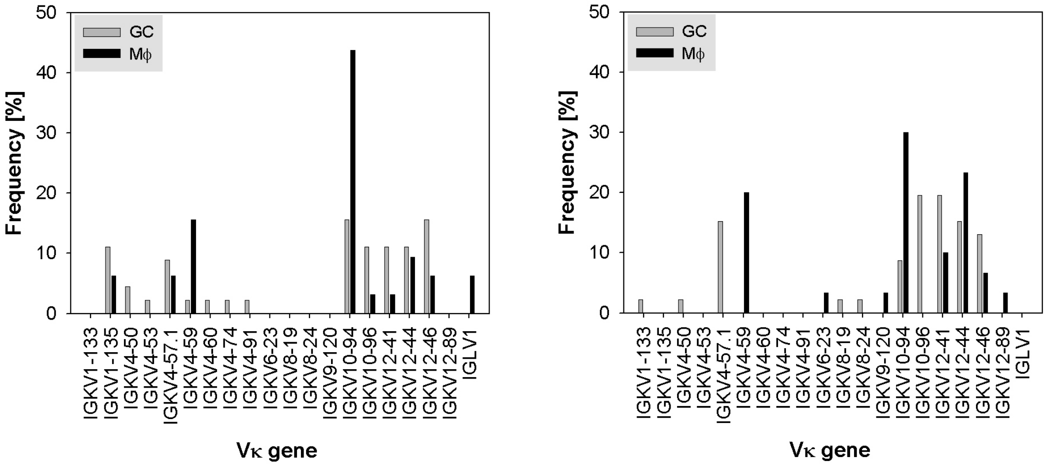

Figure A.4: V$_L$ gene segment usage among live (GC, grey) and phagocytosed (Mϕ, black) B cell fractions derived from phOx-CSA challenged BALB/c mice at days 8 (A) and 12 (B). V$_L$ gene segments were identified using the IMGT/V-Quest database [90].

A.5 IgL sequence alignments

The IgL sequence alignments are documented on the appendant CD-ROM. Sequences are aligned according to their V$_L$ gene and are compared to germline sequences. Only the nucleotides differing from the germline sequence are presented: dashes represent identity, capital letters indicate mutations. The label "GC" always refers to IgL sequences derived from live B cell fractions, whereas "M" refers to phagocytozed B cell fractions. The label "77" indicates sequences that were obtained by amplification with the IGKV4-59 (VκOx1) gene specific primer Vκ77 (Section 3.10.2).

A.6 Manufacturer listing

Manufacturer	Location, State
Alexis	Grünberg, Germany
Ambion	Austin, TX, USA
Amersham Biosciences	Freiburg, Germany
Arcturus	Sunnyvale, CA, USA
Becton Dickinson Pharmingen	San Jose, CA, USA
Bio101	Carlsbad, CA, USA
Biometra	Göttingen, Germany
Biorad	München, Germany
Biozym Diagnostics	Hessisch Oldendorf, Germany
Corning	Corning, NY, USA
Costar	Cambridge, MA, USA
Dako	Glostrup, Denmark
Eppendorf-Netheler-Hinz	Köln, Germany
FMC Bioproducts	Rockland, USA
Gibco BRL Life Technologies	Gaithersburg, MD, USA
Greiner Bio-One	Frickenhausen, Germany
Heraeus	Hanau, Germany
ICN Biomedicals	Eschwege, Germany
ImmunoK, AMS Biotechnology	Abingdon, UK
Invitrogen	Hamburg, Germany
Leica Microsystems GmbH	Wetzlar, Germany
Macherey-Nagel	Düren, Germany
Menzel	Braunschweig, Germany
Merck	Darmstadt, Germany
Microm	Walldorf, Germany
Millipore	Bedford, MA, USA
Miltenyi Biotech	Bergisch Gladbach, Germany
Molecular Probes, Invitrogen	Eugene, OR, USA
MWG	Ebersberg, Germany
Perkin Elmer Apllied Biosystems	Forster City, USA
Pierce	Rockford, IL, USA
Promega	Mannheim, Germany
Qiagen	Hilden, Germany
R&D Systems	Minneapolis, MN, USA
Roche	Mannheim, Deutschland
Roth	Karsruhe, Germany
Sakura Finetek Europe	Zoeterwoude, The Netherlands
Schärfe System	Reutlingen, Germany
Serotec	Düsseldorf, Germany
Sigma-Aldrich	Taufkirchen, Germany
TibMolBiol	Berlin, Germany
Vector	Burlingame, CA, USA
Vogel	Berlin, Germany

Table A.5: List of manufacturers.

Appendix B

Abbreviations

A488	Alexa Fluor 488
A546	Alexa Fluor 546
A555	Alexa Fluor 555
A594	Alexa Fluor 594
A647	Alexa Fluor 647
Ab	antibody
APC	antigen presenting cell
Ar	argon laser
BCR	B cell receptor
bp	base pair
BSA	bovine serum albumin
C	constant region
CD	cluster of differentiation
CDR	complementary determining region
CGG	chicken gamma globulin
CSA	chicken serum albumin
CR	complement receptor
Cy5	cyanine 5
D	diversity gene segment
DNA	deoxyribonucleic acid
DNP	2,4-dinitrophenol
dNTP	deoxynucleotide triphosphate
DZ	dark zone
EDTA	ethylene diamine tetraacetate
Fab	fragment antigen binding
FACS	fluorescence activated cell sorting
Fc	fragment crystallizable
FDC	follicular dendritic cells
FITC	fluorescein isothiocyanate
FR	framework region
GC	germinal center
HSA	human serum albumin
HeNe	helium neon laser
Ig	immunoglobulin
IgH	immunoglobulin heavy chain
IgL	immunoglobulin light chain
IHC	immunohistochemistry
i.p.	intraperitoneal
IPTG	isopropyl-beta-D-thiogalactopyranoside
J	joining gene segment

kDa	kilo dalton
LCDR3	light chain CDR3
LZ	light zone
M	molar
Mϕ	macrophage
mAb	monoclonal antibody
MHC	major histocompatibility complex
MSH	spider crab hemocyanin
NP	(4-hydroxy-3-nitrophenyl)acetyl
ORF	open reading frame
PALS	periarteriolar lymphoid sheath
PBA	PBS containing 0.5% bovine serum albumin
PBS	phosphate buffered saline
PCA	principal component analysis
PCR	polymerase chain reaction
PE	Phycoerythrin
PFA	paraformaldehyde
phOx	2-phenyloxazolone
PI	propidium iodide
PNA	peanut aggutinin
RA	rheumatoid arthritis
RF	rheumatoid factor
Rho	rhodamine
RNA	ribonucleic acid
rpm	rounds per minute
RT-PCR	reverse transcription PCR
SA	streptavidin
SLE	systemic lupus erythematosus
SHM	somatic hypermutation
SRBC	sheep red blood cells
Taq	thermus aquaticus
TCR	T cell antigen receptor
TdT	terminal deoxynucleotidyl transferase
TUNEL	TdT-mediated dUTP nick-end labeling
V	variable gene segment/region
X-Gal	5-bromo-4-chloro-3-indolyl-[β]-D-galactopyranoside

Table B.1: Abbreviations.

Acknowledgment

This thesis work was performed with encouragement and support of many colleagues and friends whom I want to thank for their efforts. I would like to thank,

Dr. Michal Or-Guil, my supervisor. Thank you for accepting me as a graduate student in the junior research group "Systems Immunology" and introducing me to the world of mathematical modeling and simulations. Thanks also for giving me the freedom and space to develop and debate (albeit sometimes crazy) theories, experiments and protocols. I very much appreciate your support, motivation and trust along the way. And of course, for giving me the opportunity and encouraging me to attend as many conferences, workshops and meetings as possible.

Prof. Dr. Hans-Dieter Volk und **PD Dr. Rudolf Manz**, for agreeing to evaluate my thesis.

Prof. Dr. Andreas Radbruch, for giving me the opportunity to perform the experiments of this thesis at the German Arthritis Research Center (DRFZ). **PD Dr. Claudia Berek**, for first getting me interested in germinal centers during my diploma thesis and for passing on her vast knowledge about B cells and in particular B cell receptor sequences.

Dr. Johannes Schuchhardt, for fruitful discussions, crazy ideas and support. **Dr. Michal Sibila** for help with the 3-D reconstructions. **Dr. Werner Zuschratter** for letting me use the confocal microscope at the IFN for acquisition of meander scans.

Anke, for endless enthusiasm, empathy and becoming a dear friend. Your assistance has been invaluable and working with you has been a pleasure. Thank you for cultivating such crazy things like the hairy egg theory, "Indianerboote bauen", Kakuro competitions and Magdeburg day and night marathon microscopy sessions. Again thank you for escorting me to the copy shop when I did the first print of this thesis, ... otherwise I might have collapsed underway. **Armin**, for phsychological support on that day the 250 GB external hard disk decided to stop working (...and got me insane). Thank you, for always being willing to help, whether to write perplexing tiny macros or to discuss the tangled world of CDR3s. Thanks to the other fellow members of the Systems Immunology group... **Nicole, Jule, Ati, Lei, Holger and Andre**, for their cooperativeness, patience and great company. I especially want to thank Ati for her assistance in doing 200 minipreps a day! Thanks to my second "felt" workgroup... **Thordis, Ben, David, Caspar, Verena, Jae, Frank, Anke** and **Ati**, for the great atmosphere, lots of fun times, cakes, "Inverterofen" and practicing how to fold a T-shirt the japanese way.

Thordis, ... die Sonne ist warm, das Gras ist grün, und von hinten kommt ein Wildschwein angerannt!!! Danke dafür, dass du meine Leidenschaft für ausgefallene Küchegeräte teilst, man kann nie genug davon haben! Auf hoffentlich noch viele wunderschöne Kochabende (wir müssen übrigens noch einen Brief schreiben, fällt mir da ein)! **Marko**, ... dafür, daß du so ein guter Freund bist auf den ich mich immer verlassen kann. Ich danke dir für deine Geduld und deine Nachsicht. ♪Alle zusammen tanzt das Brot, wir sitzen doch alle im selben Boot. Die Arme zu kurz das Lied beknackt, ein Elend im 4/4 Takt. ♪

Ich danke meiner ganzen Familie dafür, daß sie so ist, wie sie ist. Ich danke meinen beiden **Omas** für ihre Unterstüzung und Zuversicht. **Monika, Klaus und Shadow**, ich danke euch für unvergessene Ostseetage, wunderschöne Wanderungen, eure Unterstüzung und Liebe.

Mein innigster Dank geht an meine wunderbaren Eltern. Danke, für eure Unterstützung, Freundschaft und Liebe, euer Vertrauen und euren Glauben an mich. Danke, daß ihr mir von klein an gezeigt habt wie groß die Welt ist und was es alles zu entdecken gibt. ♡

This work was kindly supported by the VolkswagenFoundation

Curriculum vitæ

Dipl.-Ing. Nicole Wittenbrink
Wichertstr. 39
10439 Berlin, Germany
tel.: +49 30 44715125
e-mail: n.wittenbrink@biologie.hu-berlin.de

Education

2002 - 2007:	PhD thesis, Humboldt University of Berlin, Institute for Theoretical Biology, Research Group Systems Immunology
August 2002:	Diploma in Medical Biotechnology (Graduate Engineer), Technical University Berlin
July 1995:	Higher Education Entrance Qualification, CJD Gymnasium Versmold

Research Experience

2002 - present:	Doctoral Research in the Systems Immunology Group (Dr. M. Or-Guil) Immunology, Humboldt University of Berlin, Berlin, Germany
2001-2002:	Research Assistant in the B Cell Immunology Group (PD Dr. C. Berek) at the German Arthritis Research Centre (DRFZ), Berlin, Germany
2000-2001:	Diploma thesis in the B Cell Immunology Group (PD Dr. C. Berek) at the German Arthritis Research Centre (DRFZ), Berlin, Germany Title: "Investigation of the immune response in premature infants: Analysis of the V_H gene repertoire"
1999-2000:	Internship in the Xenotransplantation Research Group (Dr. B. Ehlers) at the Robert Koch Institute Berlin (RKI), Berlin, Germany
1999:	Internship in the Department of Molecular Genetics at Roche, Penzberg, Germany

Abstracts and Presentations

08/2007	**N. Wittenbrink**, A. Klein, M. Or-Guil. A new, central role for macrophages in retaining germinal center B cell homeostasis and preventing autoimmunity. Abstract accepted for oral presentation at the 13th International Congress of Immunology, Rio de Janeiro, Brazil.
02/2007	M. Or-Guil and **N. Wittenbrink**. Continiuous renewal of germinal center cell populations: The true strategy of affinity maturation? Contributed talk at the Anual Congress of the British Society of Immunology (BSI), Glasgow, UK.
09/2006	**N. Wittenbrink**, A. Klein, J. Schuchhardt, M. Or-Guil. Tracing the dynamics of the cellular players of the germinal center reaction. Poster presentation at the European Congress of Immunology (ECI), Paris, France.
	N. Wittenbrink, A. Klein, J. Schuchhardt, M. Or-Guil. Assessing the real size distribution of germinal centers. Poster presentation at the European Congress of Immunology (ECI), Paris, France.
05/2006	**N. Wittenbrink**, A. Klein, J. Schuchhardt, M. Or-Guil. Tracing the dynamics of the cellular players of the germinal center reaction. Poster presentation at XXIII ISAC congress, Quebec, Canada.
	N. Wittenbrink, A. Klein, J. Schuchhardt, M. Or-Guil. Assessing the real size distribution of germinal centers. Poster presentation at XXIII ISAC congress, Quebec, Canada.
07/2005	**N. Wittenbrink**, J. Schuchhardt, M. Or-Guil. Regulation of GC dynamics by macrophages: Experiment vs. Model. Poster presentation at the 6th European Conference on Mathematical and Theoretical Biology (ECMTB), Dresden, Germany.
04/2005:	**N. Wittenbrink**, C. Berek, J. Schuchhardt, M. Or-Guil. Dynamic of apoptosis and uptake of apoptotic cells in the germinal center. Poster presentation at the 15th Germinal Center Conference, Potsdam, Germany.
06/2004:	**N. Wittenbrink**. Apoptosis and negative selection in germinal centers. Talk given in the context of the Summer School on Cell Biology and Mathematical Modeling, Island of Hvar, Croatia.
03/2004	**N. Wittenbrink**, M. Or-Guil. Apoptosis and negative selection in germinal centers - Gaining insights into the evolution of antibodies. Contributed Talk at the Colloquium Biochemistry Theoretical Biology, Berlin, Germany.

12/2003:	**N. Wittenbrink**, C. Berek, M. Or-Guil. Life and death in germinal centers. Poster presentation at the 2nd Berlin Student Day of Life Sciences, Berlin, Germany.
11/2003:	**N. Wittenbrink**, C. Berek, M. Or-Guil. Life and death in germinal centers. Poster presentation at the 4th International EMBL PhD student symposium "A Life of Encounters: Recognition in Biology", Heidelberg, Germany.
09/2003	**N. Wittenbrink**, M. Or-Guil. Spatial distribution of negatively selected cells during cell evolution in lymphatic tissue. Contributed Talk at the 8th Autumn Seminar "Strukturbildung in Chemie und Biophysik", Salzwedel, Germany.

Honors and Awards

05/2006:	Outstanding poster award, XXIII ISAC congress, Quebec, Canada
12/2003:	2nd prize for poster presentation, Berlin Student Day of Life Sciences, Berlin, Germany

Publications

M. Or-Guil, **N. Wittenbrink**, A. A. Weiser, J. Schuchhardt. Recirculation of germinal center B cells: A multi-level selection strategy for antibody maturation. Immunol Rev 2007; 216:130-41.

N. Wittenbrink, M. Zemlin, K. Bauer, C. Berek. Exposure to environmental antigens induces the development of germinal centers in premature neonates. Dev Immunol 2002; 9(3):177-9.

F. Widen, M. Goltz, **N. Wittenbrink**, B. Ehlers, M. Banks, S. Belak. Identification and sequence analysis of the glycoprotein B gene of porcine cytomegalovirus. Virus Genes 2001; 23(3):339-46.

N. Wittenbrink, A. Klein, A. A. Weiser, J. Schuchhardt, M. Or-Guil. New concepts of affinity maturation as revealed by non-synchronous formation and growth of germinal centers. (*Manuscript in preparation*)

N. Wittenbrink, A. A. Weiser, M. Or-Guil. Two sides of the same coin: Comparative IgL sequence analysis of living and apoptotic germinal center B cells. (*Manuscript in preparation*)

Selbständigkeitserklärung

Hiermit erkläre ich an Eides statt, dass ich die vorliegende Arbeit mit dem Titel "New perspectives on the evolution of B lymphocytes in germinal centers" selbstständig und ohne Hilfe Dritter angefertigt habe. Sämtliche Hilfsmittel, Hilfen sowie Literaturquellen sind als solche kenntlich gemacht.

Ich habe mich anderwärts nicht um einen Doktorgrad beworben und besitze auch keinen entsprechenden Doktorgrad.

Mir ist die dem Verfahren zugrunde liegende Promotionsordnung bekannt.

Berlin, den

Nicole Wittenbrink